

Technical Report 1696
September 1995

Anomalous Behavior of the *Pd/D* System

S. J. Szpak
P. A. Mosier–Boss

EXECUTIVE SUMMARY

OBJECTIVE

The objective is to document the results obtained from the Naval Command, Control and Ocean Surveillance Center RDT&E Division (NRaD), formerly Naval Ocean Systems Center (NOSC), program on the anomalous effects exhibited by the PdID system.

RESULTS AND CONCLUSIONS

In a news conference on 23 March 1989, Martin Fleischmann and Stanley Pons announced that nuclear events could be initiated by the electrochemical compression of deuterium into a palladium lattice. When researchers around the world tried to reproduce the effects described by Pons and Fleischmann in their laboratories, the results were mixed. The nature of the announcement and the irreproducibility of the effect divided the scientific community into believers and skeptics, indicating religious fervor rather than scientific reasoning.

Shortly after the Fleischmann–Pons announcement, a program at NRaD investigated anomalous effects in the PdID system. The NRaD program investigated the PdID system using standard electrochemical techniques to determine conditions for achieving high PdID loadings. Metallurgical aspects of the PdID system and the effect of additives were also examined. Tritium content in the gas/liquid phases and radiation emissions were monitored during electrolysis. This report summarizes the investigation results.

CONTENTS

1. INTRODUCTION	1
1.1 THE ANNOUNCEMENT	1
1.2 THE TURNING POINT	2
1.3 COLLABORATION: A TRI-LABORATORY EFFORT; RESEARCH AT NRAD	2
2. THE PD/D SYSTEM	3
2.1 CONSTRUCTION OF THE PERFORMANCE ENVELOPE	3
2.2 TRIGGERING CONDITIONS	4
3. CONTRIBUTIONS FROM NRAD LABORATORY	5
3.1 THE CODEPOSITION PROCESS	5
4. PUBLICATIONS/PRESENTATIONS	6
5. CONCLUDING REMARKS	9
APPENDIX A – TECHNICAL PAPERS	A-1

Figures

1. An example of an e-mail message which reflects the views of many “skeptics” of cold fusion	1
--	---

1. INTRODUCTION

These introductory remarks illustrate the controversial climate that existed when the NRaD program investigated the anomalous effects the *Pd/D* system exhibited. These effects included, among others, excess enthalpy production at rates exceeding those usually associated with chemical reactions. The controversy concerns the origin of the observed excess enthalpy which, according to Fleischmann and Pons, is due to room temperature nuclear events involving deuterons present within the *Pd* lattice, hence, the term cold fusion. To avoid unnecessary arguments, this report refers to the phenomenon as the Fleischmann-Pons (FP) effect.

1.1 THE ANNOUNCEMENT

The announcement by Martin Fleischmann and Stanley Pons on 23 March 1989 (TV news, press release) that nuclear events could be initiated by electrochemically compressing deuterium into the palladium lattice astounded the world. They said that these events manifest themselves in the form of excess enthalpy production. Often, the production rate was such that sudden electrolyte boiling could be observed in cells operating under steady state for a long time. In these cells, the heat generation rate was consistent with that expected for nuclear processes taking place in a fast-breeder reactor.

Unfortunately, the mode of the announcement, the term cold fusion, and the invasion of the traditional physicist's domain by chemists, resulted in hostilities combined with hopes that cold fusion research would go away. The e-mail in figure 1 illustrates the continuing controversy over cold fusion.

```
Article: 1370 of sci.physics.fusion

Newsgroups: sci.physics.fusion
Subject: Re: Salt Lake and the 5 megabucks

Date: 27 Oct 90 21:54:35 GMT

Lines: 20

>
>I humbly suggest that a financial loss of $5M isn't, in itself, noteworthy.

And I not so humbly suggest that you are totally clueless. That $5M is only
the tip of the iceberg monetarily. Then there's the loss of 6 months to a
year of hundreds of scientists productivity which went into teaching these
two miscreants some basic nuclear physics (e.g. no neutrons - no fusion).
If you think I'm annoyed, you're right. I'm one of those hundreds who gave
these two the benefit of the doubt. This was foolishness on my part,
however, because if they had gone through proper peer review there would
have been no doubt.

Getting back to the money issue. Even now, after this whole thing has been
shown to be nonsense, there are still people out there getting money from
their managers to work on this. So the total cost has yet to be tallied but
it is FAR more than $5M. BTW your comparisons to movie making, etc are
irrelevant.
```

Figure 1. An example of an e-mail message which reflects the views of many "skeptics" of cold fusion.

Few of the many attempts to reproduce the reported results have been successful. However, new reports of heat generation, production of neutrons, tritium, helium - 4 and γ - and X- ray emission have been published. It appears that yesterday's pathological science is becoming today's legitimate

field for scientific inquiry. Pathological science, a term coined by Langmuir and modified by Morrison in 1991 at the Second International Conference on Cold Fusion, is the elevation of illusions to scientific truths.

1.2 THE TURNING POINT

The turning point regarding the hostile attitude toward cold fusion research appears to be The Second International Conference on Cold Fusion, held at Villa Olmo, Como, Italy (June/July 1991). In attendance, among others, was a noted German electrochemist and a former Director of the Max Planck Institute for Physical Chemistry in Berlin, Prof. H. Gerischer. By his own admission, Prof. Gerischer came to Como as a skeptical observer. He left the meeting convinced that anomalous effects do, indeed, occur in the *Pd/D* system and, in a separate memorandum, admonished German scientists with a statement: “The fact that in the Republic of Germany this work has been inhibited is no longer justified. It could be regarded as a very unfortunate gap in German research when compared with the present activity in other countries and particularly in the USA and Japan” (translation of the German text).

1.3 COLLABORATION: A TRI-LABORATORY EFFORT; RESEARCH AT NRAD

The Naval Ocean Systems Center (NOSC), now the Naval Command, Control, and Ocean Surveillance Center, Research, Test and Evaluation Division (NRaD), and the Naval Weapons Center (NWC), China Lake, reported on their early work at the Second International Conference on Cold Fusion and were recognized for providing substantial contributions to the understanding of the FP effect. Shortly after this conference, the Office of Naval Research (ONR) proposed a collaborative effort between NRaD, NWC and Naval Research Laboratory (NRL) to investigate the anomalous effects associated with the prolonged charging of the *Pd/D* system. This effort’s basic premise was “to contribute in collegial fashion to a co-ordinated tri-laboratory experiment.” Collaborative efforts are extremely useful and can accelerate progress. Unfortunately, such was not the case. In retrospect, imposing the condition of confirmation, rather than in-depth discussions, was unfortunate in view of what was known then and is known today, i.e., that the enormous complexity of the system and the unknown triggering mechanism make the reproducibility uncertain even if the procedure is followed rigorously.

Research at NRaD into the FP effect was encouraged and, to a large degree, supported by Dr. Frank Gordon, at that time the head of NRaD Department of Antisubmarine Warfare (Code 60), currently the Executive Director of NCCOSC, In Service Engineering West Division. This research resulted in many publications (see Appendix A). The goal was to understand the conditions that promote the initiation of this effect and the search for any evidence indicating their nuclear origin. In particular, we concentrated on tritium production and the monitoring of the emanating radiation (e.g. X- or γ - rays) from *Pd* electrodes prepared solely by the codeposition technique.

There was another side to consider, the climate created at that time: the scientific community was divided in two groups—the believers and the skeptics; again, an unfortunate terminology indicating a kind of religious fervor rather than scientific reasoning. The first group reported the results of their research with enthusiasm. At times, their enthusiasm overstated the significance of their results. The second group rejected the anomalous behavior as a matter of conviction, i.e., without analyzing the presented material (e.g., always asking “where are the neutrons?”). Consequently, any inquiries would have to be formulated in a manner that would not add to the already turbulent atmosphere and, yet, be directly connected to the FP effect, an interesting and potentially important energy source.

2. THE *Pd/D* SYSTEM

Let us recall the origin of the FP effect by quoting Fleischmann from his 1991 address of the Second International Conference on Cold Fusion: “Our interest in nucleation phenomena and our knowledge of the prediction of the formation of metallic hydrogen (and deuterium) at extreme compression in US and Soviet work during the mid-70’s was, in fact, a key element in the initiation of this project.” From this statement, it is obvious that high *D/Pd* atomic ratios are required to initiate the FP effect. Consequently, it appeared to us that the starting point should be the review of the relevant physico-chemical properties of the *Pd/D* system. In particular, properties exhibited by the *Pd/D* system at high pressures/high overpotentials, with emphasis on the nature of the driving force(s) associated with the transport in bulk material, the analysis of the diffusion equation, the role of the interphase in transport (e.g., changes in the interphase due to the applied electric field), were reviewed. Unfortunately, the information available pertains to low concentration of hydrogen isotopes, i.e., to the condition far removed from that required to initiate the FP effect. Thus, the question that naturally arises is how the properties of the *Pd/D* system change as the *D/Pd* atomic ratio increases. In reviewing the literature covering the metal/interstitial systems, it became obvious that two properties set the *Pd/D* system apart: the small atomic mass of hydrogen and the absence of electronic structure.

Ideally, electrode loading occurs in the following sequence. At first, all octahedral positions are filled. At this point the *D/Pd* atomic ratio is 0.6. Upon further loading, the available tetrahedral sites are filled with deuterium, yielding the maximum loading of 1.5. In reality, perfect crystals do not exist; they do contain defects. The simplest defect is the vacancy, i.e., an empty lattice space. There is a strong interaction with the interstitial hydrogen. The interstitial hydrogen is driven into the vacancy by the presence of open volume. The binding energy is equivalent to that of chemisorbed hydrogen (vacancy trapping).

Other common defects are solute and solute defect complexes, dislocations, and internal boundaries. The interactions with solute defect complexes are weaker than with vacancies. This is attributed to a lesser influence of the open volume. Their strength is, in part, due to elastic distortion and, in part, to electronic difference in H - bonding between the host and impurity atoms. Dislocations reduce the mobility of hydrogen by attractive interactions with dislocations. In the *Pd* lattice, the binding energy of H - atoms with the core dislocations is ca 0.6 eV of which 0.2 eV is ascribed to H – H interactions. Due to the absence of the open volume, the binding energies with grain boundaries are less than vacancy trapping. However, if the boundary contains a non-metallic phase which tends to form a covalent bond with hydrogen, the situation is different; binding energies in excess of 1 eV are expected.

This brief review indicates that to assure high mobility of absorbed deuterium, the *Pd* electrode should contain a small number of vacancies and dislocations, be free from impurities, especially those that might form a covalent bonding with deuterium, and its grain size should be small.

2.1 CONSTRUCTION OF THE PERFORMANCE ENVELOPE

The construction of the performance envelope, i.e., the listing of factors responsible for initiation and promotion of the FP effect is substantial. Among these factors are history of repeated charging (the $E(i)/t$ relationship), physico-chemical properties of the electrolyte, including additives (poisons), metallurgy of the *Pd* electrode and its alloys, and many unidentified factors. It would take several years to construct such an envelope. One reason for this long construction time is the lack of theoretical guidance. The various theories that attempt to explain initiation of the FP effect assume, as a

starting point of the argument, the existence of certain conditions, among them high concentration of absorbed deuterium.

Non-steady state processes, which appear as steady state because of an averaging of small perturbations, may cause the FP effect. The nature of these perturbations is not known. Several theories have been proposed to account for the observed behavior. The most promising concept is that of an oscillating plasma within the structure of the *Pd* lattice. However, conceptual difficulties arise because this plasma differs from ordinary plasmas. The deuteron concentration is ca 100 molar with an even higher electron concentration. It is not the agreement with the observation but the predictive capabilities of the model that will guide the technology transfer from research to reduction to practice. Thus, all existing theories should be re-examined with this objective in mind. In particular, the state of the system should be described and transport properties analyzed. Attention should be concentrated on the application of known theories describing the system prior to the initiation of the FP effect.

2.2 TRIGGERING CONDITIONS

The triggering conditions are as follows:

1. High *D/Pd* atomic ratio. A consensus is developing that a high atomic *D/Pd* ratio throughout the electrode structure is the necessary condition to initiate the FP effect. Numerical values have not been established; the *D/Pd* ratios as low as 0.85 and as high as 1.5 have been reported as a prerequisite to assure a successful experiment. This broad range may be due to difficulties arising from the measuring techniques employed. The reported values are the average values throughout the whole electrode which, in turn, does not exclude the possibility of localized areas (volumes) having much higher *D/Pd* ratios.
2. Metallurgical aspects. Pre-existing cracks/voids within the electrode make it useless with regard to the initiation of the FP effect. The unresolved question concerns the structural changes associated with the occurrence of excess enthalpy production. There are reports of no difference as well as remarks that electrodes producing excess enthalpy exhibit features indicating the development of hot spots with temperatures exceeding the electrode melting point.
3. Conditions at the interphase. The existence of an active interphase region reported by us at the Como meeting was discussed in connection with the dynamics of surface processes. The following points are noted: (a) inhomogeneous entrance of deuterium into the electrode interior creates localized concentration gradients; (b) Upon prolonged electrolysis, *Mg*, *Si* and *Cu* were found adsorbed on the *Pd* surface; (c) Surface morphology affects the reaction path.

3. CONTRIBUTIONS FROM NRAD LABORATORY

The NRaD research program did not seek the confirmation of the FP effect, which was the usual approach, but concentrated on topics that might help identify factors comprising the performance envelope. For this reason, the available experimental data were examined carefully and interpreted to design an experiment that would focus on reproducibility, i.e., an experiment that would simultaneously satisfy most, if not all, factors believed to be included in the performance envelope. A novel method for preparation of the working electrode, developed in this laboratory, the *Pd/D* codeposition technique, seems to provide the necessary tool. This approach was communicated by Fleischmann in his lecture, summarizing the accomplishments of the Como conference, given to the Royal Society of Chemistry. He said: "Details of an interesting new variant of the electrochemical method were reported by the collaborative group between the Naval Ocean Systems Laboratory (NOSC), San Diego and the Department of Energy (DOE), Washington, D.C. In these experiments palladium and *D* are codeposited at high negative potentials which appear to lead to an immediate generation of tritium and the detection of autoradiographic images in the immediate vicinity of the cathodes (presumably to the emission of soft X-rays); it also leads to an immediate generation of excess enthalpy."

3.1 THE CODEPOSITION PROCESS

The codeposition is a process whereby the palladium is electroplated from a Pd^{2+} -salt solution onto a substrate which does not absorb deuterium, such as gold or copper. The applied current and/or potential is adjusted to deposit palladium in the presence of evolving deuterium. The codeposition process creates a set of conditions that favor the initiation of the FP effect. These conditions include rapid absorption of deuterium by palladium and the burst-like activities. In the first case, the direct incorporation of deuterium replaces the slow process of diffusion; in the second case, the codeposition at high negative potentials results in the electrode structure which is not in equilibrium, and which, in turn, is a seat of various gradients e.g. chemical, mechanical, electrical, etc).

To restate, the codeposition process produces a repeatable electrode structure with regard to the initiation of the FP effect; it is an effective tool to examine the performance envelope. It produces conditions consistent with the reported behavior of sporadic occurrence, variable reaction path which, in turn, led to path dependent products and burst-like events. Such behavior would require threshold values and strange non-equilibrium conditions; alternatively, gradients may occur across spatial domains.

4. PUBLICATIONS/PRESENTATIONS

The topics examined and results published in refereed journals and presented at the Second International Conference on Cold Fusion (ICCF2 in 1991 at Como, Italy) and Third International Conference on Cold Fusion (ICCF3 in 1992 at Nagoya, Japan) by the NRaD group are summarized in this section. Copies of the manuscripts are included in Appendix A.

1. "On the Behavior of *Pd* Deposited in the Presence of Evolving Deuterium," J. Electroanal. Chem., **302**, 255 (1991): This short communication describes the codeposition technique and provides evidence for the production of excess enthalpy as well as the presence of some form of radiation. Due to the preliminary nature of this communication, the presented data were considered qualitative.
2. "Electrochemical Charging of *Pd* Rods," J. Electroanal. Chem., **309**, 273 (1991): A model describing the electrochemical charging of *Pd* rods is presented. The essential feature of this model is the coupling of the interfacial processes with the transport of interstitials in the electrode interior. It is shown that boundary conditions arise from the solution of the equation governing the elementary adsorption/desorption and adsorption/absorption steps and the symmetry of the electrode. Effects of the choice of rate constants on the surface coverage, the electrode potential and the time required to complete electrode charging are examined.
3. "Charging of the *Pd/H* System: Role of the Interphase," J. Electroanal. Chem., **337**, 147 (1992): The dynamics of transport of electrochemically generated deuterium across the electrode/electrolyte interphase was examined by slow scan (10 mV s^{-1}) voltammetry. The investigation covers the potential range -1.2 to $+0.4 \text{ V}$ measured vs an *Ag/AgCl* reference. It was found that a coupled, two-layer model of the interphase describes the observed behavior as a function of scan rate and electrolyte composition. The effect of chemisorbing species, e.g., CN^- ions, as well as reactive species e.g., $\text{SC}(\text{NH}_2)_2$, on the transport across the interphase is also discussed. Results are contrasted with those obtained for light water.
4. "Absorption of Deuterium in Palladium Rods: Model vs Experiment," J. Electroanal. Chem., **365**, 275 (1994): The electrochemical charging of *Pd* rods by deuterium involves a complex coupling of electrochemical, interfacial and transport processes. In order to predict the overpotential, surface coverage, and bulk loading of the electrode during charging, a model has been developed that incorporates the essential features of these processes and involves variables such as the electrochemical rate constants, the bulk diffusion coefficient and the charging current. Features of the timer dependence of the bulk loading are then compared to experimental charging curves. Microscopic observations and X- diffraction data provide further evidence for the details of the charging process.
5. "Comments on the Analysis of Tritium Content in Electrochemical Cells," J. Electroanal. Chem., **373**, 1 (1994): Expressions are given for tritium distribution between the gas and liquid phases arising from prolonged electrolysis of D_2O on *Pd* electrodes. Errors associated with commonly employed experimental procedures are evaluated. With regard to tritium production, an unambiguous resolution requires a complete mass balance. Conclusions based on partial data (e.g., electrode, electrolyte or "electrolytic" gas phase) may be misleading, particularly if production rates are either low or intermittent.
6. "Deuterium Uptake During *Pd — D* Codeposition," J. Electroanal. Chem., **379**, 121 (1994): The mode of deuterium uptake during *Pd — D* codeposition has been explored using galvanostatic perturbation techniques. The resultant relaxation curves exhibit four distinct potential-time intervals where the relaxation process is controlled by the interaction between the

transport of deuterium from the lattice to the surface to form adsorbed deuterium and the reduction of palladium from solution. These interactions are discussed in terms of the palladium + electrolyte interphase.

7. "Cyclic Voltammetry of $Pd + D$ Codeposition," J. Electroanal. Chem., in press: Processes associated with the $Pd + D$ alloy codeposition are examined by cyclic voltammetry. The voltammograms cover the potential range: +0.3 to -1.3 V (measured against an $Ag/AgCl KCl$ (sat) reference) and indicate that the partial current due to the Pd^{2+} ion reduction is diffusion limited at slow scan rates. Except for the significant increase in cathodic currents due to D_2O reduction at ca -0.25 V which occurs on freshly generated Pd surface, the shapes of voltammograms marginally differ from those recorded in the absence of Pd^{2+} ion in the electrolyte phase. A discussion of the dynamics of the interphase is presented.
8. "The Metal Hydrogen System: Interphase Participation in H— Transport" (invited lecture to be given on 24 April 95 at the 19th International Power Sources Symposium, Brighton, UK): The metal hydrogen system is a key element in the construction of ecologically preferred energy conversion/storage devices. Although reduced to practice decades ago, its effectiveness requires further examination of a number of issues, among them the role that the electrode/electrolyte interphase plays during the charging/discharging processes. The following topics in this communication are considered: Thermodynamics and kinetics of the structure of the interphase, the identity and components of the driving force(s) for the absorption/desorption of hydrogen, and the discussion of applicable transport equation. Agreement between theoretical and observed behavior is illustrated and selected design approaches affecting cell performance are explored.
9. "On the Behavior of the Pd/D System: Evidence for Tritium Production," submitted to J. Electroanal. Chem.: Evidence for tritium production in the Pd/D system under cathodic polarization is presented. A comparison of the observed distribution and that calculated, based upon the conservation of mass, leads to the conclusion that tritium is produced sporadically at an estimated rate of ca $10^3 - 10^4$ atoms per second. The results of several runs are interpreted by employing the concept of an electrode/electrolyte interphase and the accepted kinetics of hydrogen evolution. The poor reproducibility can be, in part, attributed to burst-like events averaged over a long time.
10. "Calorimetry of Open Electrochemical Cells," prepared for publication in Fusion Technology: A special case of calorimetry of open electrochemical cells, employing adiabatic enclosures, is examined. Conditions for experimental realization of such enclosures is discussed in detail. Practical arrangement and method for data collection are presented.
11. "On the Behavior of the Cathodically Polarized Pd/D System: Search for Emanating Radiation," submitted to Physics Letters A: Evidence for the emission of low intensity X— rays during cathodic polarization of the Pd/D system(s) is presented. The Pd/D system was prepared by charging with electrochemically generated deuterium, both palladium foil and palladium electrodeposited from D_2O electrolytes. Experimental and analytical procedures are described in detail.
12. "Reliable Procedure for the Initiation of the Fleischmann - Pons Effect," Proc. Second International Conference on Cold Fusion, Como, Italy, June/July 1991: Statistics on the initiation of the Fleischmann-Pons effect are rather poor. Reports presented at the first annual conference on cold fusion have indicated that, at best, only ca 1/10 of all attempts were successful in either producing excess enthalpy or yielding products associated with nuclear reactions. Here, we show that the Fleischmann-Pons effect can be reproducibly and rapidly initiated by

employing electrodes prepared by codeposition from Pd^{2+} -salts in the presence of evolving deuterium. The effectiveness of this process is examined in terms of tritium production.

13. "Comments on Methodology of Excess Tritium Determination," Proc. III ICCF, Nagoya, Japan in Frontiers of Cold Fusion, Universal Academy Press, Inc., 1993: Three methods of tritium data analysis are considered: comparison between experimental and theoretical data, total mass balance and curve fitting.

5. CONCLUDING REMARKS

The starting point in the execution of the NRaD program was the experimental examination of the *Pd* electrode while under cathodic polarization. Results were as follows:

1. The metal surface is not homogeneous with respect to deuterium absorption and the transition $\alpha PdD \rightarrow \beta PdD$ is fast. These results clearly indicate the importance of the interphase region in achieving high *D/Pd* atomic ratio as well as the rate of charging.
2. Nuclear events do occur in the course of electrochemical compression of deuterium within the *Pd* lattice. Their intensity, measured by tritium production or emanating radiation, is very low and intermittent. Their detection requires specially designed cells.
3. Electrodes prepared by codeposition are characterized by rapid initiation and higher reproducibility of the FP effect. Also, this technique represents a convenient tool for an effective development of the performance envelope.

APPENDIX A – TECHNICAL PAPERS

This section contains the technical papers that resulted from the NRaD program on the anomalous behavior of the *PdD* system. These papers have appeared in refereed journals and conference proceedings.

Preliminary note

On the behavior of Pd deposited in the presence of evolving deuterium

S. Szpak and P.A. Mosier-Boss

Naval Ocean Systems Center, San Diego, CA 92152-5000 (USA)

J.J. Smith

Department of Energy, Washington, DC 20545 (USA)

(Received 13 November 1990; in revised form 13 December 1990)

INTRODUCTION

Recently, Fleischmann et al. [1] reported that nuclear events can occur when deuterium is electrochemically compressed within the Pd–lattice. These events were reported to produce excess enthalpy, tritium, and neutrons. The exact nature of these events and the conditions leading to their initiation are poorly understood. In fact, the existence of such events is questioned by many [2]. The present position among those investigating this problem [3] is as follows: enthalpy production is a non–steady state process whose rate depends on the nature of the electrode material; however, the observed steady state production arises from an averaging of small perturbations. Nuclear events are believed to occur on the electrode surface as well as within the electrode interior.

This note reports on an alternative experimental approach to produce conditions favorable to the observation of this extraordinary behavior by exploiting the Pd/D codeposition. The approach, because an ever expanding electrode surface is created, assures the existence of non–steady state conditions as well as simplifies the cell geometry by eliminating the need for uniform current distribution on the cathode and, more importantly, eliminates long charging times effectively. Three sets of preliminary experimental results are presented here, i.e., the production of excess enthalpy, the production of tritium and the presence of some form of radiation. Due to the preliminary nature of this communication, the data are considered qualitative.

EXPERIMENTAL

A glass cell was provided with a bubbler, filled with heavy water to isolate the cell interior and, yet, allow the escape of gases generated in the course of codeposition. Two types of working electrodes were constructed. The first, Fig. 1, illustrates the arrangement for excess enthalpy measurements. Here, a copper foil, ca 4.0 cm² in area and 0.02 cm thick, attached to a glass tube, served as the cathode. A copper–constantin thermocouple, T₁, was inserted into this tube and cemented to the dry portion of the copper foil. A second, identical thermocouple, T₂, located half–way between the cathode and the Pt foil auxiliary electrode, measured the electrolyte temperature. The codeposition occurred from a solution of 0.05 M PdCl₂ (Aldrich) and 0.3 M LiCl (Mallinckrodt) dissolved in a 99.9% pure

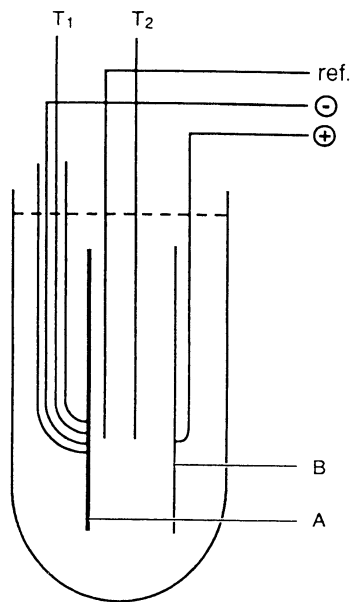


Figure A-1. An example of an e-mail message which reflects the views of many “skeptics” of cold fusion.

D₂O (Merck) under potentiostatic control (AMEL model 553). A potential of -0.8 to -2.0 V, measured against either Ag/AgCl or the Pd wire (D-charged to the $\alpha \rightarrow \beta$ transition) reference electrodes in the same solution, was applied. The cell voltage and current were monitored using a Hewlett-Packard model 7132A chart recorder. The temperature of the Cu-foil and solution were monitored using an OMEGA model 411A trendicator.

A second cell, shown in Fig. 2, was designed to detect radiation emanating during the codeposition. In this arrangement, photographic film, which was encased in light-tight and solution-impermeable envelopes, is placed in close proximity to the screen electrode.

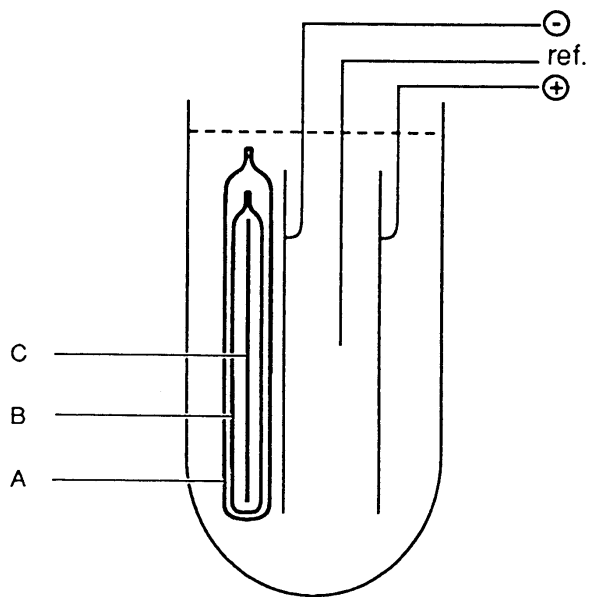


Figure A-2. Electrolytic cell for radiation detection. (A) Solution-impermeable envelope; (B) light-tight envelope; (C) photographic film.

RESULTS AND DISCUSSION

In the course of codeposition of Pd from D_2O electrolytes, the temperature of the working electrode, T_1 , was always greater by 2–4°C than that measured in the electrolyte, T_2 , Fig. 3. This indicates that the heat source is located at or within the Pd/D deposit. A suggestion that T_1 T_2 can be explained by increased resistivity of the D_2 -gas film on the electrode surface [4] is rejected on several grounds: first, a vigorous evolution of gases on both electrodes is known to promote efficient heat transfer; second, formation of a gas film is prevented by deuterium absorption and evolution; third and most important, the steep temperature rise of the cathode, indicated by ΔT in the insert Fig. 3, which was observed upon termination of flow of the cell current. Crude energy balance determinations were made periodically during each run: an excess enthalpy production between 10 and 40% was observed. Control experiments involving codeposition from light water showed a fundamental difference in the behavior observed between the Pd/D codeposition from heavy and Pd/H from light water. In the latter case, temperatures T_1 and T_2 were equal and no temperature rise was noted upon termination of the current flow.

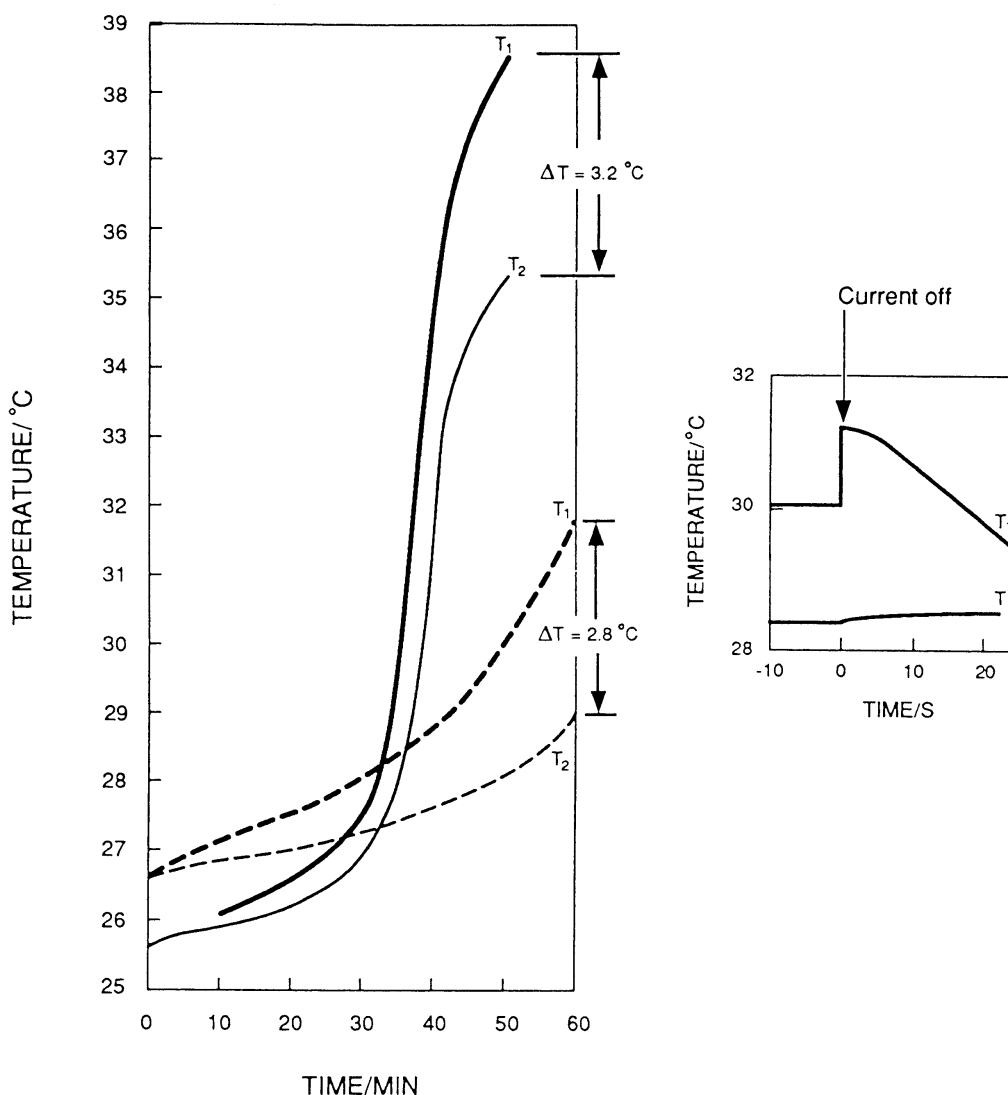


Figure A-3. Electrode/cell temperature evolution for two experiments. Thermocouple identification as in Fig. 1. Insert: jump in electrode temperature upon termination of current flow.

An example of a more accurate estimate of excess enthalpy production is illustrated in Fig. 4. To minimize heat losses, the electrochemical cell was immersed in a water bath whose temperature was kept equal, within 0.3 K, to that of the cell interior. The energy balance, however, did not include the latent heat of vaporization and the heat carried out by the evolving gases, i.e., in reality, the excess enthalpy production was somewhat greater than reported in Fig. 4. The production of excess enthalpy required 0.25×10^4 J and occurred after ca. 20 min of charging. No correlation between the variation in the cell current and potential, the temperature difference, $\Delta T = T_1 - T_2$, and the excess enthalpy production was attempted (further details will be published at a later time).

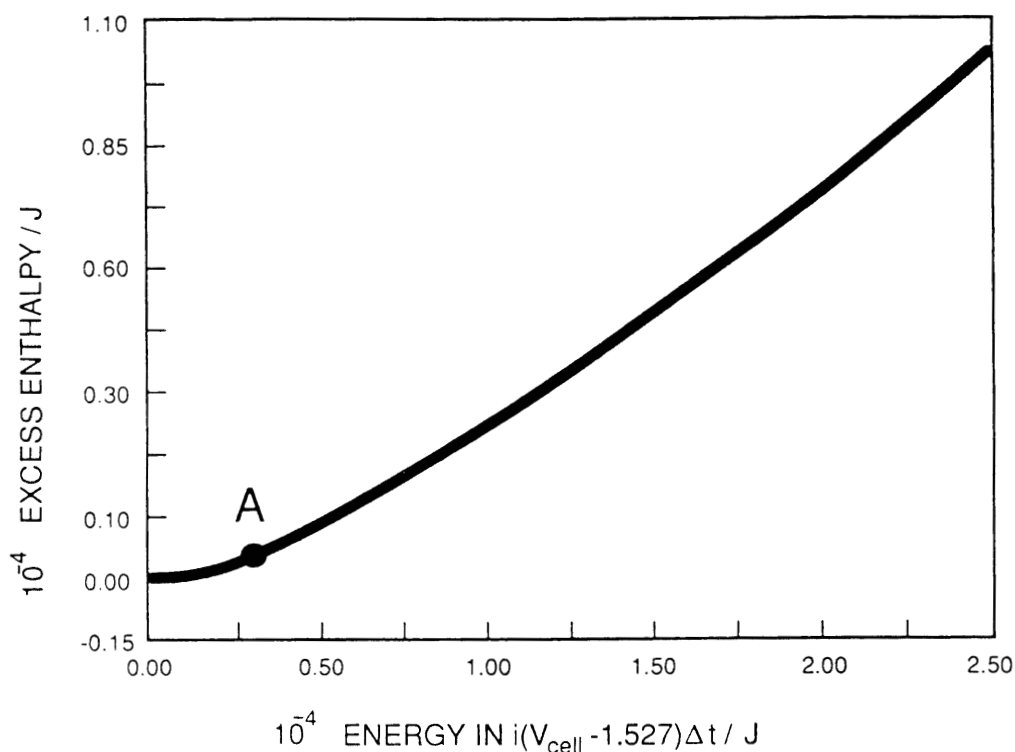


Figure A-4. Excess enthalpy production. Working electrode: Ni screen; temperature gradient between cell interior and water bath not greater than 0.3 K. Point A: energy input needed to generate excess heat, 0.25×10^4 J; time elapsed: ca. 20 min.

The analysis of spent electrolyte for tritium concentration showed an order of magnitude increase over that initially present in fresh electrolyte. In particular, the analysis of electrolytes from eight different runs showed the ^3H concentration within the range 230–270 disintegrations per min per cm^3 , compared to 30 in fresh electrolyte. It is noteworthy that this ca. ten-fold enrichment of tritium occurred after 10 to 16 h of electrolysis. This enrichment of tritium cannot be attributed to any external factors because (i) no electrolyte was added in the course of electrolysis and (ii) the cell interior was separated from the outside by a trap filled with heavy water. Appropriate precautions were taken to eliminate the interference of chemi-luminescence. The control experiments produced no tritium.

Evidence of the radiation emanating from the negative electrode is presented in Fig. 5. The developed photographic film (Kodak) shows areas exposed to the radiative flux and those partially blocked by the Ni screen electrode. The interaction between the radiative flux and this particular film suggests that the source is a low energy radiation, likely soft X-rays. What appears to be a double or triple exposure is most likely due to slight displacement of the film with respect to the electrode that occurred in the course of the 12 h codeposition. It is noted that the radiograph shown in Fig. 5 was

obtained under conditions vastly different from those reported recently [5,6], i.e., during the Pd/D codeposition rather than from Pd electrodes examined after successful completion of excess enthalpy generation. No radiation was observed in the control experiment. within the range 230—270 disintegrations per min per cm³, compared to 30 in fresh electrolyte. It is noteworthy that this ca. ten-fold enrichment of tritium occurred after 10 to 16 h of electrolysis. This enrichment of tritium cannot be attributed to any external factors because (i) no electrolyte was added in the course of electrolysis and (ii) the cell interior was separated from the outside by a trap filled with heavy water. Appropriate precautions were taken to eliminate the interference of chemiluminescence. The control experiments produced no tritium.

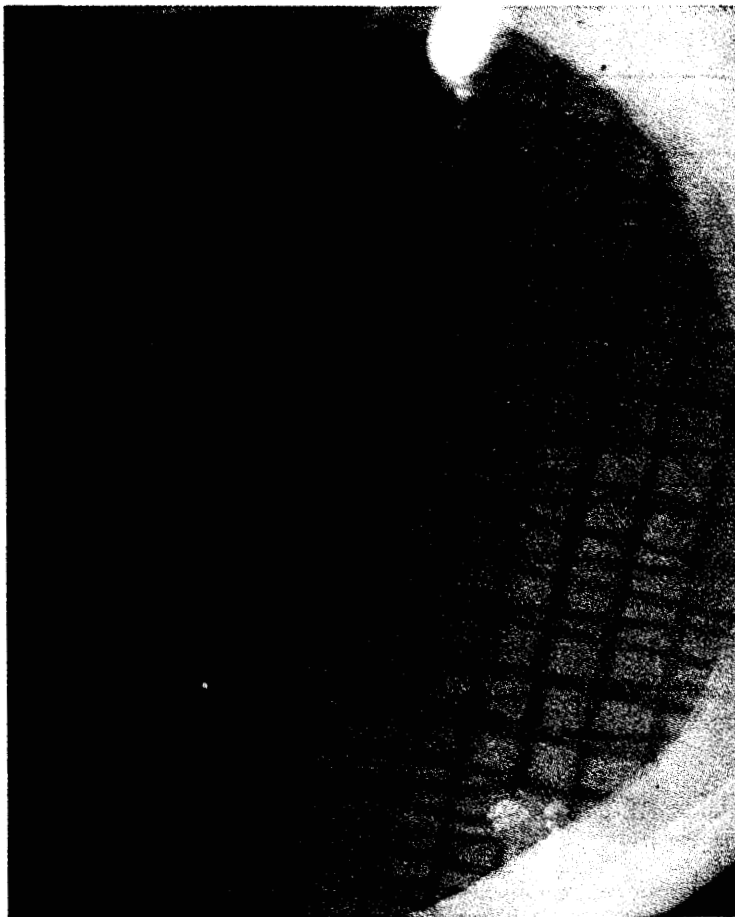


Figure A-5. Record of radiation emanating during Pd/D codeposition.

ACKNOWLEDGEMENTS

The authors express their thanks to Professors Fleischmann and Pons, and Dr. D.R. Rolison, NRL, for enlightening discussions. S.S. and P.A.M.-B. wish to thank Dr. Frank Gordon, NOSC, for encouragement and support.

REFERENCES

1. M. Fleischmann, S. Pons, M.W. Anderson, L.J. Li and M. Hawkins, *J. Electroanal. Chem.*, 287(1990) 293.
2. N.S. Lewis, C.A. Barnes, M.J. Heben, A. Kumar, S.R. Lunt, G.E. McManis, G.M. Miskelly, R.M. Penner, M.J. Sailor, P.G. Santangelo, G.A. Shreve, B.J. Tufts, M.G. Youngquist, R.W.

Kavanagh, S.E. Kellog, R.B. Vogelaar, T.R. Wang, R. Kondrat and R. New, *Nature*, 340(1989)525.

3. Panel discussion, *The First Annual Meeting on Cold Fusion Conference Proceedings*, Salt Lake City, UT, March 1990.
4. D.N. Bennion, private communication, March 1990.
5. M.C.H. McKubree, R.C. Roha-Filko, J. Chao, B. Chexal, T. Passel and J. Santucci, in *The First Annual Conference on Cold Fusion Conference Proceedings*, Salt Lake City, UT, 1990, p. 20.
6. P.K. Iyengar and M. Srinivasan, in ref. 5, p. 62.

Electrochemical charging of Pd rods

S. Szpak and C.J. Gabriel

Naval Ocean Systems Center, San Diego, CA 92152-5000 (USA)

J.J. Smith

Department of Energy, Washington, DC 20545 (USA)

R.J. Nowak

Office of Naval Research, Arlington, VA 22217-5000 (USA)

(Received 4 October 1990; in revised form 8 March 1991)

ABSTRACT

A model describing the electrochemical charging of Pd rods is presented. The essential feature of this model is the coupling of the interfacial processes with the transport of interstitials in the electrode interior. It is shown that boundary conditions arise from the solution of equations governing the elementary adsorption–desorption and adsorption–absorption steps and the symmetry of the electrode. Effects of the choice of rate constants of the elementary steps and the charging current on the surface coverage, the electrode potential and the time required to complete electrode charging are examined.

INTRODUCTION

In a recent effort [1] to account for the long charging time needed to initiate the effects reported by Fleischmann and Pons [2], in a Pd rod, certain assumptions concerning the concentration of deuterium at the electrode surface, the nature of the interaction between the diffusing deuterium and the Pd lattice and the homogeneity of the medium were made. The condition of zero flux at the center of Pd rod, used by Jorne [1], is evident; however, the condition of constant deuterium concentration at the electrode surface, although appropriate for charging from the gas phase, is open to question because, to be physically realistic, the boundary conditions must consider all processes that determine the concentration, or the flux, of the diffusing substance at the point where the influence of the interphase ceases. The nature of the interactions of diffusing hydrogen and, to a lesser degree deuterium, with the Pd lattice, has been examined in considerable detail [3–11]. To account for these interactions by a simple, first order irreversible chemical reaction may not be applicable. Moreover, a polycrystalline Pd rod can be treated as a homogeneous medium, but only under restrictive conditions.

The purpose of this work was to examine the problems associated with the charging of the palladium lattice. The charging of metals by hydrogen/ deuterium by itself is a technologically important issue aside from the interest generated by the recently described extraordinary behavior of deuterium charged Pd rods [2].

MODEL

Prior to developing the mathematics of the electrochemical charging of Pd rods, we review those aspects that tend to control the penetration of deuterium. In particular, we examine the structure of the

electrolyte/electrode interphase, the deuterium evolution reaction, interactions between the interstitials and the host lattice, and the effect of grain boundaries in the polycrystalline material. This qualitative discussion provides the basis for the formulation of simplified governing equations in which we ignore the distinction between α/β phases and employ a simple diffusion coefficient for the purpose of modeling the coupling between surface and transport (bulk) processes.

Concept of an Interphase/Charging Fluxes

Two homogeneous phases that are in contact with each other are separated by an interphase region. This region may be viewed as made up of several laminae each of which is treated as a very thin homogeneous phase [12]. Often, to simplify the treatment, an appropriately defined single homogeneous phase may be substituted [13]. The structure of the electrolyte portion of the interphase was treated by van Rysselberghe [14]; here, the structure on the metal side, with respect to transport, will be identified and examined.

Four fluxes are involved in charging the Pd metal from the gas phase. They are the adsorption and desorption fluxes, j_2 and j_{-2} , and the absorption-desorption fluxes consisting of the exchange between the species present in the metal interior and the surface, j_3 and j_{-3} , respectively. In reality, the dynamics of the surface processes are more complex [15,16]. In the case of electrochemical charging, Fig. 1, the structure is complicated further because the applied overpotential and charge transfer result in two additional fluxes, j_1 and J_{-1} . The effect of the applied potential on the transport of interstitials becomes negligible at a point close to the metal surface where diffusion is initiated.

Deuterium Evolution Reaction

The reaction path for the deuterium evolution is essentially the same as that for hydrogen [2,17], eqns. (I) to (III)

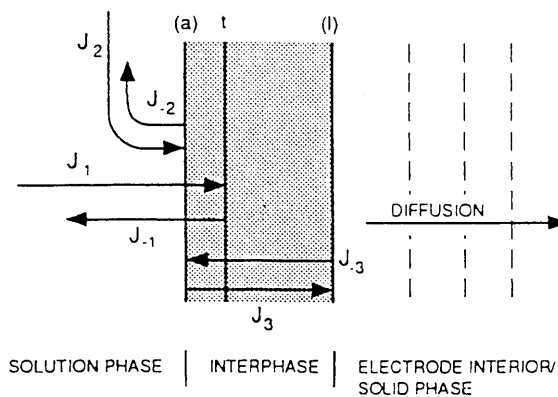
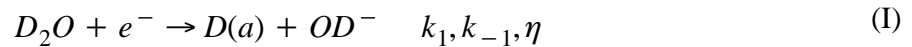
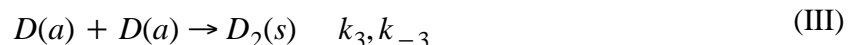


Figure A-1. Schematic representation of an interphase (fluxes included). (a) Adsorption plane; (t) charge transfer plane; (l) lattice.

followed by either



or



where (a) and (s) denote species present in an adsorbed state and in solution, respectively. Potential dependent surface coverage for special cases, e.g., the steady state condition with an a priori specified rate determining step (rds), in the absence of absorption, was examined by Gileadi and Conway [18]. They found that highest surface coverages are obtained when eqn. (III) is the rds, i.e., is proceeding more rapidly than eqn. (II), but more slowly than eqn. (I). Furthermore, if eqn. (II) is the rds, i.e., is proceeding more rapidly than eqn. (III), but more slowly than eqn. (I), the surface coverage exhibits a limiting value, determined by the ratio k_2/k_1 ; the smaller this ratio, the higher the surface coverage.

The absorption into the lattice of electrochemically generated deuterium is given by eqn. (IV)



where (l) denotes species in the lattice. The hydrogen analog of eqn. (IV) was investigated to a limited extent by Iyer et al. [19]. The inclusion of diffusional transport necessitates the separation of the interphase region from the diffusion space. The characteristic feature of the Iyer et al. model is the interdependence of the diffusion flux and the interphase reactions.

Molecular Interactions Related to Transport

There is ample experimental evidence of interactions between the interstitials and the host Pd lattice. During the transport of hydrogen as well as deuterium, a change from the α phase to the β phase occurs. This change manifests itself by the lattice expansion which is larger in the α phase than in the β phase [6]. The expansion of the Pd lattice creates localized highly stressed conditions that affect the diffusional transport [10]. This deviation from ideality occurs even at very low hydrogen concentration with the process becoming more exothermic as the concentration of H(l) increases. However, once the β phase has formed, the process becomes less exothermic. The rate of absorption increases exponentially with the increase in H(l) concentration and is attributed to an expansion of the lattice.

Quantum mechanical treatment requires that the motion of interstitials occurs by a hopping mechanism [9]. The energies of activation for the H/D species are of an order of magnitude less than for other interstitials, while the values of their diffusion coefficients are many orders of magnitude higher indicating the importance of the pre-exponential factor. The jump frequencies for H interstitials are comparable to the highest frequency of the host lattice. Of interest is the fact that the isotope effect enters through the exponential factor, i.e., contrary to the prediction based on the classical absolute rate theory [15].

Forms of Diffusion Coefficient

Here, we review the various interpretations of the diffusion coefficient to underscore the importance of interactions between the interstitials and the host lattice on their transport. Starting with the Fick's first law, eqn. (1)

$$j = -D \frac{\partial c}{\partial x} \quad (1)$$

we note that in this formulation, D is a proportionality constant relating the flux, j , to the driving force, $\partial c/\partial x$. However, as written, eqn. (1) is valid only for non-interacting solute/solvent systems. Substituting the activity for concentration, $a = c\phi$, we transform eqn. (1) into an equivalent form

$$j = \frac{cD}{RT} \frac{\partial \mu}{\partial x} \quad \mu - \mu^0 + RT \ln a \quad (2)$$

Defining $v = j/c$ as the average linear velocity of the diffusing particles, we have for the Nernst–Einstein formulation

$$f(x)dx = B^{-1}vdx \quad B = D/RT \quad (3)$$

i.e., the diffusing particles behave as if they were acted upon with the force $f(x)$ against the viscous resistance. If additional forces are affecting diffusional transport, e.g., lattice expansion, it is necessary to add the appropriate terms to the balance equation, eqn. (3), e.g., eqn. (4)

$$f(x)dx = B^{-1}vdx + \sum_i d\omega_i \quad (4)$$

Comparing eqns. (3)/(4) and (2) we note that $f(x) = -\partial\mu/\partial x$ while the comparison of eqns. (1) and (2) yields the diffusion coefficient of the form

$$D = D_0 \exp \left[-\frac{1}{RT} \int \left[f(x) - \sum_i d\omega_i/dx \right] dx \right] \quad (5)$$

Equation (5) implies that the diffusion coefficient reflects specific features associated with the transport. For example, Barrer and Jost [20] found that the transport of H(1) in the Pd lattice belongs to the “zeolitic diffusion”, where the probability of migration is proportional to the probability of finding an unoccupied site. The diffusion coefficient involving the possibility of jumps of length λ over several sites has the form

$$D_n = (n\lambda)^2(1 - \zeta)^n v \exp(-E_n/RT) \quad (6)$$

where v is the oscillation frequency, $(1 - \zeta)^n$ is the probability of finding a vacant neighboring site n times in succession and E_n is the energy of activation, most likely a slowly varying function of n . The “effective” diffusion coefficient D_{eff} is the normalized sum of individual coefficients. Evidently, for small ζ , the n -fold jumps contribute substantially while for large ζ only the first term is significant.

Kuballa and Baranowski [21], examining the transport properties at high concentration of hydrogen through the β – Pd lattice, employed the diffusion coefficient formulated on the basis of absolute rate theory, eqn. (7)

$$D = \kappa f \frac{\lambda^2}{6} z v \exp \left(\frac{S_m + S_f}{k} \right) \exp \left(-\frac{E_m + E_f}{kT} \right) \quad (7)$$

where κ is the transmission coefficient, f is the correlation factor, λ is the jump distance in the lattice, z the coordination number, v the vibration frequency in the potential well, S the entropy and E the energy. The subscripts f and m , respectively, identify the formation of a neighboring vacancy and the motion from one site to another. They concluded that within the phase, the diffusion coefficient is independent of concentration. However, at higher concentrations, many neighboring sites are occupied and both the entropy and the energy of vacancy formation must be included. The formation of new sites is associated with the mechanical distortion of the lattice, thus sharply increasing the vibrational frequency of the diffusion particle. As the concentration of hydrogen increases there is continuous change in the mechanism of transport, most likely involving the tetrahedral sites.

In yet another example, the effect of mechanical distortion on transport was examined by Voelkl [10]. Results were expressed in terms of changes of the electrochemical potential, i.e. a factor appearing in the exponent of the diffusion coefficient.

Effect of grain boundaries

Grain boundaries represent the locations of a high density of lattice imperfections. In effect, they may be viewed as internal surfaces where an exchange process,

similar to adsorption–desorption, can occur. The interaction of an interstitial with a lattice defect is energetically quite different from its interaction with the undisturbed lattice. Consequently, by eqn. (5), transport properties should differ in polycrystalline material as compared with those in a single crystal. Yet, measurements of the steady state permeation of hydrogen indicate no influence of grain boundaries. This apparent discrepancy is attributed to the absence of trap–to–trap hopping of interstitials and the filling of all traps during steady state transport [22]. By creating sinks, the tendency of interstitials to accumulate in the lattice defects modifies their transport before the steady state is realized.

H(a) / H(l)–Pd Vs. D(a) / D(l)–Pd Interphase Behavior

Common reaction paths for the hydrogen evolution reaction and deuterium evolution reaction, reported by Schuldiner and Hoare [17], do not assure identical rates of the elementary process comprising the charging of palladium rods. Qualitative observations show considerable difference in the behavior of the interfacial region between hydrogen and deuterium, notably in the rate of absorption–desorption. Rolison and Trzaskoma [23] reported a significant difference in the rate of escape of absorbed hydrogen and deuterium upon termination of the charging current. Szpak et al. [24] found similar behavior by an in situ examination of the penetration of deuterium and hydrogen by a single grain in a specially designed cell using Nomarski optics.

FORMULATION OF CHARGING EQUATIONS

Davenport et al. [25] considered absorption from the gas phase into a thin metallic film. We extend their treatment to consider a much larger solid body immersed in an electrolyte. This body is taken to consist of N layers; the i th layer having a volume V_i and the area of the dividing surface between it and the $(i + 1)$ th layer is $S_{i,i+1}$. In general: $V_i \neq V_{i+1}$ and $S_{i-1,i} \neq S_{i,i+1}$. The diffusion of deuterium in the bulk of the solid body is then considered as a process of jumping from one layer to an adjacent layer with a rate that is proportional to the interfacial area between the layers, as well as to the number of occupied sites in the initial layer and the number of vacant sites in the final layer. Consequently, we write for the time rate of change in the fractional number per unit volume of occupied sites, ζ_i in the i th layer within the bulk

$$\begin{aligned} \frac{d\zeta_i}{dt} = \frac{\kappa_d Z_m}{V_i} \left\{ S_{i-1,i} [\zeta_{i-1}(1 - \zeta_i) - \zeta_i(1 - \zeta_{i-1})] \right. \\ \left. - S_{i,i+1} [\zeta_i(1 - \zeta_{i+1}) - \zeta_{i+1}(1 - \zeta_i)] \right\} \quad i = 1, 2, 3, \dots, N \end{aligned} \quad (8)$$

where k_d is the jump rate constant and Z_m is the maximum number of available sites per unit volume.

The boundary conditions for this set of equations are determined by the physical considerations of events occurring at the first and N th layers. The reactions (I) through (IV) set the boundary conditions at the first layer in terms of corresponding fluxes. Defining the anodic current as the positive current (i.e., the flow of electrons from the working electrode to the power supply), we obtain for the charge transfer reaction, eqn. (I)

$$\frac{i_1}{T_m F} = k_{-1} [OD^-] \theta \exp\left(\frac{\alpha F \eta}{RT}\right) - k_1 [D_2O] (1 - \theta) \exp\left[\frac{-(1 - \alpha) F \eta}{RT}\right] \quad (9)$$

where Γ_m , is the maximum number of sites per unit area and θ is the fractional surface coverage. Analogously, for the charge transfer reaction eqn. (II)

$$\frac{i_2}{T_m F} = k_{-2}[D_2(s)][OD^-](1 - \theta) \exp\left(\frac{\beta F \eta}{RT}\right) - k_2[D_2O]\theta \exp\left[\frac{-(1 - \beta)F\eta}{RT}\right] \quad (10)$$

While reactions (III) and (IV) do not directly pass electrons through the interface, it is convenient to define equivalent charge transfer currents, eqns. (11) and (12), respectively

$$\frac{i_3}{T_m^2 F} = 2k_{-3}[D_2(s)](1 - \theta)^2 - 2k_3\theta^2 \quad (11)$$

$$\frac{i_4}{T_m Z_m F} = k_{-4}\zeta_1(1 - \theta) - k_4\theta(1 - \zeta_1) \quad (12)$$

In terms of these currents, the time rate of change of adsorbed deuterium is given by eqn.(13)

$$T_m F \frac{d\theta}{dt} = -i_1 + i_2 + i_3 + i_4 \quad (13)$$

and the applied current, i , is given by eqn. (14)

$$i = i_1 + i_2 + C \frac{d\eta}{dt} \quad (14)$$

where the last term in eqn. (14) gives the charging current for the interfacial layer in terms of its effective capacitance C and the time rate of change of the overpotential. The time rate of change of the absorbed deuterium in the interfacial layer between the bulk Pd and the electrolyte is governed by both the flux through the surface given in terms of the equivalent current i_4 and diffusion into the bulk, which generates the flux: $k_d Z_m^2 S_{1,2}[\zeta_1(1 - \zeta_2) - \zeta_2(1 - \zeta_1)]$, so that the time rate of change of the fractional occupation of sites in the interfacial layer is given by eqn. (15)

$$V_1 Z_m \frac{d\zeta_1}{dt} = -S_{0,1} \frac{i_4}{F} - d_d Z_m^2 S_{1,2}(\zeta_1 - \zeta_2) \quad (15)$$

Equations (13), (14) and (15) specify, in effect, the boundary conditions for eqn. (8) at the interfacial layer. The boundary condition at the Nth layer depends on the physical arrangement; e.g., with reflection symmetry at that location, the flux passing beyond the Nth layer would be zero.

The jump rate constant k_d introduced in eqn. (8) can be related to the diffusion constant by observing that, if the number of layers is large and each layer is thin, then eqn. (8), which in cartesian coordinates becomes

$$\frac{d\zeta_i}{dt} = \frac{k_d Z_m}{\delta} (\zeta_{i-1} - 2\zeta_i + \zeta_{i+1}) \quad (16)$$

where δ is the thickness of the layers, can be compared with the finite difference approximation to the diffusion equation indicating that the diffusion constant $\mathbf{D} = k_d Z_m \delta$.

Charging of Pd Rods; Numerical Solutions

For a rod (cylindrical symmetry) divided into annular layers of thickness Δr numbered from surface to center (1 to N), eqn. (8) becomes eqn. (17) (see Appendix)

$$\frac{d\zeta_i}{dt} = \frac{k_d Z_m}{\Delta r} \left(\frac{2r_i}{r_i + r_{i+1}} \right) \left[\zeta_{i-1} - \left(2 - \frac{\Delta r}{r_i} \right) \zeta_i + \left(1 - \frac{\Delta r}{r_i} \right) \zeta_{i+1} \right] \quad i = 2, 3, 4, \dots, N \quad (17)$$

where $r_i = (N - i + 1) \Delta r$ and $\zeta_{N+1} = \zeta_N$ in order to insure the condition of zero flux at the center of the rod as required by symmetry considerations. Similarly, for the interfacial layer between the electrolyte and the bulk, eqn. (15) becomes eqn. (18)

$$= - \left(\frac{2r_0}{2r_0 - \Delta r} \right) \left\{ \frac{T_m}{\Delta r} [k_{-4}\zeta_1(1 - \theta) - k_4\theta(1 - \zeta_1)] + \frac{k_d Z_m}{\Delta r} \left(\frac{r_0 - \Delta r}{r_0} \right) (\zeta_1 - \zeta_2) \right\} \quad (18)$$

where $r_0 = N \Delta r$ is the radius of the rod.

Equations (13), (14), (17) and (18) form a set of stiff ordinary differential equations that can be solved using e.g. the method of Kaps–Rentrop described by Press and Teukolsky [26] with suitable modifications to take advantage of the tridiagonal nature of the Jacobi matrix.

RESULTS AND DISCUSSION

A proposed requirement for the initiation of the effect reported by Fleischmann and Pons is that a set of conditions must be met to “switch–on” the Pd electrode. Due to a large number of these conditions it is difficult, if not impossible at the present time, to identify a dominant factor although a high degree of loading has

been assumed to be one of the necessary conditions. High overpotentials and/or charging currents have also been proposed. In the context of the present discussion, we accept the correctness of the reaction path, eqns. (I)—(IV). However, because of the lack of the rate constant data for the deuterium evolution reaction, the discussion is essentially reduced to the examination of the behavior of the set of coupled equations describing the charging process.

Construction of Solution; Input Data

The numerical solution of eqns. (13), (14), (17) and (18) requires three types of input parameters. The first is associated with the electrode/electrolyte system, the second characterizes the initial conditions, and the third comprises the rate constants whose effect on charging process is examined. The electrode/electrolyte system consists of two regions: (i) the bulk material characterized with regard to transport by the density of available bulk sites, Z_m , and the diffusion coefficient D ; (ii) the electrode/electrolyte interface described by the density of available surface sites, Γ_m , and the rate constants for all processes including the exchange reaction, eqn. (IV). The assumption employed here of concentration independent parameters represents a first approximation only, but can be easily extended to incorporate concentration dependences, if they are known.

To initiate calculations, we assume that, prior to the application of a charging current, equilibrium has been reached so that the time rate of change of η , θ , and $\zeta_i = 1, 2, 3, \dots, N$ will be zero; in addition, we require that the time rate of change of the evolution of $D_2(s)$ also be zero. The latter requirement imposes the condition that $i_2 + i_3 = 0$. Consequently, the equilibrium condition becomes $i_j = 0$; $j = 1, 2, 3, 4$. Equilibrium is characterized by the values of the three variables: η , θ , and $\zeta = \zeta_i$; $i = 1, 2, 3, \dots, N$ and determined by four equations. It follows, therefore, that an equilibrium condition may not exist for arbitrarily chosen sets of rate constants for the four reactions, eqns. (I)—(IV). For this reason, it is convenient to choose equilibrium values for θ and ζ with $\eta = 0$, viz., $\theta = \theta_0$, $\zeta = \zeta_0$ and use these values to provide the following relationships among the rate constants, eqns. (19)—(22)

$$k_{-1}[OD^-]\theta_0 = k_1[D_2O](1 - \theta_0) \quad (19)$$

$$k_{-2}[D_2(s)][OD^-](1 - \theta_0) = k_2[D_2O]\theta_0 \quad (20)$$

$$k_{-3}D_2(s)(1 - \theta_0)^2 = k_3\theta_0^2 \quad (21)$$

$$k_{-4}\zeta_0(1 - \theta_0) = k_4(1 - \zeta_0)\theta_0 \quad (22)$$

Table 1 lists the values of the parameters used in the computations described here unless noted otherwise.

Table A-1. Input data.

Parameter	value
$[D_2O]$	5.5×10^{-2} mol/cm ³
$[OD^-]$	1.0×10^{-4} mol/cm ³
$[D_2(s)]$	8.3×10^{-7} mol/cm ³
θ_0	1.0×10^{-1}
ζ_0	1.0×10^{-1}
α	5.0×10^{-1}
β	3.0×10^{-1}
Z_m	1.0×10^{-1} mol/cm ³
Γ_m	1.0×10^{-13} mol/cm ²
radius, r_0	5.0×10^{-3} cm
capacitance, C	4.0×10^{-3} F/cm ²
diff. coeff., D	1.0×10^{-5} cm ² /s
Number of layers, N ^a	10

^a Calculations for $N > 10$ (e.g. $N = 40$) yielded substantially the same results.

Electrode Charging

To relate the charging process to observable quantities and to evaluate the driving force, we calculated the surface coverage, the electrode overpotential and the amount of absorbed material. In particular, the surface coverage was selected because the operating driving force for the charging process is the chemical potential difference between the relevant species in an adsorbed state and those residing in the lattice. For the charging process to occur we require that the inequality, eqn. (23)

$$\mu(a, t) - \mu(l, t) > 0 \quad (23)$$

be fulfilled at all times. But, since $\mu(a, t) = f_1(\theta)$ and $\mu(l, t) = f_2(\zeta)$, it follows that the charging process may be conveniently examined in terms of the surface coverage which is determined by the participating processes responding to the applied charging current. The amount of material incorporated into the electrode interior and its distribution was calculated to determine whether or not a threshold value for loading has been reached and to provide information on the efficiency of the charging process.

An example of an electrode charging is shown in Fig. 2 where two time intervals are delineated. The first is of a short duration, e.g., less than 0.1 s, during which the processes within the interphase dominate. This period terminates when these processes become stationary, i.e. as $\theta(t) \rightarrow \theta_{lim}$ and $\eta(t) \rightarrow \eta_{lim}$. The second time interval, of a considerable length, is that during which actual charging of the electrode interior occurs, i.e., the fraction of available sites occupied $Q(t) \rightarrow Q_{lim}$.

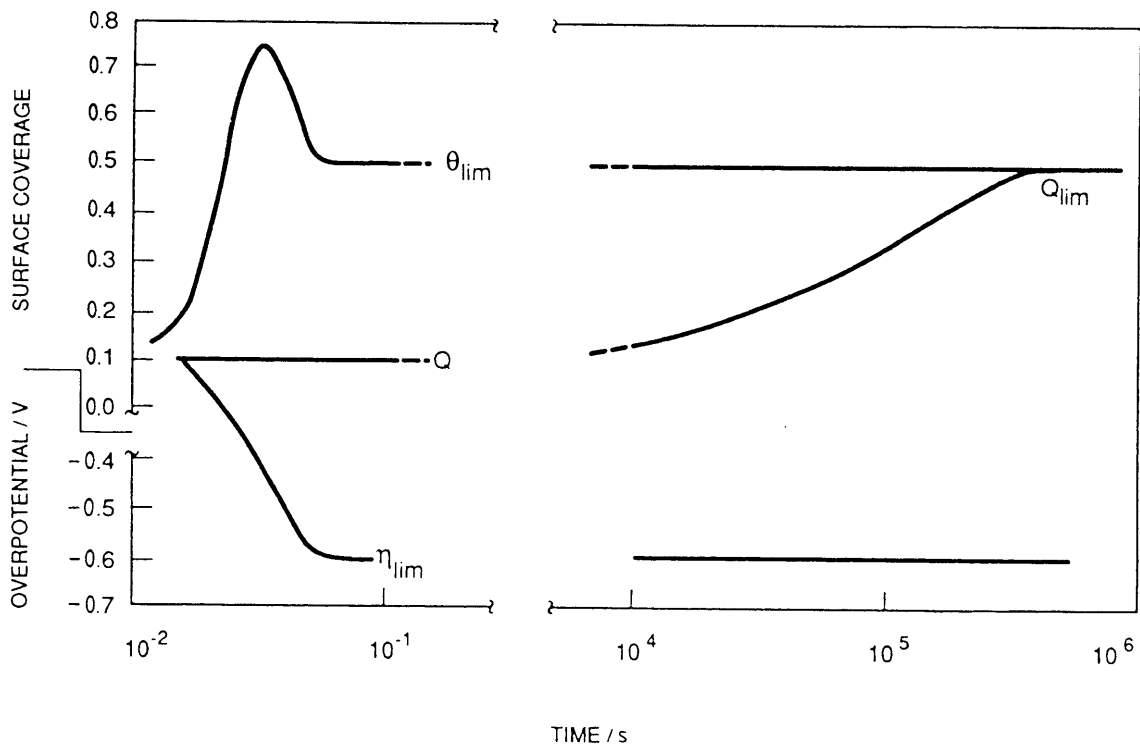


Figure A-2. Evolution of surface coverage, overpotential and concentration of interstitial in the course of electrode charging.

Electrode Initial Response to Current Flow

The assumed model, Fig. 3, provides for position dependent elementary processes, i.e., it suggests the separation of processes occurring within the interphase from those within the electrode interior. It follows that the electrode charging and the effect of rate constants can be examined within well defined time intervals, as illustrated in Fig. 2, of which the first time interval consists of three distinct time periods: the first, $0 < t < \tau_1$ represents the charging of the double layer; the second, $\tau_1 < t < \tau_2$, covers the period needed for the attainment of a quasi-stationary state; and the third $t > \tau_2$ is the time during which the electrode begins to accept interstitials, Fig. 3. For different choices of rate constants, the regions may be less distinct and the time dependence of the surface coverage and overpotential can have somewhat different forms. The amount of the interstitial material absorbed during the attainment of the quasi-steady state of surface coverage is insignificant under all conditions examined (e.g., on the order of 0.0001% above the assumed equilibrium value).

As expected, an elementary process that controls the overall reaction also controls the time dependence of both the surface coverage and overpotential. In particular, Fig. 4 illustrates the effect of an emerging rds. Here, the pairs of curves, respectively, a— a' , b— b' , etc. are the $\theta(t)$ and $\eta(t)$ that represent changes in the surface coverage and overpotential with the changing ratios of k_2/k_1 and k_3/k_1 . Clearly, as these ratios are decreased, the quasi-steady state surface coverage, θ_{lim} , increases due to enhanced adsorption and reaches a limiting value of one. Further decrease in this ratio, after $\theta_{lim} = 1.0$, causes the knee of the $\theta(t)$ curve to move to earlier times, cf. curves c and d. It is noted that within the time period examined, the amount of absorption is insignificant; consequently, as expected, an agreement with the earlier work of Gileadi and Conway [18] is evident.

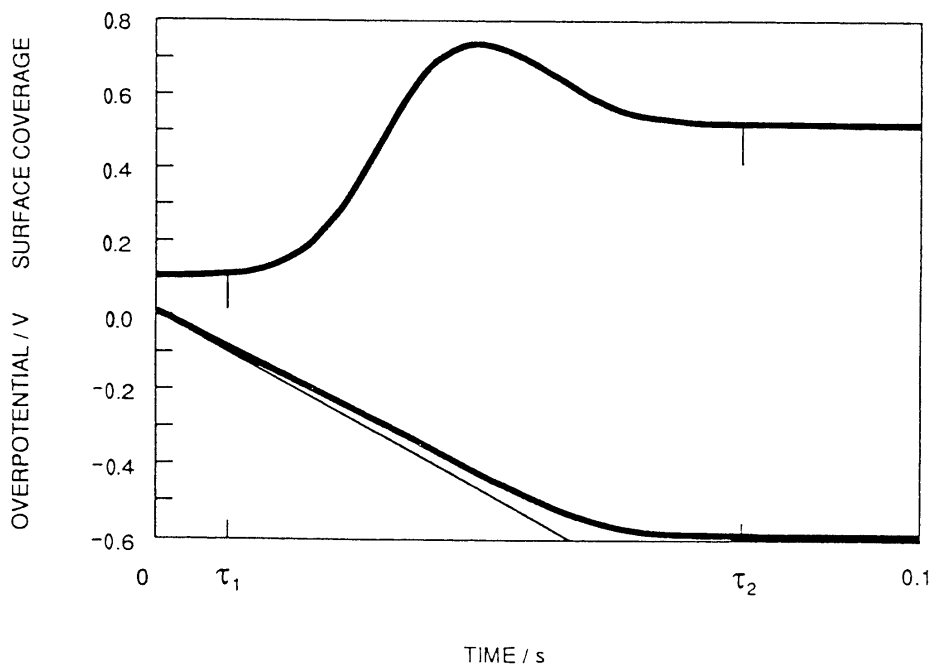


Figure A-3. Surface coverage and overpotential as a function of time. Initial period: charging of the double layer, $0 < t < \tau_1$; unsteady state, $\tau_1 < t < \tau_2$; quasi-steady state, $t > \tau_2$. Charging current: $-40 \times 10^{-3} \text{ A/cm}^2$; rate constants: $k_1 = 10^3 \text{ cm}^3/\text{mol s}$; $k_2 = 10 \text{ cm}^3/\text{mol s}$; $k_3 = 10^3 \text{ cm}^2/\text{mol s}$; $k_4 = 2.0 \times 10^5 \text{ cm}^3/\text{mol s}$.

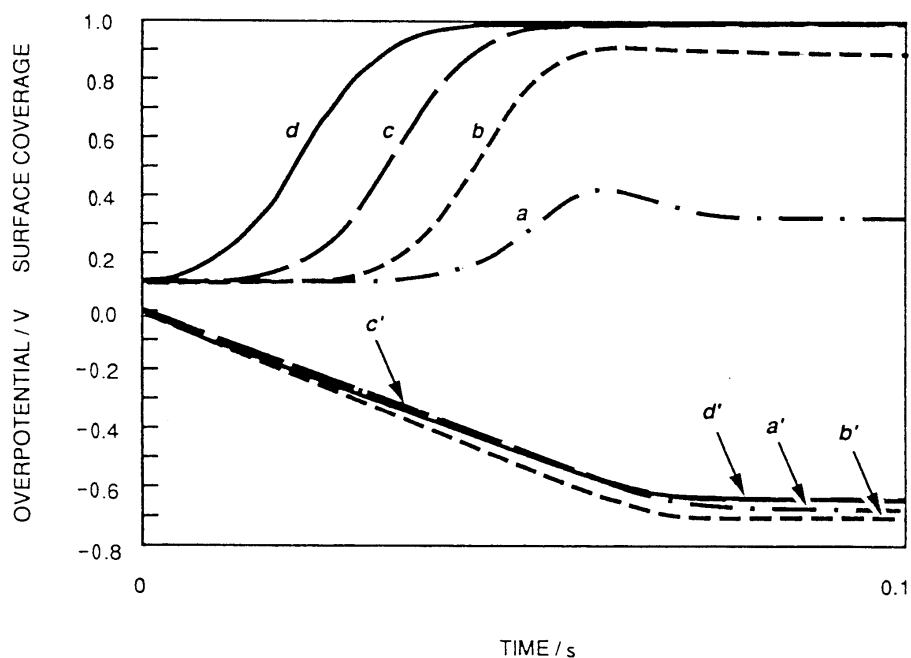


Figure A-4. Surface coverage and overpotential as a function of time. Effect of an emerging rds. Charging current: $-40 \times 10^{-3} \text{ A/cm}^2$; rate constants: $k_2 = 1.0 \text{ cm}^3/\text{mol s}$, $k_3 = 0.1 \text{ cm}^2/\text{mol s}$, $k_4 = 3 \times 10^6 \text{ cm}^3/\text{mol s}$; $k_1 = 10^2, 10^3, 10^4, 10^5 \text{ cm}^3/\text{mol s}$ for curves a, b, c, and d, respectively.

A somewhat different behavior is seen as the rds is changed from the recombination reaction, Fig. 5 curve a, to electrodesorption, Fig. 5 curve b. The effect, which is minimal in the $\theta(t)$ curve, is associated with a more negative overpotential, decreased by ca. 200 mV and a longer time required to attain the quasi-steady state. This is likely connected with the fact that the recombination reaction does not involve charge transfer.

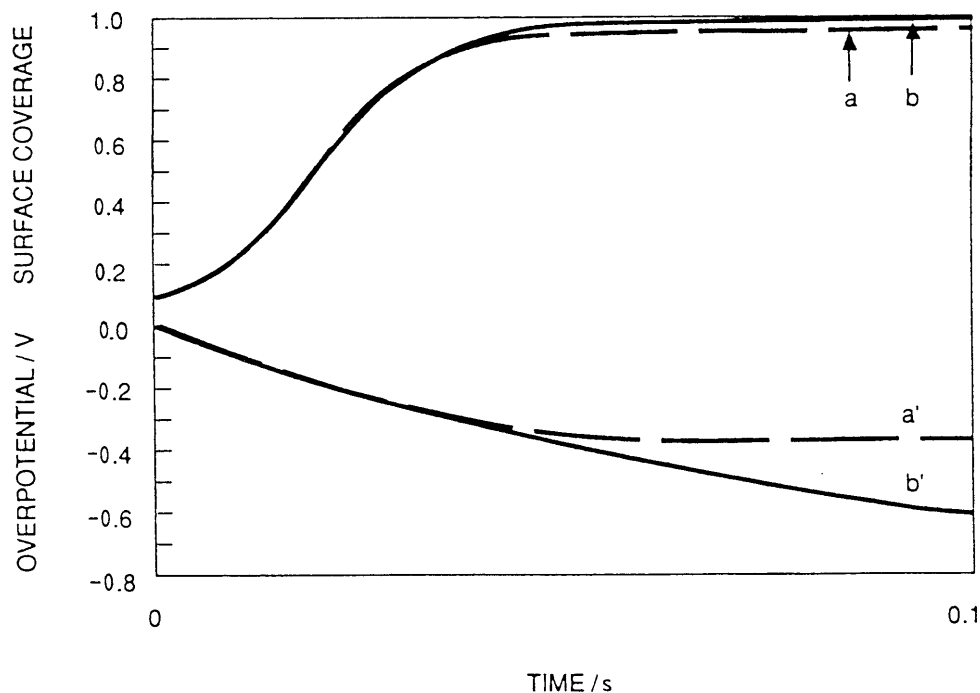


Figure A-5. Surface coverage and overpotential as a function of time. Effect of changing the rds. Charging current: $-40 \times 10^{-3} \text{ A/cm}^2$; $\theta_0 = 0.1$; $\xi_0 = 0.08$. Rate constants: $k_1 = 10^6 \text{ cm}^3/\text{mol s}$, $k_4 = 2.0 \times 10^7 \text{ cm}^3/\text{mol s}$. (a) $k_2 = 1.0 \text{ cm}^3/\text{mol s}$, $k_3 = 10^3 \text{ cm}^2/\text{mol s}$ (b) $k_2 = 10^3 \text{ cm}^3/\text{mol s}$, $k_3 = 1.0 \text{ cm}^2/\text{mol s}$.

Intuitively, the present model ascribes a dominant role to the rate of absorption, viz., the higher the rate, the faster the charging of the electrode. However, due to coupling between the surface processes, no such clear conclusion should be drawn unless the interphase (j_3, j_{-3}) controls the overall event. In general, an increase in the rate of absorption shifts the attainment of the quasi-steady state to somewhat longer times, as illustrated in Fig. 6. Also, the lower the rate of absorption, the greater the tendency to develop a maximum in the $\theta(t)$ curve, Fig. 6, curve a.

The coupling effect of the interphase processes on the surface coverage and overpotential as a function of charging current, suggested by eqns. (13) and (14), is illustrated in Figs. 7–9. Here, three cases are illustrated, viz., with the electrodesorption reaction as the rds, θ_{lim} increases with an increase in the charging current, Fig. 7; with a less clearly defined rds, θ_{lim} first increases, goes through a maximum and then decreases, Fig. 8; and with recombination/adsorption as a rather weak rds, θ_{lim} always decreases with an increase in the charging current, Fig. 9.

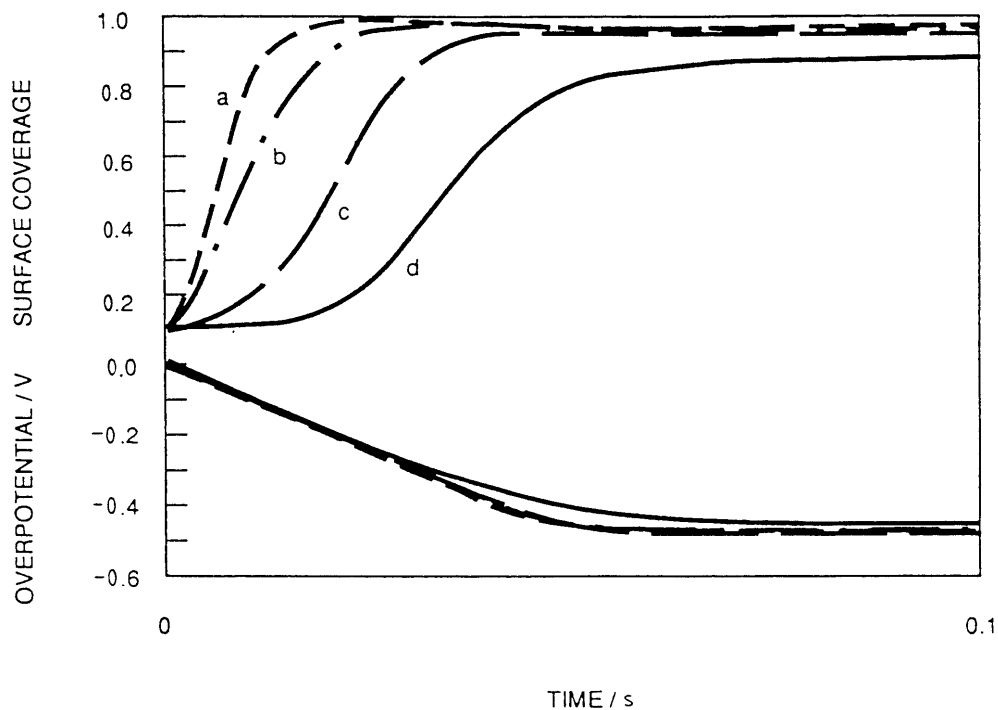


Figure A-6. Surface coverage and overpotential as a function of time. Effect of adsorption-absorption exchange rate. Charging current: $-40 \times 10^{-3} \text{ A/cm}^2$. Rate constants: $k_1 = 10^5 \text{ cm}^3/\text{mol s}$, $k_2 = 100 \text{ cm}^3/\text{mol s}$. $k_3 =$ (a) 3.0×10^4 , (b) 3.0×10^5 , (c) 3.0×10^6 , (d) $3.0 \times 10^7 \text{ cm}^3/\text{mol s}$.

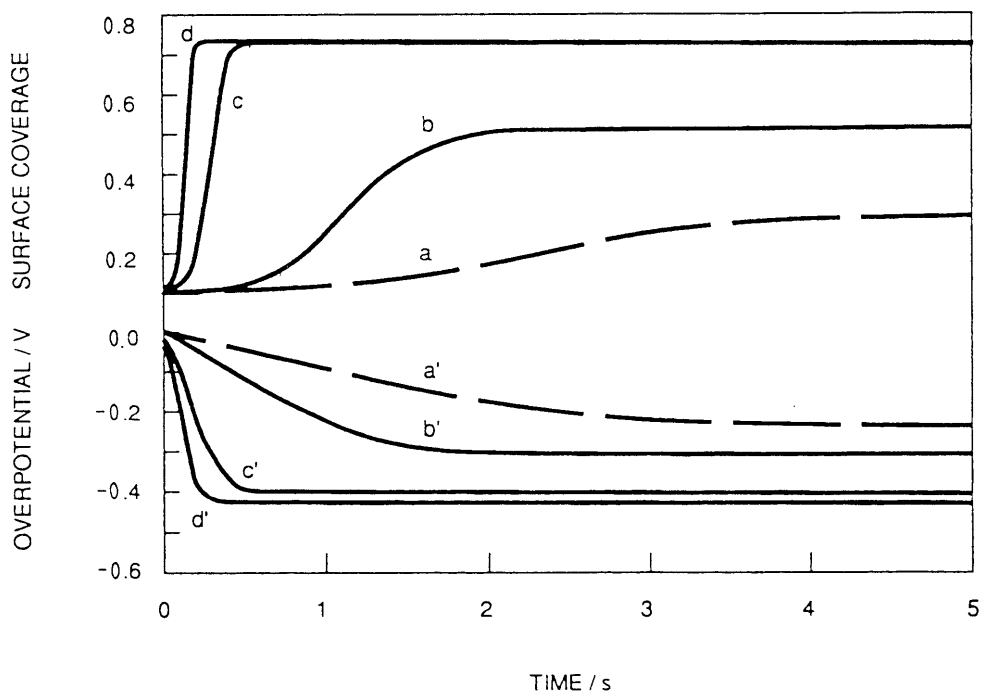


Figure A-7. Surface coverage and overpotential as a function of time. Effect of charging current. Rate constants: $k_1 = 10^5 \text{ cm}^3/\text{mol s}$, $k_2 = 10^3 \text{ cm}^3/\text{mol s}$, $k_3 = 1.0 \text{ cm}^2/\text{mol s}$, $k_4 = 2.0 \times 10^7 \text{ cm}^2/\text{mol s}$. Charging current: (a) -4.0×10^{-3} , (b) -10.0×10^{-3} , (c) -40.0×10^{-3} , (d) $-80 \times 10^{-3} \text{ A/cm}^2$.

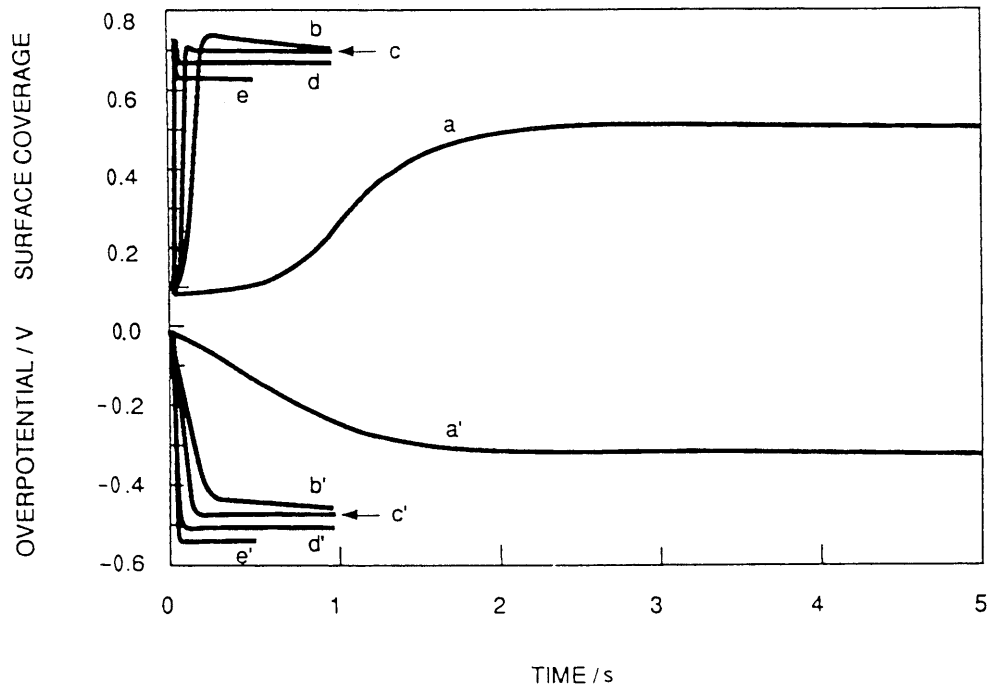


Figure A-8. Surface coverage and overpotential as a function of time: Effect of charging current. Rate constants: as in Fig 6. except for $k_3 = 10.0 \text{ cm}^2/\text{mol s}$. Charging current: (a) -10.0×10^{-3} , (b) -40.0×10^{-3} , (c) -80.0×10^{-3} , (d) -160.0×10^{-3} , (e) $-800.0 \times 10^{-3} \text{ A/cm}^2$.

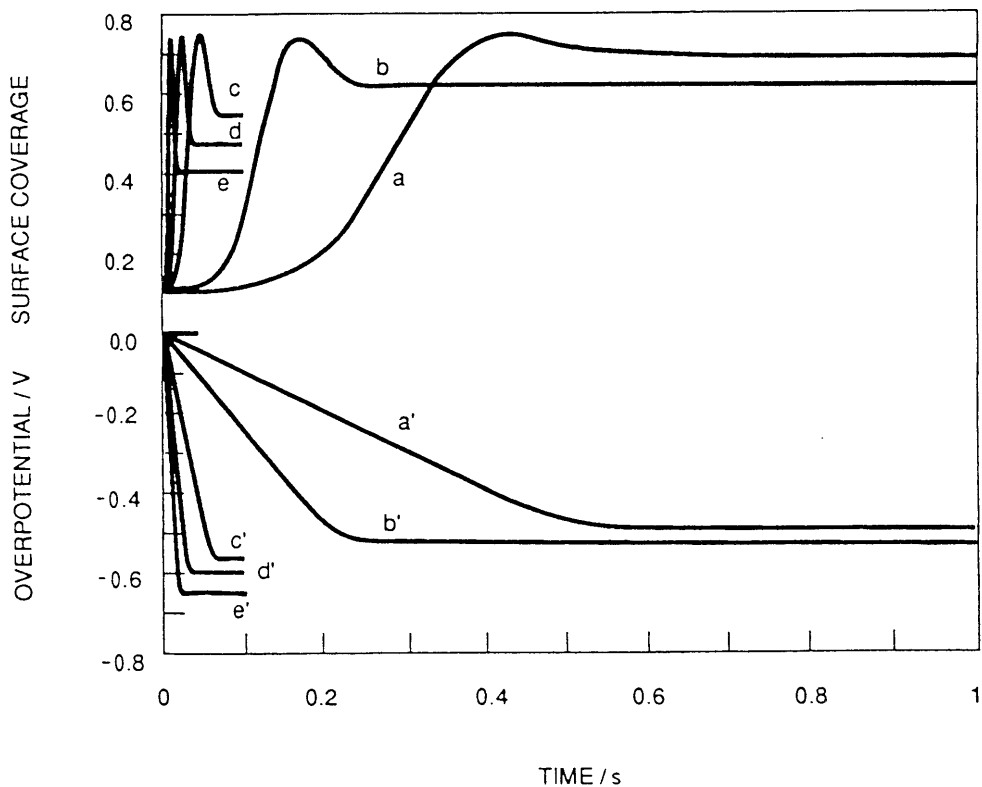


Figure A-9. Surface coverage and overpotential as a function of time: Effect of charging current. Rate constants: $k_1 = 1000 \text{ cm}^3/\text{mol s}$, $k_2 = 10 \text{ cm}^3/\text{mol s}$, $k_3 = 1000 \text{ cm}^2/\text{mol s}$, $k_4 = 2.0 \times 10^5 \text{ cm}^2/\text{mol s}$. Charging current: (a) -4.0×10^{-3} , (b) -10.0×10^{-3} , (c) -40.0×10^{-3} , (d) -80.0×10^{-3} , (e) $-800.0 \times 10^{-3} \text{ A/cm}^2$.

Charging of Electrode Interior

A threshold phenomenon has been proposed to initiate the effects reported by Fleischmann and Pons, i.e., contingent on achieving a degree of loading exceeding a certain critical value within a reasonably short period of time. In this section, we illustrate the interphase control vs. bulk transport control and show that an increase in the charging currents need not increase the level of electrode loading.

The coupling between interfacial processes and bulk transport admits, in principle, two modes of charging control. This is illustrated in Figs. 10, and 11. To demonstrate the transition from interphase to transport control, we calculated the time dependences $\theta(t)$, $\eta(t)$ and the normalized amount of absorbed deuterium in terms of $Q(t) = \sum_{i=1}^N V_i \xi_i(t) / \sum_{i=1}^N V_i$ for the values of the diffusion coefficient differing by several orders of magnitude. As expected and illustrated in Fig. 10, the initial electrode response is independent of the diffusion coefficient. The quasi-steady state was established within 0.5 s. However, as soon as the build-up of absorbed deuterium has begun, θ and Q vary almost linearly with time. For an unrealistic value of the diffusion coefficient, (e.g., $D = 10^{-4} \text{ cm}^2 \text{ s}^{-1}$), θ and Q

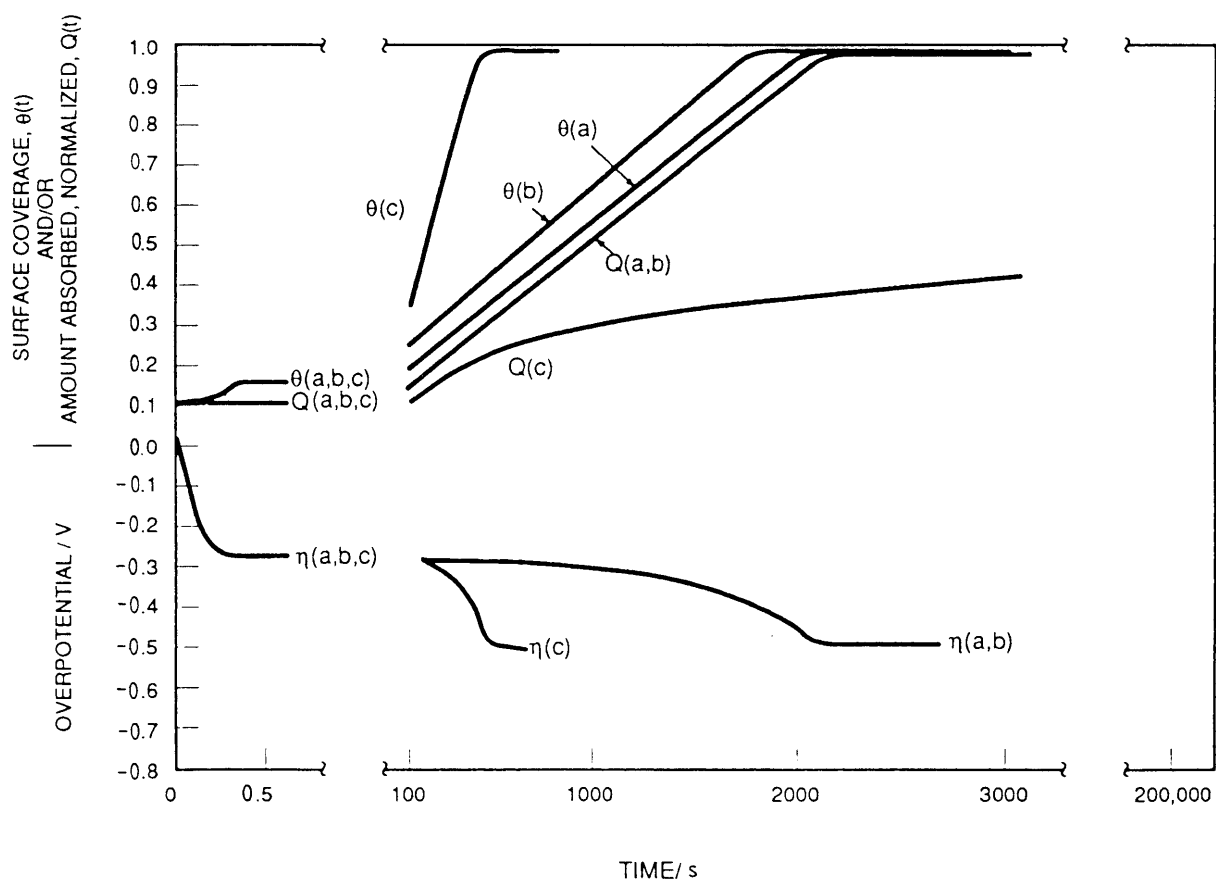


Figure A-10. Time dependent overpotential, η , surface coverage, θ , and normalized amount of absorption as a function of diffusion coefficient. (a) $10^{-4} \text{ cm}^2/\text{s}$; (b) $10^{-8} \text{ cm}^2/\text{s}$; (c) $10^{-10} \text{ cm}^2/\text{s}$. Charging current: $0.1 \text{ A}/\text{cm}^2$. Rate constants: $k_1 = 10^3 \text{ cm}^3/\text{mol s}$, $k_2 = 10 \text{ cm}^3/\text{mol s}$, $k_3 = 10^3 \text{ cm}^2/\text{mol s}$, $k_4 = 2 \times 10^5 \text{ cm}^3/\text{mol s}$.

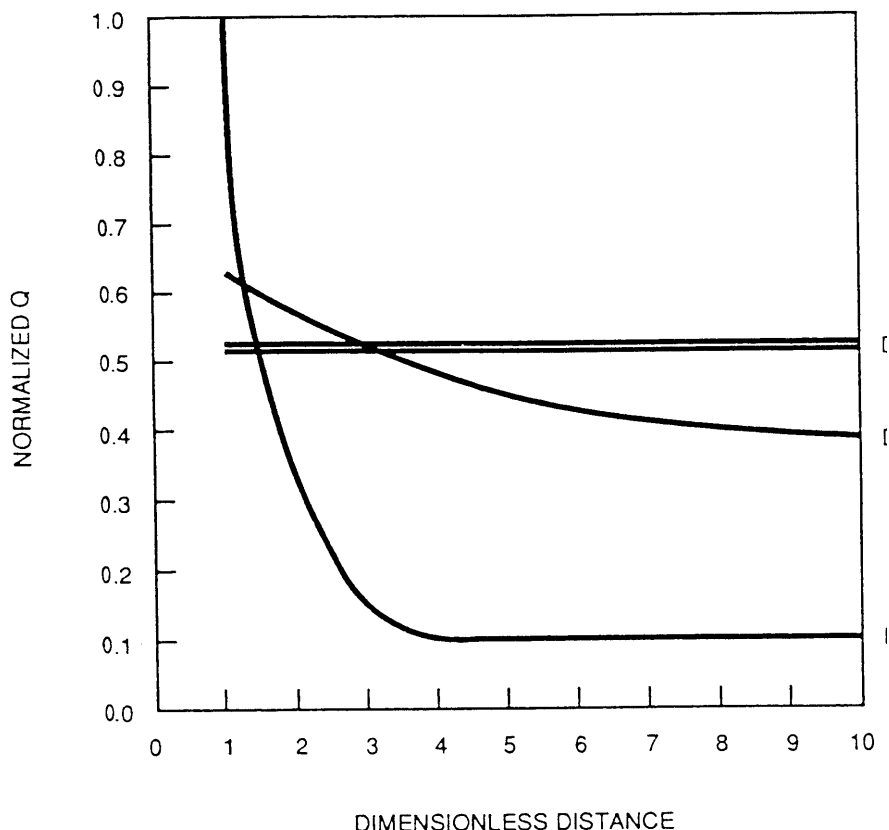


Figure A-11. Normalized amount of absorbed material as a function of distance. Diffusion coefficients (in cm^2/s) indicated; other data as in Fig. 10.

reached their limiting values almost simultaneously. This is consistent with interphase control. The transition to transport control, however, is not sharp and the electrode exhibits a mixed control for a substantial range of diffusion coefficients, e.g., $10^{-6} < \mathbf{D} < 10^{-8} \text{ cm}^2 \text{ s}^{-1}$. In particular, for the set of input parameters in the example illustrated in Fig. 10, the electrode charging is under diffusion control only when $\mathbf{D} = 10^{-8} \text{ cm}^2 \text{ s}^{-1}$ or less. This transition from interphase to diffusion control manifests itself by an increase in the slope $d\theta/dt$ and a substantial delay in the achievement of full saturation of the electrode interior. The distribution of the filling of the available sites, Fig. 11, further illustrates the transition from the interphase to bulk diffusion control.

Another example of the effect of the complex interplay between the interphase processes at two charging current densities is shown in Fig. 12. Contrary to intuitive expectations that an increase in the charging currents should increase loading, the model predicts that, with a specific set of rate constants, a lower level of loading can result with no reduction in charging time observed.

CONCLUDING REMARKS

Qualitatively, the model reflects the complicated nature of the charging process. It indicates that difficulties may be encountered in controlling the charging process because of the large number of factors that may affect one or more of the interphase processes. Quantitative analysis could not be carried out because the relevant data were not available and the use of kinetic parameters associated

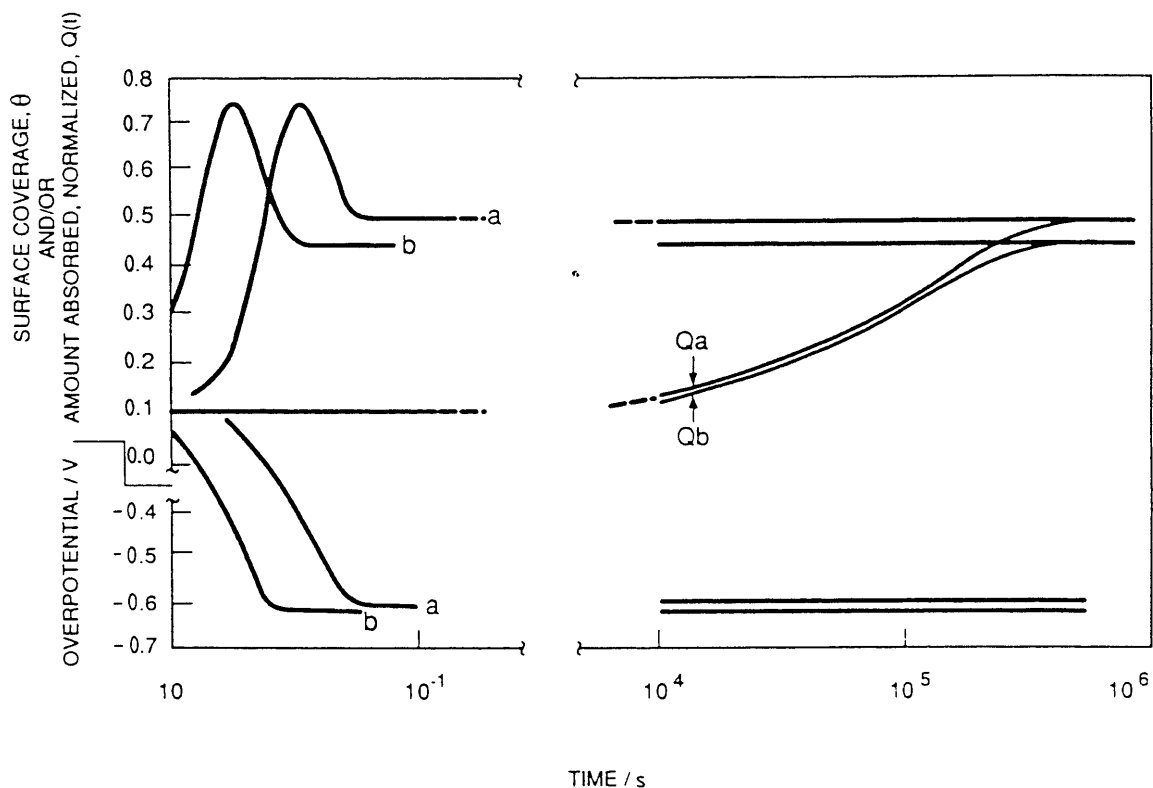


Figure A-12. Effect of charging current on electrode loading. (a) 0.05 A/cm²; (b) 0.1 A/cm². Rate constants: $k_1 = 10^3$ cm³/mol s; $k_2 = 10$ cm³/mol s; $k_3 = 10^3$ cm²/mol s; $k_4 = 2 \times 10^5$ cm³/mol s.

with the hydrogen evolution reaction cannot be justified in view of recent results [23]. Other simplifications, e.g., the constancy of input parameters can be corrected (for example, a concentration dependent diffusion coefficient could be included). A more serious deficiency is the employment of the simplest interphase when, in fact, a supercharged region exists.

ACKNOWLEDGEMENT

The authors wish to thank Professors Fleischmann and Pons for helpful comments.

APPENDIX: DERIVATION OF EQNS. (17) AND (18)

The cross section of the rod of length L and radius r_0 is partitioned into N annular layers of thickness Δr . With the layers labeled from 1 to N from the outer surface to the center, respectively, the volume V_i of the i th layer and the interface surface $S_{i,i+1}$ between the i th and $(i + 1)$ th layers are:

$$V_i = \pi(r_i^2 - r_{i+1}^2)L \quad (1A)$$

$$S_{i,i+1} = 2\pi r_{i+1}L \quad (2A)$$

where $r_i = (N - i + 1)\Delta r$. Consequently, the relevant surface to volume ratios are

$$\frac{S_{i-1,i}}{V_i} = \frac{2r_i}{r_i^2 - r_{i+1}^2} = \left(\frac{2r_i}{r_i + r_{i+1}} \right) \frac{1}{\Delta r} \quad (3A)$$

and

$$\frac{S_{i,i+1}}{V_i} = \frac{2r_{i+1}}{r_i^2 - r_{i+1}^2} = \frac{2r_i}{r_i + r_{i+1}} \left(1 - \frac{\Delta r}{r_i}\right) \frac{1}{\Delta r} \quad (4A)$$

Substitutions of these ratios into eqn. (8) yields

$$\frac{d\bar{\zeta}_i}{dt} = d_d Z_m \Delta r \left(\frac{2r_i}{r_i + r_{i+1}} \right) \left[\frac{\zeta_{i-1} - 2\zeta_i + \zeta_{i+1}}{\Delta r^2} + \frac{1}{r_i} \left(\frac{\zeta_i - \zeta_{i+1}}{\Delta r} \right) \right] \quad (5A)$$

which, upon rearrangement becomes eqn. (19). The ratios given in eqns. (3A) and (4A) become, for $i = 1$

$$\frac{S_{0,1}}{V_i} = \left(\frac{2r_0}{2r_0 - \Delta r} \right) \frac{1}{\Delta r} \quad (6A)$$

and

$$\frac{S_{1,2}}{V_i} = \frac{2r_0}{2r_0 - \Delta r} \left(1 - \frac{\Delta r}{r_0}\right) \frac{1}{\Delta r} \quad (7A)$$

since $r_1 = r_0$ and $r_2 = r_0 - \Delta r$. Substitution of eqns. (6A) and (7A) into eqn. (17) yields eqn. (18).

The form of eqn. (5A) shows the relationship of eqn. (5A) to the diffusion equation written in cylindrical coordinates and approximated by finite differences. Generally, $k_d Z_m \Delta r$ would be identified with the diffusion coefficient and the ratio $2r_i/(r_i + r_{i+1})$ set equal to one as, in the limit, Δr approaches zero. However, here we retain the ratio as Δr is not necessarily small enough to take the limit, but do identify the diffusion coefficient as $k_d Z_m \Delta r$.

REFERENCES

1. J. Jorne, J. Electrochem. Soc., 137(1990) 369.
2. M. Fleischmann and S. Pons, J. Electroanal. Chem., 261(1989) 301; err. 263 (1989) 187. 3
3. Wagner, Z. Phys. Chem., A159 (1932)459; A193 (1944)386.
4. R. Fowler and E.A Guggenheim, Statistical Thermodynamics, Cambridge University Press Cambridge, 1949.
5. H.-G. Fritsche, Z. Naturforsch., 38a (1983)1118.
6. M. von Stackelberg and P. Ludwig, Z. Naturforsch., 19a (1964)93.
7. B. Dandapani and M. Fleischmann, J. Electroanal. Chem., 39(1972)323.
8. H. Brodowsky, Z. Phys. Chem., N.F., 44(1965)9.
9. R.M. Stoneham, Ber. Bunsenges. Phys. Chem., 76(1972)816.
10. J. Voelkl, Ber. Bunsenges. Phys. Chem., 76(1972)797.
11. E. Wicke and G.H. Nernst, Ber. Bunsenges. Phys. Chem., 68(1964)224.

12. R. Defay, I. Prigogine, A. Bellamans and D.H. Everett, *Surface Tension and Adsorption*, Longmans, Green and Co, Ltd., London, 1966.
13. H.-D. Ohlenbusch, *Z. Elektrochem.*, 60(1955)603.
14. P. van Rysselberghe, in J.O'M. Bockris and B.E. Conway (Eds.), *Moderns Aspects of Electrochemistry*, Vol. 4, Plenum Press, New York, 1966, p. 1.
15. W. Auer and H.J. Grabke, *Ber. Bunsenges. Phys. Chem.*, 78(1974)58.
16. E. Fromm, H. Uchida and B. Chelluri, *Ber. Bunsenges. Phys. Chem.*, 87(1983)410.
17. S. Schuldiner and J.P. Hoare, *J. Electrochem. Soc.*, 105(1958)278.
18. E. Gileadi and B.E. Conway, *J. Chem. Phys.*, 39(1963)3420.
19. R.N. Iyer, H.W. Pickering and M. Zamanzadeh, *J. Electrochem. Soc.*, 136(1989)2463.
20. R.M. Barrer and W. Jost, *Trans. Faraday Soc.*, 45(1949)928.
21. M. Kuballa and B. Baranowski, *Ber. Bunsenges Phys. Chem.*, 78(1974)335.
22. G. Sicking, M. Glugla and B. Huber, *Ber. Bunsenges. Phys. Chem.*, 76(1972)418
23. D. Rolison and P.P. Trzaskoma, *J. Electroanal. Chem.*, 287(1990)375.
24. S. Szpak, P.A. Mosier-Boss and J.J. Smith, unpublished results, 1990.
25. J.W. Davenport, G.J. Dienes and R.A. Johnson, *Phys. Rev.*, 25(1982)2165.
26. W.H. Press and S.A. Teukolsky, *Comput. Phys.*, May/June (1989)88.

Charging of the Pd/ n H system: role of the interphase

S. Szpak *, P.A. Mosier-Boss and S.R. Scharber **

Naval Ocean Systems Center, San Diego CA 92152-5000 (USA)

J.J. Smith

Department of Energy, Washington DC 20585 (USA)

(Received 12 November 1991; in revised form 16 March 1992)

ABSTRACT

The dynamics of transport of electrochemically generated deuterium across the electrode/electrolyte interphase was examined by slow scan (10 mV s^{-1}) voltammetry. The investigation covers the potential range -1.2 to $+0.4$ V measured vs. an Ag/AgCl reference. It was found that a coupled, two-layer model of the interphase describes the observed behavior as a function of scan rate and electrolyte composition. The effect of chemisorbing species, e.g. CN^- ions, as well as reactive species, e.g. $\text{SC}(\text{NH}_2)_2$, on the transport across the interphase is also discussed. Results are contrasted with those obtained for light water.

1. INTRODUCTION

The interest in the physicochemical properties of the Pd/ n H, $n = 1,2$, system is prompted by the recent reports that nuclear events are induced by electrochemical compression of deuterium within the palladium lattice [1,2]. The magnitude of this compression, or the degree of loading of the palladium lattice with deuterium during electrolysis, is governed by the processes occurring at, and within, the electrode/electrolyte interphase. These processes both determine the structure of the interphase and define the correct boundary conditions for the solution of the diffusion equation governing the transport of n H interstitials generated during electroreduction of $n\text{H}_2\text{O}$ [3,4]. The literature on this subject is voluminous [5–9] but, with a few exceptions [5], limited to light hydrogen. Direct transfer of this information to the transport of deuterium is inappropriate, as shown by microscopic examination of the development of electrode surface morphology following prolonged electrolysis of these two systems [10].

*To whom correspondence should be addressed.

**Permanent address: San Diego Mesa College, San Diego, CA 92111, USA.

The purpose of this communication is to examine the properties and behavior of the palladium/electrolyte interphase in the presence of evolving deuterium and/or hydrogen and to accentuate the differences in interaction between these isotopes and the palladium electrode surface. This is of particular interest in determining the conditions for the initiation of the Fleischmann–Pons effect by the co-deposition technique [11]. We selected slow scan cyclic voltammetry as the primary experimental technique. The advantages of this technique have been pointed out by, among others, Capon and Parsons [6] and Chevillot et al. [9].

2. EXPERIMENTAL

A single-compartment, three-electrode cell was employed throughout. The potential scan was controlled by a PAR, model 362, potentiostat. The reference electrode consisted of a fritted chamber in which an Ag/AgCl wire was immersed in saturated KCl solution in $^n\text{H}_2\text{O}$. This arrangement minimizes Cl^- contamination of the electrolyte of interest. The working electrode was electrodeposited palladium on a gold sphere with a surface area of ca. $5 \times 10^{-2} \text{ cm}^2$, from a bath containing 0.05 M PdCl_2 (Aldrich) and 0.3 M LiCl (Mallinckrodt) dissolved in $^n\text{H}_2\text{O}$ (Merck), followed by rinsing in the electrolyte of interest. The use of a gold substrate assured the containment of hydrogen or deuterium within the palladium film and made it possible to vary the thickness and morphology of the palladium deposits in a controlled manner. This approach allowed us to discriminate between bulk and surface effects. A coiled platinum wire was placed around the working electrode to provide a uniform current density distribution. All chemicals were of the highest commercially available quality (analytical reagent grade) and used as received, except when adjusting the pH of the electrolyte. For lowering the pH in light water, concentrated ^1HCl was used; for heavy water, the deuterated hydrochloric acid was prepared as follows: $^2\text{H}_2\text{O}$ was added to Al_2Cl_6 (Aldrich) and the gaseous ^2HCl was bubbled into a vessel containing $^2\text{H}_2\text{O}$. To increase the pH, LiO^nH prepared from metallic lithium (Alfa), was used.

3. STRUCTURE AND DYNAMICS OF THE INTERPHASE

Whenever two phases are brought in contact with each other, an interphase region is created. In electrochemical systems, because of the distribution of electrical charges, the behavior of the Pd/ ^nH -interphase under non-equilibrium conditions can only be described by a multilayer model, in which each layer is of uniform composition and infinitesimal thickness [12]. The structure of the electrolyte side of the interphase associated with the hydrogen evolution reaction and the operating driving forces for the Volmer, Heyrovsky—Horiuti and Tafel paths—in the absence of absorption—has been given by van Rysselberghe [3]. Much less information has been assembled for the solid component of the interphase where the high solubility and mobility of the $n \text{ H}$ interstitials contribute to the complex nature of the Pd/ ^nH interphase.

One specific example of such a non-autonomous interphase has been considered by Bucur and Bota [13]. They postulated a palladium/electrolyte interphase consisting of two sharply defined regions with discontinuous physicochemical properties. In effect, they considered a common adsorption surface in contact with, and affected by, homogeneous solid and liquid phases. The adsorption plane is in contact with the double layer and with a very thin region, the λ layer, where the concentration of hydrogen is much higher than that which is weakly adsorbed, H(a) , or present in the bulk palladium H(II) . In the present discussion, although we retain the Bucur—Bota model, we emphasize its non-autonomous character. Thus, we define a transfer zone λ^* , eqn. (1),

$$\lambda^* = \lambda_s + \lambda_e \quad (1)$$

where λ_s and λ_e denote those segments (layers) of the solid and electrolyte phase that actively participate in, and/or dominate, the transport of ^nH between them, as illustrated in Fig. 1. By splitting the

interphase into several distinct layers, we are able to identify processes that control the transport of ${}^m\text{H}$ during the potential sweep and the effect of electrolyte composition and electrode surface morphology on that transport. To this end, we have investigated the effect of scan rate, pH, weakly adsorbable ions and surface active species.

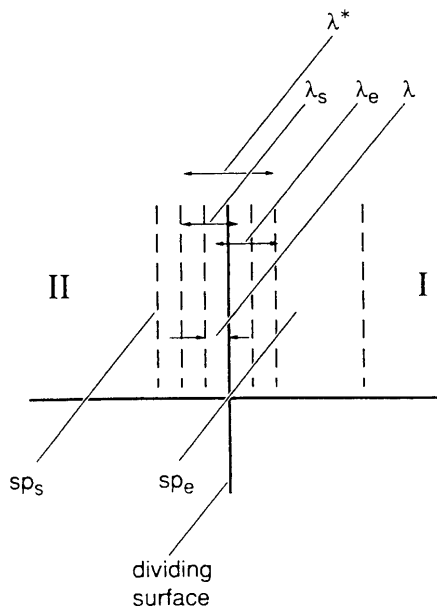


Figure 1. Electrode/electrolyte interphase: λ , Bucur–Bota [13] transfer zone; λ^* , a coupled, two-layer segment of an interphase; λ_s , λ_e , metal and electrolyte side of the two-layer segment; sp_s , sp_e , space charge layers.

As required by the non-autonomous character of the interphase, the λ^* layer is an active element of the interphase responding to, and being affected by, the transport across it. For example, the thickness λ^* is affected by charged species, especially those that are strongly adsorbed. It is also affected by the extent of anodic polarization and is attributed to specifically adsorbed negative charges (anions) and oriented ${}^m\text{H}_2\text{O}$ dipoles within the adsorption layer. The excess negative charges within this layer promotes an accumulation of positive charges (deuterons) held in the transfer layer so that the λ_s layer may extend deeper into the palladium electrode. Also, the anodic current modifies (restructures) the electrode surface by enhancing the transport of ${}^m\text{H}$ which, in our opinion, is an autocatalytic effect.

4. RESULTS AND DISCUSSION

Our experimental results, presented here in the form of voltammograms, were employed to elucidate the behavior of electrochemically generated deuterium on palladium electrodes. The basis for the discussion is the splitting of the interphase into parts reflecting the structure of the metal side, s, and separately, the electrolyte phase, e.

4.1. General Features of the Pd/ ${}^m\text{H}$ Voltammograms

Typical voltammograms covering the Pd/ ${}^m\text{H}$ region -1300 to $+400$ mV, shown in Fig. 2, are similar to those reported by others [5–9]. Of the two branches, the more revealing and interesting is the anodic branch, because it is here that the characteristic features associated with the ${}^m\text{H}$ transport across the interphase are displayed. An important factor affecting the shape of voltammograms is the electrode surface morphology. On smooth and thin electrodeposits of palladium on gold, peak B is poorly defined compared with peak C. In contrast, both peaks are clearly seen on black palladium

electrodes, i.e. on electrodes prepared at higher current densities. The scanning electron micrograph photograph of the smooth palladium electrode, Fig. 2(a), shows the growth of crystallites on a smooth surface whereas the black palladium surface is porous and consists of an agglomerate of spherical particles of submicrometer size, Fig. 2(b). Therefore, the difference in the shape of voltammograms are due to a surface-to-volume effect of the palladium electrode, a conclusion reached earlier by Chevillot et al. [9]. It was shown that black palladium has an increased number of boundaries where the preferential absorption occurs [10,14], and that hydrogen sorption, I.e. combined adsorption and absorption processes, is much more irreversible in thin films than in bulk palladium [8]. A small cathodic peak, peak D, is observed in the voltammograms on black palladium films but not on smooth palladium. It is unlikely that this peak is due to the reduction of an oxide as the potential scan was terminated prior to oxide formation. Since the black palladium films are thicker and have more surface area as well as more boundaries, peak D is assigned to adsorbed ^mH .

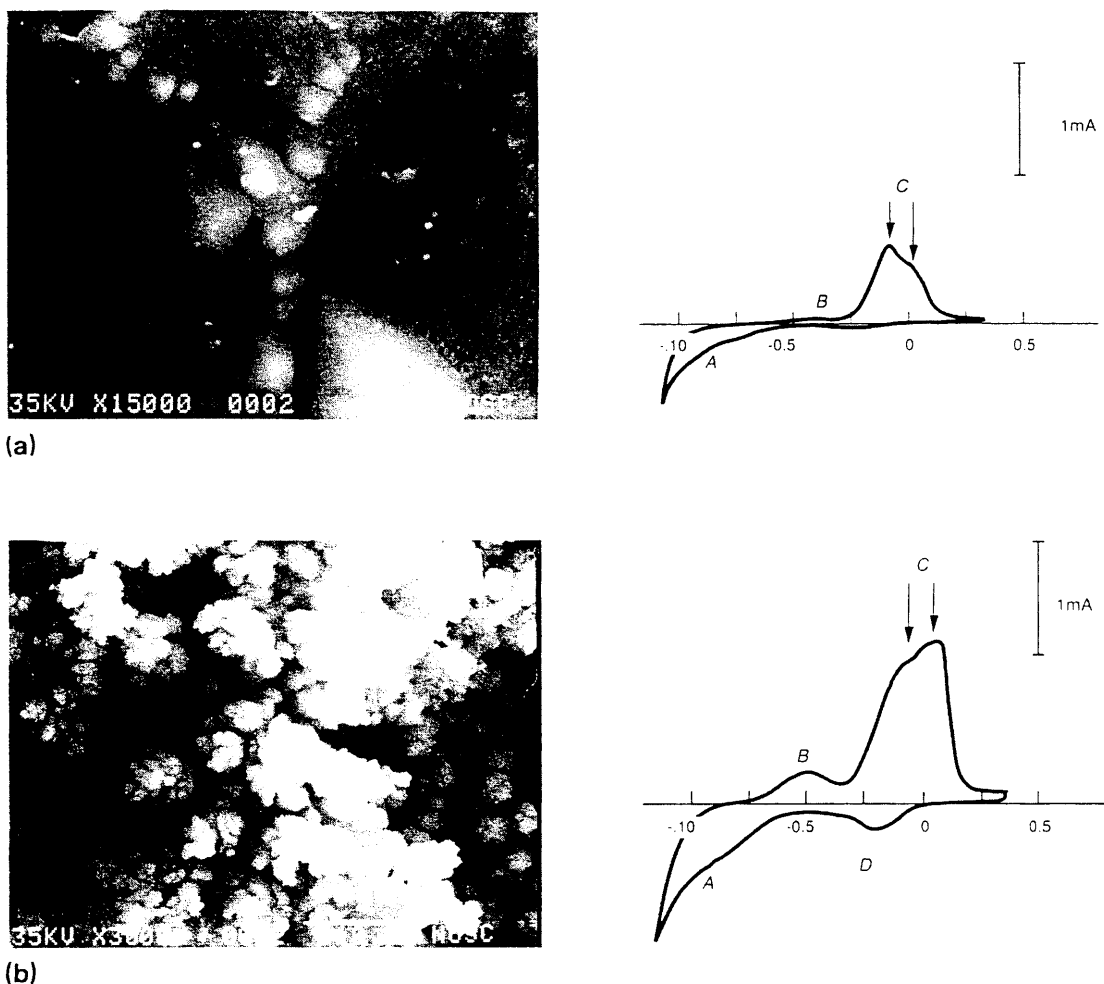


Figure 2. Scanning electron micrographs of palladium electrode surface and corresponding voltammograms, scan rate 10 mVs^{-1} , electrolyte $0.3 \text{ M LiCl/D}_2\text{O}$: (a) smooth (electrodeposited at $500 \mu\text{A}$); (b) black palladium (electrodeposited at $500 \mu\text{A}$ for 60 min, followed by $50 \mu\text{A}$ for 3 min).

The positive scan of the voltammograms shows two peaks, labeled B and C, of which peak C is actually composed of two closely spaced peaks, C_1 and C_2 . These peaks are generally referred to as “weak” and “strong” adsorption or, more appropriately, to weakly and strongly bound hydrogen. Since peak C occurs at a higher potential and has a higher free energy of adsorption, it is attributed to

strongly bound hydrogen. With regard to Fig. 1, we assign peaks B and C to the reoxidation of ${}^n\text{H}$ in the λ_e and λ_s regions respectively. Since peak C is actually a superposition of two closely spaced peaks, implying that there are two forms of strongly bound ${}^n\text{H}$, there are at least three forms of hydrogen present in the electrode/electrolyte interphase.

A somewhat better insight into the role of the interphase can be obtained by examining Fig. 3. Figures 3(a) and 3(b) were constructed by varying the potential range scanned. In particular, Fig. 3(a) shows voltammograms that terminate at +400 mV with an increasing span in the negative direction, while Fig. 3(b) illustrates the behavior obtained by anchoring the lower limit at -1200 mV and varying the upper limit. A very small anodic current is observed in the former case, Fig. 3(a), starting the scan at the rest potential, i.e. -118 mV, and terminating at +400 mV. On the return sweep, two peaks appear, at 0.0 mV and at -400 mV, peaks D₁ and D₂. A decrease in the lower limit causes the anodic current to increase and leads to the formation of peaks B, C₁ and C₂; simultaneously, there is a decrease in peaks D₁ and D₂. Different behavior is seen when the upper limit is varied. Termination of the positive scan anywhere within the broad peak B results in a retracing of the anodic segment, see Fig. 3(b). When the scan reversal is initiated at more positive potentials, i.e. outside peak B, a small peak at -150 mV appears which first increases in magnitude and reaches a maximum for scan reversals terminating at the potential of peak C₁. Continuation of scan reversal further into the anodic region, results in a return to a featureless shape of the cathodic segment.

These observations lead to the tentative conclusion that the structure and properties of the λ^* part of the interphase are potential dependent. At potentials less than or equal to +400 mV, the λ_e part of the interphase is electrochemically active (e.g. presence of adsorption sites), provided that no deuterium is present in the λ_s segment. The behavior of the $I-\eta$ curves, i.e. the appearance of the cathodic peak at -150 mV, shown in Fig. 3(b), suggests the presence within the interphase of charged species containing deuterium, perhaps a $[\text{}^2\text{H} \dots \text{}^2\text{H}]^+$ complex.

Incidentally, there is a degree of similarity between the electrochemical path and that associated with the solid-gas system. In the latter, Auer and Grabke [15] found that three states of the ${}^n\text{H}$ atom exist and play a role in the reaction $\text{H}_2 \rightarrow 2\text{H}(\text{II})$: first, $\text{H}(\text{II})$ residing in the bulk interstices; second, H adsorbed on palladium atoms on the outer surface; third, $\text{H}(\lambda^*)$ adsorbed at the interstices of the inner surface. All these forms are in equilibrium during the adsorption-desorption process. In both electrochemical and solid-gas systems, the dynamic character of the interphase is driven by the energetics associated with the transport of the interstitials.

4.2. Stabilization of Voltammograms

The voltammograms of the Pd/ ${}^n\text{H}$ region, as in many other complex systems, require several cycles for stabilization. In the present case, as illustrated in Fig. 4, five to ten cycles were usually needed. In general, it was found that the presence of surface active species in the electrolyte reduced significantly the number of cycles needed to stabilize the voltammograms, also shown in Fig. 4. The depth of penetration of diffusing n H interstitials into the palladium electrode is fixed by the stability of the interphase which, in turn, assures stabilization of the voltammograms [16]. This interpretation is in agreement with the concept illustrated in Fig. 1, i.e. when viewing the interphase as composed of two parts, λ_s and λ_e , we conclude that the chemisorbed CN^- ion promotes lesser variation in the concentration of the reactive species with the time dependent overpotential, while the presence of an isopotential point, point P, can be interpreted as the accumulation of ${}^n\text{H}$ within the λ^* layer [17].

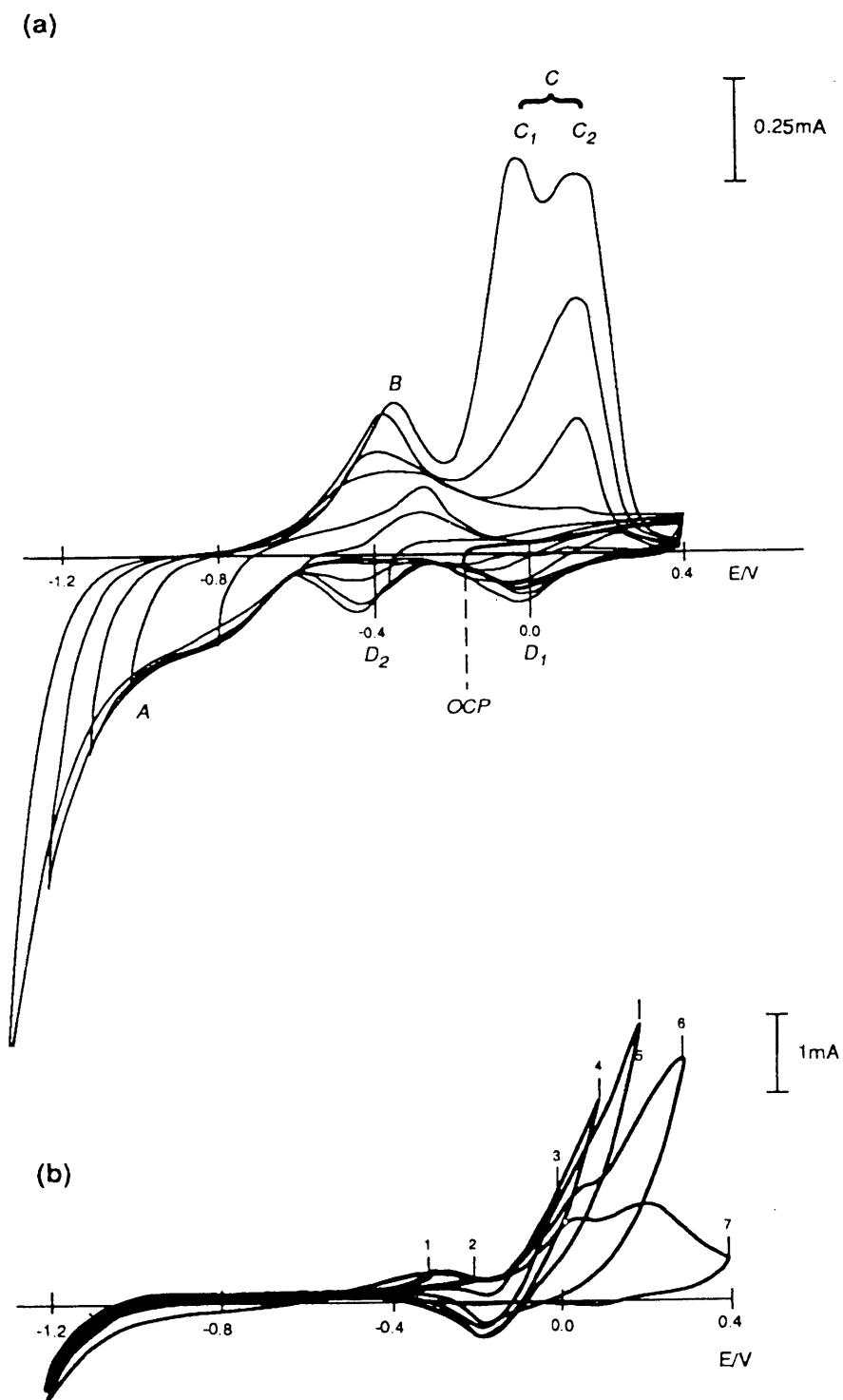


Figure 3. Evolution of voltammograms: (a) as a function of lower scan reversal for a fixed (+400 mV) upper limit potential, reversals at -300, -500, -700, -900, -1000, -1100 and -1200 mV, OCP = -0.118 V vs. Ag/AgCl reference; (b) as a function of upper scan reversal for a fixed (-1200 mV) lower limit potential, reversals at -300 (1), -200 (2), -100 (3), 0.0 (4), +100 (5), +200 (6), and +400 (7) mV.

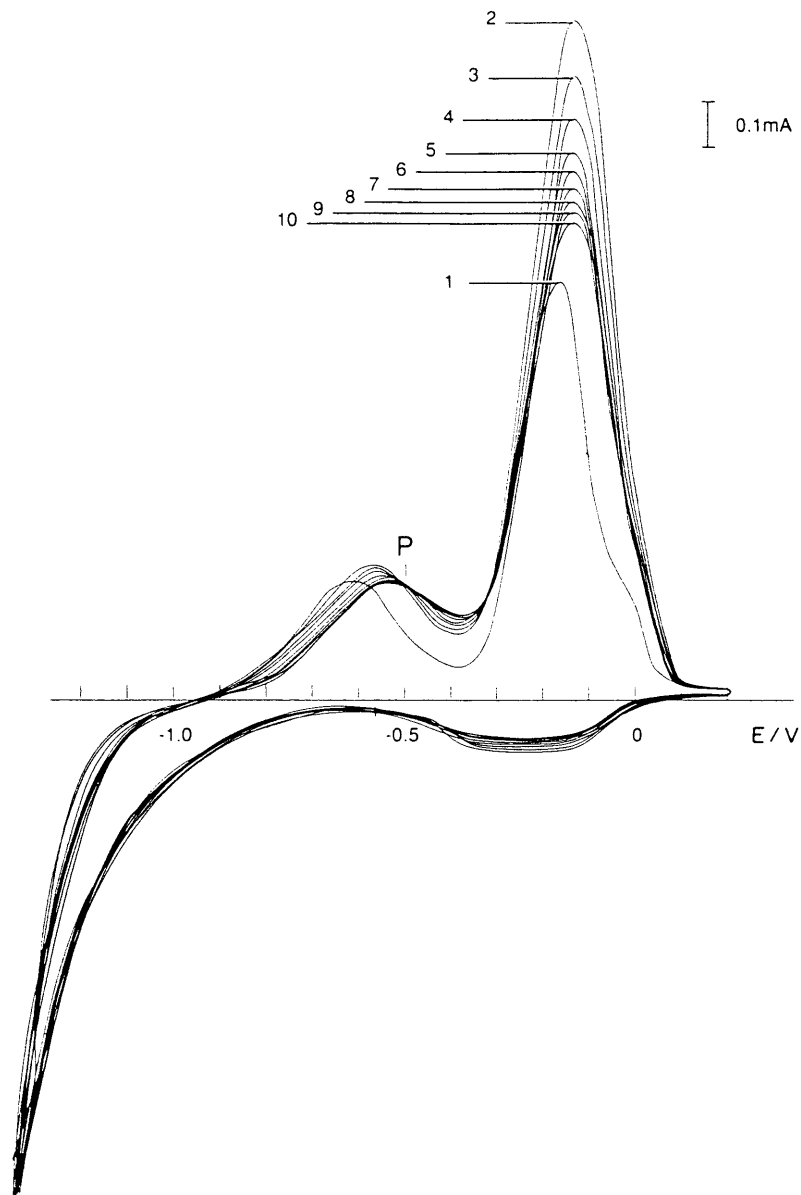


Figure 4. Effect of cycling, electrode surface black palladium, solution $0.3 \text{ M}^1 \text{ Li}_2\text{SO}_4/\text{D}_2\text{O}$, pH 4, scan rate 10 mVs^{-1} , P isopotential point.

4.3. Effect of Scan Rate

The effect of scan rate is shown in Fig. 5. The major effects of an increase in the scan rate are the disappearance of peak A during the negative scan, an increase in area of peak B, and a shift of peak B to higher potentials during the positive scan. The shift in potential of peak B is limited to a relatively narrow range of scan rates, i.e. to rates greater than 10 but less than 100 mV s^{-1} ; the latter scan rate separates the transport phenomena from surface kinetics [13,18]. In contrast, peak C shows relatively little change either in area or position with increasing scan rate. We assume that as interstitial hydrogen, ${}^m\text{H}(\text{II})$, leaves the bulk palladium metal and enters the solution phase, it first traverses the λ^* layer (which consists of the first $200\text{--}500 \text{ \AA}$ of the metal [13]) and the adsorption layer. Once in the adsorption layer, the ${}^m\text{H}(\lambda_e)$ can either reoxidize or it can enter the space charge layer. In terms of eqn. (1), the effect of scan rate illustrates the influence of the individual parts of the interphase, cf. Fig. 1.

Peak C is due to the reoxidation of strongly bound hydrogen, i.e. hydrogen that resides in the λ_s layer, see Fig. 1. Consequently, if the rate of transport of hydrogen into the λ_s layer is equal to or greater than the rate of the charge transfer, then the concentration of ${}^2\text{H}(\lambda_s)$ should remain relatively constant. This will result in a peak which shows little or no effect with scan rate, as in the case of peak C. Conversely, peak B is assigned to the reoxidation of weakly bound hydrogen, i.e. hydrogen which resides in the λ_e layer, Fig. 1. If the rate of transport into the λ_e layer is slow relative to the charge transfer, then the opposite effect is expected, i.e. peak B increases in size with increasing scan rate.

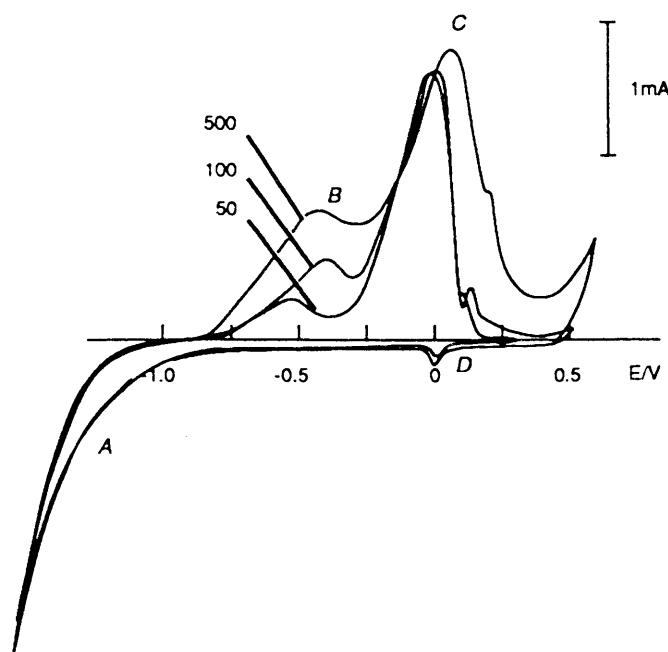


Figure 5. Effect of scan rate, electrode surface black palladium, solution 0.3 M LiCl/D₂O, ph 7, scan rates in millivolts per second indicated.

4.4. Voltammograms in Heavy vs. Light Water

One of the conditions believed to prevent the initiation and/or terminate the Fleischmann–Pons effect is the presence of light water in the electrolyte. Its effect on the shape of voltammograms is illustrated in Fig. 6, in particular on the shape and position of peak C. As the concentration of light water is increased, peak C₁ loses its identity (points P₁, P₂, P₃), while peak C₂ increases in peak height and is shifted to higher potential. While there is no change in either the magnitude or position of peak B, peak A becomes an inflection point and a greater number of sweeps are needed for stabilization of the voltammograms as the concentration of light water is increased.

Figure 7(a) shows the effect of adding light water to heavy water during cycling. The results are similar to those described for the mixed ${}^1\text{H}_2\text{O}$ – ${}^2\text{H}_2\text{O}$ solvents shown in Fig. 6. Finally, the effect of adding heavy water to light water during cycling is shown in Fig. 7(b). It is noted that, as in the previous case, it takes a greater number of sweeps to stabilize the voltammograms shown in Fig. 7. Although more work is needed to establish the effect of mixed solvents on the shape of the voltammograms, nevertheless the present results clearly indicate that exchange of protons and deuterons within the palladium lattice occurs at sufficiently high cathodic overpotentials, (i.e. greater than -1.0 V, the so-called Tafel region).

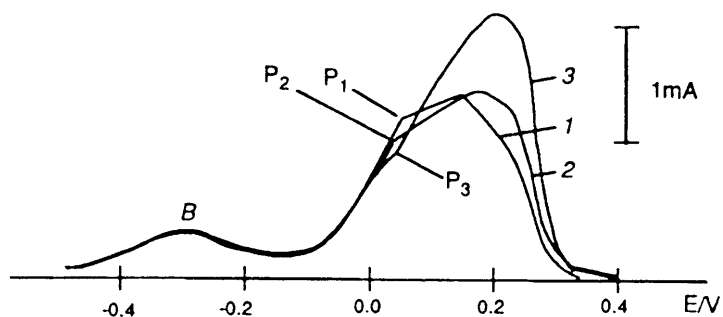


Figure 6. Effect of addition of light water, electrode surface black palladium electrolyte, 0.3 M Li_2SO_4 , $\text{p}^{\text{H}} 12$, scan rate 10 mV s^{-1} : curve 1, 10 ml D_2O , 2 ml H_2O ; curve 2, 10 ml D_2O , 5 ml H_2O ; curve 3, 10 ml D_2O , 10 ml H_2O .

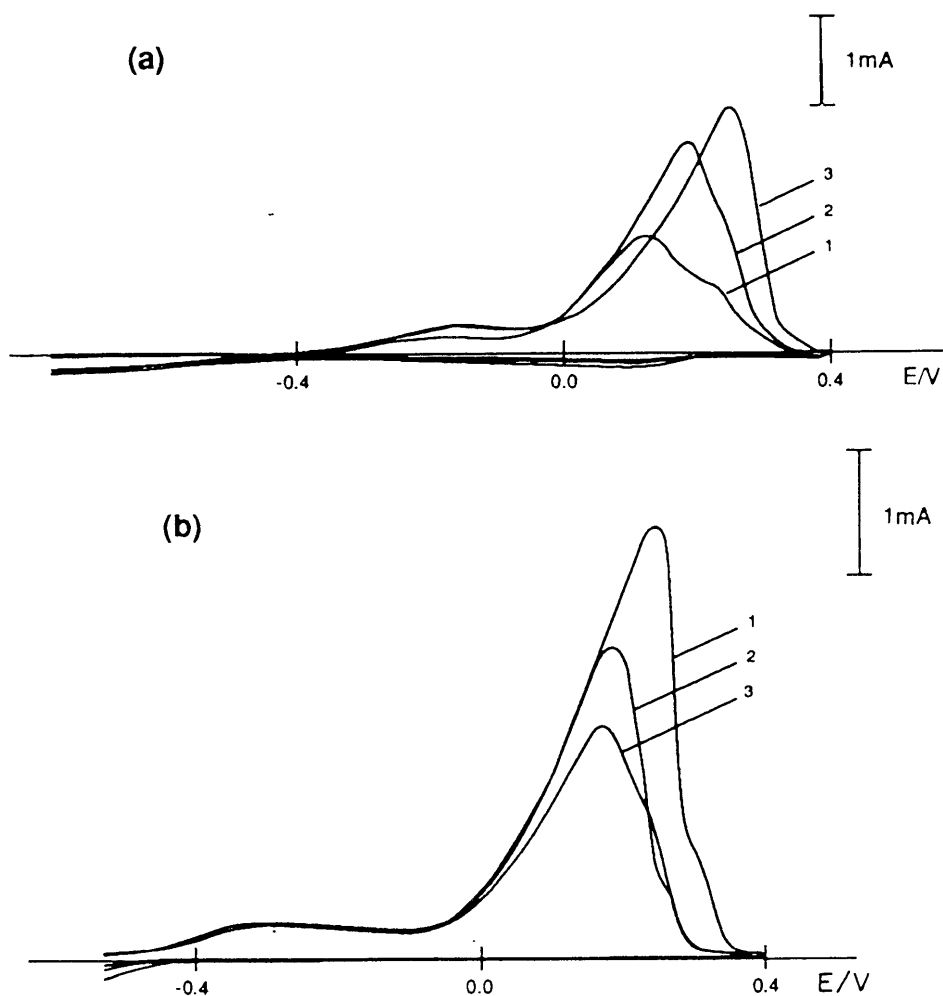


Figure 7. Effect of mixing solvents during cycling. (a) Effect of addition of light water to heavy water: curve 1, 7 ml $^2\text{H}_2\text{O}$; curve 2, add total 3 ml $^1\text{H}_2\text{O}$ after the first scan; curve 3, add total 7 ml $^1\text{H}_2\text{O}$, scan taken after cycling for 3h. (b) Effect of addition of heavy water to light water; curve 1, 8 ml $^1\text{H}_2\text{O}$; curve 2, add 8 ml $^2\text{H}_2\text{O}$, scan taken after 1 cycle; curve 3, scan taken after cycling for 45 min. Electrolyte 0.3 M Li_2SO_4 , $\text{p}^{\text{H}} 12$, scan rate 10 mV s^{-1} .

4.5. Effect of pH

Figure 8 illustrates the effect of pH on the voltammograms. In acidic and neutral electrolytes (pH 4 and pH 7) where the charge transfer kinetics are similar, the voltammograms overlap. However, in an alkaline electrolyte (pH 12), where the kinetics are different, there is an enhancement in peak B and a corresponding reduction in peak C with a slight displacement of the latter to a lower potential. The relation between the magnitudes of peaks B and C and their position on the potential scale arises from the interplay between the bulk and surface processes. As a rule, the peaks are better defined in alkaline solutions and the observed effects are greater for electrolytes containing Cl^- ions. In terms of the concept of the λ^* phase, in alkaline solutions containing Cl^- ions, becomes dominant.

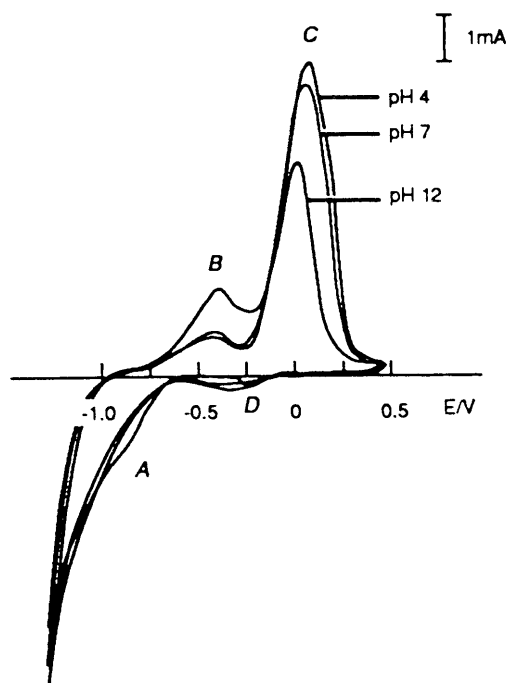


Figure 8. Effect of pH, electrode surface black palladium, solution 0.3 M $\text{Li}_2\text{SO}_4/\text{H}_2\text{O}$, scan rate 10 mV s^{-1} , pH indicated.

4.6. Effect of Weakly Adsorbable Ions

The effect of weakly adsorbed anions on the voltammograms was investigated by changing electrolyte composition but not ionic strength. In particular, Fig. 9(a) illustrates how a change in an anionic species affects the shape of the voltammogram. In slightly acidic and neutral electrolytes (at pH 4 or pH 7), no differences between the voltammograms obtained for KCl and K_2SO_4 electrolytes are observed. However, at pH 12 the presence of Cl^- ions enhances peaks B and D, with the corresponding changes in peak C. The appearance of peak D indicates that not all the ^3H atoms are transported into the palladium lattice. Therefore, Cl^- in the presence of OH^- inhibits diffusion of ^3H into the metal, a conclusion reached earlier by Breiter [19]. The change in peak C indicates that the adsorbed Cl^- ion in alkaline electrolytes competes with O^{2-}H^- ions. According to Bucur and Bota [13] the thickness of their postulated layer is greatly affected by the adsorption properties of the anionic species occurring in solution.

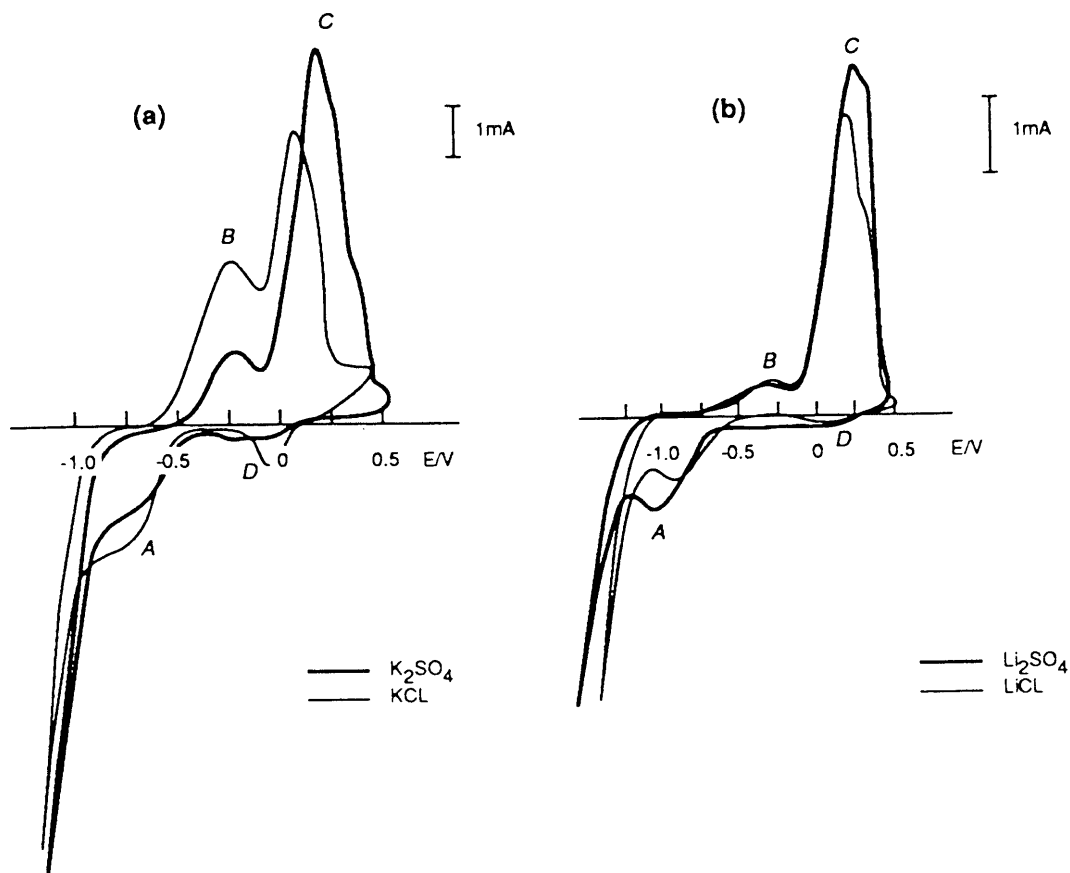


Figure 9. Effect of the supporting electrolyte, scan rate 10 mV s^{-1} , electrode surface black palladium, pH 12, solvent D2O: (a) 0.3 M potassium salts (Cl^- , SO_4^{2-}); (b) 0.3 M lithium salts (as above), SO_4^{2-} thick line, Cl^- thin line.

When the K^+ ion is replaced by Li^+ , no significant differences are observed in the voltammograms, as shown in Fig. 9(b), regardless of the pH or the counterion. Such behavior is attributed to specific adsorption of the Li^+ ion. The influence of electrolyte composition and pH on peaks B and D is related to the adsorbability of the species present in the electrolyte, a conclusion also reached by McBreen [5].

4.7. Effect of Surface Active Species

Among species strongly adsorbed on the palladium electrode surface are the CN^- ion and thiourea. Figure 10 shows the effect of adding KCN to the electrolyte, i.e. the effect of the CN^- ion lying flat on the palladium surface [20]. Within the potential range examined, the addition of CN^- results in a loss of peaks A, B and D as well as loss of the component of peak C which occurs at a more negative potential. However, with positive scans terminated at higher positive potentials, e.g. at 1.0 V vs. Ag/AgCl reference, shown in Fig. 10, peaks A and D reappear. Evidently, a strongly adsorbed (chemisorbed) species modifies the structure of the electrode/electrolyte interphase in a different manner than less strongly adsorbed species. In particular, the presence of CN^- does not prevent the diffusion of ^2H atoms into the palladium lattice, in agreement with the results obtained by McBreen [5]. It appears, however, that the CN^- ion does inhibit the outgassing of $^2\text{H}(\lambda^*)$ out of the λ_s into the λ_e layers. The single anodic peak observed in the voltammogram is attributed to reoxidation of ^2H within the palladium layer in closest contact to the solution phase, i.e. the λ_e layer. Therefore, it would

appear that the two overlapping components of peak C are assigned to reoxidation of $^2\text{H}(\lambda_e)$ and in the $^n\text{H}(\lambda_s)$ layers respectively.

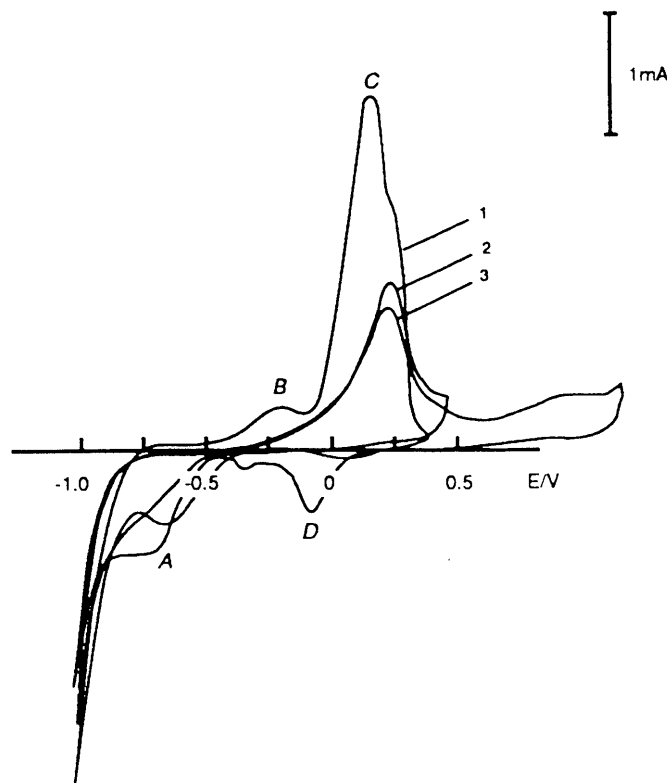


Figure 10. Effect of addition of CN^- . Electrode surface black palladium, solution 0.3 M $\text{Li}_2\text{SO}_4/\text{D}_2\text{O}$, pH 12, scan rate 10 mVs^{-1} , final concentration of KCN was 10^{-3} M : curve 1, before addition of KCN; curve 2, after addition of KCN positive scan terminated at +500 mV; curve 3, positive scan terminated at +1000 mV.

The addition of thiourea, ca. 10^{-3} M , to the electrolyte greatly alters the voltammograms, as shown in Fig. 11 where the voltammograms obtained in the absence and presence of $\text{SC}(\text{NH}_2)_2$ are displayed. With the addition of thiourea, the anodic peak B becomes an inflection occurring at ca. 300 mV more positive and the much broader peak C, also displaced by 300 mV, retains its structure (the two closely spaced peaks). At still higher positive potentials, a new peak is observed. Of note is the dependence of the shape of the negative branch of the voltammograms. When the positive sweep is terminated before substantial oxidation of adsorbed and/or absorbed ^2H occurs, the negative sweep retraces the positive sweep. When terminated at the point of inflection, a peak in the negative sweep appears which is shifted more negative by ca. 300 mV with respect to the peak observed in the absence of thiourea. The magnitude of this peak decreases as the terminating potential is more positive, until the terminating potential exceeds 1.2 V, at which point two new peaks appear. These latter two peaks may be due to the reduction of sulfur compounds adsorbed on the surface or may indicate surface restructuring associated with electrode polarization [14].

5. CLOSING REMARKS

The quantitative description of the ^nH transport across the interphase requires that both the interphase structural features and the kinetics of the processes, which lead to the formulation of applicable boundary conditions, be specified. Two models have been advanced. In one approach, Bucur and Covaci [18] formulated a set of equations describing the transport of hydrogen from the electrode

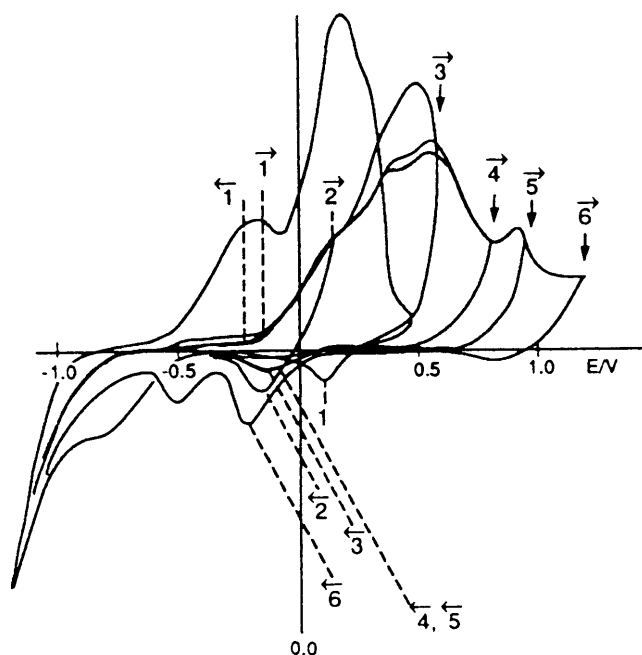


Figure 11. Effect of addition of $\text{CS}(\text{NH}_2)_2$, electrode surface black palladium, solution 0.3 M $\text{Li}_2\text{SO}_4/\text{D}_2\text{O}$, pH 12, scan rate 10 mV s^{-1} , final concentration of $\text{CS}(\text{NH}_2)_2$ was 10^{-3} M .

interior to the charge transfer plane by invoking mass balance equations. A more general discussion of the transport was given recently by Szpak et al. [4] in which they adopted a modified van Rysselberghe [3] concept of the interphase region as representing the $\text{Pd}/^m\text{H}_2\text{O}$ system by including absorption process(es), i.e. the penetration of ^mH into the palladium lattice. While discussing the properties of the interphase, it is important to note that the movement of the absorbed interstitial is accompanied by profound local changes arising from lattice expansion, especially at the $\alpha \rightarrow \beta$ transition plane [21].

Qualitatively, during the negative scan, as the concentration of $^m\text{H}(\text{a})$ increases with the applied overpotential, so does the amount of $^m\text{H}(\lambda^*)$ which, in turn, diffuses into the bulk metal, $^m\text{H}(\text{II})$. During the discharge, the elementary processes are reversed in direction while retaining the same mechanism within the bulk electrode. On the surface, $^m\text{H}(\lambda_e)$ undergoes oxidation with the distribution of the driving force depending on the reaction path. In particular, at low anodic current densities, an equilibrium $\text{H}(\lambda_s) \rightarrow \text{H}(\lambda_e)$ can be assumed. At higher currents, however, a non-equilibrium situation may develop owing to the slowness of either the transfer step or diffusion through the palladium lattice. In such a case, the rate-determining step is identifiable.

General features of the voltammograms pertaining to the $\text{Pd}/^m\text{H}_2\text{O}$ system, i.e. (i) peaks are observed in the positive direction but rarely in the negative, (ii) a number of scans is required to stabilize a voltammogram, and (iii) a coupling between the forms of adsorbed-absorbed ^mH exists, indicate strong involvement of the interphase. The lack of distinct features during the negative scan suggests that the ^mH atom, formed upon reduction of $^m\text{H}_2\text{O}$, is transported across the λ_s layer directly into the palladium lattice. The existence of the inflection point A, Fig. 4, appearing in the course of light water reduction which in heavy water often becomes a well defined peak, Fig. 9(b), we propose is attributed to the difference in the number of reactive sites on the electrode surface arising from the difference in the rate at which the ^mH cross the λ_s layer, this rate being faster for light hydrogen. The elimination of this peak upon addition of CN^- ions means that the total number of sites has been

reduced. It should be noted that the shape of peak A is strongly dependent upon the history of the electrode, scan rate, pH and solution composition. This suggests that this peak arises from the restructuring of the λ^* layer occurring at more positive potentials, a conclusion reached earlier by Bucur and Bota [13].

The complex nature of the interaction between the λ_e and λ_s layers is further shown by the shape of voltammograms obtained in the presence of thiourea. Here, the formation of $\cdots S$ bonds 'affects not only the space charge layer in the λ_e but also the λ_s segments of the interphase. In conclusion, we suggest that, in the course of the palladium electrode charging, the interphase is not a passive element but an active participant.

ACKNOWLEDGEMENT

The authors wish to express their gratitude to Drs. D.R. Rolison (NRL) and R.J. Nowak (ONR) for penetrating discussions. Special thanks to Dr. Frank Gordon (NOSC) for his interest, encouragement and support.

REFERENCES

1. M. Fleischmann, S. Pons and M. Hawkins, *J. Electroanal. Chem.*, 261(1989)301.
2. M. Fleischmann, S. Pons, M.W. Anderson, L.J. Li, and M. Hawkins, *J. Electroanal. Chem.*, 287(1990)293.
3. P. van Rysselberghe, Some Aspects of the Thermodynamic Structure of Electrochemistry, in J.O'M. Bockris (Ed.), *Modern Aspects of Electrochemistry*, Vol. 4, Plenum, New York, 1966.
4. S. Szpak, C.J. Gabriel, J.J. Smith and R.J. Nowak, *J. Electroanal. Chem.*, 309(1991)273.
5. J. McBreen, *J. Electroanal. Chem.*, 287(1990)279.
6. A. Capon and R. Parsons, *J. Electroanal. Chem.*, 39(1972)275.
7. R.R. Adzic, M.D. Spasojevic and A.R. Despic, *J. Electroanal. Chem.*, 92(1978)31.
8. J. Horkans, *J. Electroanal. Chem.*, 106(1980)245.
9. J.-P. Chevillot, J. Farcy, C. Hinnen and A. Rousseau, *J. Electroanal. Chem.*, 64(1975)39.
10. D.R. Rolison and P.P. Trzaskoma, *J. Electroanal. Chem.*, 287(1990)375.
11. S. Szpak, P.A. Mosier-Boss and J.J. Smith, *J. Electroanal. Chem.*, 302(1991)255.
12. R. Defay, I. Prigogine and A. Bellemans, *Surface Tension and Adsorption*, Engl. trans., D.H. Everett, Longmans, Green & Co, London, 1966.
13. R.V. Bucur and F. Bota, *Electrochim. Acta*, 26 (1981)1653; 27(1982) 521; 28 (1983)1373.
14. S. Szpak and P.A. Mosier-Boss, unpublished results, 1990.
15. W. Auer and H.J. Grabke, *Ber. Bunsenges.*, 78(1974)58.
16. H.S. Carslaw and J.C. Jaeger, *Conduction of Heat in Solids*, Oxford University Press, London, 1948.

- 17 D.F. Untereker and S. Bruckenstein, *Anal. Chem.*, 44(1972)1009.
- 18 R.V. Bucur and I. Covaci, *Anal. Chem.*, 30(1985)1237.
- 19 M.W. Breiter, *J. Electroanal. Chem.*, 90(1978)425.
- 20 J. Sommers, M.E. Kordesch, Th. Lindner, H. Conrad, A.M. Bradshaw and G.P. Williams, *Surf. Sci.*, 188 (1987) L693.
- 21 M. V. Stackelberg and P. Ludwig, *Z. Naturforsch.*, 19A (1964)93.

Absorption of deuterium in palladium rods: model vs. experiment

S. Szpak, P.A. Mosier-Boss and C.J. Gabriel

Naval Command, Control and Ocean Surveillance Center, RDT and E Division, San Diego, CA 92152-5000 (USA)

J.J. Smith

Department of Energy, Washington, DC 20585 (USA)

(Received 19 February 1993; in revised form 6 July 1993)

ABSTRACT

The electrochemical charging of Pd rods by deuterium involves a complex coupling of electrochemical, interfacial and transport processes. In order to predict the overpotential, surface coverage and bulk loading of the electrode during charging, a model has been developed that incorporates the essential features of these processes and involves variables such as the electrochemical rate constants, the bulk diffusion coefficient and the charging current. Features of the computed time dependence of the bulk loading are then compared with published experimental charging curves. New microscopic observations and X-ray diffraction data provide further evidence for the details of the charging process.

1. INTRODUCTION

In an earlier paper [1] we presented a model describing the charging of Pd rods by electrochemically generated deuterium. This model, which is based upon the coupling of interfacial processes with the diffusional transport of interstitials, offers certain predictive capabilities with respect to the charging process. In particular, we examined the effect of the magnitude of the rate constants of the electrochemical steps and the charging current on the surface coverage, the electrode potential and the electrode charging. Subsequently, Riley et al. [2] reported on the experimentally observed absorption of deuterium into the Pd lattice of cathodically polarized electrodes and presented results with which the predictions of our model are qualitatively in good agreement. We take this agreement as evidence for the general validity of the model and its assumptions and use the results as a basis for a refined interpretation of the charging process.

While our previous discussion of the model [1] was essentially limited to the examination of the behavior of a set of coupled differential equations, this paper presents the comparison of the model and its predictions with experiment using the data of ref. 2. We explore the relationship between the various operating fluxes and the initial charging rate as well as the asymptotic level of the electrode charging. We include new results based upon an examination of microscopic observations and X-ray diffraction data of a charged Pd electrode. Finally, we conclude with a discussion of the strengths and weaknesses of the model in the light of the experimental evidence.

2. INTERPRETATION OF EXPERIMENTAL DATA OF RILEY ET AL.

The data published by Riley et al. [2] show four characteristic features of the D/Pd system during charging: (i) the existence of an apparent threshold value for the cathodic current density (CD) above which the initial charging rate does not increase, implying the existence of a CD-dependent charging mode(s); (ii) an unexpected dependence of the asymptotic electrode loading on the charging CD, i.e., the appearance of a maximum (ref. 2, Fig. 5); (iii) a slower rate for "unloading" than for "loading," which implies that the rate of transport between the metal electrode and bulk electrolyte, i.e., across

the interphase, depends on the direction—an unlikely situation for diffusion control; (iv) an initial charging rate that depends, for the most part, inversely on the diameter of the Pd electrode.

In their interpretation, by assuming diffusion control, Riley et al. have considered only events occurring in the electrode interior and have disregarded the influence of a non-autonomous interphase on the charging process. In what follows, we discuss their data in the context of our model and offer a somewhat different interpretation from that provided in ref. 2, showing that (i) and (ii) are natural consequences of the model while (iii) and possibly (iv) require the presence of more complex mechanisms.

In the interpretation of the charging data of ref. 2, it is convenient to introduce the concept of the charging efficiency for a cylindrical electrode of radius r , defined here as the ratio of the absorbed deuterium to that which is generated by electrolysis at a current density j within a time interval Δt and given by

$$\epsilon = \frac{Z_m F}{2} \frac{r}{j} \frac{\Delta Q}{\Delta t} \quad (1)$$

where Z_m is the maximum number of available sites per unit volume, F is the Faraday constant and ΔQ is the corresponding change in the loading ratio Q of deuterium to palladium, conveniently expressed in terms of the D/Pd atomic ratio since Z_m is taken here to be the number density of Pd. The first factor on the right-hand side in eqn. (1) is a constant (equal to $5.45 \times 10^3 \text{ C cm}^{-3}$ for a Pd electrode) independent of the manner in which the experiment is carried out; the second factor is controlled by the investigator. The third factor is the measured charging rate and reflects the time dependence of the charging efficiency ϵ for an experiment. The initial charging efficiency characterizes the interphase processes independently of the electrode geometry, so that the initial charging rate varies with r as $1/r$. This relationship is independent of the details of the model.

The processes associated with the electrolytic charging of the Pd electrode are shown in Fig. 1. As indicated, there are six fluxes in operation, resulting in a large number of governing parameters. Because of the large number of parameters involved, the predicted results are not necessarily computed with the same values of CD or electrode radius as those for which the experiments were done. Rather, a limited number of values are chosen to illustrate possible model behavior, with the idea in mind that a more elaborate procedure for choosing the model parameters could produce a better experimental fit if in fact the model does exhibit the proper behavior.

The model parameters that we have used here are listed in Table 1. Several of the parameters differ from those used earlier in ref. 1 where we provided a qualitative description of Pd/D charging. In this paper, in order to obtain agreement with the experimental data reported in ref. 2, we have chosen model parameters accordingly. Of particular significance are the changes in Γ_m , θ_0 and ξ_0 . The surface density of sites, Γ_m , was taken to be 0.005 of the maximum number of surface sites consistent with our choice of Z_m . The initial values of surface coverage and bulk loading, θ_0 and ξ_0 , were chosen to be consistent with the observation of Riley et al. [2] that the equilibrated loading is essentially zero.

2.1. Threshold CD; Charging Efficiency; Asymptotic Charging Level

Using the parameters in Table 1 and the diffusion coefficient for β -PdD, the results of model calculations for a cylindrical electrode of radius 0.05 cm charged at current densities ranging from 30 to 240 mA cm⁻² are shown in Figs. 2 and 3. It is seen that the calculated charging curves reproduce well the experimental data reported in ref. 2, Fig 5. In particular, Fig. 2 is a family of charging curves as a

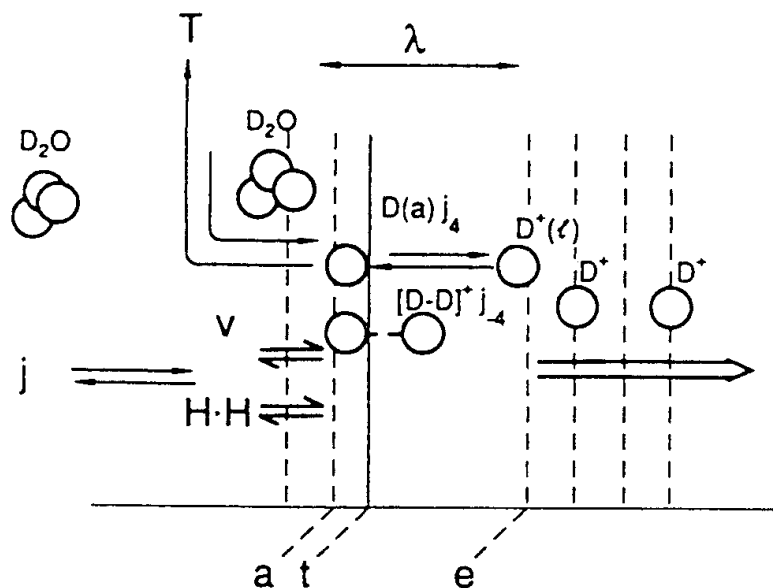


Figure 1. Concept of the Pd/D₂O interphase [1,5,7]: a, adsorption layer; t, charge transfer layer; e, surface dividing the interphase and the bulk electrode; l, lattice; j, total current; H.H., Heyrovsky-Horiuti path; T, Tafel path; V, Volmer path; j₄ and j₋₄, adsorbed–adsorbed exchange; l, non-autonomous interphase region.

Table 1. Input data for model calculation (cf ref. 9).

Parameter	Value
[D ₂ O]	$5.5 \times 10^{-2} \text{ mol cm}^{-3}$
[OD ⁻]	$1.0 \times 10^{-4} \text{ mol cm}^{-3}$
[D ₂ (s)]	$8.3 \times 10^{-7} \text{ mol cm}^{-3}$
k ₁	$1000 \text{ cm}^3 \text{ mol}^{-1} \text{ s}^{-1}$
k ₂	$100 \text{ cm}^3 \text{ mol}^{-1} \text{ s}^{-1}$
k ₃	$1000 \text{ cm}^2 \text{ mol}^{-1} \text{ s}^{-1}$
k ₄	$1.0 \times 10^7 \text{ cm}^3 \text{ mol}^{-1} \text{ s}^{-1}$
Z _m	$0.113 \text{ mol cm}^{-3}$
Γ _m	$1.4 \times 10^{-11} \text{ mol cm}^{-2}$
C	$4.0 \times 10^{-3} \text{ F cm}^{-2}$
α	0.5
β	0.3
θ ₀	1.0×10^{-5}
ζ ₀	5.0×10^{-5}
N	10

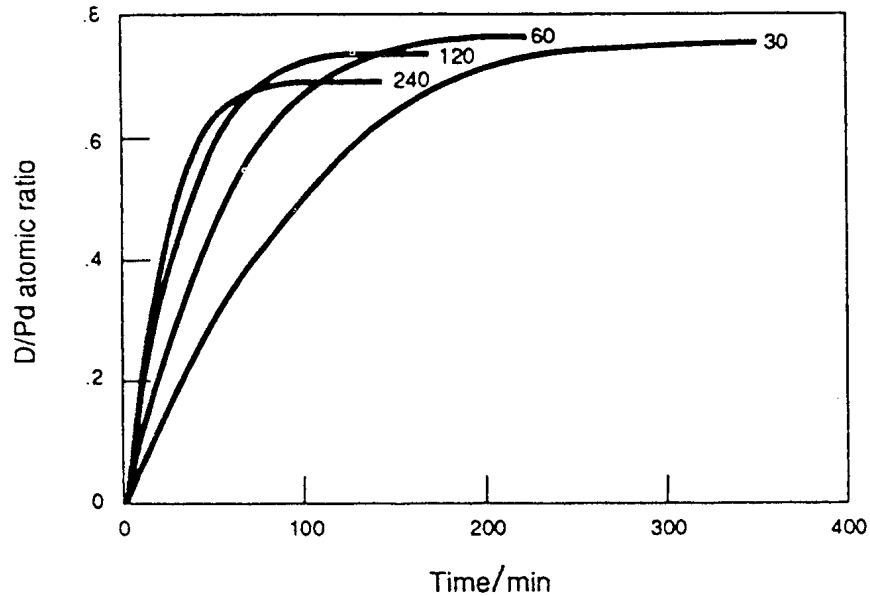


Figure 2. Model calculation of loading curves as a function of current density: electrode radius 0.05 cm; current densities are indicated in mA cm⁻²; diffusion coefficient 1.6×10^{-6} cm² s⁻¹, other parameters are listed in Table 1.

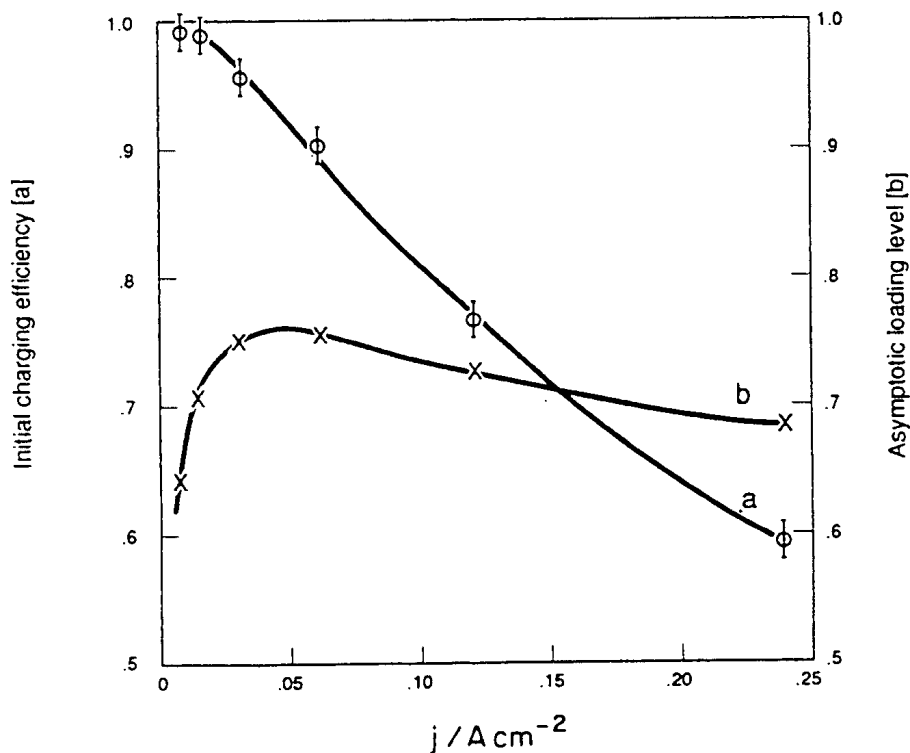


Figure 3. Model calculations as a function of current density: a, initial charging efficiency; b, asymptotic loading level; electrode radius 0.05 cm; diffusion coefficient 1.6×10^{-6} cm² s⁻¹; other parameters are listed in Table 1.

function of CD and illustrates that the model predicts a saturation of the initial charging rate. Figure 3, curve A plots the initial charging efficiency calculated by eqn. (1) and Fig. 3, curve B the asymptotic loading level obtained from the curves of Fig. 2. The model predicts a brief period of rapidly varying

charging rate, depending on the electrode capacitance, which would not be observable experimentally, therefore the initial charging rates used in eqn. (1) were obtained graphically from expanded versions of the data shown in Fig. 2 and consequently contain a measurement error. In terms of the model, what has been referred to in ref. 2 as a threshold effect in the charging rate with increasing CD may in reality be a saturation of the charging rate caused by a decrease in the effectiveness of the Volmer path with respect to the Heyrovsky–Horiuti path for charge transfer, coincidentally resulting in a charging efficiency that appears to be inversely proportional to the current density. Further, the maximum in the measured loading curve asymptotic levels as a function of CD, i.e., characteristic feature (ii) (see Fig. 3 and eqn. (II) of ref. 1), probably results from the same shift in the charge transfer rather than from changes in the Tafel path or the absorption of deuterium, since only the Volmer and Heyrovsky–Horiuti paths (eqn. (I) and (II) of ref. 1 respectively) exhibit a CD (overpotential) dependence.

It is of interest to note that earlier calculations that did not include desorption (the Heyrovsky–Horiuti path) showed an instability in the computed overpotential, suggesting that the shift in balance between adsorption and desorption plays an essential role in the electrode charging. However, a direct computation of the charging currents for the two paths, which we have not done, would be desirable to clarify this behavior.

2.2. Electrode Loading vs. Unloading

Evidence of an active interphase is provided by the difference in the loading and unloading rates and the incomplete unloading which leaves 0.1–0.15 D/Pd remaining, i.e., characteristic feature (iii). This behavior is not consistent with diffusion control. The observed asymmetry between the loading and unloading time dependences would not be predicted by a linear diffusion model. Such a model would be analogous to ordinary diffusion with constant initial bulk concentration, yielding a solution that is the product of a time-dependent factor containing geometrical information, but not initial conditions, and a function of the difference between the initial bulk concentration and the surface concentration (see e.g. eqn. 2.4.1. of ref. 3, p. 97). Although this asymmetry would be consistent with surface control as predicted by the model if e.g., $k_{-4} \gg k_4$ in eqn. (IV) of ref. 1, this choice does not reproduce well the other characteristic features (i) and (ii) and fails to predict incomplete unloading. Further, this asymmetry cannot be explained by diffusion alone even if $D_\alpha < D_\beta$ by about an order of magnitude [4] because of the required continuity of flux across the $\alpha \rightarrow \beta$ dividing plane. The continuity of flux and the low D/Pd ratio for the α phase would result in a very thin α region that can be identified with the interphase itself. Consequently, another mechanism(s) must be considered in seeking the explanation for this observation. For example, the incomplete unloading at a CD of 60 mA cm⁻² or larger may be due to blocking of the electrode surface by an oxide layer in as much as the applied current would exceed the diffusion current associated with the transport of absorbed deuterium out of the Pd lattice.

Evidently there exists a mechanism(s) that causes the absorbed deuterium to affect the loading and unloading rates differently. If we assign an active role to the interphase as suggested by the surface morphology (see the subsequent discussion of the interphase), then a mechanism is provided. To illustrate this, the electro-chemical potential of the adsorbed deuterium contains a contribution resulting from the electrode overpotential while that in the bulk is affected by contributions involving the electronic as well as mechanical interactions. Upon current reversal (during unloading) the magnitude of the driving force may be different and the asymmetry would follow naturally.

2.3. Effect of Electrode Radius

The effect of the electrode radius on the calculated charging curves is shown in Fig. 4, where the diffusion coefficient for β -PdD was used. It illustrates agreement with the experimental data (see ref. 2, Fig. 6) except for the electrode with a radius of 0.1 cm. The anomaly in the latter concerns the initial portions of the measured charging curves for which there is no observed difference in slope between the data for radii of 0.05 and 0.1 cm, requiring that the initial charging efficiency be proportional to the electrode radius—an unrealistic condition. Otherwise, eqn. (1), which predicts the slopes of the charging curves to have a $1/r$ dependence initially, is well satisfied. All three calculated curves exhibit an initial charging efficiency of 0.78, whereas the measured curves of ref. 2, Fig. 6 show an initial charging efficiency of about 0.8 for the 0.05 and 0.2 cm radii data and a unrealistically high value of about 1.6 for the 0.1 cm radius data. Because the reduction rates have no dependence of the asymptotic charging level on the radius of the electrode and apparently none is observed.

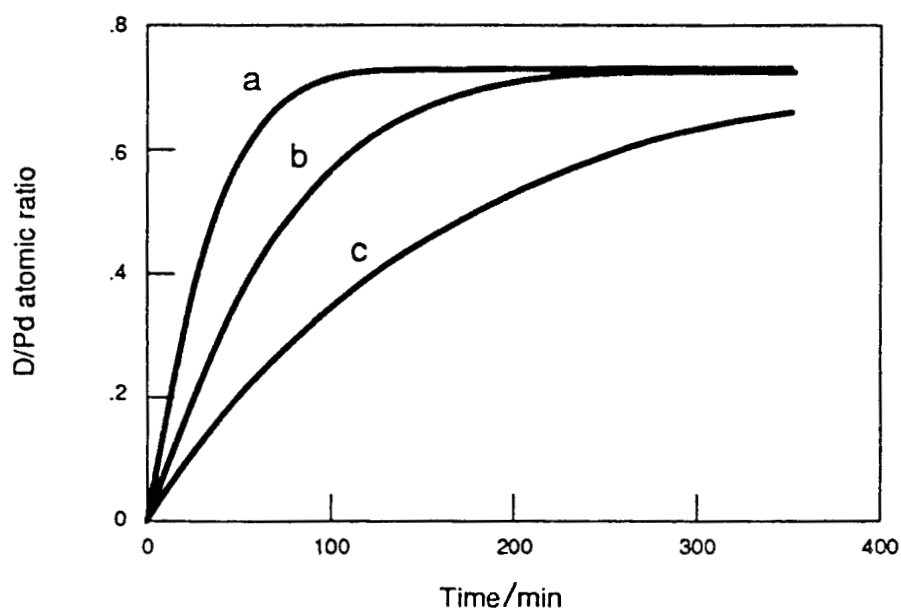


Figure 4. Model calculation of loading curves as a function of electrode radius: a, 0.05 cm; b, 0.1 cm; c, 0.2 cm; current density 120 mA cm^{-2} ; diffusion coefficient $1.6 \times 10^{-6} \text{ cm}^2 \text{ s}^{-1}$; other parameters are listed in Table 1.

2.4. Electrode-Loading Mode

Participation of the interphase in the course of the electrode charging can be examined numerically by changing the value of the diffusion coefficient used in the model computations. As the diffusion coefficient is made smaller, a shift to transport control must occur. The effect of varying the diffusion coefficient on the charging curves is illustrated in Fig. 5. At the highest CD a significant change is noted in the shape of the charging curve for the diffusion coefficient of $1.6 \times 10^{-7} \text{ cm}^2 \text{ s}^{-1}$. In contrast, at the lower CDs only a small change is achieved for the same changes in the diffusion coefficient, indicating a relative increase in surface control at lower CD as expected. This further indicates that a transition between diffusion and surface control occurs within the practical range of current densities at the diffusion coefficient operable in the system. A comparison with Fig. 5 of ref. 2 suggests that the observed charging rates were limited by diffusion at CDs of 60 mA cm^{-2} and greater, while for lower CDs the limitation may have been the surface reactions.

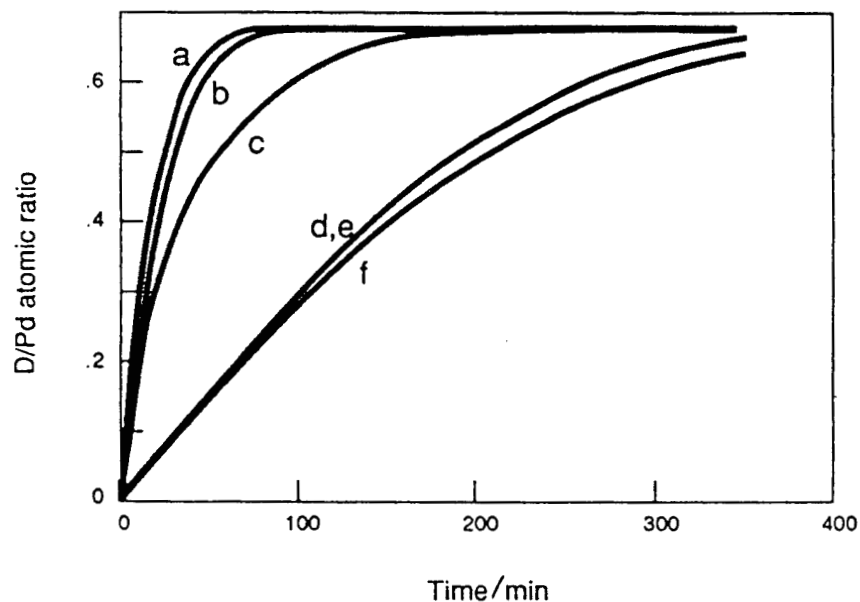


Figure 5. Model calculation of loading curves for current densities $j/\text{mA cm}^{-2}$ and diffusion coefficients $D/\text{cm}^2 \text{s}^{-1}$: a, $j = 240$, $D = 1.6 \times 10^{-5}$; b, $j = 240$, $D = 1.6 \times 10^{-6}$; c, $j = 240$, $D = 1.6 \times 10^{-7}$; d, $j = 15$, $D = 1.6 \times 10^{-5}$; e, $j = 15$, $D = 1.6 \times 10^{-6}$; f, $j = 15$, $D = 1.6 \times 10^{-7}$; electrode radius 0.05 cm; other parameters are listed in Table 1.

Figure 5 also indicates that a more realistic treatment of the bulk diffusion to include differences in diffusion coefficients for α - and β -PdD would not predict significantly different charging curves except at higher CDs, where there is diffusion control of the charging process.

3. EVOLUTION OF THE PDD/D₂O INTERPHASE

The surface inhomogeneity with regard to the absorption of hydrogen isotopes and the composition of the interphase, as revealed by X-ray diffraction spectroscopy, provide further evidence for the active participation of the interphase in the course of charging–discharging processes. The experimentally observed difference in the loading and unloading rates and the presence of residual deuterium in the Pd electrode suggest that other processes, beyond those contained in the model, play a significant role.

3.1. Surface Inhomogeneity

The active participations of the Pd surface manifests itself as inhomogeneous changes in the surface morphology of Pd electrodes during their prolonged exposure to evolving hydrogen and deuterium as reported by Rolison et al. [5]. Another way to demonstrate the inhomogeneity of a Pd surface, particularly with regard to absorption, is to view it using Nomarski optics [6] so that regions of preferred absorption can be differentiated. An example of the experimental arrangement is illustrated in Fig. 6. A Pd wire, heat treated at the recrystallization temperature to ensure large grains, was mounted in an epoxy resin, polished (diamond paste on silk followed by a light polish with 0.05 m Al 203 on microcloth) and etched (anodic etch in 50% HCl). A hole was drilled through which a Pt counterelectrode was inserted and the cell was closed with a thin Mylar film. The so-constructed cell was connected to a power source and placed in a metallograph (Leco Neophot 21) equipped with Nomarski optics. Images of the electrode surface were continuously recorded on videotape. The observed changes within a single grain, which is outlined, are illustrated in Fig. 7. It is unlikely that

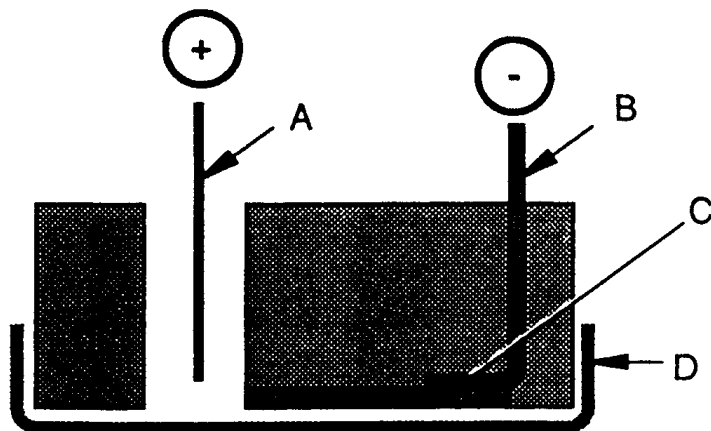


Figure 6. Electrolytic cell for examination of an electrode surface by Nomarski optics: A, Pt counterelectrode; B, Cu wire spot welded to a Pd electrode; C, etched Pd surface; D, Mylar film.



Figure 7. Preferred locations of D_2 penetration into a single Pd grain as obtained by electronic subtraction of Nomarski images. After cathodically charging the Pd electrode at 5 mA for 30 min, an image was recorded. This image was digitized and the image of the grain at rest potential was subtracted out. The subtracted image is shown with the individual grain outlined. The magnification of the microscope is X 400.

the changes observed in the grain can be attributed to the surface or near-surface cracking that has been found after long charging times at high current densities [7]. Rather, these changes are attributed to localized volume extension and indicate that even within a single grain there are preferred sites of absorption—a conclusion also reached by Rolison et al. [5].

3.2. Supercharged Region

The present model employs a simple, passive interphase. In actuality, as indicated by Bucur and Bota [8], the H atoms accumulate in the interphase, i.e. a supercharged region exists. To explore

further the Pd/D₂O interphase, we examined the time evolution of the in situ X-ray spectra covering a rather narrow 2θ range from 35° to 55° . For this purpose a cell, shown in Fig. 8, connected to a potentiostat (PAR model 363) was placed in an X-ray diffraction system (Rigaku RU 200 H). The cell body and stem, on to which a Pd foil (Cu clad on one side to ensure containment of the deuterium) was attached, were constructed out of a chemically inert material (TPX). The cell was provided with a thin polyethylene window, which minimized scattering of the X-rays, and a small hole in the top of the cell body, which permitted both the escape of gas and the addition of electrolyte as needed. The cell was assembled in a dry box.

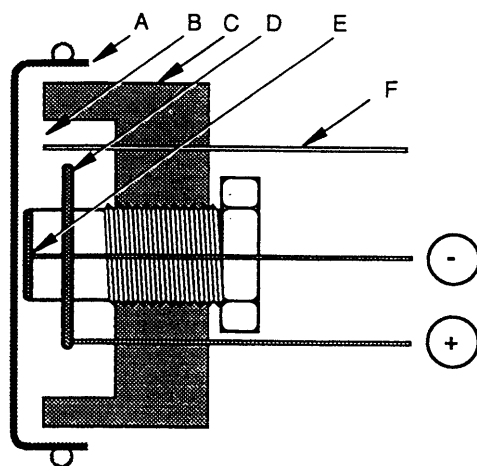


Figure 8. Electrolytic cell for in situ X-ray spectroscopy; A, polyethylene window; B, electrolyte cavity; C, cell body (TPX); D, Pt counterelectrode; E, Pd foil; F, Pd reference electrode.

Figure 9 shows the diffraction spectra for the Pd foil at rest potential (spectrum A) and at subsequent times and potentials (spectra B—E). At rest potential the polycrystalline Pd foil exhibits two peaks: one at 40.377° and another at 46.924° due to reflections from the 200 and 111 planes respectively. After 2 h of charging at 1.5 V negative overpotential, during which the electrode appearance had not changed, new peaks at 37.758° and 45.025° emerged, indicating formation of the β -PdD phase (spectra B and C). Comparison of the ratios of the 111 peaks to the 200 peaks for the Pd and β -PdD phase leads to the conclusion that deuterium preferentially enters the Pd lattice through the 111 sites. This conclusion agrees well with that based on theoretical calculations [9]. With prolonged charging, the silvery color of metallic palladium changed to black. After 24 h of charging, the recorded spectrum shows only two peaks attributed to the β -PdD phase (spectrum E). The 111 and 200 reflection peaks have shifted to lower values, indicating further expansion of the lattice. With continued charging, these peaks have broadened (spectra D and E) but their peak positions have stayed relatively constant. We interpret both this broadening and the shift to lower 2θ angles as indicating the presence of a supercharged layer.

4. STRENGTHS AND WEAKNESSES OF THE MODEL

Models are used both to simulate a complex reality by simpler arrangements and to display the essential features of a physical system. Often even a simplified model clarifies the interpretation of ambiguous data and avoids lengthy calculations that might be irrelevant to the problem considered. In the present case even our simple model indicates that the observed charging behavior of Pd electrodes cannot be explained solely by the diffusion characteristics of deuterium in the bulk but must include consideration of the surface reactions as well. This is especially true at lower CDs.

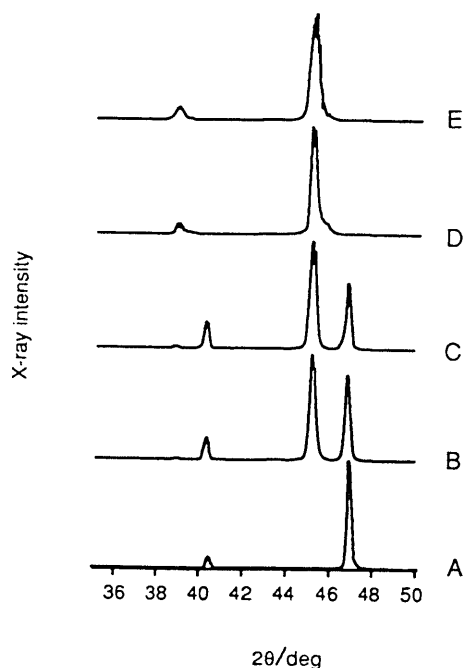


Figure 9. Progress in electrode loading by X-ray spectra: A, metallic Pd; B and C, transition from metallic to β -PdD phase; D and E, β -PdD phase (see text for overpotentials and charging times).

We have applied a model where the structure of the interphase as well as the operating driving forces are determined by participating processes occurring in both contacting phases. However, we have treated the interphase as a passive element, i.e. in effect assuming that the surface is homogeneous with respect to the chemical potential. Such an assumption is not realistic (see Fig. 7), although it might be justified on the basis of the existence of the supercharged region. Clearly an assumption of uniform surface coverage of the Pd rod cannot be made. Even so, the model does remarkably well in predicting a saturation of the initial charging rate and a non-monotonic dependence of the asymptotic charging level on CD. The time required to obtain a full charge is also predictable with reasonable model parameters. This model provides a framework within which questions such as the relative influence of the Volmer and Heyrovsky—Horiuti charge transfer paths as a function of CD can be considered.

Although the model does predict some small asymmetry in loading and unloading, it does not appear able to predict as large an effect as was observed and it does not predict the incomplete electrode unloading at all. Evidently, a more realistic model should incorporate an active interphase that will provide mechanisms for asymmetric loading and also explain why the charging rate and level can differ from electrode to electrode.

ACKNOWLEDGMENT

The authors thank Dr. F. Gordon for his enthusiastic support of this project.

REFERENCES

1. S. Szpak, C.J. Gabriel, J.J. Smith and R.J. Nowak, *J. Electroanal. Chem.*, 309(1991)273.
2. A.M. Riley, J.D. Seader, D.W. Pershing and C. Walling, *J. Electrochem. Soc.*, 139(1992)1342.

3. J.D. Fast, *Interaction of Metals and Gases*, Vol. II, Barnes and Noble, New York, 1971.
4. M. V. Stackelberg and P. Ludwig, *Z. Naturf. A*, 19 (1964)93.
5. D. Rolison, W.E. O'Grady, R.J. Doyle and P.P. Trzaskoma, *Anomalies in the surface analysis of deuterated palladium*, Proc. First Ann. Conf. on Cold Fusion, Salt Lake City, UT, 1990 p. 272.
6. W. Lang, *Nomarski Differential Interference–contrast microscopy*, Zeiss Informations, Oberkochen, 1968.
7. S. Gurswamy and M.E. Wadsworth, *Metallurgical aspects in cold fusion experiments*, Proc. First Ann. Conf. on Cold Fusion, Salt Lake City, UT, 1990 p. 314.
8. R.V. Bucur and F. Bota, *Electrochim. Acta*, 29(1984)103. 9 H.–G. Fritsche, *Z. Naturf. A*, 38 (1983)1118.

Comments on the analysis of tritium content in electrochemical cells

S. Szpak, P.A. Mosier-Boss and R.D. Boss

Naval Command, Control and Ocean Surveillance Center RDT&E Division, San Diego, CA 92152-5000 (USA)

J.J. Smith

Department of Energy, Washington, DC 20585 (USA)

(Received 12 July 1993; in revised form 10 November 1993)

1. INTRODUCTION

Following the report by Fleischmann and Pons [1] in 1989 that nuclear events, including the production of tritium, can be initiated in electrochemical cells during the electrolysis of heavy water on Pd cathodes, tritium production has been claimed in a number of publications, a list of which was compiled by Storms [2] and more recently reviewed by Chien et al. [3]. However, substantial difficulties have been encountered in reproducing reported data and considerable controversy remains concerning the occurrence of such events, including tritium production.

Tritium production is typically ascertained from its distribution among the cell components during prolonged electrolysis. The tritium production rate, if any, can best be examined in closed cells and determined from a total mass balance [4]. However, the majority of researchers use open cells where the rate of tritium production is calculated from enrichment in the electrolyte phase, the gaseous phase or both. This enrichment is often computed under conditions of constant electrolyte volume which implies continuous additions and withdrawals of electrolyte, a somewhat unrealistic undertaking. Most reported instances of tritium production involve low levels (e.g. of the order of 10^4 – 10^5 atoms $S^{-1} cm^{-2}$ [4]; data analysis at such levels requires extreme care, particularly in open-cell experiments.

In this paper we examine the limitation(s) of commonly used expressions for the distribution of tritium in the gas and liquid phases during prolonged electrolysis and comment on the methodology of data acquisition. Furthermore, we emphasize the difficulties that may arise in interpreting the results obtained by these procedures. We note that these expressions were derived for the simplest model of deuterium evolution on D-saturated Pd electrodes.

2. DERIVATION OF EXPRESSIONS—MASS BALANCE CONSIDERATION

The fluxes associated with the electrolysis of water in cells employing hydrogen-absorbing cathodes [5], are summarized in Fig. 1. The gaseous products generated during electrolysis of heavy water, i.e. D_2 and/or DT evolving at the cathode C and O_2 at the anode A, are catalytically recombined in a separate vessel R. Because of the absorption of hydrogen isotopes by the cathode material, the hydrogen flux produced by electrolysis is divided into three streams: entering the electrolyte by the Heyrovsky–Horiuti path or other exchange processes, entering the gaseous phase (recombiner) by the Tafel path and entering the bulk electrode by absorption. If tritium is produced (consumed) during the experiment, either the magnitude of these fluxes changes or other appropriate fluxes should be considered. The mass balance can be written for the closed system (total mass balance) or, for greater flexibility in the experimental arrangement and data interpretation, separately for each part of the system (the electrolyte, the recombiner and the electrode). The mass balance of tritium in the electrolyte is of special interest since conclusions have often been based on measurements of the electrolyte phase [2,3].

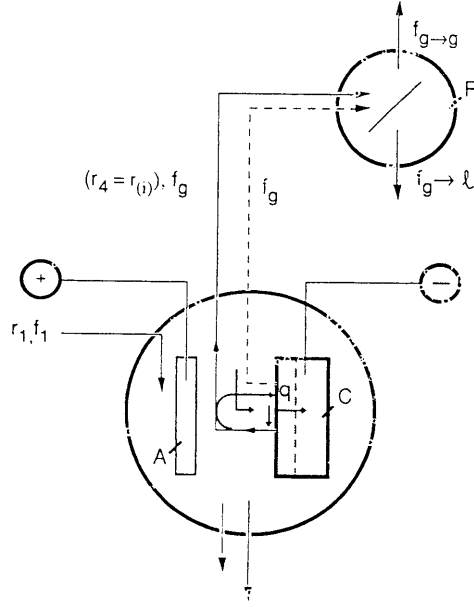


Figure 1. Mass balance on electrolyte: r , rates of mass change (subscripts 1, 2, 3 and 4 indicate electrolyte addition, removal by sampling, evaporation and electrolysis respectively); f , tritium mass fraction (subscripts g and l denote gas and liquid phases); cell components are shown by bold lines (A, anode; C, cathode; R, recombiner); concentration is schematic.

The time dependence of tritium concentration in the electrolyte phase is calculated by solving the equation

$$\frac{d(fm)}{dt} = \sum_n f_n r_n + kq \quad n = 1, 2, \dots \quad (1)$$

subject to experimental conditions specified by

$$\frac{dm}{dt} = \sum_n r_n \quad (2)$$

where f denotes the tritium mass fraction, m is the mass of electrolyte and the subscript n identifies the relevant process. Specifically, r_1 is the rate of D_2O addition to replenish that removed by electrolysis, r_2 , r_3 and r_4 (also called $r(i)$) are the rates of removal due to sampling, evaporation and electrolysis respectively, and kq ($k \leq 1$) is that fraction of tritium, produced or consumed in the electrode interior q , that has been transferred to the electrolyte phase irrespective of the transport mode. As written, eqn. (1) implies that if tritium is generated within the electrode, it is transferred to the electrolyte phase or if it is consumed, it is removed from the electrolyte phase. Tritium balance on the recombiner and electrode are formulated in an analogous manner with the inclusion of the relevant fluxes identified in Fig. 1.

Substitution of (2) into (1) yields an equation of the type

$$\frac{dy}{dt} + P(t)y = Q(t)$$

which has the solution

$$y = y(0) \exp \left[- \int_0^t P dt \right] + \exp \left[- \int_0^t P dt \right] \int_0^t Q \exp \left[\int_0^t P dt \right] dt \quad (3)$$

2.1. Tritium in the Electrolyte Phase

Analytical solutions of eqn. (3) describing tritium concentration in the electrolyte phase for two experimental procedures, i.e. constant electrolyte volume and intermittent sampling, are as follows.

2.1.1. Open Cell and Constant Electrolyte Volume. When the cell is operated at constant mass of electrolyte, i.e. compensating for all losses by a continuous supply of electrolyte, we have (note that since $dm/dt = 0$, $m(t)=m(0)$)

$$m(0) \frac{df}{dt} + sf[r(i) + r_2] = f_1 r_1 + kq \quad (4)$$

where we have taken $sf = f_2$, where s is the isotopic separation factor (see Section 4.2 for further discussion). With $P = s[r(i) + r_2]/m(0)$ and $Q = (f_1 r_1 + kq)/m(0)$, the solution of eqn. (4) is

$$f = f(0) \exp(-t/\tau) + \frac{f_1 r_1 + kq}{sr(i) + r_2} [1 - \exp(-t/\tau)] \quad (5)$$

where $\tau = m(0)/(sr(i) + r_2)$. When additional constraints are imposed, e.g., $r_1 = r(i)$, $r_3 = 0$, $f_1 = f(0)$, we obtain

$$f = f(0) \exp(-t/\tau) + \frac{f(0)}{s} [1 - \exp(-t/\tau)] + \frac{kq}{sr(i)} [1 - \exp(-t/\tau)] \quad (6)$$

Rearranging eqn. (6), we obtain

$$\frac{f}{f(0)} = s - (s - 1) \exp(-t/\tau) + \frac{kq}{sr(i)f(0)} [1 - \exp(-t/\tau)] \quad \tau = \frac{m(0)}{sr(i)} \quad (7)$$

which is the form employed by Lin et al. (6) and Adzic et al. (7), with the last term determining the generation rate. In this formulation, the difference between the calculated distribution, without the production term, and the experimentally observed concentration is attributed to tritium generation, in particular to that portion that has been transferred to the electrolyte phase. The isotopic separation factor s employed here is defined in terms of the D/T atomic ratio.

A plot of tritium concentration in the electrolyte phase versus dimensionless time t/τ is shown in Fig. 2, curve (a), for $q = 0$, while that in the “electrolytic” gas phase is shown by curve (a’). Suppose

that at $t/\tau = 1$ (point A) a continuous production of tritium is initiated; the net result is new curves (b) and (b') for the electrolyte and recombined phases respectively. These curves are analogous to curve (a) but asymptotically approach the value $s + kq/sr(i)f(0)$. If, as reported [2,3], tritium production is a burst-like event followed by direct transfer to the gas phase, then the situation is different, i.e. the build-up in the electrolyte phase remains unchanged (curve (c)) but the tritium concentration in the gas phase is displaced (curve (c')) which would effectively change the value of the separation factor s . While these results are interesting, the model assumes experimental conditions of known concentration of tritium in the electrolyte, without requiring sampling, and constant volume (i.e. $r_2 = 0$ and $r_1 = r(i)$). Neither of these assumptions is physically reasonable and, in practice, they are not usually met. These considerations lead to the following much more realistic case of intermittent sampling and addition.

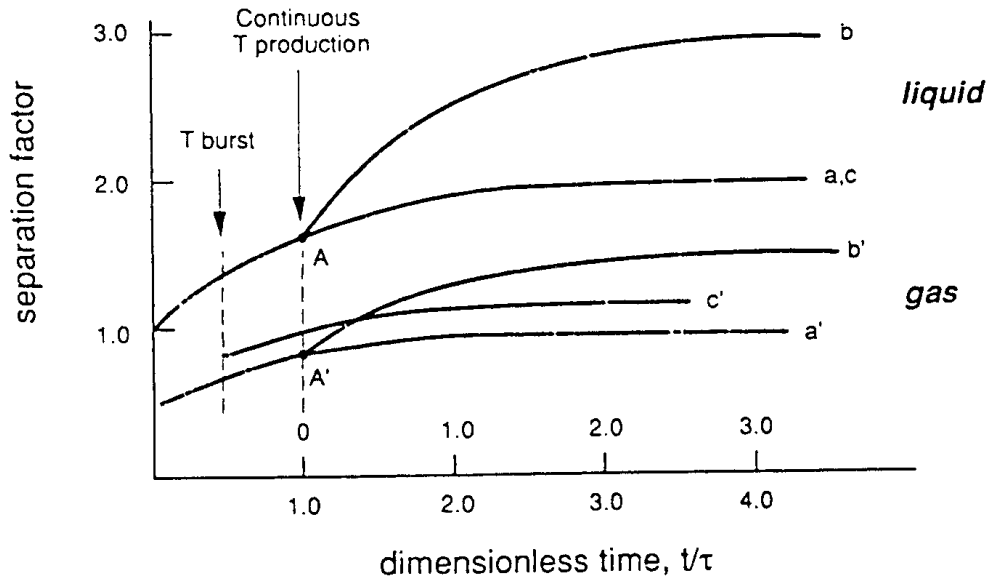


Figure 2. Calculated tritium distribution between the electrolyte and “electrolytic” gas phase as a function of dimensionless time (calculations for $s = 2$): (a), (a') liquid and gas phases for $q = 0$; (b), (b') liquid and gas phases for $q > 0$; (c') gas phase enrichment by pulse production, as indicated.

2.1.2. Open Cell and Intermittent Sampling. A more realistic sampling procedure is illustrated in Fig. 3, from which the tritium concentration in open cells is calculated as follows. An initial charge $m(0)$ is electrolyzed at a constant cell current I for a specified time t , when a sample is withdrawn (to be analyzed for tritium), after which D_2O is added to restore the original volume. Thus the rates r_1 and r_2 are zero, except when solvent is added or sample is removed, and $r(i)$ is constant for a constant cell current (Faraday law). If the radioactive decay (ca. 0.5% per month) and the loss by evaporation are neglected, the time rate of change of tritium content between sampling is obtained by substituting eqn. (2), with $r_1 = 0$ and $r_2 = 0$, into eqn. (1) and solving the resulting eqn. (3) which, with $P = (s - 1)r(i)/[m(0) - r(i)t]$ and $Q = kq(t)/[m(0) - r(i)t]$, yields

$$f(t) = [m(0) - r(i)t]^{s-1} \times \left[\frac{f(0)}{m(0)^{s-1}} + \int_0^t \frac{kq(t)}{[m(0) - r(i)t]^s} dt \right] \quad (8)$$

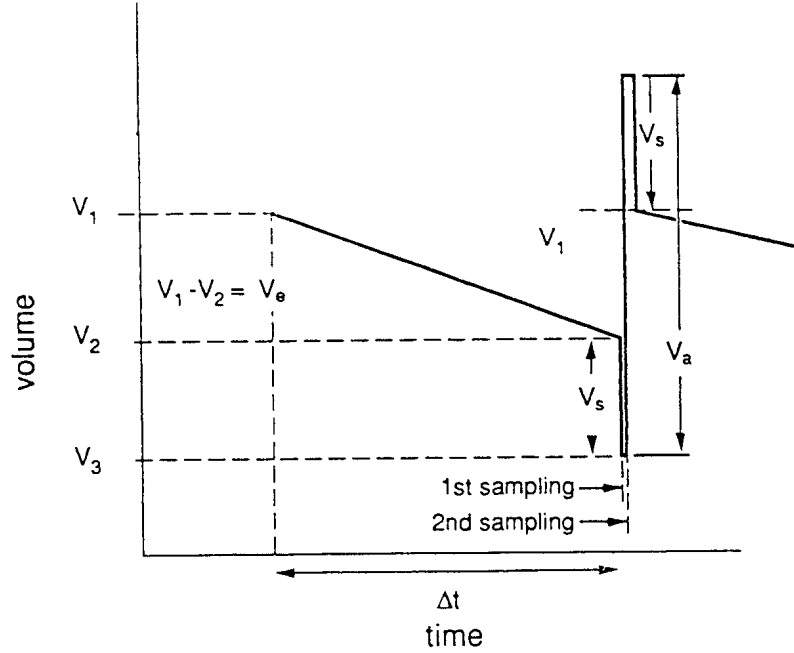


Figure 3. Sampling procedure for tritium generation in open cells: $V_{el} = IM_{D_2O}\Delta t/2F_p$ is the volume lost by electrolysis; V_s is the sampling volume; V_a is the electrolyte volume added to restore prior conditions.

In practice, when using eqn. (8) and assuming that the generation rate q is constant, the integral

$\int_0^t [m(0) - r(i)t]^s dt$ can be treated as a weighting factor. For $kq = \text{const}$, eqn. (8) can be written as

$$f = f(0) \left[\frac{m(0) - r(i)t}{m(0)} \right]^{s-1} + \frac{kq}{(s-1)r(i)} \left\{ 1 - \left[\frac{m(0) - r(i)t}{m(0)} \right]^{s-1} \right\} \quad (9)$$

Equations (7) and (9) both suggest that the evidence for tritium production can be obtained by determining its concentration in the electrolyte phase alone, but only if the isotopic separation factor s is either constant or a known function of time. Plots of tritium distribution and build-up as a function of time as predicted by eqns. (7) and (9) are shown in Fig. 4. Curve (a') illustrates the time dependence of eqn. (7) corrected for sampling. Curve (b) is the time dependence predicted by eqn. (9). As can be seen, curves (a') and (b), when properly corrected for sampling effects, are nearly equivalent; hence either equation can be used for data analysis.

2.2. Balance on Recombiner

Because of the conditions imposed, i.e. constancy of the separation factor and a relatively low rate of tritium production [4], the mass balance on the recombiner can provide additional information. The tritium mass balance on the catalytic converter, working with an efficiency ϵ_r , is given in terms of the tritium mass fraction:

$$f_g = \epsilon_r f_{g \rightarrow 1} + (1 - \epsilon_r) f_{g \rightarrow g} \quad (10)$$

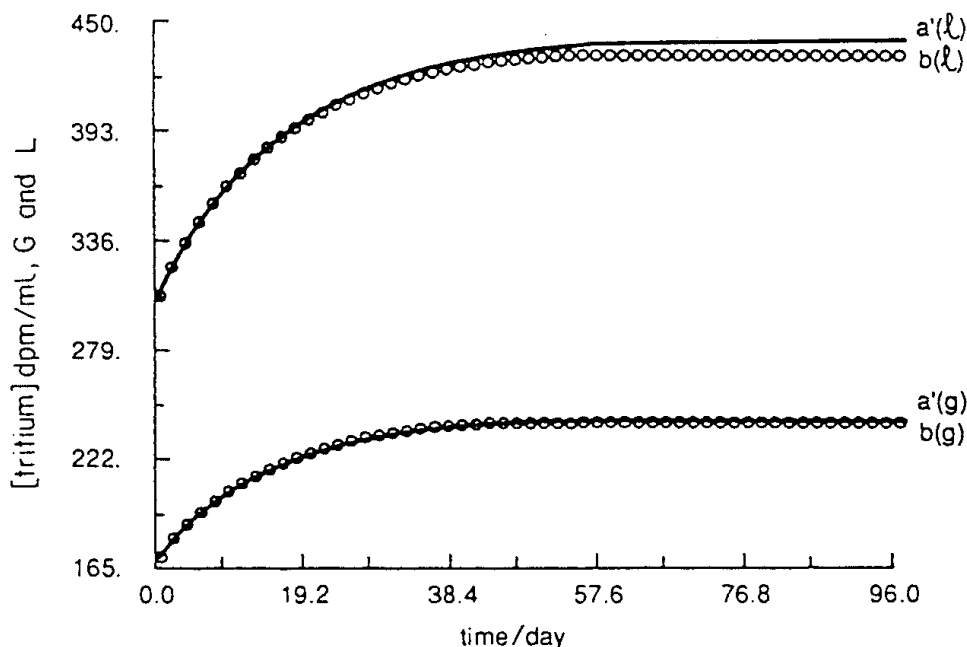


Figure 4. Calculated tritium distribution (simulated data) between “electrolytic” gas and electrolyte phases as a function of time: (a’) time dependence of eqn. (7) corrected for damping; (b) time dependence of eqn. (9). Input data: $s = 1.8$; initial $[^3\text{H}] = 300 \text{ dpm ml}^{-1}$.

where subscript $g \rightarrow l$ refers to the mass fraction found in the liquid collected during catalytic conversion and $g \rightarrow g$ indicates the fraction that is lost due to the inefficiency of the recombiner. Assuming perfect mixing in the catalytic converter and recognizing that the rate of reaction of D_2 with O_2 is faster than that of DT , we must introduce a second separation factor, i.e. $s^* = f_{g \rightarrow l} / f_{g \rightarrow g}$, which, when substituted into eqn. (11), yields

$$f_g = f_{g \rightarrow l} \left(\epsilon_r + \frac{1 - \epsilon_r}{s^*} \right) \quad (11)$$

Since s^* is not generally known, care must be taken to provide a sufficiently large catalyst area to match the rate of recombination with the rate of the gas evolution, so that $\epsilon_{r \rightarrow 1}$, thereby removing the term which contains s^* . Failure to do so would produce a systematic underestimation of the tritium content in the gas phase.

3. DATA ACQUISITION–EXPERIMENTAL PROCEDURE

In principle, any cell design may be employed. In practice, cells are usually constructed in such a manner as to provide a uniform current density distribution on the Pd cathode which is totally immersed in an electrolyte. Operating cells are considered to be open systems if the evolving gases are allowed to escape and/or are catalytically recombined in a separate compartment. The solvent evaporation rate must be minimized by either installing a reflux condenser or providing a cooling jacket. In what follows, uncertainties associated with tritium analysis and sampling procedure are assessed.

3.1. Tritium Analysis

The commonly used analytical procedure employed to measure tritium content is the liquid scintillation technique. In this technique, a sample is added to a scintillation cocktail (e.g. Fisher

Scientific ScintiVerse E Universal LSC Cocktail). The prepared solutions are then counted for a given amount of time, depending upon the accuracy required, in a scintillation counter such as the Beckman LS 6000 LL. Care must be taken to ensure stabilization and adequate compensation for chemiluminescence and photoluminescence. Samples containing dissolved Pd²⁺ ions should first be distilled to dryness before the distillate is added to the scintillation cocktail. Chemiluminescence from alkaline solutions can be eliminated by the addition of glacial acetic acid. Shielding in the detector compartment is necessary to reduce the cosmic-ray-induced γ -ray background.

We have determined the accuracy of this method using replicate samples; the results are summarized in Table 1. As can be seen, the results all fall within ± 1 standard deviation. It should be noted that count times depend on the concentration of tritium. For example, high levels of T, such as are present in samples from Cambridge Isotopes Laboratories Ltd. (ca. 350 dpm ml⁻¹) require times of about 200 min, while D₂O samples with low tritium concentrations (e.g. those from Isotec Inc.) require longer count times for the same accuracy.

Table 1. Error estimate for tritium content in heavy water.

Sample	[³ H]/dpm ml ⁻¹	
	<i>A</i>	<i>B</i>
1	346	19.6
2	343	18.9
3	343	19.7
4	345	19.0
5	346	18.5
Average	345 \pm 4	19.1 \pm 1.2

A, D₂O with high ³H content (source: Cambridge Isotopes, lot no. F 3791), counting time 240 min.

B, D₂O with low ³H content (source: Isotec Inc., lot no. PV 0651), counting time 600 min.

Error in counting efficiency: A, ± 4 ; B, ± 1.2 .

3.2. Sampling Procedure

A sampling procedure is illustrated in Fig. 3. Initially, an electrolyte of known tritium content is placed in an electrochemical cell and electrolyzed at constant cell current I for a time period t . At this time, a known volume of electrolyte is removed and analyzed for tritium content. The electrolyte volume is adjusted and a second sample is removed for tritium analysis. In this manner, the electrolyte volume and concentration are accurately known for the beginning of the next time interval. Concurrently D₂, DT and O₂ gases are catalytically recombined to form D₂O (or DTO) and the resulting liquid is collected in a separate vessel for tritium analysis. The design of the recombining vessel must assure that the samples taken out for tritium analysis are representative of the total D₂O and DTO recombined throughout a given time interval.

In addition to analytical errors (Table 1), there are uncertainties in the electrolyte volume owing to sampling as well as the constancy of cell current and measurements of the time intervals. To illustrate the magnitude of these uncertainties, a representative sample of data from several experiments is assembled in Table 2 for the sampling procedure described in Fig. 3. The first column lists the

electrolyte volume V_1 at the beginning of a particular time period. This initial volume is reduced to V_2 by electrolysis at the cell current I for a time interval Δt , and by sampling to V_3 . To restore the electrolyte volume, an additional volume V_a of D_2O with a known tritium content is added and, after mixing, a second sample is removed from the cell for analysis. The remaining volume is the new initial volume V_1 for the next time interval. It should be noted that the second sample provides a means by which to estimate the magnitude of the sampling errors, as shown by the calculated and observed tritium content (Table 2, columns 5 and 6). The data in Table 2 indicate that the greatest source of error in these analyses is due to the uncertainty in the tritium measurement itself and not the volume measurements.

Table 2. Error estimate in initial conditions (volume) by tritium content measurements.

V_1/ml	$10^{-5} I\Delta t/\text{As}$	V_2/ml	V_a/ml	$[^3\text{H}]/\text{dpm ml}^{-1}$	
				Observed	Calculated
40.30 ± 0.06	7.41	36.15 ± 0.08	8.89 ± 0.01	16.1 ± 1.2	15.8 ± 1.0
39.47 ± 0.08	6.284	35.94 ± 0.09	11.85 ± 0.01	15.2 ± 0.9	15.9 ± 1.1
41.84 ± 0.17	6.045	38.45 ± 0.17	5.93 ± 0.01	18.9 ± 1.2	18.5 ± 0.9
50.31 ± 0.05	10.28	44.54 ± 0.05	8.21 ± 0.01	411 ± 4	412 ± 4
47.89 ± 0.06	11.72	41.31 ± 0.06	6.59 ± 0.01	425 ± 4	424 ± 4

Uncertainties: time, ± 10 s, cell current I , ± 0.001 A. Syringes for sample removal and D_2O addition were calibrated prior to use to minimize volume errors; the largest source of error is the tritium measurement itself.

These experiments typically run for a month or more. The first three rows are results from an experiment using low tritiated D_2O . We are showing the results from three different days, or time intervals, during the course of that experiment. The last two rows are from an experiment using D_2O with a higher initial tritium content and the results tabulated are from two different time intervals.

The uncertainties in V_1 and V_2 , the volumes at the beginning and end of a time interval Δt , reflect the propagation of error from prior samplings.

4. RESULTS AND DISCUSSION

Two approaches to the interpretation of the data are considered: a curve-fitting technique and a comparison of calculated and observed values. As written, eqn. (2) specifies the sampling procedure, thereby indicating whether eqn. (7) or eqn. (9) is more suitable. For example, the necessary condition leading to eqn. (7) is the maintenance of a constant electrolyte volume throughout the duration of an experiment. In practice, this condition is violated by sampling and electrolysis. However, there is no need to maintain the electrolyte volume constant when employing eqn. (9). The only requirement is that the values for the volume, tritium content and cell current be known accurately at the beginning of each time period.

4.1. Curve-Fitting Technique

In general, curve-fitting techniques are adequate when simple and clearly defined models describe the physical situation and when large amounts of data have been collected, typically over a long period of time. Below, we apply curve fitting to determine whether it is useful in the analysis of the tritium concentration data.

Equation (9) has two adjustable parameters which are coupled to one another, namely, the isotopic separation factor s and the tritium generation rate q . We have tested the evaluation of these quantities by applying a computer-aided analysis utilizing, for example, the Nelder-Mead algorithm which adjusts these parameters in such a way as to minimize the sum of the squares of the residuals. In a general case, two additional parameters associated with experimental procedures should be included, namely the faradaic and recombining efficiencies ϵ_f and ϵ_r . The first parameter arises from the reduction of oxygen generated at the anode and dissolved in electrolyte; the second is due to differences in the kinetics of the reaction of D_2 and DT molecules with oxygen.

To assess the usefulness of the curve-fitting technique, simulated data for tritium in the gas and liquid phases were generated by solving the differential equations describing the rate of change of tritium in the electrolyte, on the recombining electrode and in the gas phase. The simulated data were generated both with and without superimposed 1% Gaussian noise. Figure 5 shows the simulated data with superimposed 1% Gaussian noise for an a priori given cell current profile and low continuous production of tritium beginning on day 40. Analysis of the data set by computer-assisted fitting shows strong coupling between the adjustable parameters. The results are given in Table 3 and imply that, even for this simple case, the interpretation is ambiguous. Clearly, when the noise-free data are fitted for only the first 40 days (Table 3, column 1) the resulting values for the parameters are in excellent agreement with the values used to generate the data set. When the same procedure is applied to the noise-added case it shows a substantial degradation of the accuracy of the determined parameters (Table 3, column 2). When the data are expanded to include the last 10 days (Table 3, columns 3 and 4), i.e. when $q > 0$, the resulting fits decrease significantly in accuracy. Indeed, the plot shown in Fig. 5(b), for the residuals versus the day, is a clear indication of a failed fit attempt. The residuals are not Gaussian deviations but are clearly systematic. These deviations persist in the noise-added case (Fig. 5(c)), but are masked to a great extent by the noise.

One of the more interesting points regarding the 50 day computer analyses (Table 3, columns 3 and 4) is the evaluation of faradaic efficiencies greater than 100%. This results in the calculation of an artificially large replenishment volume. Consequently, additional amounts of tritium are added to the system and, in effect, the faradaic efficiency becomes a production term. Indeed, when this amount of "excess" tritium is calculated, it is actually larger (on an atoms per second basis) than the fitting parameter of q . This shows that in order to evaluate any value for the production (consumption) of tritium, great care must be taken with regard to the determination of all other parameters.

The computer program used to analyze the data was modified to include a parameter d which is the time at which tritium generation occurs. The results of this computer analysis are summarized in Table 3, column 5. Although the faradaic efficiency is greater than 100%, the computer analysis yielded a generation rate of $7837 \text{ atoms s}^{-1}$ beginning on day 41.97. This compares remarkably well with the values used to generate the data set. A more sophisticated treatment is required to analyze examples of multiple bursts of tritium production; we have not yet investigated this situation.

4.2. Expected Versus Observed Behavior

The distribution of tritium between the "electrolytic" gas phase and the electrolyte arises from competition involving the various surface and bulk processes. In the absence of current (at equilibrium), this distribution is dictated by the equality of chemical and electrochemical potentials. With the current flowing, however, the separation factor is the dominant governing parameter in the distribution of tritium between the gas and liquid phases. Theoretical aspects of the separation factor have been thoroughly discussed by, among others, Bockris and Srinivasan [8] and Conway and Salomon [9], and those pertaining to the Pd/D system have been considered by Dandapani and Fleischmann [10].

When either eqn. (7) or eqn. (9) is employed, constancy of isotopic separation is assumed. It has been shown that, if tritium concentration data are available for both phases as a function of time, a curve-fitting technique provides a means of determining the value of the separation factor s . Application of this technique to several experimental runs has consistently yielded a separation factor of 1.8, which compares reasonably well with $s = 2$ reported in the literature [2,3]. Once the separation factor is known, the distribution of tritium between the gas and liquid phases can be calculated for any given cell current profile. If an excess of tritium is detected, its source, with either a constant or a

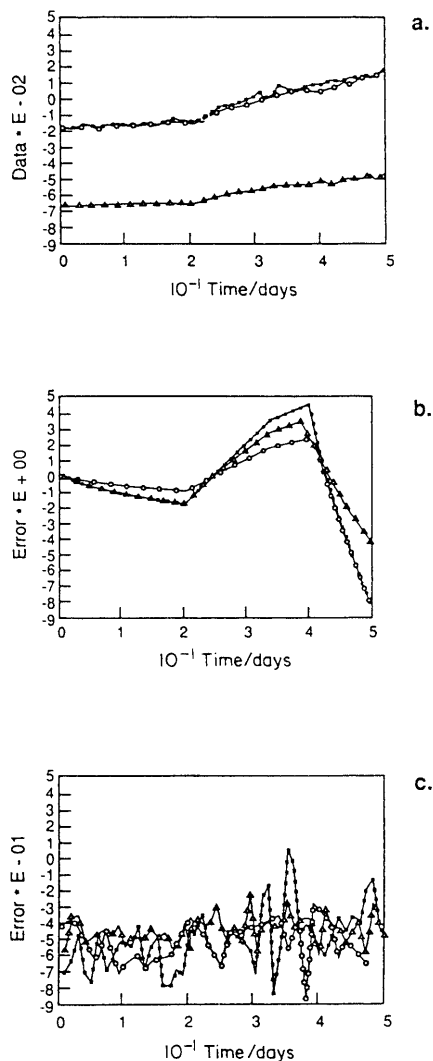


Figure 5. Summary of curve-fitting results for simulated data (see Table 3 for input parameters): (a) plots of data points and computer-generated curves as a function of time (this data set includes Gaussian noise); (b) plots of residuals (no Gaussian noise); (c) plots of residuals with 1% Gaussian noise on data. ■, liquid sample prior to addition of electrolyte to restore volume; ○, liquid sample after adding electrolyte; △, gas phase data.

Table 3. Computer analysis of simulated data.

	First 40 days, no noise	First 40 days with noise	All 50 days, no noise	All 50 days with noise	All 50 days ^a with noise
S	1.79959	1.80108	1.7989	1.79882	1.79429
ϵ_f	100.379	100.690	106.762	106.076	105.814
$q/$ (atoms s ⁻¹)	6.26512	1601.78	-1057.97	676.810	7837.44
Goodness of fit	1.00000	0.985501	0.993660	0.985784	0.988925
Commencement of ³ H generation	—	—	—	—	41.9715

Input data: $I = -50$ mA for 480 h, $I = -300$ mA for 720 h; $q = 10^4$ atoms s⁻¹ for 240 h, commencing at 1680 h; $s = 1.8$, $\epsilon_r = 1.00$; $S^* = 1.00$, $\epsilon_f = 1.00$, $+q = 10^4$ atoms s⁻¹.

^a In this computer analysis, the subroutine was modified to include a fifth parameter d , the time at which tritium production occurs.

time-dependent generation rate, can be located within either the interphase or the bulk electrode. Regardless of the location, magnitude and time dependence of the source, the fluxes leading to the distribution of tritium between the gaseous and liquid phases must originate at the adsorption plane. After the reduction of D_2O/DTO , three distinct transport paths are possible: (i) adsorbed T atoms can exchange only with D atoms of the D_2O molecules of the liquid phase; (ii) T atoms may enter the gas phase directly; (iii) adsorbed species may diffuse in the electrode interior. Path (iii) would strongly influence the distribution by controlling the concentration of adsorbed tritium and must therefore be considered whenever total mass balance is attempted. In practice, neither the constancy of tritium generation nor a single transport path can be assumed, thus making a detailed interpretation more speculative, as illustrated in Figs. 6 and 7 where Pd electrodes with two different surface, morphologies were employed. Figure 6 illustrates the distribution of tritium when the electrolysis was carried out on a dense metallic thin-film Pd electrode, while Fig. 7 summarizes the results obtained with a mossy dendritic electrode produced during the Pd/D code-position process [11].

Examination of the data presented in Fig. 6 shows that the tritium content in the electrolyte phase follows the calculated values within the limits of experimental error. Initially, the tritium content in the gas phase is much greater than that calculated for the isotopic separation factor. Such an increase in tritium content in the gas phase could be interpreted as evidence of tritium production. If this were the case, then the generated tritium would have to be transferred directly into the gas phase. In terms of the fluxes, this would mean that the surface processes leading to nucleation and growth of gas bubbles are faster than those responsible for tritium exchange with the incoming D_2O molecules (path (ii)). Another explanation could be offered, namely that the constancy of the s factor was not preserved within the time interval examined. Also, a time-dependent preferred absorption process into the uncharged electrode may account for the observed data. The existence of several possible explanations shows clearly that it is not possible, at this time, to come to a definitive conclusion regarding any possible tritium production/consumption.

We have applied the analysis to the tritium data reported by Bockris et al. [12] (Fig. 7). This distribution implies that the s factor is dependent on cell current and time, yielding a normal distribution, with $s = 2$ during the codeposition period (i.e. the first 80 h). Shortly after the cell current is tripled, a drastic change in the tritium distribution occurs and an excess of tritium appears in both phases. In terms of the model (eqns. (7) and (9)) tritium production has occurred with preferred transfer to the gas phase ($s = 1.2$). This situation remains unchanged until shortly before the next sampling (Fig. 7, point B). At this point, the tritium distribution yields an apparent s factor of 2.7. Assuming the constancy of the s factor, the model suggests burst-like production with preferred transfer to the electrolyte. The lower than expected tritium content in the gas phase would indicate that the burst occurred just before sampling (point B) since the reported tritium content is an average over the collection period. This high activity diminished with time and returned to normal with $s = 2.0$ (Fig. 7, point C).

The isotopic separation factor is a complex function representing the dynamics of the electrode-electrolyte interphase involving the various equilibria and transport and exchange processes [13]. Some variations in the s factor are thus expected. Whether or not a change from $s = 2.7$ to $s = 1.2$ is realistic and corresponds to the change in the dynamics for the same charging conditions remains an open question. Therefore it would appear that additional information (e.g. total mass balance) is highly desirable if definitive statements are to be made.

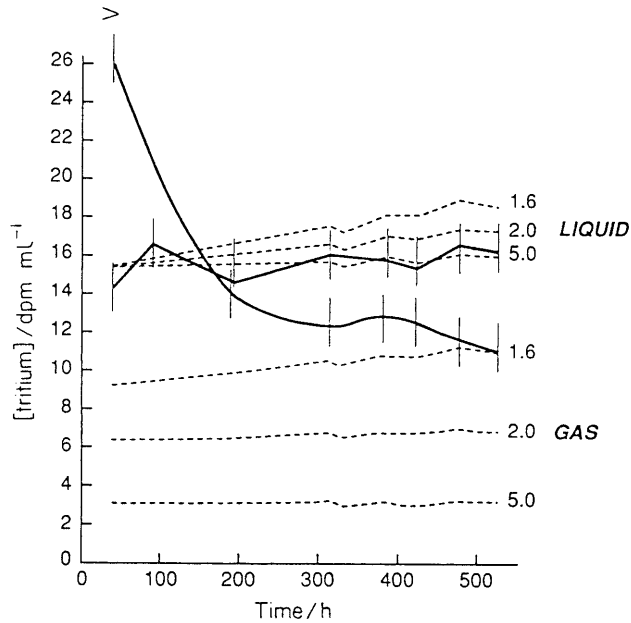


Figure 6. Tritium distribution as a function of time (electrode, thin film with a smooth surface prepared by electrodeposition; mode of operation, constant-current electrolysis in open cells): —: computed distribution using the isotopic separation factors indicated; - - - measured tritium content in the electrolyte and gas phase.

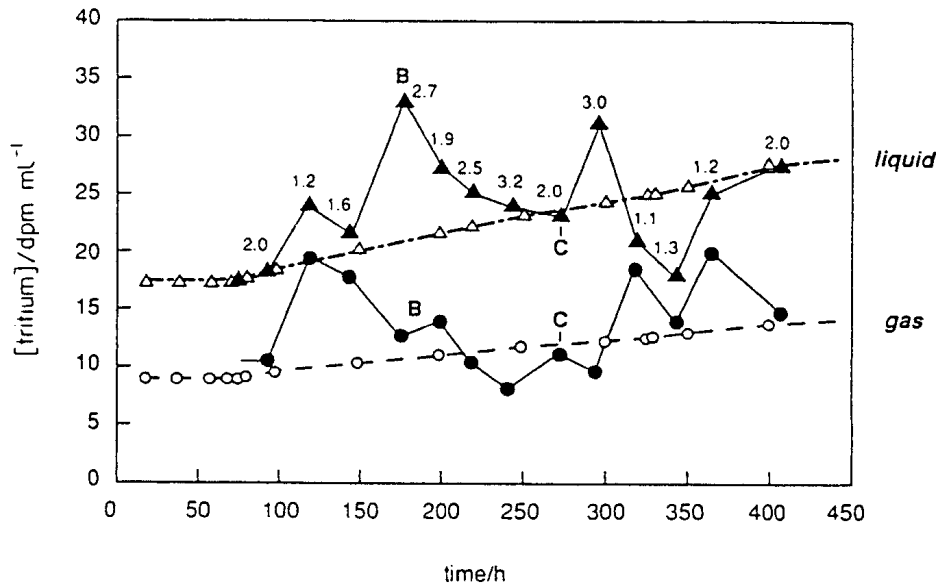


Figure 7. Tritium distribution as a function of time (electrode, prepared by codeposition from PdCl_2 solution; mode of operation, open cell with cell current profile indicated): — calculated distribution using $s = 2.0$; - - - experimentally measured tritium content (data from ref. 12). Experimental s values are indicated.

5. CONCLUDING REMARKS

An analysis of commonly employed experimental procedures and theoretical concepts has led to the following conclusions.

(i) Irrespective of the production term, the isotopic separation factor can be reliably determined by computer-aided analysis if tritium concentration data in both the gas and electrolyte phases are available.

(ii) Apparent changes in the isotopic separation factor, as a function of cell current and time, identify the dominant process(es).

(iii) The design of the "electrolytic" gas recombining vessel must assure that samples are representative of the total D₂O and DTO contents, i.e. the area of the catalytic surface must be sufficiently large to yield 100% efficiency.

(iv) The greatest source of error is the determination of tritium content, particularly at low concentrations. The error can be substantially reduced by increasing the counting time.

(v) When operating open cells with multiple samplings, care must be taken to assure good control of the electrolyte volume. Additional sampling is advisable to establish initial conditions for the next time interval accurately.

As a final closing remark, we should like to point out that one of the difficulties in providing irrevocable evidence of nuclear activities in open electrochemical cells via tritium analysis arises from, and is aggravated by, intermittent and/or low generation rates. Such random events tend to prevent reproducibility despite a strict control of experimental conditions, and low generation rates could easily be too small to be reliably differentiated from zero. Therefore the most reliable method of determining tritium generation is through the use of closed cells, i.e. by taking the difference in tritium contents in all cell elements before and after completion of an experiment.

ACKNOWLEDGMENTS

The authors would like to thank Dr. C.J. Gabriel for computer analysis of the simulated data and Dr. D.R. Rolison for her comments during the preparation of this manuscript.

REFERENCES

1. M. Fleischmann, S. Pons and M. Hawkins, *J. Electroanal. Chem.*, 261(1989) 301.
2. E. Storms, *Fusion Technol.*, 20(1991)433.
3. C.-C. Chien, D. Hodko, Z. Minevski and J. O'M. Bockris. *J. Electroanal. Chem.*, 338 (1992)189.
4. 4F.G. Will, K. Cedzynska, M.C. Yang, J.R. Peterson, H.E. Berge— son, S.C. Barrowes, W.J. West and D.E. Linton, *Proc. 2nd Conf. on Cold Fusion, Como, 29 June—July 4 1991, Italian Physical Society, Bologna, 1991, p. 373.*
5. S. Szpak, C.J. Gabriel, J.J. Smith and R.J. Nowak, *J. Electroanal. Chem.*, 309 (1991) 273.
6. G.H. Un, R.C. Kainthla, N.J.C. Packham, O. Velev and J.O'M. Bockris, *Int. J. Hydrogen Energy*, 15 (1990) 537.
7. R.E. Adzic, D. Gervasio, I. Bae, B. Cahan and E. Yeager, *Proc. 1st Annu. Conf. on Cold Fusion, Salt Lake City, UT, 28—31 March 1991, National Cold Fusion Institute.*

8. J. O'M. Bockris and S. Srinivasan, *J. Electrochem. Soc.*, III (1964) 844, 853, 858.
9. B.E. Conway and M. Salomon, *Ber. Bunsenges. Phys. Chem.*, 68 (1964) 331.
10. B. Dandapani and M. Fleischmann, *J. Electroanal. Chem.*, 39 (1972) 323.
11. S. Szpak, P.A. Mosier—Boss and J.J. Smith, *J. Electroanal. Chem.*, 302 (1991) 255.
12. J.O'M. Bockris, C.C. Chien, D. Hodko and Z. Minevski, *Frontiers of Cold Fusion, Proc. 3rd Int. Conf. on Cold Fusion*, October 1992, Nagoya, Universal Academy Press, Tokyo, 1993.
13. G. Sandroek, S. Suda and L. Schlapbach, *Topics in Applied Physics, Vol. 2, Hydrogen in Inter-metallic Compounds*, Springer Verlag, 1992, Ch. 5.

Deuterium uptake during Pd–D codeposition

S. Szpak ^a, P.A. Mosier-Boss ^a, J.J. Smith ^b

^a Naval Command, Control and Ocean Surveillance Center, RDT&E Division, San Diego, CA 92152-5000, USA

^b Department of Energy, Washington, DC 20585, USA

Received 24 September 1993; in revised form 12 April 1994

ABSTRACT

The mode of deuterium uptake during Pd–D co-deposition has been explored using galvanostatic perturbation techniques. The resultant potential relaxation curves exhibit four distinct potential–time intervals where the relaxation process is controlled by the interaction between the transport of deuterium from the lattice to the surface to form adsorbed deuterium and the reduction of palladium from solution. These interactions are discussed in terms of the palladium + electrolyte interphase.

Key words: Galvanostatic perturbation; Deuterium uptake; Pd–D codeposition

1. INTRODUCTION

Although the hydrogen evolution reaction has been studied extensively since the turn of the century, details of how to maintain, for example, a high surface coverage of adsorbed hydrogen and, in the case of the Pd electrode, to promote a high ratio of absorbed hydrogen to palladium remain unclear. Recently, we described sorption of electrochemically generated deuterium in terms of interfacial events [1] and emphasized the role of the interphase [2]. Of particular interest is the significantly higher efficiency of electrochemical charging compared with that of charging from the gas phase [3]. This poses the question as to what role, if any, the electrode potential plays in maintaining a high D/Pd atomic ratio. It is often assumed that there is little difference, apart from the usual isotopic effect, between the behavior of the Pd + H system, where a great deal of information is available, and that of the Pd + D system. However, this assumption, is not always valid; for example, Rolison et al. [4] clearly illustrated the difference in the development of surface morphology associated with a prolonged evolution of deuterium and hydrogen on Pd cathodes.

In this paper, we explore the mode of deuterium uptake during the process of Pd–D codeposition. The sequence of events is expected to be the same as in the charging of a solid electrode but they should be more clearly defined because of the formation of a new electrode surface which is not affected by prolonged contact with solution.

2. EXPERIMENTAL AND RESULTS

The experimental approach selected here is that of the examination of the electrode response to a programmed constant current pulse. The corresponding time rate of change of the electrode potential, measured versus a reference electrode, provides the required information on the participating processes.

2.1. Cell, Apparatus, Pulse Generation and Recording

A two-compartment glass cell, separated by a fritted disk, was used. The working electrode consisted of a set of 14 Pt wires, 0.05 cm in diameter ($A = 1.96 \times 10^{-3} \text{ cm}^2$), embedded in an acrylic block and separately connected through a switching arrangement to a controlled power source. The Pt wire electrodes were separated from each other by a distance of 3 mm and were arranged in two rows 8.5 mm apart. The counter-electrode and reference electrode were respectively a Pt mesh and Ag | AgCl in saturated KCl dissolved in D_2O . An unstirred D_2O solution, 0.05 M in PdCl_2 and 0.3 M in LiCl, served as the electrolyte. Current pulses were generated by a computer-driven potentiostat (PAR model 173) with a 276 IEEE computer interface.

2.2. Charging Curves and Potential Relaxation

A summary of the electrode potential response $\Phi(t)$ to the perturbation in the form of a constant current density pulse j and the return to equilibrium condition is shown in Fig. 1. Typically, on charging, four distinct time intervals can be identified in which the $\Phi(t)$ function differs. The first time interval, $0 < t < t_1$, is characterized by a rapid change in Φ and exhibits an extremum at Φ_1 , point A. This is followed by an interval $t_1 < t < t_2$, where the electrode potential asymptotically approaches a constant value Φ_2 . In the remaining two time intervals, $t_2 < t < t_3$ and $t_3 < t < t_4$, the $\Phi(t)$ relation is almost linear but with slightly different slopes. The interphase relaxation behavior, displayed in the form of $\Phi(t)|_{j=0}$ and $\Phi(t)|_{j>0}$, is shown in Fig. 1 by the broken curves a, b, c, and a', b', c' respectively. The complexity of the relaxation process increases with the current pulse duration. When the current flow is interrupted before the first plateau is reached, i.e. along the asymptotic approach, the potential relaxes in a manner resembling an exponential relation (curve a).

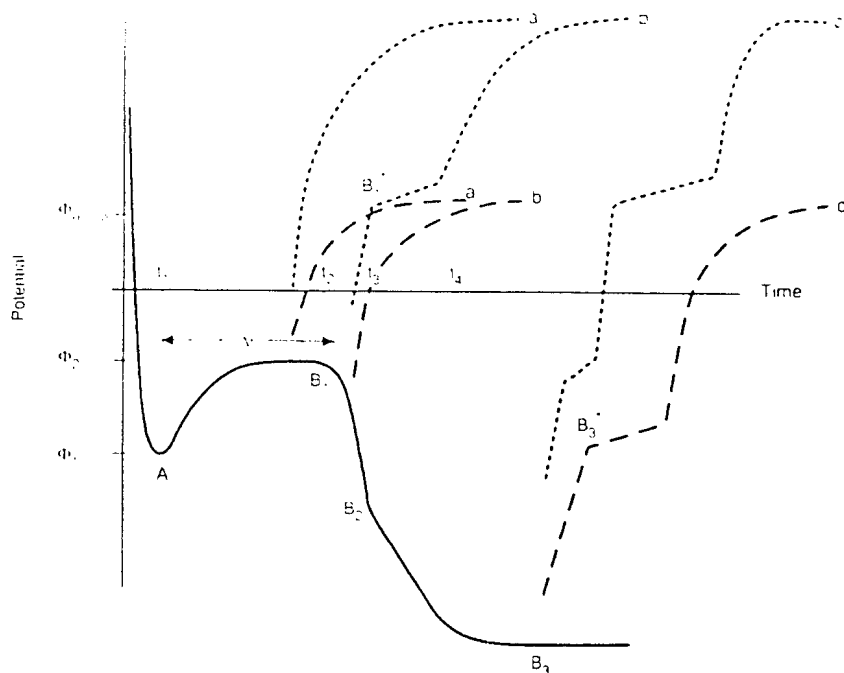


Figure 1. Idealized representation of the $\Phi(t)$ response to a galvanostatic pulse (solid curve) and the $\Delta\Phi(t)$ relaxation on current interruption at points indicated (broken curves): point A, onset of crystallization (nucleation); period Δt represents an asymptotic approach to a complete coverage by PdD_x deposit; points B_1, B_2, \dots, B_n indicate a change in the reaction path. Curves a, b, c for $\Phi(t)|_{j=0}$; curves a', b', c' for $\Phi(t)|_{j>0}$.

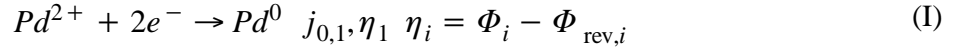
Qualitatively, the shape of the $\Phi(t)$ curve is independent of the magnitude of the applied cathodic current density pulse; the duration of the characteristic time intervals decreases almost exponentially with increases in pulse current. For example, the onset of crystallization (Fig. 1, point A) occurs at 230 ms when the current density pulse j is $-5 \times 10^{-3} \text{ A cm}^{-2}$ and shortens to 1.2 ms when $j = -2 \times 10^{-1} \text{ A cm}^{-2}$. This behavior indicates that an increase in the magnitude of current density pulse leads to a compression in time which, if not accounted for, can result in a loss in resolution of the relaxation curves. Also, as in the case of charging, the potential relaxation is characterized by well-defined regions. These regions are associated with a change in the reaction path as the electrode returns to its rest potential or is forced to a new stationary state.

3. FACTORS AFFECTING THE SHAPE OF THE CHARGE-DECAY CURVES

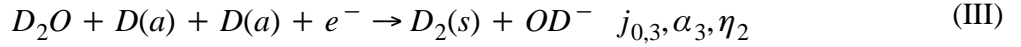
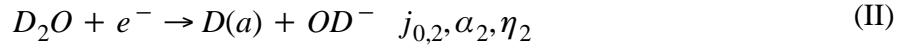
In interpreting the $\Phi(t)$ curves in terms of the dynamics of the interphase region, we first review factors pertinent to the D–Pd codeposition process, namely reaction paths, kinetics of deuterium evolution with emphasis on the associated surface coverage, and the structure of the interphase and its simulation by an electric circuit analog.

3.1. Reaction Paths

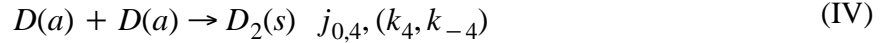
Reactions participating in the Pd–D codeposition are the reduction of Pd^{2+} ions



and the reduction of heavy water



followed by the evolution and absorption of deuterium



where (a), (s) and (l) denote adsorbed, solution and lattice species. The charge transfer processes (Eqs. (I)—(III)) occur independently, i.e. the overall charge transfer process is viewed as the sum of the respective individual contributions.

3.2. Electrode Kinetics: Basic Equations

When considering the Pd deposition in the presence of evolving deuterium, it is sufficient to take into account those events that follow the formation of Pd adions/adatoms. If similar with other electrocrystallization processes, the rate-controlling path for the reduction of Pd^{2+} ions may proceed via surface diffusion or by charge transfer control [5]. Under normal circumstances, surface diffusion is the controlling factor. During codeposition, and within the current density pulse duration where the evolution of surface morphology dominates, charge transfer control is favored:

$$j_1 = -j_{0,1} \exp[-(1 - \alpha_1) f \eta_1] \quad (\text{I})$$

where $f = F/RT$.

The surface activities of freshly deposited Pd are coupled with individual processes associated with deuterium evolution, namely charge transfer at points where no D is present (Eq. (II)) or at points where D is present (Eq. (III) , recombination (Eq. (IV)), or desorption of D₂ by diffusion into the liquid phase or removal by bubble formation. During codeposition, two cases can be distinguished: deuterium evolves (i) on a totally bare electrode surface (Volmer path)

$$j_2 = -j_{0,2}(1 - \theta) \exp [-(1 - \alpha_2)]f\eta_2 = (1 - \theta)j_2(\eta_2) \quad (2)$$

or (ii) on occupied sites (Heyrovsky path)

$$j_3 = -j_{0,3}\theta \exp [-(1 - \alpha_3)]f\eta_3 = \theta j_3(\eta_3) \quad \eta_2 \approx \eta_3 \quad (3)$$

yielding the total current of deuterium evolution

$$j_2 + j_3 = j_2(\eta_2) + \theta[j_3(\eta_2) - j_2(\eta_2)] \quad (4)$$

The precise form of the $j(\eta)$ relationship is less important than the relative ratio of the partial currents, $j_1/(j_2 + j_3)$. However, while examining the dynamics of the interphase during codeposition, attention should be directed to ascertaining how the density of D adsorption active sites relates to the overpotential and the rate of Pd deposition. Because of the continuous formation of a new surface, the electrode area grows, thereby reducing the overpotential as well as the exchange current density with respect to that existing immediately before. Small changes in surface area may produce substantial changes in local $j_{0,1}$ which, in turn, will give rise to a non-uniform distribution of charge transfer current density. Also, the activity of the surface is strongly affected by the growth form and, through it, by the density of surface defects.

3.3. Structure of the Interphase

Thermodynamic considerations relate the measured potential to the affinity of the elementary charge transfer processes [6,7]. Consequently, the structure and properties of the Pd + H₂O interphase can be derived from analysis of a charged Pd electrode responding to anodic currents. On this basis, Bucur and Bota [8] concluded that there is an accumulation of hydrogen on the metal side of the interphase and that the mobility of the adsorbed hydrogen affects the transfer equilibria. They also noted the effect of surface morphology; in particular, they suggested that the surface of black Pd acts as a hydrogen trap when in contact with an electrolyte but not when in contact with a gaseous phase. Somewhat later, Schlappbach [9] presented the following picture. The equilibrium position of the hydrogen surface atoms is different from that given by lattice periodicity in the bulk. Further, with an increase in the surface coverage, adsorbed H atoms form both disordered and ordered phases. He also noted that adsorption can induce relaxation (or reconstruction) of the surface, i.e. it can be viewed as adsorption-absorption induced alteration of structure (change in the inhomogeneity of material). Chemisorbed hydrogen occupies sites on top of the first layer and also sites between and underneath the top surface atoms, i.e. in agreement with hydrogen accumulation on the metal side [8].

As previously [2,10], we stress the nonautonomous character of the Pd + D interphase and note its active participation during transport of interstitials. The nonhomogeneity of the deuterium distribution may extend further into the bulk because spatial structures can be generated due to a concentration-dependent diffusion coefficient, thus contributing to the complex behavior of the interphase [11]. As a rule, investigation of the behavior and properties of the electrode + electrolyte interphase is limited to examination of the solution side [7]. The reason for this approach is that the electric field does not affect thermodynamic properties of metals. However, for hydrogen absorbing electrodes, a case can

be made that the external electric field penetrates the interphase to some extent, especially during the transport across the interphase. The ensuing concentration gradients make the electrode inhomogeneous with respect to its composition. Furthermore, the driving force is the gradient of the chemical potential in the bulk only if the electric field does not affect the energetics of the system, i.e. if the action of the electric field does not polarize molecules. The question that arises is whether or not the molecules/atoms within the interphase are polarized; if they are, then the strength of the electric field must be included when discussing the uptake of deuterium. Consequently, the relative importance of mechanical distortion of the lattice and of the electric field must be assessed.

3.4. ELECTRIC CIRCUIT ANALOG

When the adsorbed species participate in the charge transfer process, the electrode surface itself can be regarded as either a reactant or a product. Thus its properties enter into the formulation of the appropriate rate equations. In the case of adsorbed reactants, the overall reaction path and the sequence of events are derived from the basic relation $\Phi(t) = \Phi(\theta_1, \theta_2 \dots; j_1, j_2, \dots)$. A somewhat simpler functional dependence can be formulated for Pd–D codeposition. Although there are five reaction paths, and therefore five fluxes, there is only one surface coverage θ of interest, that of adsorbed deuterium. A common time–dependent Galvani potential difference $\Phi(t)$ drives three reactions, represented by Eqs. (I)—(III), through two overpotentials η_1, η_2 . Thus we can write

$$\Phi(t) = \Phi[\theta; j_1(\eta_1), j_2(\eta_2), j_3(\eta_2)] \quad (5)$$

Following the differentiation of Eq. (5)

$$\frac{d\Phi}{dt} = \frac{\partial\Phi}{\partial\theta}|_{j_1, j_2, \dots} \frac{d\theta}{dt} + \sum_i \frac{\partial\Phi}{\partial j_i}|_{\theta, \eta, j \neq j_i} \frac{dj_i}{dt} \quad i = 1, 2, 3 \quad (6)$$

we assign a physical meaning to each term on the right–hand side and interpret the $\Phi(t)$ behavior via the use of an electric circuit analog. To derive this analogy, we employ, as in our previous paper [1] the conservation of charge

$$C \frac{d\Phi}{dt} = j - (j_1 + j_2 + j_3) \quad (7)$$

and the deuterium mass balance

$$\Gamma_m F \frac{d\theta}{dt} = j - (j_1 + j_2 + j_3) \quad (8)$$

Combining Eqs. (7) and (8), we eliminate one partial current (either j_2 or j_3) and obtain

$$C \frac{d\Phi}{dt} \pm \Gamma_m F \frac{d\theta}{dt} = j^* \quad (9)$$

where C is the effective potential–independent capacitance on the solution side of the interphase, Γ_m is the maximum number of sites per unit area and j^* is the sum of rates of all but one of the processes expressed as currents and the plus or minus sign indicates the way in which Eqs. (7) and (8) were combined (i.e. by addition or subtraction). Solving for $d\theta/dt$ and substituting in Eq. (6), we obtain

$$\begin{aligned} & \left(1 \pm \frac{C \partial\Phi}{\Gamma_m F \partial\theta} \right) \frac{d\Phi}{dt} \\ &= \frac{j^*}{\Gamma_m F} \frac{\partial\Phi}{\partial\theta}|_{j_1, \dots} + \sum_{j \neq j_i} \frac{\partial\Phi}{\partial j_i}|_{\theta, j_1, j_2, \dots} \frac{dj_i}{dt} \end{aligned} \quad (10)$$

Identifying the term $(1/\Gamma_m F)(\partial\Phi/\partial\theta)$ with the adsorption capacitance C_{ad}^{-1} and taking $C_{ad} \gg C$ and $\partial\Phi/\partial j_i = R_i$, we further simplify to obtain

$$\frac{d\Phi}{dt} = \frac{j^*}{C_{ad}} + \sum R_i \frac{dj_i}{dt} \quad (11)$$

where the R_i are the respective faradaic resistances.

4. INTERPRETATION OF THE $\Phi(t)$ CURVES

The events associated with the deuterium uptake in the course of Pd–D codeposition are derived from the characteristic features of $\Phi(t)$ curves. Three features are examined: the change in slope, the amount of absorbed deuterium, determined by anodic pulse current, and the transport of deuterium within the interphase.

4.1. Change in Slope

A common feature observed in all cases of charging and discharging, to a varying degree, is the change in the slope of the $\Phi(t)$ curve which, in turn, is related to the change in the reaction path (Eq. (11)). To simplify the mathematics, we consider the potential relaxation under zero external cell current, ($j = 0$). Under this condition, $\Phi(t)$ is viewed as a mixed potential which, in the absence of Pd^{2+} ions, arises from two partial currents: oxidation of deuterium via the Volmer path and reduction via the Heyrovsky path [12]. In the presence of Pd^{2+} ions, the cathodic partial current $-j_1$ replaces the Heyrovsky path and drives the oxidation of deuterium with the current j_2 ; the deuterium is supplied to the charge transfer plane by transport from the metal side of the interphase j^* . Accordingly, Eq. (11) becomes

$$\frac{d\Phi}{dt} = \frac{j^*}{C_{ad}} + \left(\frac{\partial\Phi}{\partial j_1} \frac{dj_1}{dt} + \frac{\partial\Phi}{\partial j_2} \frac{dj_2}{dt} \right) \quad (12)$$

which, with $j_1 + j_2 = 0$, yields $dj_1/dt = -dj_2/dt$, resulting in

$$\frac{d\Phi}{dt} = \frac{j^*}{C_{ad}} + (R_1 - R_2) \frac{dj}{dt} \quad (13)$$

Eq. (13) implies that the observed change in the slope of the $\Phi(t)$ curves, on either charge or discharge, must be attributed to a change in the reaction path. This conclusion is supported by the fact that at the point of change (e.g. points B_1 and B_2 in Fig. 1) conditions at the charge transfer surface remain unchanged; consequently, the term j^*/C_{ad} in Eq. (13) could not be substantially affected.

4.2. Deuterium Uptake

Scanning electron microscope examination of the surface revealed that, within the first time interval, as the $d\Phi(t)/dt$ asymptotically approaches zero, the Pd deposition (and/or PdD_x codeposition) proceeds via nucleation with overlapping layers. During this period, the $\Phi(t)$ curve is dominated by the surface coverage which obeys Eq. (8) and which, after neglecting contributions due to the Heyrovsky and Tafel paths, yields

$$\Gamma_m F \frac{d\theta}{dt} = j_2(1 - \theta) - k_s\theta - j_1\theta \quad (14)$$

where the first term on the right-hand side denotes an increase in surface coverage arising from the Volmer path, the second term reduces it by absorption and the third term reduces it further by creating

new surface (i.e. new adsorption sites). Viewing the codeposition as one-dimensional growth, the term θ is, in fact, the fraction of sites occupied by the absorbed deuterons (ξ in Ref. 1). If we take its value as zero at point A in Fig. 2, an integration of Eq. (14) yields

$$\theta(t) = \frac{j_2}{j_2 + k_5 + j_1} \left[1 - \exp \left(- \frac{j_2 + k_5 + j_1}{\Gamma_m F} t \right) \right] \quad (15)$$

Eq. (15) implies that a change in composition of the codeposited PdD_x should follow the change in the $\Phi(t)$ curve, i.e. should approach saturation asymptotically. The D/Pd atomic ratio along the asymptote can be determined by reversing the current flow. The results of such current reversal are illustrated in Fig. 2 where a charging current of $5 \times 10^{-3} \text{ A cm}^{-2}$ was selected to display the progression of deuterium loading and the reversal was made at the points indicated. The D/Pd ratios, where $D = D(a) + D(l)$, calculated from the Q_a/Q_c ratio were 0.42, 0.68, 0.98 and 1.02 at the times indicated. Further, Eq. (15) is in agreement with the observed effect of the pulse current density $-j_1$ on the initial behavior of the $\Phi(t)$ curve.

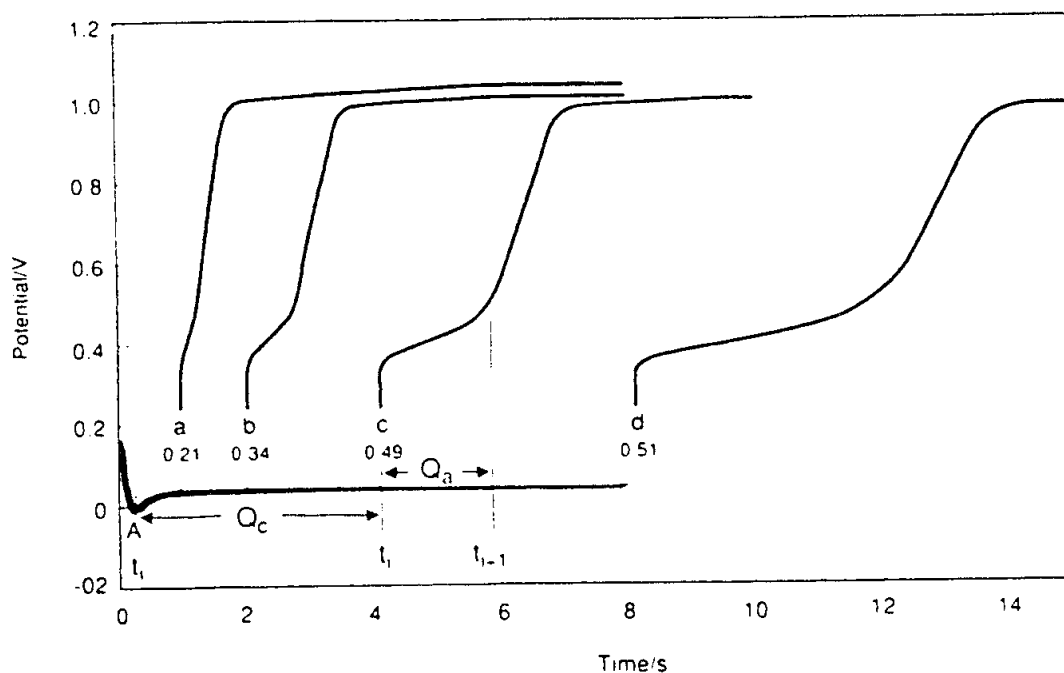


Figure 2. The $\Phi(t)$ behavior upon cell current reversal following various times of codeposition process. Determination of D/Pd atomic ratio. Cathodic current density $j = -5 \times 10^{-3} \text{ A cm}^{-2}$; anodic current density $j = 5 \times 10^{-3} \text{ A cm}^{-2}$; cell current reversal at 1, 2, 4 and 8 s; corresponding $\Phi(t)$, curves a, b, c and d respectively. Ratio $Q_a/Q_c = j(t_{i+1} - t_i) / |-j(t_i - t_1)|$ is indicated.

It can be seen that Eq. (15) represents the situation well at the beginning of the codeposition. Immediately after the onset of crystallization there is an increase in the electrode area with concurrent lowering of the overpotential and a rapid adsorption of deuterium. This rapid adsorption of deuterium early in the process is also supported by cyclic voltammetry [13] and X-ray diffraction [14] data. The fall in overpotential is attributed to both the expansion of the surface area and the adsorption of deuterium. The effect of $-j_1$ is via the generation of new surface sites affecting reactions (II) and (III) but the functional relation is not clear at this time. As a first approximation, we assume the simplest relation between the rate of Pd deposition and the formation of new adsorption sites, that of

proportionality, i.e. $(1 - \theta) \propto -j_1$ which, in turn, accelerates the Volmer reaction and slows down remaining paths.

4.3. Deuterium Transport Within the Interphase

Limited information on deuterium transport within the Pd lattice and across the interphase can be derived by examining the electrode response after current reversal. The uniform composition of the PdD_x is consistent with the rapid sorption of deuterium into the freshly deposited Pd. At the moment of the cathodic current interruption, the amount of sorbed deuterium, expressed in terms of the charge transferred, is $Q_D = -(j_2 + j_3)/t$. Following the cell current interruption, the $\Phi(t)$ curves can be examined under conditions of either zero cell current (Fig. 3) or cell current reversal (Fig. 4).

In the first case, each $\Phi(t)$ curve exhibits two features: (i) approximately linear regions, AB and BC, with changing slope at point B, and (ii) decreasing slopes of these segments, as shown in Table 1, with increasing length of the codeposition period, i.e. with the thickness of the PdD_x layer. By Eq. (13), with $j = 0$, the linear segments of the $\Phi(t)$ curves imply that the change in partial current(s) is compensated by the j^* term since C_{ad} remains essentially constant. This compensation occurs via the generation of surface active sites and the resupply of deuterium to the charge transfer plane. The linear relation can be maintained only if the supply of deuterium from the interior to the charge transfer plane is fast, i.e. if $j^* \gg |-j_1|$. The second characteristic point, i.e. the decrease in slope with an increase in the codeposition time, is also consistent with uniform distribution of absorbed deuterium through the growing PdD_x layer and the fast equilibration between the lattice deuterium D(l) and the adsorbed deuterium D(a). It is noteworthy that the approach to the rest potential does not follow the square-root dependence or the logarithmic relationship, thus indicating coupling between bulk and surface processes at all times. During this time, as the potential approaches constant value, the rate at which D(a) reacts further, i.e. the equilibration between sorbed and adsorbed deuterium is faster than subsequent D(a) reactions.

The effects of an anodic current following the termination of the codeposition on the $\Phi(t)$ curves are shown in Fig. 4. In particular, the electrode responses to $j = 5.0 \times 10^{-3} \text{ A cm}^{-2}$ and $j = 10^{-2} \text{ A cm}^{-2}$ are compared with the response to zero cell current. Several features are noteworthy. First, the general shape of the relaxation curve is unchanged. However, the slopes of the segments are steeper owing to forced oxidation of adsorbed deuterium D(a), and the amount of recovered (oxidized) deuterium is less which indicates that the supply of deuterium from the bulk to the metal side of the interphase is replaced by diffusion. The latter does not invalidate the fast exchange between the D atoms within the interphase and those populating the charge transfer surface sites.

The anodic $\Phi(t)$ curves provide a qualitative measure of the respective processes. Of interest is the appearance of a third segment, which is particularly pronounced at $j = 10^{-2} \text{ A cm}^{-2}$ (Fig. 4). Since there are only two distinct paths associated with either reduction or oxidation, this new feature represents either the order-disorder phase transition [9] or the existence of energetically different states of the adsorbed deuterium [13].

5. CONCLUDING REMARKS

Models for the PdD_x + D₂O interphase suggest fine spatial structure (as far as D concentration is concerned), i.e. the interphase consists of laminae which are homogeneous with respect to deuterium concentration. The interphase is characterized as follows.

(1) The nonautonomous character of the interphase and its active participation in the course of sorption is accentuated by the codeposition process.

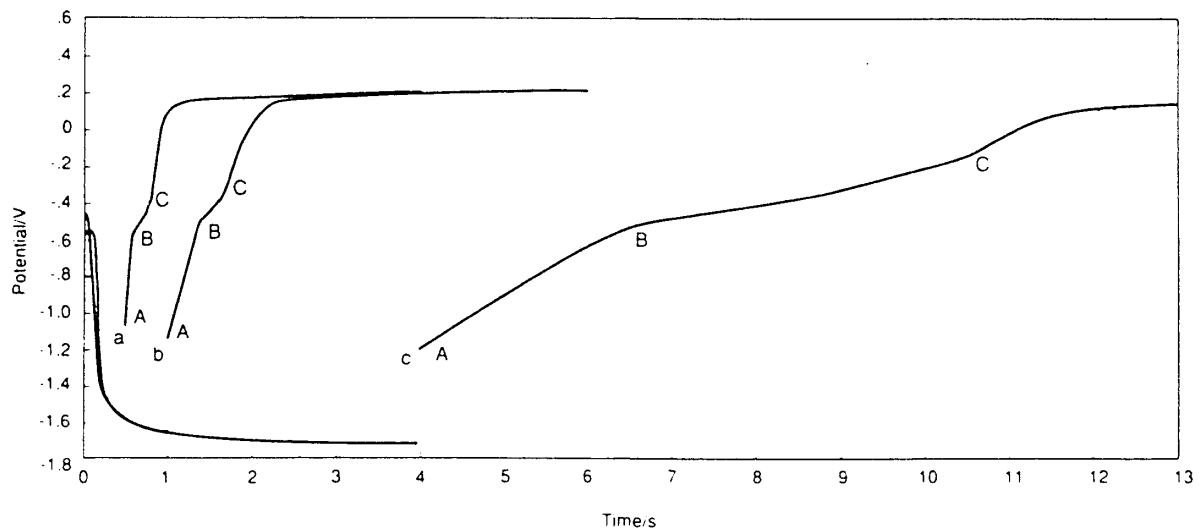


Figure 3. Approach to electrode rest potential $\Phi(t)|_{j=0}$ upon termination of the codeposition. Cathodic current density $j = -10^{-1} \text{ A cm}^{-2}$ terminated at 0.5 s, 1 s and 4 s (curves a, b, and c respectively).

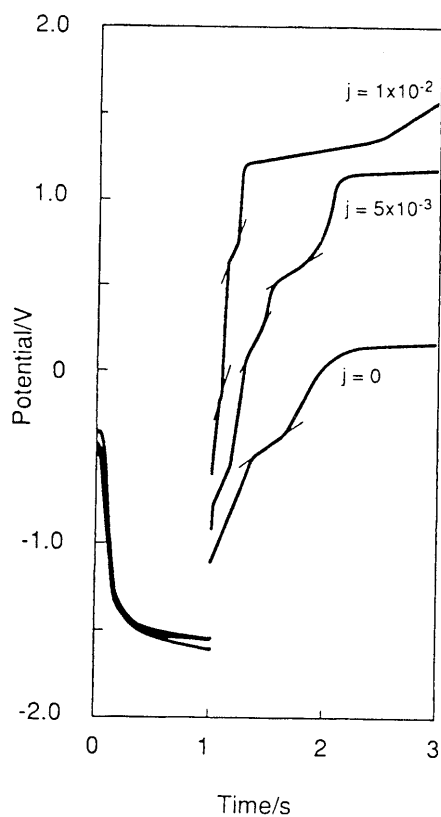


Figure 4. The $\Phi(t)$ behavior as a function of current reversal (indicated): codeposition current density $j = -10^{-1} \text{ A cm}^{-2}$; codeposition time, 1 s.

Table 1. Slopes of linear segments, AB + BC in Fig. 3, as a function of Q.

$Q(/As)$	Segment AB (V/s^{-1})	Segment BC (V/s^{-1})
2×10^{-5}	23.0	7.30
4×10^{-5}	11.1	3.17
10^{-4}	5.6	0.7
2×10^{-4}	1.8	0.53
8×10^{-4}	0.27	0.08

(2) The surface-controlled sorption rates (e.g. metal-hydrogen energy conversion systems) are of technological importance.

(3) The $\Phi(t)$ curves display changes in the reaction paths as well as the complexity of the inter-phase region.

ACKNOWLEDGEMENT

The authors wish to acknowledge the contributions of Dr. S.R. Scharber.

REFERENCES

1. S. Szpak, C.J. Gabriel, J.J. Smith and R.J. Nowak, *J. Electroanal. Chem.*, 309 (1991) 273.
2. S. Szpak, P.A. Mosier—Boss, S.R. Scharber and J.J. Smith, *J. Electroanal. Chem.*, 337 (1992) 273.
3. M. Smialowski, *Hydrogen in Steels*. Pergamon. London, 1962. Ch.3.
4. D.R. Rolison, W.E. O'Grady, R.J. Doyle and P.P. Trzaskoma, *Proc. 1st Conf. on Cold Fusion*, Salt Lake City. UT. National Cold Fusion Institute. 1990.
5. J.O'M. Bockris and G.A. Razunaney. *Fundamental Aspects of Electrocrystallization*, Plenum Press, New York, 1967.
6. M. Enyo and T. Maoka, *J. Electroanal. Chem.*, 108 (1980) 277. [7] P. van Rysselberghe in J.O'M. Bockris (Ed.), *Modern Aspects of*
7. *Electrochemistry*, Vol. 4, Plenum, New York. 1966.
8. R.V. Bucur and F. Bota, *Electrochim. Acta.* 28 (1983) 1373; 29 (1984)103.
9. L. Schlapbach in T. Bressani, E. Del Giudici and G. Preparala (Eds.) in *The Science of Cold Fusion*, SIF. Bologna, 1991
10. S. Szpak, P.A. Mosier—Boss, S.R. Scharber and J.J. Smith, *J. Electroanal. Chem.*, in press.
11. A.L. Samgin, V.I. Tsidlikovski and A.N. Baraboshkin, *Proc. 3rd Int. Conference on Cold Fusion*, Nagoya, Japan, Universal Academy Press, Inc., Tokyo. 1993.
12. K.J. Vetter, *Electrochemical Kinetics*, Academic Press, New York. 1967, p. 607.

13. S. Szpak, P.A. Mosier—Boss, S.R. Scharber and J.J. Smith, *J. Electroanal. Chem.*, in press.
14. S. Szpak, P.A. Mosier—Boss and J.J. Smith. *J. Electroanal. Chem.*, in press.

Cyclic voltammetry of Pd + D codeposition

S. Szpak ^{a,*}, P.A. Mosier-Boss ^a, S.R. Scharber ^{a,1}, J.J. Smith ^b

^a Naval Command, Control and Ocean Surveillance Center, RDT & E Division, San Diego, CA 92152-5000, USA

^b Department of Energy, Washington, DC 20585, USA

Received 23 July 1993; in revised form 10 November 1993

ABSTRACT

Processes associated with the Pd + D alloy codeposition are examined by cyclic voltammetry. The voltammograms cover the potential range: +0.3 to –1.3 V (measured against an Ag/AgCl/KCl (sat) reference) and indicate that the partial current due to the Pd²⁺ ion reduction is diffusion limited at slow scan rates. Except for the significant increase in cathodic currents due to D₂O reduction at ca. –0.25 V which occurs on a freshly generated Pd surface, the shapes of the voltammograms marginally differ from those recorded in the absence of Pd²⁺ ions in the electrolyte phase. A discussion of the dynamics of the interphase is presented.

Keywords: Interphase dynamics; Cyclic voltammetry; Pd + D codeposition

1. INTRODUCTION

In earlier work [1] we constructed a model of the Pd|D₂O interphase wherein we defined a transfer zone λ^* consisting of two interdependent layers, i.e. λ_e which is located within the metal and in contact with λ_s in the electrolyte phase. These two layers interact with one another during the transfer of deuterium. The degree of their participation is dependent upon the applied potential and the solution composition. We concluded that the driving force acts across the interphase whose properties can be expressed as a function of composition and applied overpotential: $\lambda^* = f(c_1, c_2, \dots, \eta)$. In particular, as the overpotential η becomes more cathodic, negative charges accumulate in the interphase, resulting in an extension of the λ_e layer and a higher D⁺ content within the subsurface layer. Furthermore, we observed that weakly adsorbed deuterium is sensitive to the surface-to-volume ratio while strongly adsorbed deuterium is only slightly affected. On this basis, we identified three energetically different states of deuterium residing within the interphase λ^* which, in turn, determine the boundary conditions for deuterium sorption. Of course, each of the energetically different states, when acted upon with the same driving force, exhibit different transport velocities.

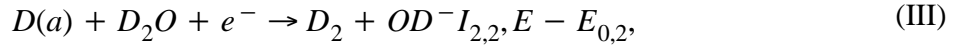
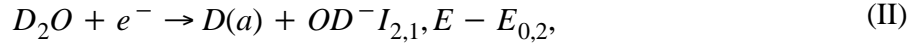
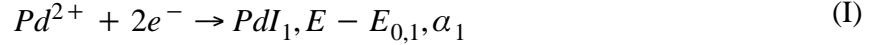
In this paper, we examine the Pd + D codeposition process(es) by employing standard programmed perturbation of the interphase in the form of potential scanning. A gold substrate was used to assure containment of deuterium. Details of the experimental arrangement have been described previously [1].

*To whom correspondence should be addressed.

¹Present address: San Diego Mesa College, San Diego, CA 92111, USA.

2. CODEPOSITION REACTIONS

The total current I associated with the process of Pd + D codeposition is divided into a contribution I_1 needed for the reduction of Pd^{2+} ions and a contribution I_2 needed for the evolution of deuterium from D_2O molecules:



The kinetics of Pd^{2+} reduction are complex, involving a number of steps [2–4]; the path leading to the evolution of deuterium is equally complex [5]. The formulation of the kinetic expressions for a simple case of parallel non-interacting processes is discussed in detail by Bockris and Reddy [6] and summarized graphically in Fig. 1. The driving force for each partial reaction is given by $\eta = E - E_{0,n}$, $n = 1, 2, \dots$, where E denotes the Galvani potential difference and $E_{0,n}$ are the respective equilibrium potentials. However, since the codeposited deuterium interacts with Pd to form an alloy, the reversible potentials $E_{0,1}$ and $E_{0,2}$ must be redefined. According to Gorbunova and Polukarov [7], there is a shift in $E_{0,n}$ in the positive direction by the amount $\Delta G/zF$ given by

$$\Delta G = \frac{X-1}{X}U + RT \ln X \quad (1)$$

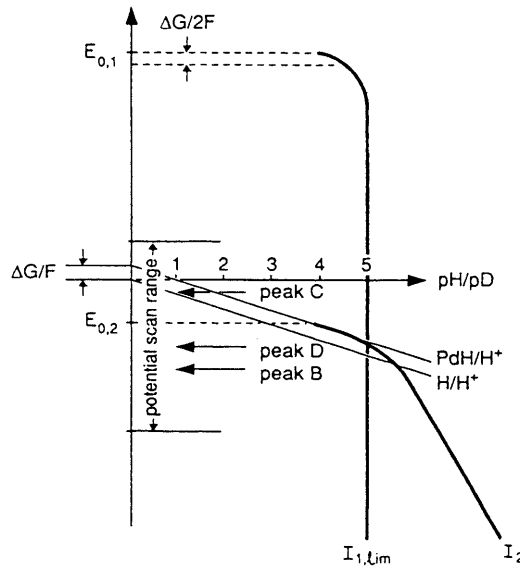


Figure 1. Representation of processes associated with Pd+D codeposition. Potential scan range and partial currents are superimposed on the Pourbaix diagram for the $\text{H}_2\text{O} + \text{H}_2$ system. ($I_{1, \text{lim}}$ refers to the rate of Pd^{2+} ion reduction and I_2 is a measure of D_2 generation).

Here, ΔG is the molar Gibbs energy of the alloy component in the alloy and U is the integral heat of formation of the alloy. In this expression, the first term represents the change in bonding energy and the second is the contribution due to a change in entropy. The total current is the sum of all the partial currents for eqns. (I)–(III):

$$j = \sum I_n \quad (2)$$

In what follows, we retain the independence of partial currents and correct for the Pd + D alloy formation by replacing the term $E_{0,n}$ appearing in the overpotential η with $(E_{0,n} + \Delta G/z_n F)$. The form of the I_n vs. $E - E_{0,n}$ relation depends upon the experimental arrangement. For example, for slow scan voltammetry in the region under investigation, I_1 of eqn. (1) is expected to be diffusion limited while the current associated with the reduction of heavy water is controlled by the dynamics of the inter-phase.

3. EVOLUTION OF VOLTAMMOGRAMS

The effect of two factors on the evolution of the shape of voltammograms is considered, namely the number of cycles and the Pd^{2+} ion concentration.

3.1. Stabilization of voltammograms

Typical evolution of the voltammograms, covering the potential span -1.3 to $+0.3$ V in which codeposition of Pd and D_2 takes place, is illustrated in Figs. 2 and 3 for two Pd^{2+} ion concentrations. Initially, during the negative scan, a featureless $I-\eta$ relation with a substantial increase in cathodic current at potentials more negative than -1.0 V is recorded. On the return sweep, however, a cathodic peak appears at -1.0 V (peak A, insert to Fig. 2(a)) followed by a retracing of the negative branch until a potential of -0.60 V is reached. At somewhat more positive potentials, oxidation of weakly and strongly adsorbed deuterium occurs at -0.50 V and -0.05 V respectively. With subsequent scans, a shift of the entire voltammogram to more cathodic currents is observed. This is attributed to the continuous reduction of Pd^{2+} ions in the potential range $+0.3$ to -1.3 V. Stabilization of the voltammograms coincides with the evolution of the electrode surface morphology. As the number of cycles increases, the electrode surface morphology evolves from that of dispersed individual crystallites to a fully developed porous surface. This is illustrated in Figs. 4(a), 4(b) and 4(c) which show scanning electron micrographs of the electrode surface after the first, third and sixth cycles. Evidently, the surface is morphologically fully developed after the sixth cycle. With further cycling, the surface area becomes larger and the Pd layer becomes thicker.

3.2. Effect of Pd^{2+} Ion Concentration

Four peaks are observed in the voltammograms which we refer to as A, B, C and D. Qualitatively, the scans in the positive direction are similar to those obtained in the absence of Pd^{2+} ions in the electrolyte [1]. As noted, the voltammograms shown in Figs. 2 and 3 are shifted in the negative direction. This shift is proportional to the Pd^{2+} ion concentration in the electrolyte phase. The effect of Pd^{2+} ion concentration is more evident in the negative scan. As shown in Figs. 2 and 3, the shape of the voltammograms is strongly dependent upon the Pd^{2+} ion concentration. In particular, peak A is present at low Pd^{2+} ion concentration and only appears during the first few cycles, and peak B is broader. Regardless of Pd^{2+} ion concentration, peak B encompasses the same potential range. With increasing cycle number peak B shifts to more positive potentials.

The effect of the solution composition on the shapes of peaks C and D is interesting. Initially, at low Pd^{2+} ion concentration, peak C consists of two closely spaced peaks which, with subsequent cycling, shift to more positive potentials and merge to form a single broad peak (Figs. 2(a) and 2(b)). At higher Pd^{2+} ion concentration, regardless of the cycle number, peak C is a superposition of two peaks which, however, remain at the same potential. In contrast, peak D exhibits different features, namely at low Pd^{2+} ion concentration it consists of two peaks D_1 and D_2 , regardless of the scan

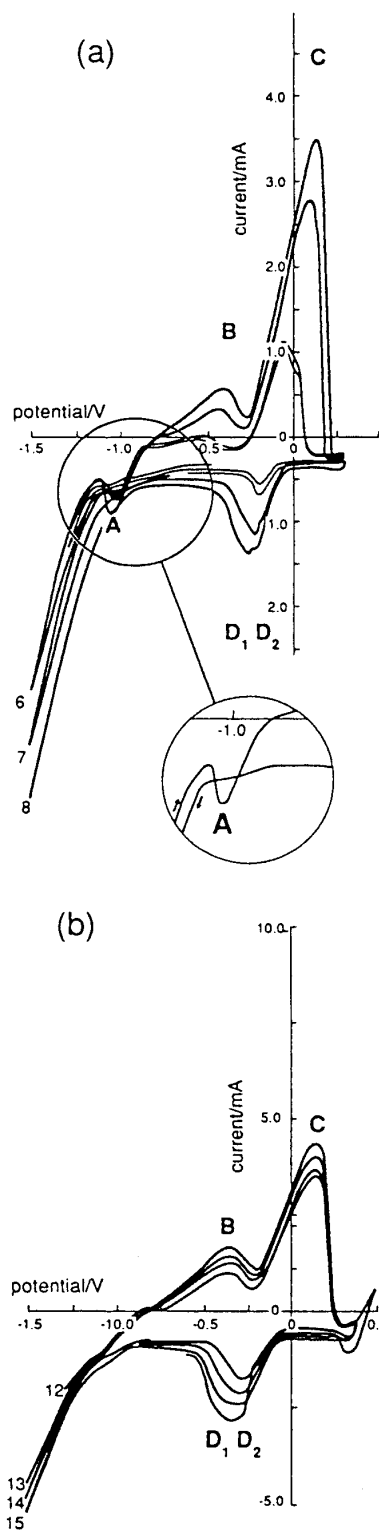


Figure 2. Evolution of the electrode response to potential scan: scan range, +0.3 to -1.3 V; scan number indicated; solution composition, 0.025 M PdCl₂ +0.3 M LiCl in D₂O. (a) Initial stage: scan numbers 6–8. The insert indicates current “cross-over” (scan direction indicated). (b) Voltammograms of morphologically fully developed working electrode: scan numbers 13–15.

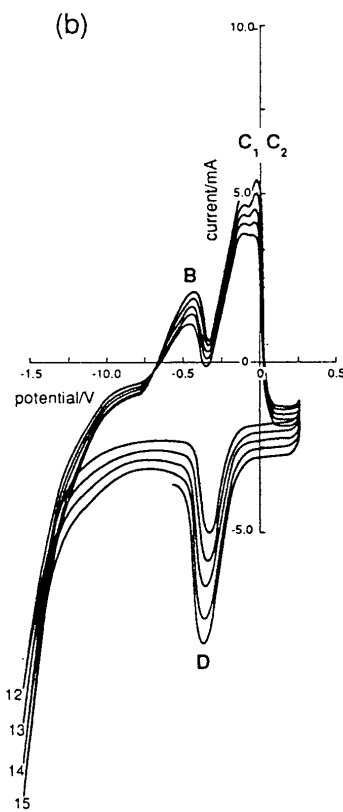
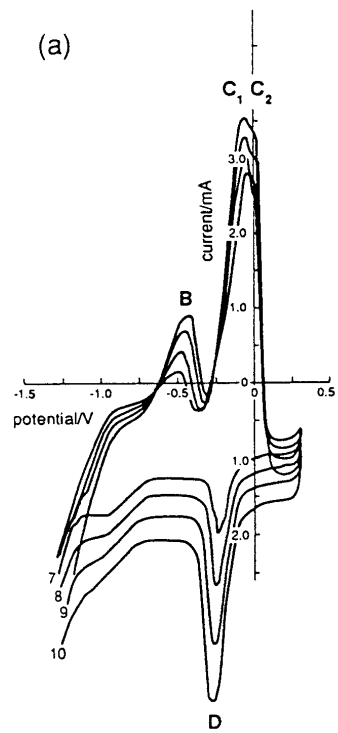


Figure 3. Evolution of electrode response to potential scan: scan range, +0.3 to -1.3 V; scan number indicated; solution composition, 0.05 M PdCl_2 + 0.3 M LiCl in D_2O . (a) Initial stage: scan numbers 7–9. (b) Scan numbers 12–15.

number, while peak C remains a single peak (Figs. 3(a) and 3(b)). Furthermore, at high Pd²⁺ ion concentration, D is a single peak. It is noteworthy that at both high and low Pd²⁺ ion concentrations peak D shifts to more negative potentials during cycling and that the separation between peaks C and D decreases with increasing Pd²⁺ ion concentration.

4. QUALITATIVE INTERPRETATION OF VOLTAMMOGRAMS

In an attempt to determine the sequence of events and the magnitude of the processes associated with the codeposition of the Pd + D alloy via slow scan voltammetry, we assume that each partial current I_n in eqn. (2) is given by

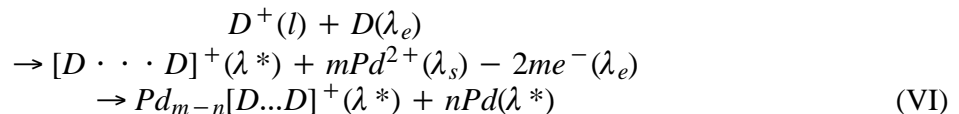
$$\frac{I_n}{A(t)} = F \left[\sum_n D_n z_n \frac{\partial c_u}{\partial x} + \sum_m \Gamma_m \frac{d\theta_m}{dt} \right] \quad (3)$$

where $A(t)$ is the area of the charge transfer plane and Γ_m is the number of sites available for adsorption. The other symbols have their usual meaning. The first term on the righthand side represents the contribution due to diffusion while the second term is attributed to adsorption processes. The interpretation of the voltammograms is aided by Fig. 1, where the current–potential relations are superimposed upon the Pourbaix diagram for the E–H₂O system (the E–D₂O system is only slightly different). Owing to the low concentration of Pd²⁺ ions and the slow potential scan, I_1 is assumed to be diffusion limited. Hence the first term on the righthand side of eqn. (3) can be regarded as a constant. Consequently, changes in the magnitude of current I are due to changes in surface coverage. Additionally, the shape of the voltammograms is affected primarily by the kinetics of adsorption. As indicated by eqns. (II)–(V) and discussed in ref. 5, the dependence of surface coverage on the electrode potential is complex.

In the context of Fig. 1, if $E_{0,2} < E < E_{0,1}$ only the reduction of Pd²⁺ ions is possible. As the electrode potential becomes more negative, i.e. when $E < E_{0,2}$, reduction of D₂O commences with the formation of a Pd + D alloy. The potential–independent cathodic current recorded for the potential range + 0.3 to ca. 0.0 V is in agreement with the assumption that the reduction of Pd²⁺ ions occurs at its limiting rate. Also, the continuous formation of a new surface is evident from the negative shift of the voltammograms.

4.1. Dynamics of the Interphase During Negative Sweep

A more detailed picture of the dynamics of the interphase during Pd + D codeposition is presented in Fig. 5 where the dominant fluxes consistent with the shape of the voltammogram are indicated. In particular, Fig. 5(a) defines specific regions of the potential scan where significant changes occur in the dynamics of the interphase. At equilibrium ($E = E_{eq}$) the composition of the interphase is such as to maintain equality of the chemical potentials with net zero fluxes across all segments of the interphase (Fig. 5(b)). However, as soon as the electrode is polarized, the composition of the interphase changes. In the potential range $E_{0,2} < E < E_{eq}$ the metallic Pd layer is deposited onto the [D ... D]⁺(λ*) interphase



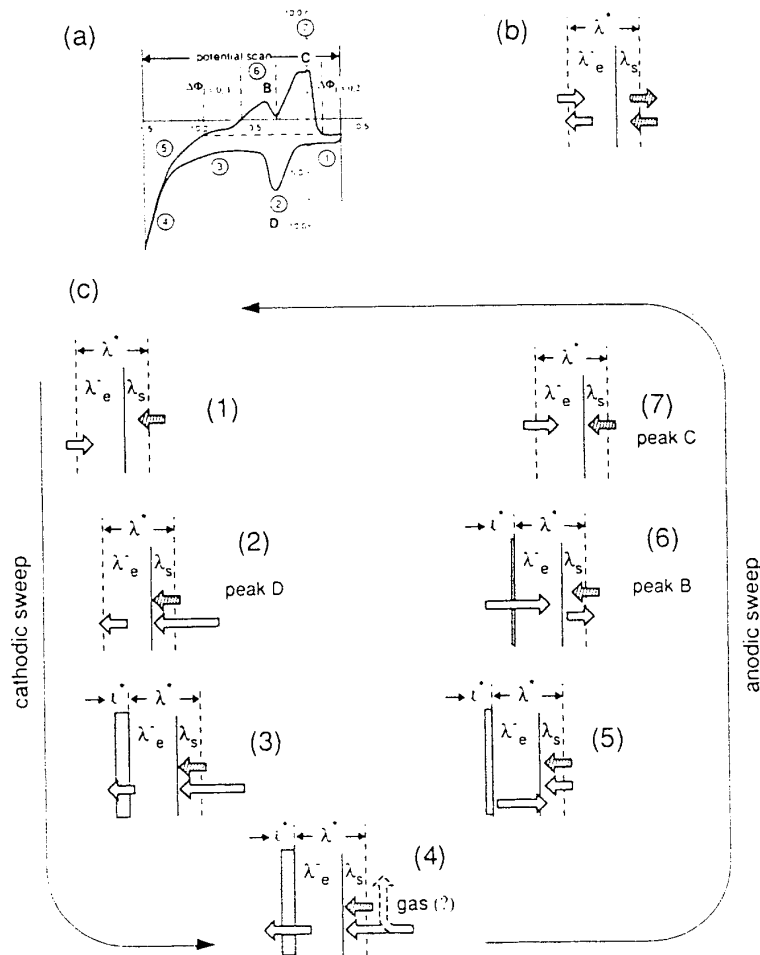
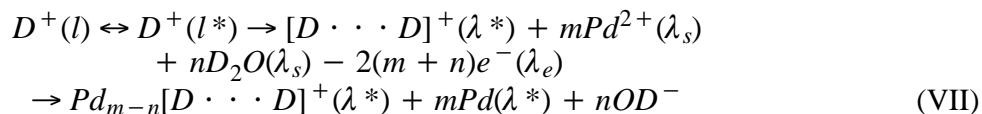


Figure 5. Dynamics of interphase: (a) regions of interest with regard to voltammogram; (b) fluxes and their magnitudes at equilibrium (rest potential); (c) fluxes and their relative magnitudes within regions defined in (a).

which, in turn, disturbs the interphase by redistributing the elements, as indicated by both the direction and length of the arrows in Fig. 5(c(1)). At this stage, the composition of the interphase is controlled by the rate of formation of the metallic layer and the transport of absorbed deuterium D(1) into the λ_e layer of the interphase. The freshly deposited Pd layer further modifies the interphase by restructuring the surface. The electrode response when E is only slightly more negative than $E_{0,2}$ (Fig. 5(c(2))) is of interest. At this point a significant increase in the cathodic current is observed (peak D) which is attributed to the high activity of the freshly prepared Pd layer, probably arising from surface restructuring and the creation of new adsorption sites. A direct consequence of the simultaneous rapid accumulation of sorbed deuterium in the λ_e layer and the deposition of metallic palladium is the formation of a thin layer 1* with a high D/Pd atomic ratio (Fig. 5(c(3))). This layer becomes part of the bulk electrode and represents a barrier for D transport because of the strong dependence of the diffusion coefficient on the D/Pd atomic ratio [8]. Symbolically, this situation is represented by



The overlapping peaks D_1 and D_2 suggests a simultaneous filling of available sites which are energetically slightly different. Significant increases in the number of these sites results in a merging of peaks D_1 and D_2 present at higher Pd^{2+} ion concentration. With further polarization, e.g. when $E \ll E_{0,2}$, the dynamics of the Interphase changes, namely with an increase in the cathodic overpotential, the reaction path for deuterium evolution reaction changes [1,5]. We interpret this to conclude that the expanding electrode surface is saturated with deuterium, the amount of which is determined by the overpotential. Consequently, the excess of adsorbed deuterium may desorb into the gas phase (Fig. 5(c(4))).

4.2. DYNAMICS OF THE INTERPHASE DURING POSITIVE SWEEP

The events occurring on the return sweep, i.e. covering the potential region in the opposite direction, are illustrated in (Figs. 5(c(5))–5(c(7))). On the return sweep, the reduction of Pd^{2+} ions proceeds at the same rate $I_{1,\text{lim}}$, but the total cathodic current becomes less as the potential becomes more positive. In particular, within the potential range $E < E_{1=0,1}$ it is uncertain whether the decrease in cathodic current is due to a lower rate of deuterium generation or the oxidation of sorbed deuterons leaving the interphase region (Fig. 5(c(5))). However, as soon as the potential equals or exceeds $E_{1=0,1}$, i.e. when the cathodic current equals $I_{1,\text{lim}}$, oxidation of adsorbed deuterium commences resulting in peak B, and it terminates at $E_{1=0,2}$ (cf. Figs. 2 and 3). This situation is illustrated in Fig. 5(c(6)) and described symbolically by



This conclusion is supported by the slight displacement noted for higher Pd^{2+} ion concentration, as well as by the slight shift of peak B in the positive direction with increasing number of scans (cf. Figs. 2 and 3). The characteristic features of the voltammograms, namely coalescing and separating peaks (e.g. C and D) due to either scan number or Pd^{2+} ion concentration, reflect the cooperation between the participating processes and the properties of the electrodeposits. The dependence on the scan number enters via the evolution of electrode morphology modifying the local $I-\eta$ distribution while the increased Pd^{2+} ion concentration changes the number of adsorption sites as well as the rate of growth of the Pd + D layer. The presence of energetically different adsorbed deuterium affects the transport across the interphase, resulting in the separation of closely spaced peaks. However, the coalescing of peaks indicates an increase in the concentration of one fraction of energetically different adsorbed deuterium.

It should be noted that, strictly speaking, the term “absorbed deuterium” includes the deuterium present in both the Pd bulk and the interphase λ_e . Furthermore, the Pd absorbed deuterium system results reversibly in the formation of α - and β -PdD. Cyclic voltammetry does not distinguish the processes by which the palladium deuterites are formed or decomposed nor those by which the bulk deuterium is transferred to the interphase region. In our discussion, “absorbed deuterium” refers to the deuterium present in the electrode interphase region. At this time, about all that can be said about the processes occurring within the bulk and at the bulk electrode interphase region is that, during the charging process, deuterium enters the electrode interphase through adsorbed states and then transits the electrode interphase into the bulk. On oxidation, a reverse process occurs in which the bulk absorbed deuterium enters the electrode interphase, subsequently leading to an unloading of the Pd. The mechanisms in Fig. 5(c) describe the processes occurring within the electrode and electrolyte interphase.

5. CONCLUDING REMARKS

(1) The existence of the double peaks C_1 , C_2 on the positive scan and $D1$, $D2$ on the negative scan, observed at low Pd^{2+} ion concentration, and their locations are due to small differences in the respective transfer rates of energetically different adsorbed deuterium.

(2) The disproportionate increase in current at D corresponds to substantial absorption of deuterium by a freshly generated Pd surface. At more negative potentials, while the Pd reduction current continues at its limiting value (the actual current increases above the initial limiting value because of the increasing Pd surface area), the decrease in current indicates the formation of a thin layer I^* which acts as a barrier, slowing the diffusion of interstitials.

REFERENCES

1. S. Szpak, P.A. Mosier-Boss, S.R. Scharber and J.J. Smith, *J. Electroanal. Chem.*, 337 (1992)147,
2. M.F. Bell and J.A. Harrison, *J. Electroanal. Chem.*, 41(1973)15.
3. J.A. Harrison, R.P. Hill and J. Thompson, *J. Electroanal. Chem.*, 47 (1973) 431.
4. J.A. Harrison, H.B. Sierra Alcazar and J. Thompson, *J. Electroanal. Chem.*, 53 (1974)145.
5. S. Szpak, C.J. Gabriel, J.J. Smith and R.J. Nowak. *J. Electroanal. Chem.*, 309(1991)273.
6. J. O'M. Bockris and A.K.N. Reddy, *Modern Electrochemistry*, Vol. II, Plenum Press, New York, 1972, p. 1223.
7. K.M. Gorbunova and Yu.M. Polukarov in C.W. Tobias (Ed.). *Advances in Electrochemistry and Electrochemical Engineering*, Vol. 5, Interscience, New York, 1967.
8. J.O'M. Bockris, D. Hodko and Z. Minevski in T. Bressani, E. Del Giudice and G. Preparata (Eds.), *The Science of Cold Fusion*, Conference Proceedings, Italian Physical Society, Vol. 33, SIF. Bologna, 1991.

THE METAL HYDROGEN SYSTEM: INTERPHASE PARTICIPATION IN H-TRANSPORT

P.A. Mosier-Boss and S. Szpak

Naval Control, Command and Ocean Surveillance Center

RDT&E Division, SanDiego, CA 92152-6171

and

J.J. Smith

US Department of Energy, Washington, DC 20585

ABSTRACT

The metal/hydrogen system is a key element in the construction of ecologically preferred energy conversion/storage devices. Although reduced to practice decades ago, its effectiveness requires further examination of a number of issues, among them the role that the electrode/electrolyte interphase plays during the charging/discharging processes. In this communication the following topics are considered: Thermodynamics and kinetics of the structure of the interphase, the identity and components of the driving force(s) for the absorption/desorption of hydrogen, and the discussion of the applicable transport equation. Agreement between theoretical results and observed behavior is illustrated and selected design approaches affecting cell performance are explored.

INTRODUCTION

With an increased awareness of the environment and how human activities impact the ecosystem, current trends in the development of energy storage systems are to employ more environmentally compatible materials. In particular, recent years have witnessed increased interest and activity in the development of a hydrogen economy, with particular emphasis on using hydrogen as the fuel in energy generating devices, eg, hydrogen/oxygen fuel cells or, more pertinent to this communication, as a component in the negative electrode of the metal/hydrogen (Me/H) rechargeable battery systems.

Although the first intermetallic hydride was developed 30 years ago and despite construction of the first prototype metal hydrogen electrode 20 years ago, Me/H electrodes experience many shortcomings, viz., high cost of alloys, poor hydrogen storage capabilities, difficult activation, pyrophoricity, problems of impurities, thermodynamic instabilities and corrosion in alkaline media. Recent results derived from efforts to address these shortcomings have led to the conclusion that an interphase is an important factor maximizing the cell performance. (Ohnishi et al, 1993; Ciureanu et al, 1993).

In this communication we examine the dynamics of the interphase region as it relates to the performance of Me/H cells. To accomplish this goal, we review the concepts and characteristic features of the Me/H system under nonequilibrium conditions using the Pd/H system as a model.

ME/H SYSTEM: STRUCTURE OF THE INTERPHASE

An interphase region is formed whenever an electrode is in contact with an electrolyte. In the simplest case, the interphase region takes the form of the electrical double layer. In reality, whenever an electrode is in contact with electrolyte, a multilayer interphase region is formed (Defay et al. 1951). This is a non-autonomous region, ie, a region whose properties are affected by the contacting phases. A further important feature of the structure of the interphase is that it is modified by participating processes (van Rysselberghe, 1966).

The origin of surface tension on metals is attributed to auto-diffusion of atoms from the surface to the bulk resulting in lattice contraction of the surface atoms, changes in spacing between atomic layers and polarization effects (Defay et al, 1951). The simplest model of the Pd/H interphase is illustrated in Fig. 1a (Schlapbach, 1991). Here, the Pd surface is in contact with gaseous hydrogen. Following the dissociative adsorption, the Pd surface undergoes a reconstruction process to accommodate adsorbed hydrogen and a redistribution of adsorption sites (Protopopoff and Marcus, 1991). As the concentration of adsorbed hydrogen increases, the physically adsorbed hydrogen penetrates the surface and occupies sites underneath the first atomic layer. This chemisorbed hydrogen promotes a strong surface reconstruction.

When the Pd electrode is in contact with an aqueous electrolyte, a new situation arises. The inclusion of electrolyte modifies the interphase by adding a complex structure on the solution side. In this new situation, hydrogen is brought to the surface by charge transfer reaction and split into two streams: one entering the metal lattice, the other escaping as gaseous hydrogen. The resulting interphase structure is illustrated in Fig. 1b. According to this model, cathodic polarization produces weakly adsorbed hydrogen which is transferred into the Pd lattice by a twostep process: (i) hydrogen entering the interphase $H(a) \rightarrow H(\lambda^*)$ and (ii) transiting into the bulk electrode, $H(\lambda^*) \rightarrow H(b)$. Briefly, in this model, a palladium/electrolyte interphase consists of two sharply defined regions with discontinuous physico-chemical properties (Bucur and Bota, 1983). However, there exists a common adsorption surface in contact with, and affected by, homogeneous solid and liquid phases. This concept was further extended by emphasizing its non-autonomous character (Szpak et al. 1992). In particular, they defined a transfer zone $\lambda^* = \lambda_s + \lambda_e$, where λ_s and λ_e denote those segments of the solid and electrolyte phase that actively participate in, and/or dominate, the transport of hydrogen between the latter, Fig. 1c (Szpak et al. 1994). By splitting the interphase into several distinct layers, it is possible to identify processes that control the transport of hydrogen during the potential sweep and to examine the effect of electrolyte composition and electrode surface morphology on that transport. These observations lead to tentative conclusions that the structure and properties of the λ^* part of the interphase are potential dependent. Also, it is apparent from the behavior of the current/potential (j/η) curves generated by slow scan voltammetry that the interphase region contains positively charged species, perhaps the $[H...H]^+$ complex proposed by Horiuti and subject of a spirited discussion between Horiuti and Bockris (Horiuti, 1961). Curiously, there is a degree of similarity with the solid/gas system where three energetically different states of hydrogen exist (Auer and Grabke, 1974).

DYNAMICS OF THE INTERPHASE

The question that arises naturally: Is the interphase an active element in the course of hydrogen transport across it? The answer is yes. Furthermore, if an analogy to the behavior of a thoroughly investigated liquid/liquid interphase can be invoked, then the review of the latter would be helpful in guiding the discussion concerning the dynamics of hydrogen transport. The use of this analogy seems natural inasmuch as the solid/liquid interphase is also a system under tension as indicated by, eg, the lattice contraction/extension following adsorption (Lennard-Jones and Dent, 1928). The evidence indicates that, in all systems the dynamic character of the interphase is driven by the energetics associated with the transport itself.

Taking as a common starting point that a surface separating two phases can be visualized as a membrane in tension or compression, we can examine its behavior under any prescribed set of events. For example, at low concentration of transported species, the rate of transport in liquid/liquid systems varies with time in a manner resembling a pumping action of the interphase (Szpak, 1961). This action clearly identifies the interfacial region as a separate phase and indicates that time-dependent driving forces act upon the transported species. As the concentration of the material at the interphase

increases, the pumping action is often transformed into violent eruptions (Nassenstein and Kraus, 1956). Violent eruptions are associated with rapid release of stored energy, again identifying the interphase as a kind of interfacial engine, a term coined by Sternling and Scriven (1959) while discussing instabilities arising from small temperature or concentration fluctuations accompanying the transport of a substance between two immiscible phases. Clearly, the interphase region constitutes an active element whose activity can be modified by a number of factors, all being the manifestation of changes in the energy content of the interphase.

HYDROGEN SORPTION IN ELECTROCHEMICAL SYSTEMS

The examination of the role of the interphase is facilitated by an experimental arrangement where the surface to volume ratio is maximized, as illustrated in Fig. 2, and where the effect of surface morphology is clearly displayed. This requirement can be satisfied by employing palladium black (Chevillot et al. 1975) or by a codeposition process whereby palladium is electroplated from aqueous solution in the presence of evolving hydrogen (Szpak et al. 1992).

The interphase dynamics is particularly well displayed by slow scan voltammetry of the codeposition process. During the charge transfer the interphase region is an open system in which a number of consecutive processes takes place. These processes include transport of the reactants from the bulk to the electrode surface by diffusion, adsorption on the electrode surface, charge transfer and desorption of the reaction products followed by transport of reaction products away from the electrode surface. In a discharging battery, the same processes occur; however, in a battery the electrons ultimately flow into an external circuit where the electrical work is delivered. The dynamics of the codeposition process is best discussed by considering Fig. 3 which is the schematic representation of the superposition of the j_n/η ; $n = 1, 2$ relation of partial currents upon a portion of a Pourbaix diagram indicating thermodynamic stability of water. The driving force for each partial charge transfer reaction is given by $(\Delta\Phi - \Delta\Phi_{0,n})$ where $\Delta\Phi$ is the Galvani potential difference and $\Delta\Phi_{0,n}$'s are the respective equilibrium potentials. Here, we assume independent charge transfer reactions and ignore the small shift in the Galvani potential difference associated with the alloy formation (Gorbunova and Polukarov, 1967).

A detailed picture of the dynamics of the interphase during the codeposition is presented in Fig. 4, where the dominant fluxes consistent with the voltammogram shape are indicated. At equilibrium, the composition of the interphase is such as to maintain equality of chemical potentials resulting in no net flux across all segments of the interphase. However, as soon as the electrode is polarized, the composition of the interphase changes, as indicated by the magnitude and direction of transported species, solid arrows for the $\text{Pd}^{2+} + 2e^- \rightarrow \text{Pd}$ reaction, and open arrows for the hydrogen flux. The electrodeposition of metallic palladium at the diffusion limited rate occurs throughout the potential span investigated, cf. Fig. 3. In particular, upon initiation of the cathodic sweep, Fig. 4 segment 1, only the reduction of Pd^{2+} ions occurs. Within this potential range, only the hydrogen present in the bulk electrode can enter the interphase region, specifically the λ_s part of the interphase. The situation changes abruptly at point D where the hydrogen sorption is rapid. At this point a significant increase in cathodic current is observed which is attributed to the high activity of the freshly prepared Pd layer arising, most likely, from surface restructuring and the creation of new adsorption sites. At more negative potentials, Fig. 4, segment 3, sorption into the freshly formed palladium layer is fast while slower transport by diffusion into the bulk initiates the formation of a resistive (supercharged) layer, I^* . A direct consequence of the simultaneous rapid accumulation of sorbed hydrogen in the λ_s -layer and the deposition of metallic Pd is the formation of thin layer, I^* , having a high H/Pd ratio. This layer becomes part of the bulk electrode and represents a barrier for H transport due to the strong dependence of the diffusion coefficient on the H/Pd atomic ratio. As the cathodic polarization is

increased, the resistive layer increases the hydrogen concentration in the interphase to the point where the Tafel recombination is the dominant reaction, Fig.4, segment 4.

Upon scan reversal the interphase behaves as follows: Immediately after scan reversal, Fig. 4 segment 5, the partial current j_2 becomes less while j_1 remains at its limiting value. This change in ratio results in thinning of the supercharged region. With further increase in the electrode potential, the cathodic current becomes less than $j_{1,lim}$ indicating reversal of j_2 due to the oxidation of the weakly adsorbed hydrogen, Fig. 4 segment 6, followed by the oxidation of strongly adsorbed hydrogen, Fig. 4 segment 7.

The slow scan voltammetry indicates that the oxidation of weakly and strongly adsorbed species is independent of each other which means that the transition between these species is slow and that hydrogen diffusion into the bulk electrode occurs after a complete saturation of the surface. Structurally, this means that the interaction of screened protons modifies the potential field near metallic ions, and the repelling action tends to dilate the crystal structure. To a first approximation, this effect is proportional to the coefficient of compressibility of the metal. The dilation of structure propagates in the whole volume of palladium beginning at the surface (Chevillot et al. 1975).

TRANSPORT IN BULK PHASES

Because of the non-autonomous character of the interphase, its activity cannot be separated from activities of the contacting phases. Here, the effect of transport in the electrolyte phase is of lesser interest for two reasons: (i) The concentration of reactant (H_2O molecules) generating hydrogen on the electrode surface is sufficiently high so that mass transport is irrelevant and (ii) the hydrogen surface coverage is controlled by charge transfer kinetics. However, the effect of surface active additives affecting the kinetics of adsorption must be included. On the other hand, transport of absorbed hydrogen as well as the components of the driving force acting within the bulk electrode, are of considerable interest. Thus, a detailed examination of the driving forces operating within the bulk electrode is essential.

To assist in the analysis of the mutual interaction between the interphase and the bulk, we first review the structural aspects of the solid phase. In general, defects in metals that affect hydrogen transport are: point defects, solute defect complexes, dislocations and internal boundaries and isolated metal clusters. The simplest point defect is the vacancy, ie, an empty lattice space. A strong interaction (attraction) exists between the interstitial hydrogen and the open-volume character of the defect, that is, the interstitial hydrogen is driven into the vacancy by the presence of the open-volume. The binding energy is similar to that of chemisorbed hydrogen.

The interaction of hydrogen with solute and solute-defect complexes is weaker than with vacancies. The strength of interaction is influenced by elastic distortion and by electronic differences in H-bonding between the host and impurity atoms. The open-volume effects produced by the lattice strain are less than those generated by vacancies thus resulting in weaker interactions. As the H atom approaches the dislocation, the binding energy changes. Mobility of interstitial H atoms is reduced by attractive interactions with dislocations. The interaction between internal boundaries and interstitial hydrogen are of special interest. In fully metallic boundaries, the binding energies are much less than for vacancy trapping. The smallness of interaction is related to the absence of open-volume defects on these boundaries. However, if the boundary contains a non-metallic phase which tends to form a covalent bond to the H atom, the situation is different; the binding energy is substantially higher. In addition, the boundary plays another role: it provides paths for accelerated diffusion. The accelerated diffusion is ascribed to a reduced vacancy formation in the excess volume of the boundary. Note that

the diffusion of interstitial H does not depend on vacancies; thus, the acceleration of diffusion may be related to the reduction of saddle-point energies at the boundaries. The acceleration of diffusion at higher concentration may be due to saturation of deep trapping. There is an indication that small metal clusters (on the order of 40 atoms) can trap as many as eight H atoms per metal atom. For clusters containing more than 40 atoms, the behavior is that of metallic phase (Cox et al. 1990).

MODELING

From a practical point of view two factors are of interest while designing a Me/H system, viz., the amount of stored hydrogen and the rate at which it can be moved between phases. In general, when modeling a charging/discharging cell, one must take into account the material balance, Faraday's law, Ohm's law and the polarization equation (Szpak, 1991). When modeling the Me/H system, we also have to include the effect of the interphase and hydrogen transport between, and within, particles making up the porous structure of the Me/H electrode. The latter effect will be described by the form of the auxiliary equations.

The development of a general model is not a trivial undertaking since charging/discharging of a metal hydride is a very complicated process. To illustrate, we consider the electrochemical charging of Pd rods, recently a topic of considerable interest. A model has been developed that incorporates the essential features of these processes and involves variables such as the electrochemical rate constants, the bulk diffusion coefficient and the charging current (Szpak et al. 1991). This simplified model predicts rather well the experimentally observed behavior of the charging of the palladium rods (Riley et al. 1992). The data show a number of characteristic features during charging, among them (i) the existence of an apparent threshold value for the cathodic current density; (ii) a slower rate for "unloading" than for "loading" the bulk electrode; and (iii) an initial charging rate that depends, for the most part, inversely on the radius of the Pd electrode. These features, in turn, imply the following: (i) cell current density controls the mode of charging/discharging; (ii) directional transport across the interphase—an unlikely situation for a passive interphase and diffusion control; and (iii) importance of geometrical considerations.

The difference in the loading and unloading rates and the incompleteness of unloading provide additional evidence for active participation of the interphase. The observed asymmetry is inconsistent with the linear-diffusion model because such a model would be analogous to ordinary diffusion with constant initial bulk concentration. Evidently, there exists a mechanism(s) that causes the adsorbed hydrogen to affect the loading and unloading rates differently. If we assign an active role to the interphase then a mechanism suggested by the slow scan voltammetry is provided. In particular, the force driving hydrogen across the interphase contains a contribution due to the electrode overpotential, affecting the λ_e layer, as well as contributions involving the electronic and mechanical interactions, influencing the λ_s part. Upon current reversal, the magnitude of the driving force is different and the asymmetry follows naturally. The transition between the diffusion and surface control, accounting for the observed difference in the mode of charging/discharging, occurs within the practical range of current densities.

Electrochemical charging of Pd electrodes involves coupling of interfacial processes with transport of interstitials in the electrode interior. Obviously, boundary conditions arise from the solution of equations governing the elementary adsorption-desorption and adsorption-absorption steps and the symmetry of the electrode. The active participation of the interphase manifests itself as inhomogeneous changes in surface morphology during prolonged exposure to evolving hydrogen. One way to demonstrate the inhomogeneity of the surface, particularly with respect to absorption, is to view the surface using Nomarski optics (Szpak et al. 1991). Such an inhomogeneity can be viewed as time

dependent boundary conditions and, if combined with the concentration dependent diffusion coefficient, may lead to the formation of space structures (metastable regions) localized near the surface (Samgin et al. 1992).

A more complete model would include: conservation of energy from which the temperature distribution is determined; and recognition that the interphase constitutes an active, non-autonomous element in the transport of hydrogen. Thus, the Me/H model will have to include the effects of a changing interphase as well as the effects of electrode matrix and grain boundaries. The electrode matrix refers to the porous electrode structure while the grain boundaries refer to the metallurgical aspects within individual particles. The appropriate equations would have to be formulated to include coupling of the electrode–electrolyte processes within a multiphase environment while the transport within the individual particles would have to consider the presence of grain boundaries (Zeschmar, 1983).

CLOSING REMARKS

Models are used both, to simulate a complex reality by simpler arrangements and to display essential features of a physical system. Often, a simple model clarifies the interpretation of ambiguous data and avoids lengthy calculations that might be irrelevant to the problem being examined. We have applied a model where the structure of the interphase, as well as the operating driving forces, are determined by participating processes occurring in both contacting phases. We have treated the interphase as a passive element by assuming that the surface is homogeneous with respect to the chemical potential. Such an assumption is not realistic although it might be justified on the basis of the existence of the supercharged layer, I^* . Even so, this relatively simple model does remarkably well in predicting a saturation of the initial charging rate as well as the time required to obtain a full charge. Although this model predicts some small asymmetry in loading and unloading, it does not predict the magnitude of the asymmetry and it cannot account for the incomplete electrode unloading. Evidently, a more comprehensive model must be formulated that would provide mechanisms for asymmetric loading/unloading and to specify conditions leading to reproducible charging/discharging.

A final remark: The fundamental characteristics of the Me/H system are (i) uniqueness in electronic structure; (ii) binding sites of H atoms and their relationship to binding energy; (iii) sensitivity of interactions to cluster size; (iv) the question whether the most active sites are in an excited state or in the ground state. The Pd/H system is a system with strong proton lattice coupling and weak H-H repulsive forces.

ACKNOWLEDGEMENT

This work was supported, in part, by the Office of Naval Research and, in part, by the Naval Command, Control and Ocean Surveillance Center, RDT&E Division Exploratory Development Program.

REFERENCES

- Auer, W. & Grabke, H.J. (1974) *Ber. Bunsenges.*, **78**, 58
- Chevillot, J.-P., Farcy, J., Hinnen, C. & Rousseau, A. (1975) *J. Electroanal. Chem.*, **64**, 39
- Ciureanu, M., Strom-Olsen, J.O., Ryan, D.H., Rudkowski, P. & Rudkowska, G. (1993) 184th Electrochemical Society Meeting, New Orleans LA
- Cox, D., Farget, P., Brickman, R., Hahn, M.Y. & Keldor, R. (1990) *Catal. Lett.*, **4**, 271

- Defay, R., Prigogine, I. & Bellemans, A. (1951) **Surface Tension and Adsorption**, Longmans, Green & Co, Ltd.,
London W1,
- Gorbunova, K.M. & Polukarov, Yu. M. (1967) Electrodeposition of Alloys, in **Advances in Electrochemistry**, Ch.W. Tobias, ed., vol. 5, Interscience Publishers, 1967
- Horiuti, J (1961) The Mechanism of the Hydrogen Electrode, in **Transactions of the Symposium on Electrode Processes**, chapter 2, J. Wiley & Sons, Inc., New York - London
- Lennard-Jones, J.E. & Dent, B.M. (1928) Proc. Roy. Soc., **A 121**, 247
- Nassenstein, H. & Kraus, W. (1956) Chem.-Ing. Technik, **28**,220
- Ohnishi, M., Matsumura, Y., Kuzuhara, M., Watada, M. & Oshitani, M. (1993) 184 th Electrochemical Society Meeting, New Orleans, LA
- Protopopoff, E. & Marcus, P. (1991) J. Chim. Phys., **88**, 1423
- Riley, A.M., Seader, J.D., Pershing, D.W. & Walling, C. (1992) J. Electrochem. Soc., **139**, 1342
- van Rysselberghe, P. (1966) Some Aspects of Thermodynamic Structure of Electrochemistry, in **Modern Aspects of Electrochemistry**, vol. IV, J.O'M. Bockris, ed., Plenum Press, New York
- Samgin, A.L., Tsidlikovski, V.I. & Baraboshkin, A.N., The Third International Conference on Cold Fusion, Poster 22-P-4
- Schlapbach, L. (1991) Hydrogen and its Isotopes in and on Metals, in **The Science of Cold Fusion**, A. Volta Center for Scientific Culture, Como, Italy,
- Sterling, C.V. & Scriven, L.E. (1959) A.I.Ch.E. J., **5**,514
- Szpak, S. (1961) **Dissertation**, University of Pennsylvania
- Szpak, S. (1991) Experimental Simulation of Porous Electrodes, in **Techniques for Characterization of Electrodes and Electrochemical Processes**, chapter 14, J. Wiley & Sons, Inc., New York
- Szpak, S., Gabriel, C.J., Smith, J.J. & Nowak, R.J. (1991) J. Electroanal. Chem., **309**, 273
- Szpak, S., Mosier-Boss, P.A., Scharber, S.R. & Smith, J.J. (1992) J. Electroanal. Chem., **337**, 147
- Szpak, S., Mosier-Boss, P.A., Gabriel, C.J. & Smith, J.J. (1994) J. Electroanal. Chem., **365**, 275
- Zeaschmar, G. (1983) J. Applied Phys., **54**, 2281

FIGURE CAPTIONS

Fig. 1 - Concepts of the metal/hydrogen(water) interphase

Fig. 1a - The Pd/H₂(g) system. A simplified model of the Pd/H₂(g) interphase and associated processes: (i) dissociation of molecular hydrogen and solution of H atoms in the bulk on the interstitial sites (after Schlapbach, 1991)

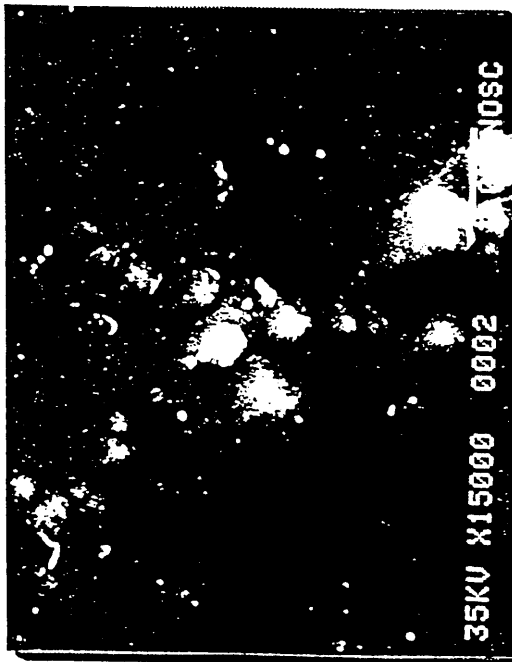
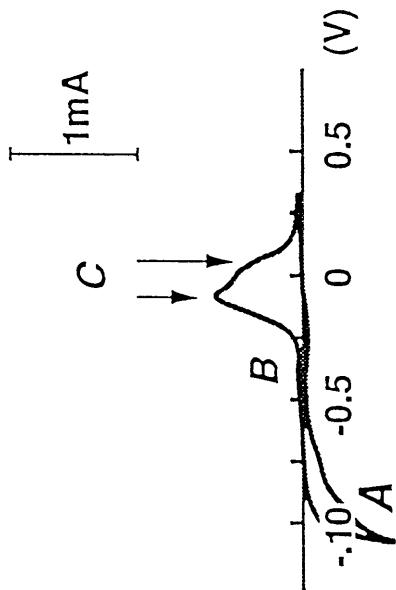
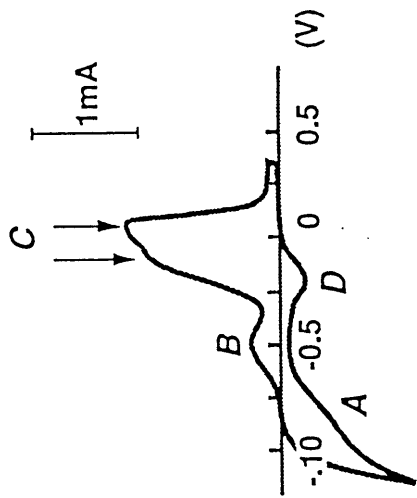
Fig. 1b - The Pd/H₂O system. A model illustrating partial steps of the overall H⁺/H redox reaction and H absorption (after Bucur and Bota, 1983)

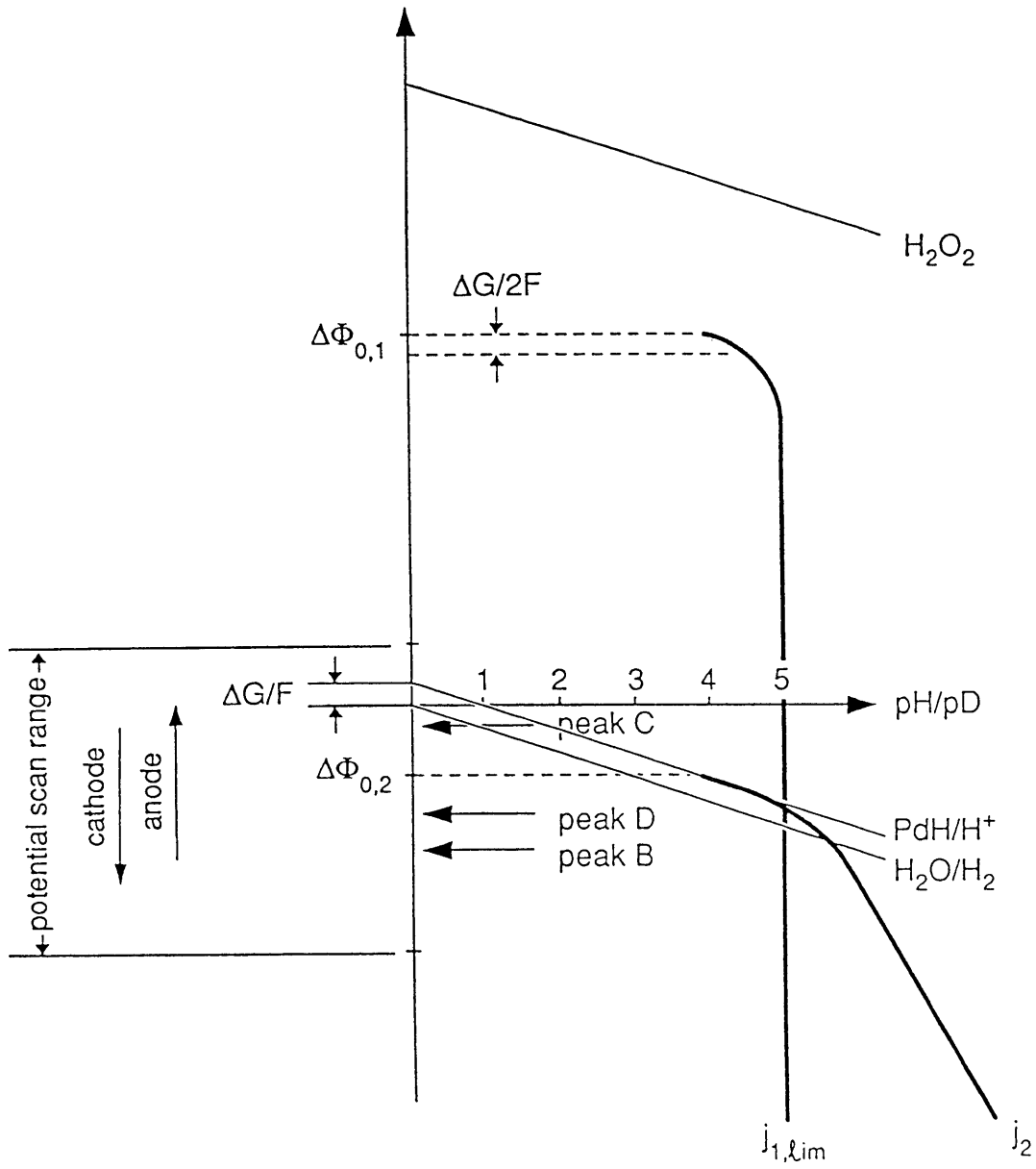
Fig. 1c - The Pd/H₂O system. A model illustrating the complexity of the interphase; a - adsorption layer; t - charge transfer layer; e - surface dividing the interphase and the bulk electrode; l - lattice; j - total cell current; H • H - Heyrovsky-Horiuti path; T - Tafel path; V - Volmer path; j₄ and j₋₄ - adsorbed/absorbed exchange fluxes; λ* - non- autonomous interphase region (after Szpak et al. 1994)

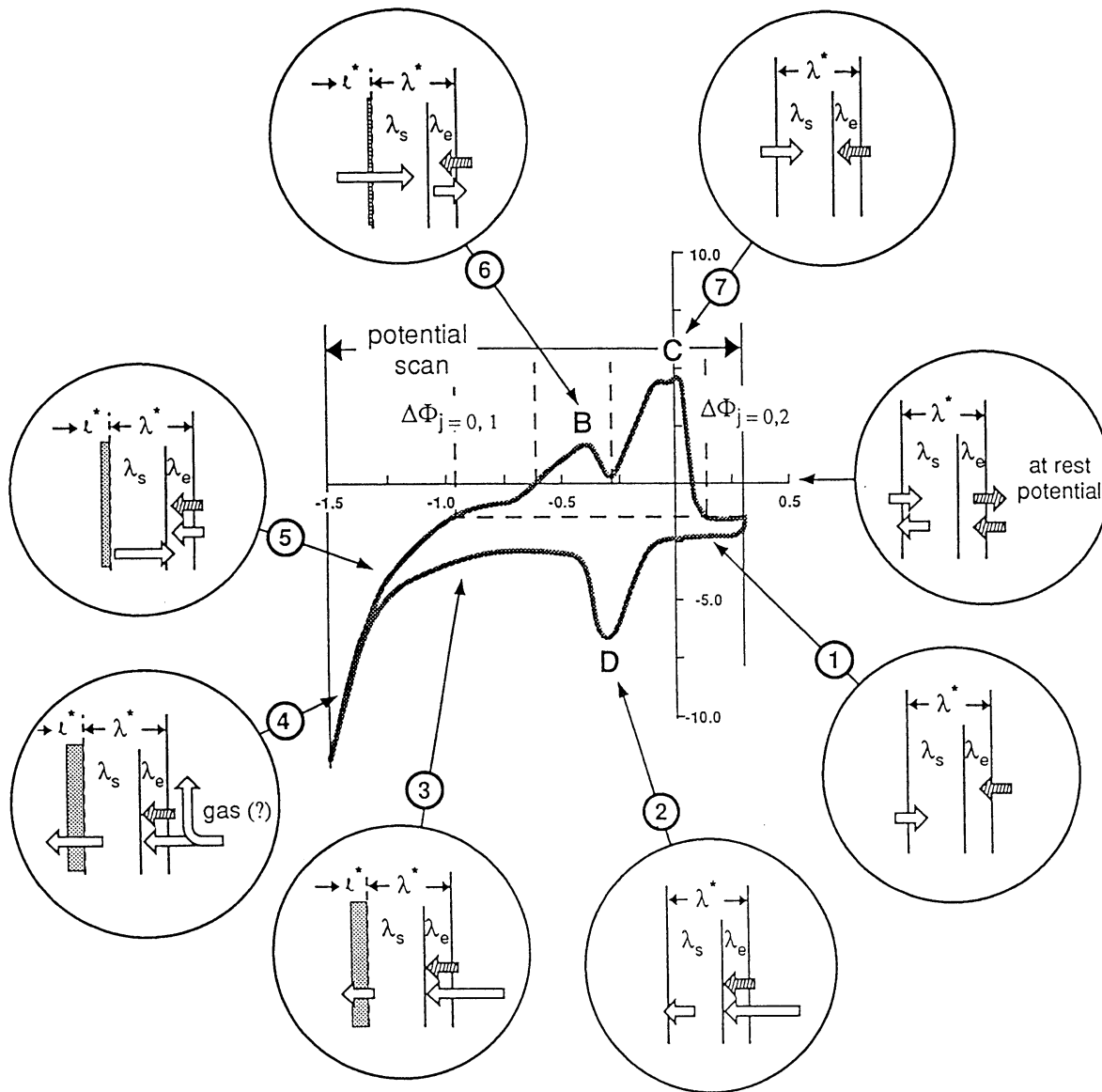
Fig. 2 - Scanning electron micrographs of palladium surface and corresponding voltammograms on smooth and palladized surfaces.

Fig. 3 - Representation of processes associated with Pd-H codeposition. Potential scan range and partial currents are superimposed on the Pourbaix diagram for the H₂O – H₂ system. (j_{1,lim} refers to the rate of Pd²⁺ ion reduction and j₂ is a measure of H₂ generation (after Szpak et al. 1994)

Fig. 4 - Dynamics of the Pd/H₂O interphase. Fluxes and their magnitude within regions defined in voltammogram.







ON THE BEHAVIOR OF THE Pd/D SYSTEM: EVIDENCE FOR TRITIUM PRODUCTION

S. Szpak, P.A. Mosier-Boss,¹ and R.D. Boss

Naval Command, Control and Ocean Surveillance Center RDT & E Division San Diego,
CA 92152 - 5000

and

J.J. Smith

Department of Energy, Washington, DC 20585

ABSTRACT

Evidence for tritium production in the *Pd/D* system under cathodic polarization is presented. A comparison of the observed distribution and that calculated, based upon the conservation of mass, leads to the conclusion that tritium is produced sporadically at an estimated rate of ca 10^3 – 10^4 atoms per second. The results of several runs are interpreted by employing the concept of an electrode/electrolyte interphase and the accepted kinetics of hydrogen evolution. Observation of burst-like events followed by longer periods of inactivity yield poor reproducibility when distributions are averaged over the total time of electrolysis.

1.0 INTRODUCTION

An early report on the behavior of the *Pd/D*- system, with atomic ratio $[D]/[Pd] > 0.8$, suggested that fusion of deuterium atoms occurs within the *Pd*- lattice when the system is under prolonged cathodic polarization(1). Among the observed behavior attributed to nuclear events, is the production of tritium which, for a number of reasons, appears to be an appropriate topic for investigation: First, a half century ago Oliphant *et al.*(2) reported that transmutation of deuterium into tritium and hydrogen occurs when a perdeutero inorganic compound, *e.g.*, $(ND_4)_2SO_4$, is bombarded with low energy deuterons. Second, a theoretical treatment concerning the occurrence of nuclear events when deuterium is electrochemically compressed in condensed matter indicate that tritium production can arise from *d-d* reaction in which the excited state of 4He decays into $t + p$ (3). Third, by simple mass balance arguments, low rate production of tritium has been reported by, among others(4), Will *et al.* (5) whose closed cell measurements make a compelling argument for excess tritium as a product of electrolysis. Finally, the analytical methods for the determination of tritium content are now well developed.

Below, we present data on tritium content and its distribution recorded in the course of electrolysis, in closed systems, of heavy water containing low level amounts of tritium. Our conclusions are based on the applicability of a model that was constructed before the present controversy evolved(6). In the course of charging the *Pd*- lattice with electrochemically generated deuterium, we have observed periods of detectable production of tritium. These periods occur sporadically and appear to be controlled, to a degree, by the structure of the interphase.

2.0 EXPERIMENTAL

The experimental procedure employed follows closely that described previously(7). Here, we provide a short summary of cell design and operation, analytical method for tritium analysis, including error estimates, and rationale for the manner in which the data are presented. We report data obtained from two sets of experiments, *viz.*, (i) electrolyte–gas phase tritium distribution recorded at about

¹author to whom correspondence should be addressed.

24 hour intervals with intermittent electrolyte additions using an arbitrarily selected cell current profile and (ii) a three-phase distribution occurring within the time period required to reduce the initial volume of electrolyte by half at *a priori* selected constant cell current.

2.1 Electrolytic Cell; Current Profile

The electrochemical cell and recombiner are shown in Fig. 1. Each cell, with graduated wall to provide an additional check on the volume of electrolyte, was connected to a recombiner containing a catalyst (supplied by Ciner, Inc.) of sufficiently large surface area, (*ca* 100 cm²), to assure nearly complete recombination of evolving gases. The working *Pd*- electrode was prepared as follows: a *ca* 3.0 cm² *Cu*- foil was wrapped around a glass rod, Fig. 1 – insert. Onto this foil a thin film of *Ag* was deposited from a cyanide bath. Although both metals act as an effective barrier for deuterium penetration, silver was added to provide a far better lattice match with the electrodeposited *Pd*- layer. The *Pd*- electrodes of two vastly different surface morphologies were prepared; one with a smooth surface by deposition from a *Pd*(*NH*₃)₂*Cl*₂ – *H*₂*O* solution at low current densities followed by drying prior to use, and the second with a mossy (dendritic) surface by electrodeposition from a *PdCl*₂ – *LiCl* – *D*₂*O* solution in the presence of evolving deuterium. The placement of the counter electrode, made of a tightly coiled *Pt* wire, assured uniform current distribution on the working electrode. The cells were assembled in a dry box containing argon atmosphere.

The electrochemical charging of the *Pd*- electrodes was under galvanostatic control by a power source delivering constant current with 0.1 % ripple (EC & C Par model 363 potentiostat/galvanostat). The composition of electrolyte employed during charging is given in the respective figure captions. To increase the detection sensitivity, only heavy water with low tritium content, *ca* 19 dpm/ml (supplied by Isotec, Inc.), was used.

2.2 Sampling Procedure; Tritium Analysis

The sampling procedure is illustrated in Fig. 2. A known volume of electrolyte and tritium content, $V(t_1)$, is electrolyzed at a constant cell current, i , for a period of $\Delta t = t_2 - t_1$. During this time period the electrolyte volume is reduced by $V_e(t_2) = iM_w\Delta t/2F\rho$. At time t_2 , a sample is withdrawn, further reducing the electrolyte volume by V_s . Typically, immediately after sampling, the electrolyte volume is restored by addition of the electrolyte in the amount of $V_a(t_3) = 2V_s + V_e$. After a few minutes (to allow for mixing) a second sample, $V_s(t_4)$, is removed for tritium analysis. Removal of a second sample, following the electrolyte addition, assures that the electrolyte volume and tritium content are accurately known at the beginning of the next time interval. The sampling and addition procedures were carried out without the interruption of the cell current flow. Occasionally samples were removed without electrolyte addition.

Tritium content of the samples was measured by a liquid scintillation technique. In particular, 1 ml of sample is added to 10 ml of Fischer Scientific ScintiVerse E Universal LSC cocktail in a borosilicate vial. The prepared solutions were counted for 600 min in a Beckman LS 6000 LL scintillation counter. This instrument reports counts per minute (cpm) and disintegration per minute (dpm) with a 2 σ error. To eliminate interference from chemiluminescence, all electrolyte samples were distilled to dryness and the distillate was analyzed for tritium content. Samples collected in the recombiner required no pretreatment.

The determination of the tritium content in the working *Pd*- electrode is a two-step procedure, namely the transfer of sorbed tritium into a liquid phase followed by scintillation counting. Two methods were employed to accomplish this transfer: (i) by anodic oxidation of sorbed tritium and

(ii) by the method described by Will *et al.* (5) involving the dissolution of the *Pd*- electrode in *aqua regia*. In the first case, the working electrode, while under cathodic overpotential, was rinsed by flushing the cell with $NaCl - H_2O$ solution to remove all D_2O containing tritium and placing it under the anodic overpotential of +0.5 V vs *Ag/AgCl* reference. In the second case, the *Pd*- electrode was dissolved in *aqua regia* and neutralized with $CaCO_3$. As with the electrolyte samples, the resultant solutions from both treatments were distilled to dryness, followed by scintillation counting of the distillate.

Error analysis included the assessment of the precision of measurements in (i) electrolyte volume, (ii) sampling/addition time intervals, (iii) constancy of cell current and (iv) tritium analysis. On the basis of an extensive investigation(7), we concluded that the largest error, as indicated by the instrument readout and determined by standard procedures, is in the tritium analysis. The typical error of 1.2 dpm is not the statistical error of counting but the cumulative uncertainty due to the propagation of error determined by a procedure commonly employed in the presentation of experimental data.

2.3 Intrapphase Tritium Distribution

In the presentation of data and the subsequent analysis, we assume the validity of the model of the electrode-electrolyte interphase subject to restrictive conditions, of which one is the constancy of the isotopic separation factor. As shown in (7), the time dependence of tritium content in an open cell, operating galvanostatically with intermittent sampling, is given by Eq. (1)

$$f(t) = [m(0) - r(i)t]^{s-1} \left[\frac{f(0)}{m(0)^{s-1}} + \int_0^t \frac{q(t)}{[m(0) - r(i)t]^s} dt \right] \quad (1)$$

which, for $q(t) = const \neq 0$, we have Eq. (2)

$$f(t) = f(0) \left(\frac{m(0) - r(i)t}{m(0)} \right)^{s-1} + \frac{q}{(s-1)r(i)} \cdot \left\{ 1 - \left[\frac{m(0) - r(i)t}{m(0)} \right]^{s-1} \right\} \quad (2)$$

while, for $q(t) = 0$ it reduces to Eq. (3)

$$f(t) = f(0) \left(\frac{m(0) - r(i)t}{m(0)} \right)^{s-1} \quad (3)$$

where, f is the tritium mass fraction, m is the mass of the electrolyte phase, $r(i) = iM_w/2\mathcal{F}$ denotes the rate of change associated with the passage of cell current i , q is the rate at which tritium is added/removed from the solution phase by whatever process including transport of tritium generated in the bulk electrode, and s is the isotopic separation factor. The isotopic separation factor is defined here as $s = \left(\frac{c_T}{c_D} \right)_g / \left(\frac{c_T}{c_D} \right)_l$ and should be inverted to conform to values usually cited in the literature. A thorough discussion of the derivation of the above equations can be found in (7).

3.0 DISCUSSION

The long term electrolysis in open cells, with accompanying addition and removal of electrolyte, makes the determination of tritium production by total mass balance an unsuitable technique. This is especially true, should the tritium production be either low level or intermittent, due to the

propagation of error. We believe that a more appropriate procedure is based on the employment of the separation factor derived from the experimentally determined tritium content in both liquid and gaseous phases. Assuming that the Faraday law is obeyed, the ratio c_T/c_D in the gas phase is equal to the ratio of the corresponding faradaic currents, i_T/i_D , and tritium production is indicated by the difference between the calculated and observed data. In what follows, we examine the structure of the interphase, the origin and constancy of the isotopic separation factor and provide an interpretation of experimental data.

3.1 Structure of the Interphase; Transport Paths

The thermodynamic structure of the electrode/electrolyte interphase was formulated by van Rysselberghe(8). For the present purpose, we include the metal side and indicate only the relevant processes that influence the magnitude as well as the constancy of the isotopic separation factor, Figs. 3a – 3c. Irrespective of the operating rate determining step, species undergoing electroreduction, $c_m^{(r)}$; $m = D_2O, DTO$, are in equilibrium with those in the bulk (b) electrolyte, *i.e.*, $c_m^{(r)} \leftrightarrow c_m^{(b)}$. Superscript (*r*) refers to the location where the reactive species affect the rate through their electrochemical potentials, the *r*- plane, Fig. 3a. The reaction product, in an adsorbed state, $c_m^{(a)}$, is in equilibrium with those dissolved in the electrolyte, $c_m^{(b)}$, and when its solubility limit is exceeded, gas bubbles, which also are in equilibrium with the bulk electrolyte, are formed. The set of restrictive conditions that assures the constancy of the separation factor is: (i) evolution reaction of hydrogen isotopes is independent of each other, *i.e.*, $i = i_D + i_T$; (ii) sufficiently high overpotentials are applied so that the reverse reactions may be neglected; and (iii) system operates in a stationary state, *i.e.*, equilibria between various species are established resulting in $d\theta_m/dt = 0$ (9). Under these conditions, the tritium distribution occurs *via* path **A** whereby the cell current *i* is divided into i_T and i_D and the hydrogen evolves from the electrolyte phase at the *n*- plane.

For the deuterium absorbing electrode material, the concept of the interphase must be extended to include the metal side as indicated in Figs, 3b and 3c by λ . If tritium is produced within the bulk electrode and transferred to the electrolyte phase, it must be first brought to the adsorption plane (*a*- plane). The constancy of the *s*- factor requires an equilibrium condition between species located within the interphase while the applicability of Eqs. (1) – (3) demands that all tritium bearing species first enter the electrolyte phase, *i.e.*, follow path **A**, Fig. 3b. The latter condition requires the presence of a charged nH ; $n = 1,2,3$ species in the λ - layer that interacts with the OD^- ion. The existence of such species, *e.g.*, $[T \cdots T]^+$, $[D \cdots T]^+$, $[D \cdots D]^+$, was postulated in our recent publication(10). If, however, the conditions are such that transport to the electrolyte phase is prevented, path **B** becomes operative, resulting in substantial enrichment of the gas phase, Fig. 3c.

3.2 Evaluation of the separation factor

The reaction path for the evolution of hydrogen isotopes, H, D, T, is the same and is given by Eqs. (I) – (III),



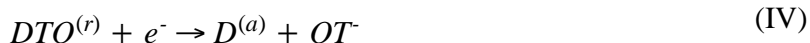
followed by either



or



However, the reaction path for tritiated heavy water must be modified, *e.g.*, the controlling discharge step, Eq. (I), is split into two paths, Eqs. (IV) and (V)



and



The same considerations apply when the rate determining step resides in either the Heyrovsky–Horiuti path, Eq. (II), or the Tafel path, Eq. (III).

A general form of an equation governing the charge transfer is

$$i_n = k_n c_n^{(r)} \cdot f(\theta_n) \cdot \exp(-\beta \eta) \quad \beta RT; \eta = E_{rev} - E(i); n = D, T \quad (4)$$

where the $f(\theta_n)$ function depends on the reaction path(9). Other symbols have their usual meaning. The atomic ratio in the gas phase, $(c_T/c_D)_g$, is the ratio of currents producing D_2 and DT , respectively. To obtain this ratio it is necessary to write Eq. (1) for both currents, *i.e.*, i_T and i_D and take a quotient, Eq. (5)

$$\left(\frac{c_T}{c_D}\right)_g = \frac{k_T c_T^{(r)} \cdot f(\theta_T)}{2k_D c_D^{(r)} \cdot f(\theta_D) + k_T c_T^{(r)} f(\theta_T)} \quad (5)$$

The factor of 2 in Eq. (5) appears because the D_2 molecules are produced by i_D and, on account of an equal probability of paths, Eqs (Ia) and (Ib), also include one half of those produced by i_T . For heavy water with low levels of tritium, $c_D \gg c_T$ and, if the Volmer path is the rate determining step, then $f(\theta_n) = 1 - \theta_D - \theta_T$ is equal for both reactions, yielding the distribution in the gas phase, Eq. (6),

$$\left(\frac{c_T}{c_D}\right)_g = \frac{k_T c_T^{(r)}}{2 \cdot k_D c_D^{(r)}} \quad (6)$$

Theoretical considerations state that the isotopic separation factor is not affected by tritium concentration in the electrolyte, providing that $c_D \gg c_T$ (9). In writing Eqs. (5) and (6), we ignore the slight difference in the applied overpotential, *i.e.*, we assume that the difference in the rest potentials is insignificant.

3.3 INTERPRETATION OF DATA

In what follows, we provide a qualitative description of the tritium distribution as determined from the observed vs computed values of the D/Pd system under cathodic polarization. Following this, we supplement the description with a quantitative assessment; particularly, we select for discussion three aspects, *viz.*, assessment of observed behavior, data analysis and the rate of tritium generation and, finally, the location of tritium generating sites.

3.3.1 Qualitative Assessment

A qualitative assessment of tritium distribution between the electrolyte and gas phases resulting from a prolonged evolution of deuterium generated by the electrolysis of D_2O is given in Figs. 4–7. The electrolyses were carried out under varying cell current profiles and composition of additives. For convenience, changes in cell current, times of sampling and recombiner efficiency are indicated in respective figures (axes i , V_a and ϵ_r) while actual experimental data are provided in the appendix.

Three distinct scenarios can be seen from the data: (i) prolonged electrolysis without tritium production, (ii) sporadic tritium production with periods of inactivity wherein the isotopic separation factor is at or near the normal value for T/D systems throughout, and (iii) sporadic tritium production in which selective enhancement of the gas phase tritium level occurs. For all times in some cases, and for most time in all cases, there is good agreement between the calculated and observed tritium distribution, namely the experimental (solid line) and calculated (dashed line) fall within experimental error (shaded area). Those instances where significant deviation between the observed and expected concentration of tritium in both phases occurs indicates the periods of tritium production. In the figures, these regions are indicated by arrows, q_n ; $n = 1, 2, 3, 4$.

The first scenario: Tritium distributions summarized in Figs. 4a and 4b serve as examples of the absence of tritium production over the *ca* three weeks of duration of the electrolyses in solutions containing different additives, thereby also serving as blank tests of the model calculation for different charging profile. It is seen that the observed and calculated values are in good agreement.

The second scenario: In contrast, Figs. 5 and 6 show active periods of the type (ii) mentioned above. In Fig. 5, one active period of approximately three days duration, (6/21 – 6/23), occurs 30 days after the initiation of charging. Figure 6a shows two active periods, (4/19 – 5/3, 5/19 and 5/21), separated by 14 days of inactivity. In these instances the isotopic separation factor does not change and the enrichment occurs in both the electrolyte and gas phases. The constancy of the isotopic separation factor, $s = 0.68 \pm 0.04$, indicates that the reaction path for the cathodic charge transfer did not change, either in the course of prolonged electrolysis or between runs and, that tritium generated during the active periods first entered the electrolyte phase resulting in the isotopic distribution controlled by the electrodic reaction. Evidently, the distribution of tritium between the phases follows transport *via* route **A**, Fig. 3b, and the active period is therefore manifested by an increase in tritium concentration in both phases.

The third scenario: The data summarized in Fig. 7 show an active period in which tritium enrichment is limited to the gaseous phase only. This enrichment occurs shortly after the completion of the co-deposition process and is subsequently followed by a period of inactivity. The time dependent tritium concentration in the electrolyte agrees at all times with the computed values when $s = 0.67$. This selective enrichment of the gaseous phase suggests that path **B** is the method of transport. The return to a normal distribution indicates a transition from path **B** to path **A**. This behavior suggests that tritium production occurs shortly after completion of the co-deposition process and is affected by the morphology (mossy, dendritic) of the Pd- surface. The transition from path **B** to path **A** implies an active participation of the interphase region which, most likely, is attributed to the restructuring of the electrode surface as well to the enhanced concentration of hydrogen isotopes within the interphase region during the co-deposition process. A more detailed discussion of the dynamics of the interphase in the course of codeposition is outside the scope of this communication. A detailed presentation of the restructuring processes can be found in ref. (11).

We wish to remark that the absence of tritium production, Figs. 4a and 4b, means only that within the investigated period no activities were observed. It does not assure that they could not occur at some later date, a position expressed also by Bennington *et al*(12).

3.3.2 Data Analysis; Quantitative Aspects

The essential difference between the method employed here and elsewhere(4) concerns selection of the numerical value of the isotopic separation factor. This number is usually taken from the literature and may, or may not, represent the kinetic and thermodynamic properties of the interphase pertinent

to the experimental conditions. Here, the value of the s - factor is determined individually for each experimental run by selecting that value which best fits the recorded data.

In principle, the rate of tritium production is calculated by subtracting Eq. (3) from either Eq. (1) or Eq. (2). Taking as an example results plotted in Fig. 5, the difference between the observed and calculated tritium concentration in the electrolyte phase, on 6/22, is ca 4.0 dpm/ml. Tritium generation rates are estimated by a curve fitting technique(9) or by computer modeling in which an arbitrarily selected q - value is inserted into the experimental data and computer matched to obtain agreement with the observed distribution throughout the duration of the experiment. A good agreement was recorded for rate of tritium generation when $q = 610_3$ atoms/sec during period 6/21 – 6/22. This would indicate a total production of $5.2 \bullet 10^8$ tritium atoms.

An estimate of tritium production rate by a computer modeling technique is illustrated in Figs. 6a and 6b. In particular, the computed tritium distribution, with $q(t) = 0$, and data tabulated in Table A - I, is shown in Fig. 6a (solid circles) while the actual experimental distribution is shown by the open circles. Using the previous argument, we identify two periods of tritium production, the first occurring between 4/21 and 5/1 and the second starting on 5/18. The experiment was terminated on 5/21. The results of computer modeling based on tritium production: on 4/21 - 4/23 with $q_1 = 4 \bullet 10^3$ at/sec for $\Delta t = 3.016 \bullet 10^3$ min., on 5/18 with $q_2 = 3 \bullet 10^3$ at/sec. for $\Delta t = 1.442 \bullet 10^3$ min., on 5/19 with $q_3 = 7 \bullet 10^3$ at/sec for $\Delta t = 1.421 \bullet 10^3$ min., and on 5/20 with $q_4 = 3 \bullet 10^3$ at/sec for $\Delta t = 1.489 \bullet 10^3$ min. are shown in Fig. 6b. An excellent agreement with experimental distribution is evident with the total tritium production of $1.8 \bullet 10^9$ atoms.

The data shown in Fig. 7 provide the evidence for tritium production through the enrichment of the gas phase while retaining agreement between the computed and experimental point in the liquid phase. Unfortunately no estimate of the total amount of tritium production can be reliably made because of poor recombination efficiency. The poor efficiency means that the tritium content is, in reality, substantially higher than indicated (due to the faster rate of D_2/O_2 vs that of DT/O_2).

3.3.3 Tritium Generation Sites

The question of the location of the generation site for tritium production during the electrolysis of D_2O on a Pd - electrode cannot be resolved by the method just described. Data in Figs 5 – 7 were interpreted in terms of Eqs. (1) - (3) As written, these equations ignore the tritium absorption by the Pd - lattice and consequently, cannot provide any information concerning the location of the generating sites. However, this omission does not invalidate conclusions reached as long as $c_T \ll c_D$.

As in the earlier work of Will *et al.* (5), the resolution of this problem is sought by employing a total mass balance which, in addition, requires the determination of tritium content in the bulk of the Pd - electrode. The amount of tritium generated during several runs and its three-phase distribution is tabulated in Table I. This table lists the experimental conditions, columns 1 – 5, the distribution of tritium among the liquid, gas and bulk electrode, columns 6 - 8. A net increase in tritium content is indicated in columns 9 and 10 as either gain in dpm or in the number of tritium atoms produced in the course of an experiment. The latter is calculated by the method described above.

Data assembled in Table I are in general agreement with results obtained under conditions of intermittent sampling, Figs. 4 – 7. Three conclusions can be made, however: First, the long time between samplings obliterates the fine details of the behavior of the Pd/D system. For example, on the basis of the mass balance, rows 1, 2 and 4, no statement can be made concerning production of tritium or lack thereof, since the apparent change is much less than the analytical error and is,

therefore, not significantly different from no change. Second, tritium production, if any, takes place within, or in the close proximity of the interphase. Only when Al^{3+} ions were added to the electrolyte, was tritium detected in the bulk electrode. Third, electrolysis on dendritic surfaces (following the co-deposition) favors transport of tritium to the gas phase via path **B**.

4.0 Concluding Remarks

Because of the controversial nature of the Pd- lattice assisted nuclear events, we have refrained from speculations and concentrated on presentation and interpretation of experimental data. We have limited the discussion to one aspect only because the correlation with, for example, excess enthalpy production, would require an on-line detection system sensitive enough to record the low level activity. In conclusion, we emphasize the following points:

1. Every effort was made to minimize analytical errors in the closed system. Although closed cells are considered superior to closed system arrangements for the detection of tritium generation in electrolytic cells, a closed cell, by design, represents an integrating system which may not be desirable if you are ascertaining the nature of the tritium generation. In this communication, we have shown that the cell/recombiner assembly and our experimental protocols yield results identical with those obtained using closed cells. This is due to the fact that the greatest source of error in both experimental approaches is in the tritium content measurement itself and not in the electrolyte volume.
2. The evidence for tritium production is based on the difference between the computed and observed concentration of tritium, the non-equilibrium distribution of tritium and the total mass balance. Only accepted concepts and well established procedures lead us to the conclusions offered.
3. One of the characteristic features of the behavior of the Pd/D system is the sporadic nature of “burst-like” tritium generation. Short times between samplings are necessary to facilitate the display of the “burst-like” behavior. Such “burst-like” behavior would not be detectable using a closed cell system.
4. Present data indicate that tritium production takes place within the interphase with the distribution governed primarily by path **A**. A speculative argument can be presented to indicate that the generated tritium is forced into the bulk electrode by conditions at the solution side of the interphase, *e.g.* addition of Al^{3+} ions, and that electrode surface morphology tends to affect the two-phase distribution, *e.g.*, dendritic surfaces tend to promote transport via path **B**.

ACKNOWLEDGEMENT

The authors acknowledge the interest and support received from Dr. Frank Cordon (NCCOSC – NISE West).

REFERENCES

1. M. Fleischmann and S. Pons, *J. Electroanal. Chem.*, **261**, 301(1989)
2. M.L. Oliphant, P. Harteck and Lord Rutherford, *Nature*, **133**, 413 (1934)
3. J. Schwinger, **Nuclear Energy in Atomic Lattice**, The First Annual Conf. on Cold Fusion, p. 130, Salt Lake City, UT, 1990
4. E. Storms, *Fusion Techn.*, **20**, 433 (1991)

5. F.G. Will, K. Cedzynska, M.—C. Yang, J.R. Peterson, H.E. Bergeson, S.C. Barrowers, W.J. West and D.C. Linton, **Studies of Electrolytic and Gas Phase Loading of Palladium with Deuterium**, The Science of Cold Fusion, Proc. II Annual Conf. on Cold Fusion, Como (Italy), 1991
6. R.V. Bucur and F. Bota, *Electrochim. Acta*, **29**, 103 (1984)
7. S. Szpak, P.A. Mosier-Boss, R.D. Boss and J.J. Smith, *J. Electroanal. Chem.*, **373**, 1 (1994)
8. P. van Rysselberghe, Some Aspects of the Thermodynamic Structure of Electrochemistry, in *Modern Aspects of Electrochemistry*, J.O'M. Bockris, ed., vol. 4, Plenum Press, New York, NY , 1966
9. J. O'M. Bockris and S. Srinivasan, *J. Electrochem. Soc.*, 111844(1964); 111,853(1964); **111**, 858 (1964)
10. S. Szpak, P.A. Mosier—Boss, S.R. Scharber and J.J. Smith, *J. Electroanal. Chem.*, **337**, 147 (1992)
11. L. Schlapbach, **Surface properties and activation**, in *Topics in Applied Physics*, vol. II, chapter 2, Springer – Verlag, Berlin 1978
12. S.M. Bennington, R.S. Sokhi, P.R. Stonadge, D.K. Ross, M.J. Benham, T.D. Beynon, P. Whitney, I.R. Harris and J.P.G. Farr, *Electrochim. Acta*, 34,1323 (1989)

TABLE I: THREE PHASE TRITIUM DISTRIBUTION
(BY MASS BALANCE)

SYSTEMS	Volume/ml at		ϵ_r	Tritium/dpm/ml			$T - T(t_f) - T(t_0)$		
	t=0	t=t _f		T(t)/dpm/ml at t=0	Liquid	Gas	Electrode	dpm	atoms
Ag/0.3M LiCl	49.71	23.55	0.97	18.9±1.2	22.4±1.2	15.2±1.1	-	-14±50	
(Cu)Pd/0.1M LiOD	49.7	23.66	0.998	18.9±1.2	24.1±1.2	13.1±1.1	ND	-28±50	
(Ag)Pd/0.1M LiOD + 80ppm Al	49.72	29.49	1.00	18.0±1.2	25.4±1.2	13.3±1.1	2.3±1.3	123±50	5.1x10 ¹¹
(Ag)Pd/0.3M LiOD +231 ppm Al	49.69	19.79	0.97	16.5±1.2	20.3±1.2	13.1±1.1	0.9±1.3	-27±50	
(Au)Pd/0.3M LiCl ^b (co-dep)	46.72	11.8	0.56 (1.00)	14.5±1.9	25.4±2.1	13.4±1.8 (29.1)	ND ^(a)	90±80 (637)±80	2.6x10 ¹²
(Au)Pd/0.3M LiCl ^b (co-dep)	37.1	16.1	0.50 (1.00)	17.0±1.9	25.1±2.1	13.4±1.8	ND ^(a)	60±60 (336)±60	1.3x10 ¹²

(a) determined by method of Will et al (5).

ND - not detectable

(b) Sample were counted for 240 min instead of 600 min

FIGURE CAPTIONS

Fig. 1 - Experimental cell and recombiner assembly (schematic)

a — Electrolytic cell; **b** — Recombiner
insert - detail of cell assembly

Fig. 2 - Sampling profile for constant cell current density

$V(t_1)$ initial volume (also, initial volume for any charging period); $V(t_2)$ – volume after the passage of charge $i\Delta t$; V_s - sample volume; V_a - volume added; t_2 - time of first sampling; t_3 - electrolyte addition time; t_4 - time of second sampling.

Fig. 3 - Structure of the interphase; tritium distribution paths

r - reaction site; a - adsorption site; e - charge transfer site; n - nucleation and gas evolution plane

3a - Fluxes on non-absorbing electrode: $i = i_D + i_T$ denote cell current and currents producing gaseous deuterium and tritium

3b - Fluxes on absorbing electrode - path **A**

3c - Fluxes on absorbing electrode - path **B**

Fig. 4 - Two-phase tritium distribution ($s = 0.71$)

computed - dashed; experimental - solid line

Fig. 4a - Electrode: area -3.67 cm^2 ; Cu-Ag-Pd (deposited from $\text{Pd}(\text{NH}_3)_2\text{Cl}_2$)

Electrolyte: 0.01 M PdCl_2 - 0.3 M LiCl – D_2O

Additive: 100 ppm BeSO_4 in 0.1 M Li_2SO_4

Fig. 4b - Electrode: area -3 cm^2 ; Cu-Ag-Pd (deposited from $\text{Pd}(\text{NH}_3)_2\text{Cl}_2$)

Electrolyte: 0.3 M LiOD

Additive: 113 ppm B_2O_3

Cell current, electrode addition and recombining efficiency indicated by arrows along the time coordinate (i , V_a and ϵ_r respectively)

Fig. 5 - Two-phase tritium distribution ($s = 0.71$)

computed – dashed; experimental – solid lines

Electrode area: 2.5 cm^2 ; Cu-Ag-Pd deposited from $\text{Pd}(\text{NH}_3)_2\text{Cl}_2$

Electrolyte: $2.6 \cdot 10^{-3} \text{ M PdCl}_2$ – 0.31 M LiCl

Additive: 200 ppm MgCl_2

indicated: points of electrolyte addition; recombers efficiencies; cell current (mA)

Fig. 6 - Two-phase tritium distribution ($s = 0.63$)

Electrode area: 2.7 cm^2 ; Cu-Ag-Pd deposited from $\text{Pd}(\text{NH}_3)_2\text{Cl}_2$

Electrolyte: 0.33 M Li_2SO_4 (50 ml)

Additive: 100 ppm BeSO_4

indicated: cell current; recombining efficiency; electrolyte additions

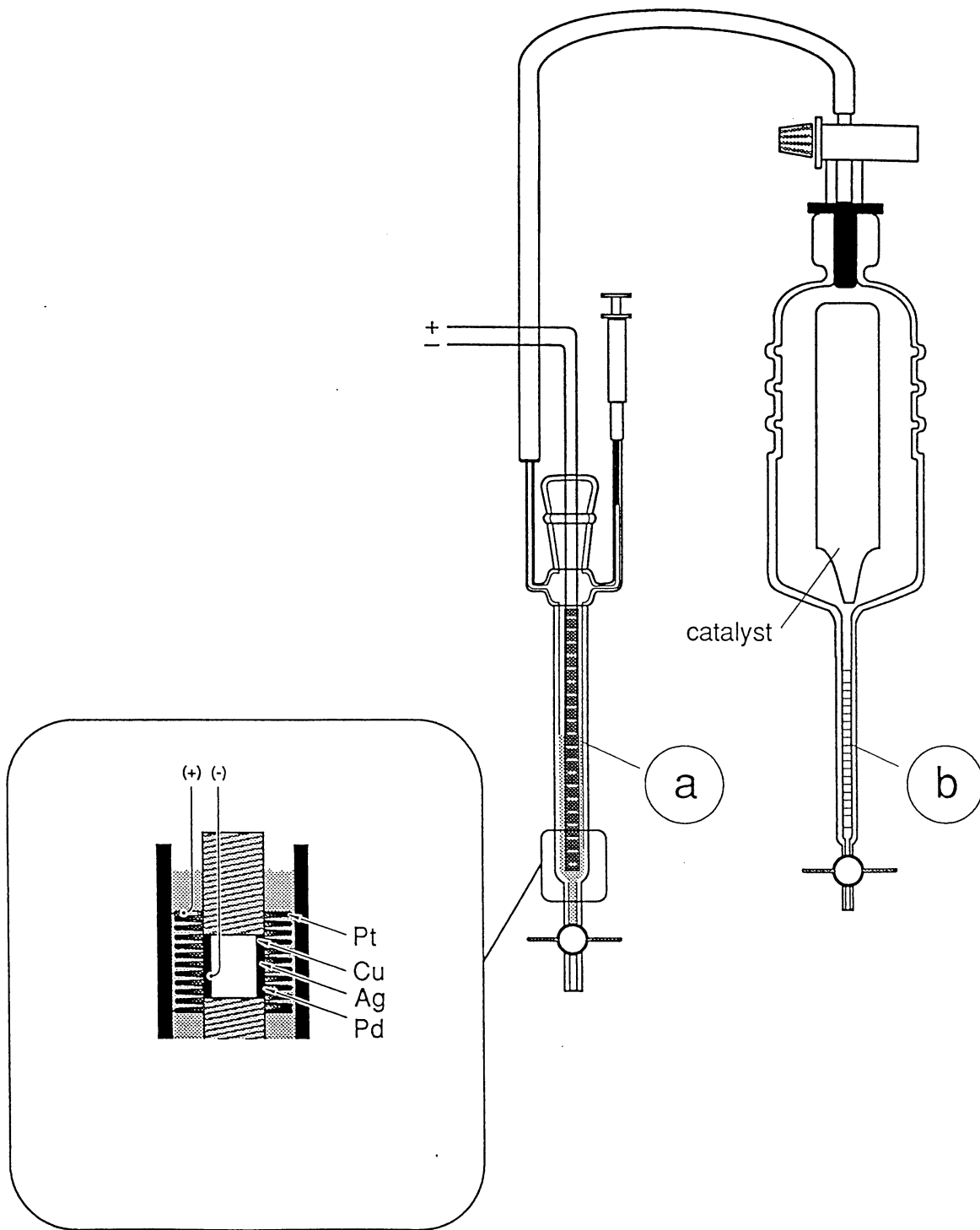
Fig. 7 - Two-phase tritium distribution ($s = 0.67$)*

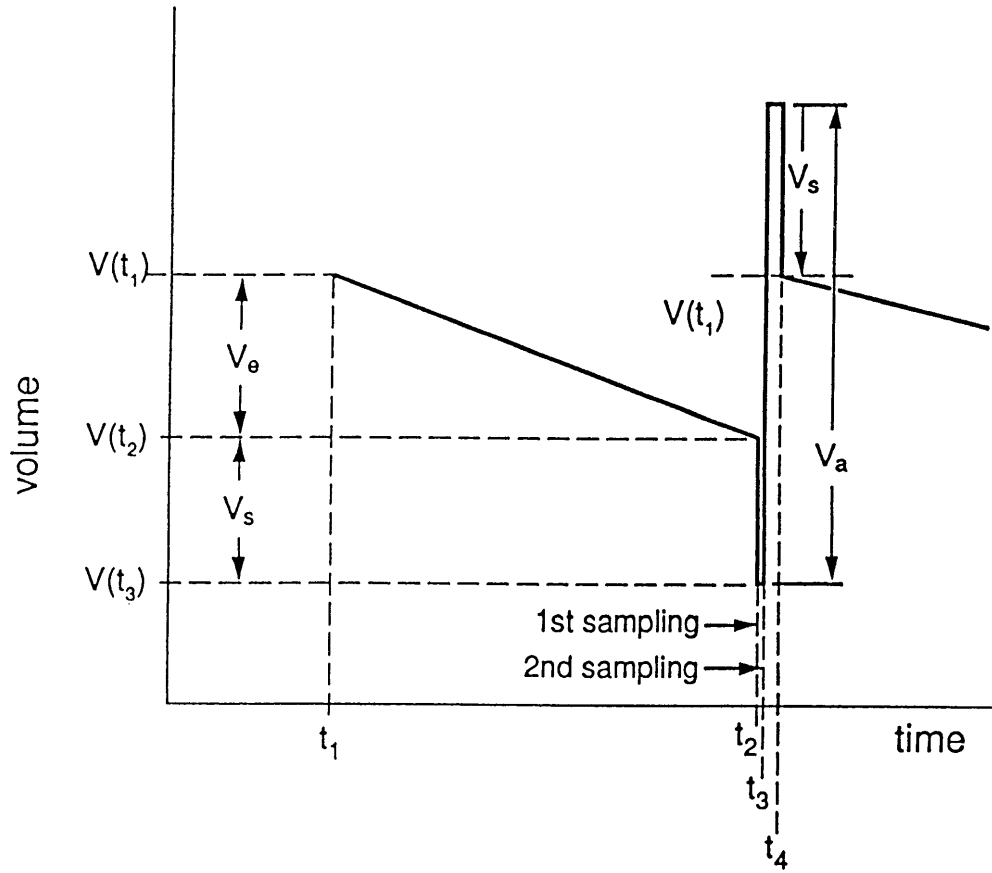
Electrode: prepared by co-deposition

Electrolyte: 0.05 M PdCl_2 + 0.6 M LiCl

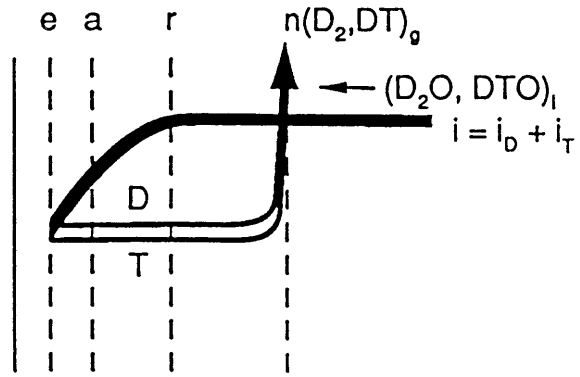
indicated: cell current; recombiner efficiency; D_2O addition

*Note: the s - value computed using data of the last seven days

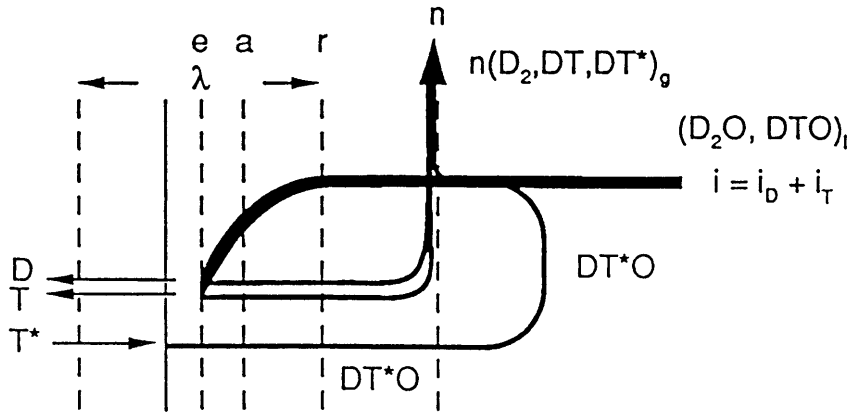




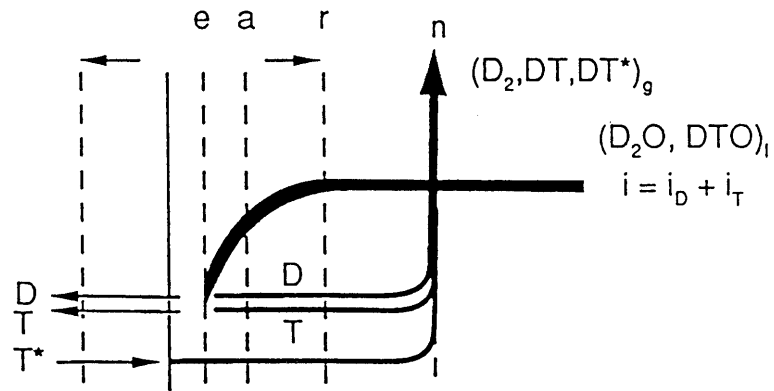
(a)

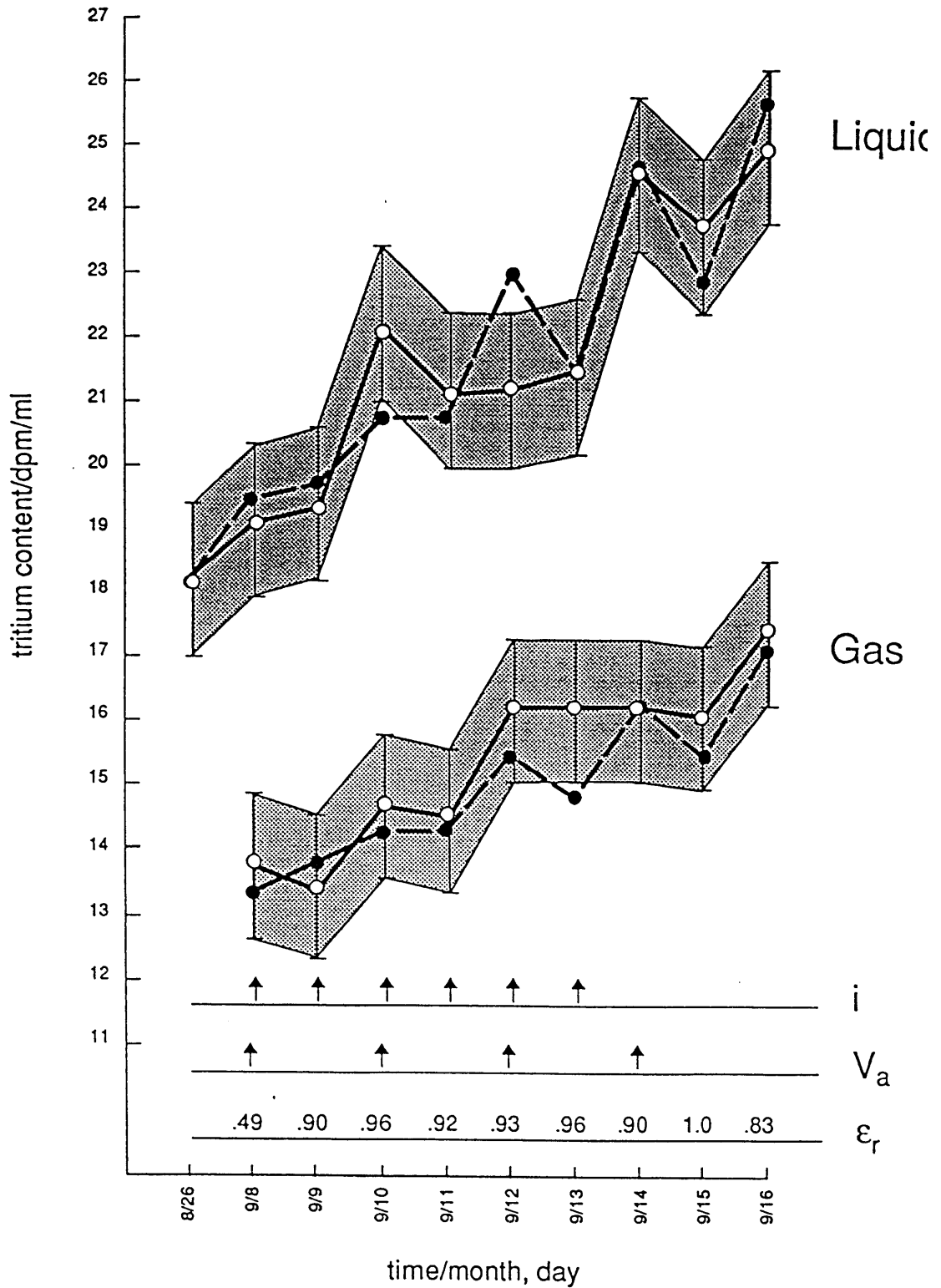


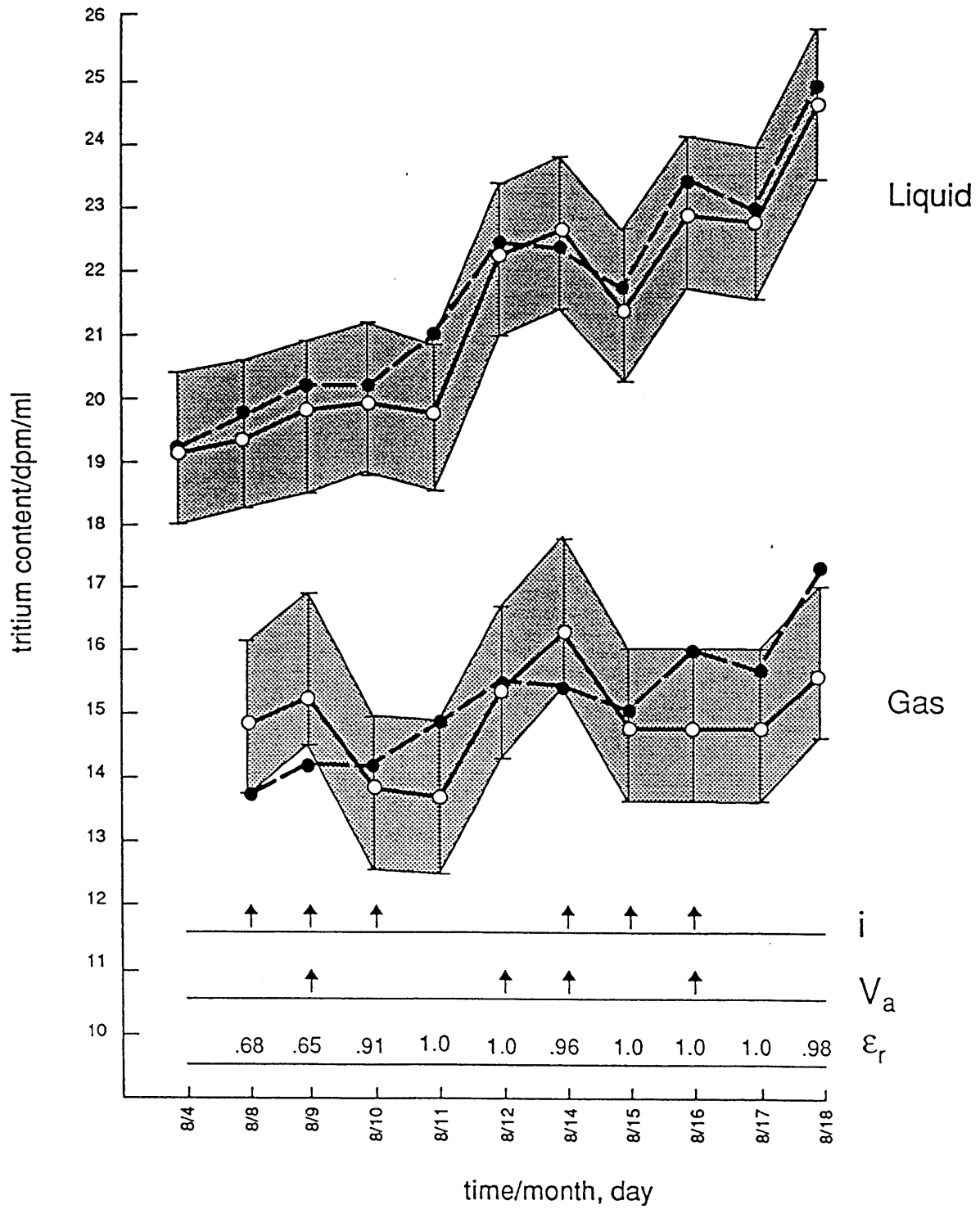
(b)

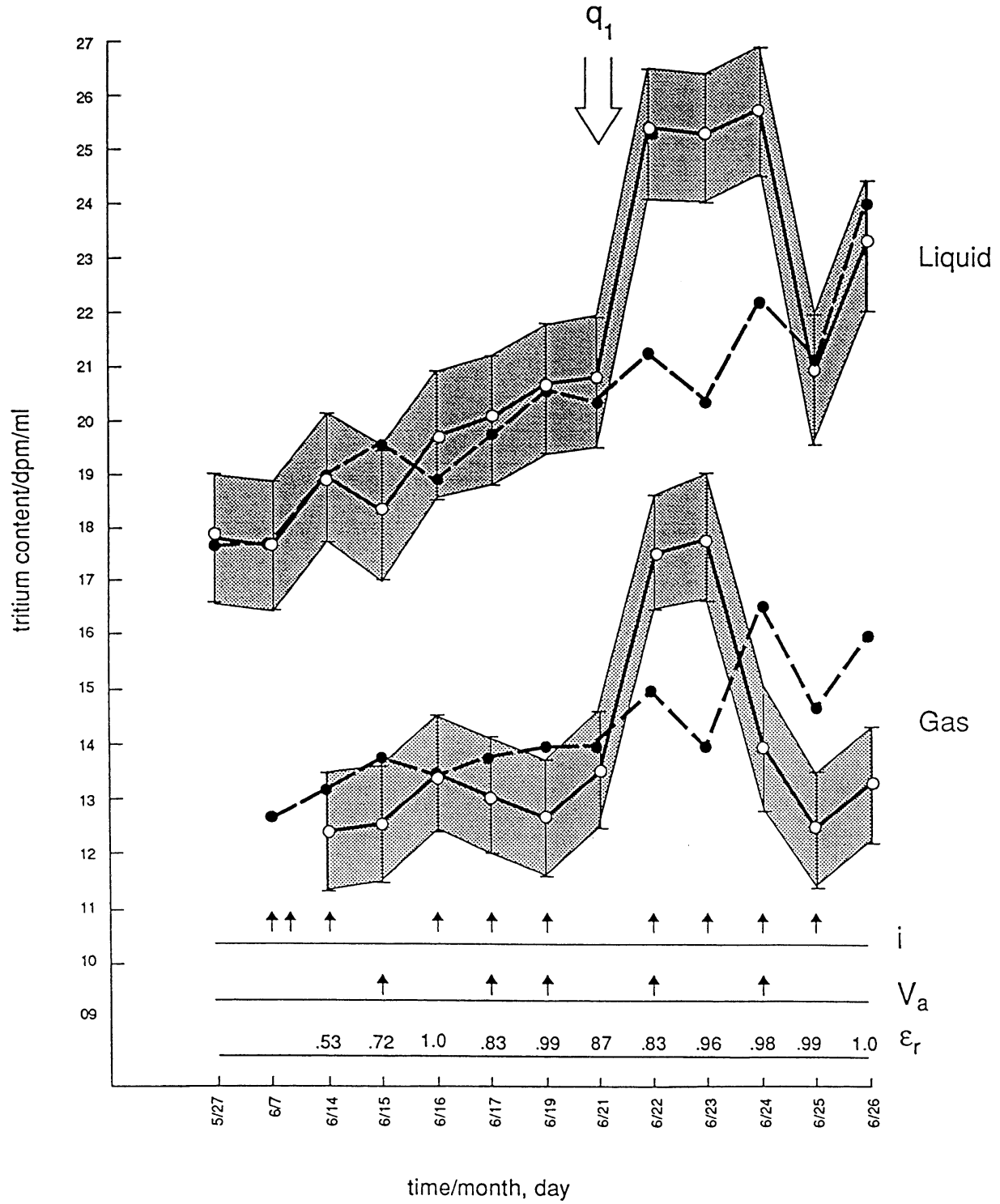


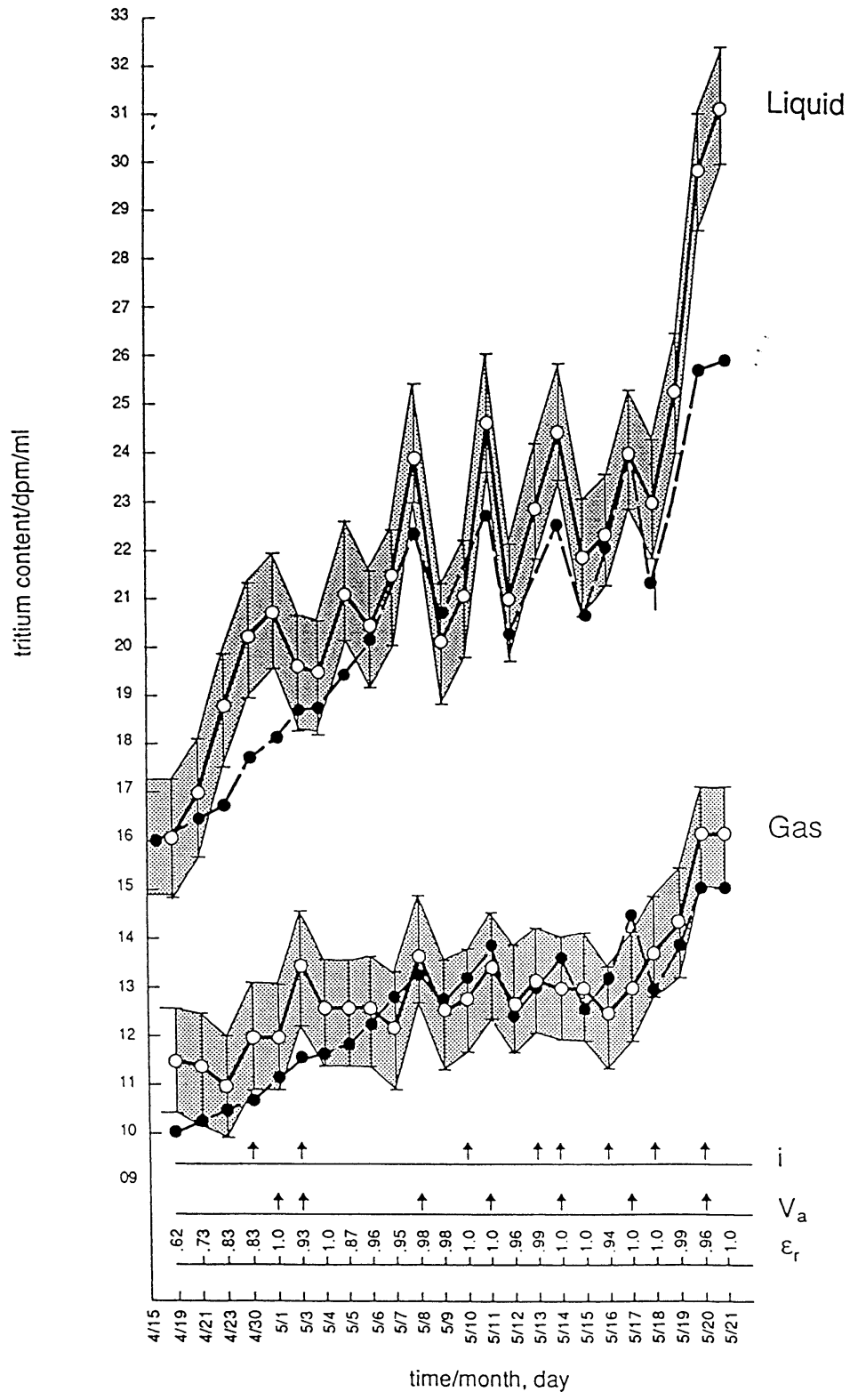
(c)

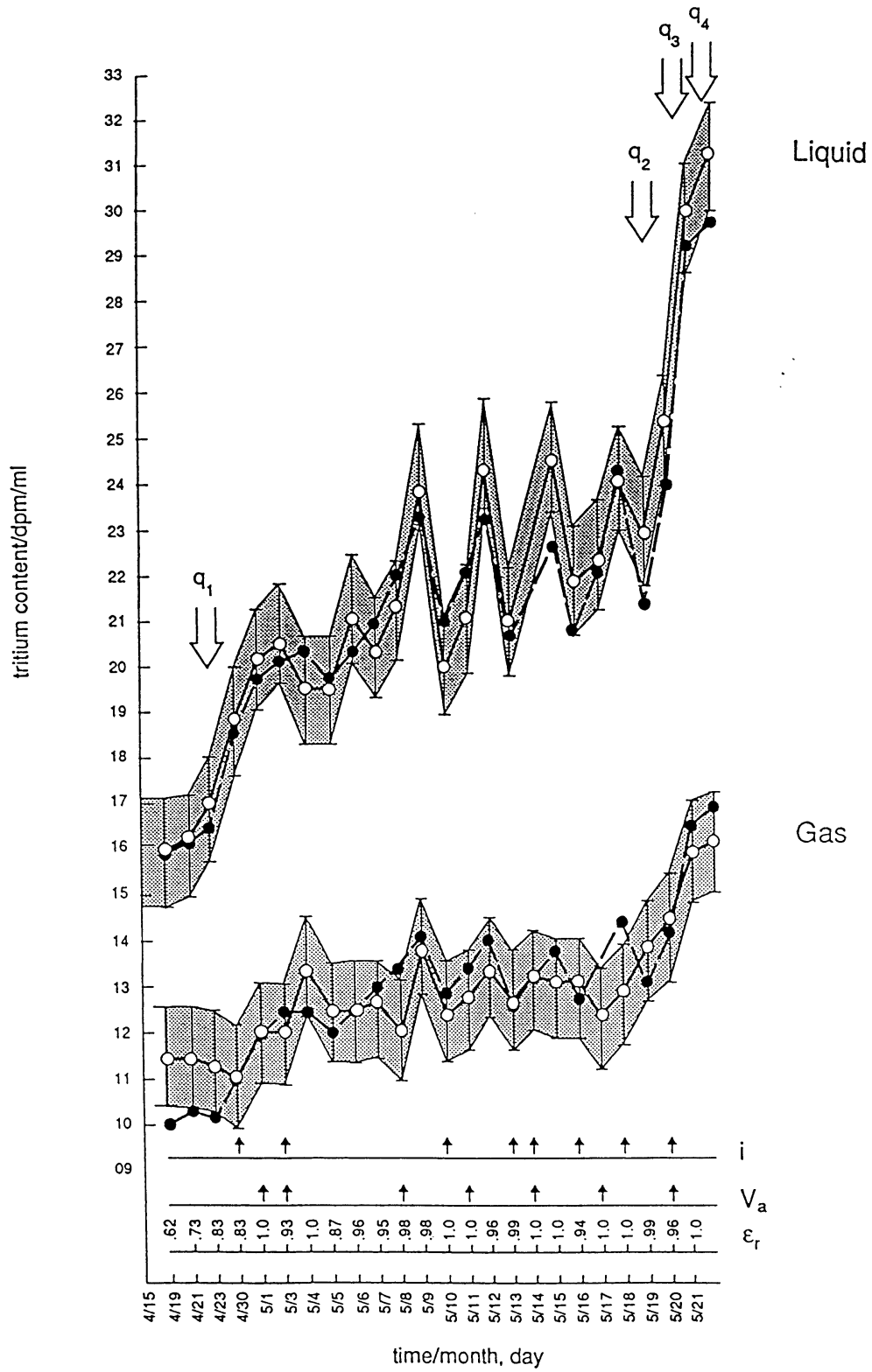


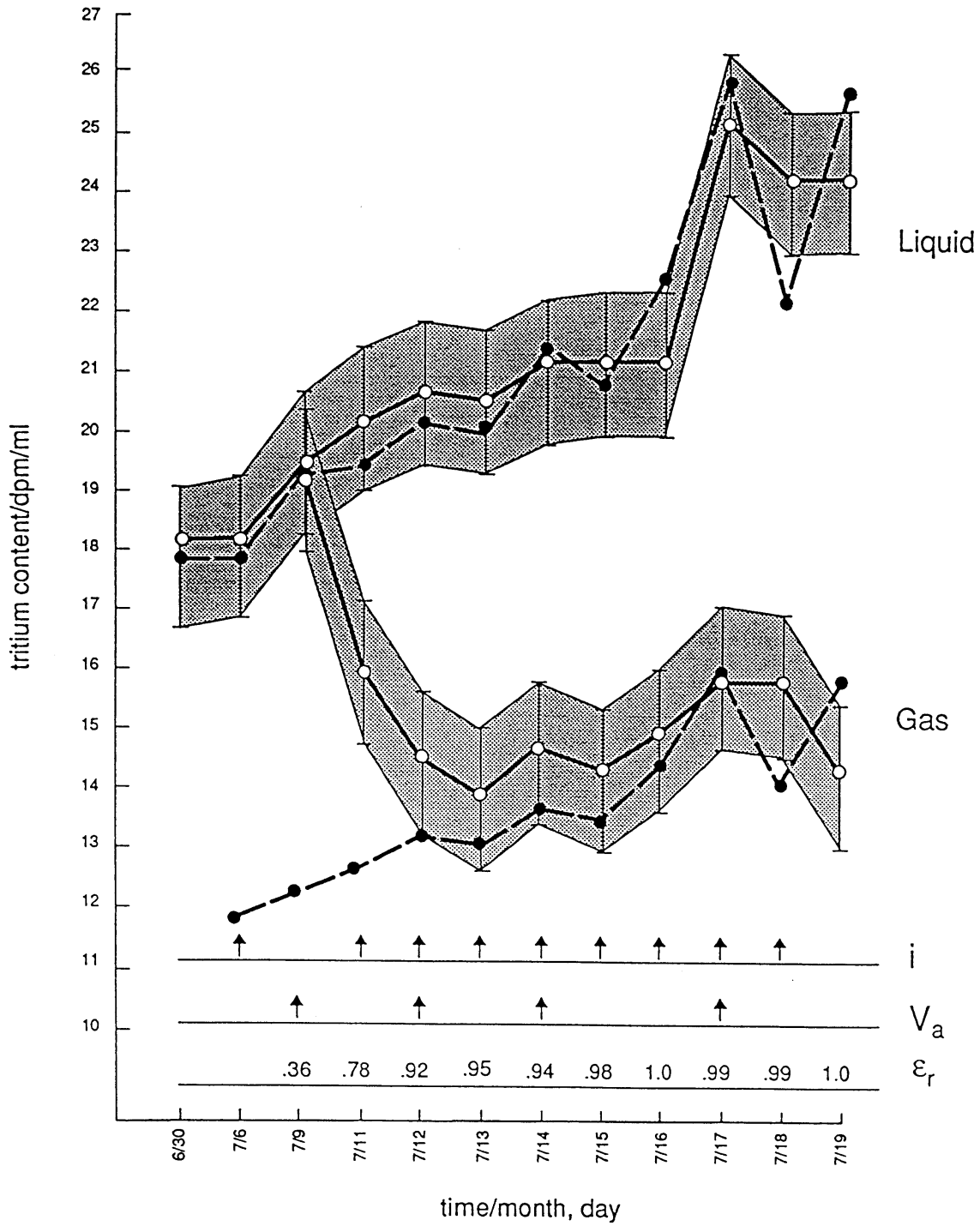












APPENDIX

Experimental data relevant to the computation of tritium distribution, using Eq. (3), are tabulated in Tables A-I through A-V. They are assembled to supplement the information provided in the respective figure captions.

Table A-I: Inventory of Input Parameters for Figure 4a

Run: 26 Aug to 16 Sept 1993

Electrolyte - volume: 24.82 ± 0.01 ml

- composition: 0.01 M PdCl_2 + 0.3 M LiCl in D_2O with $T = 18.2 \pm 1.2$ dpm/ml

- additions: (a) 0.1 M Li_2SO_4 + 102 ppm Be (as BeSO_4) in D_2O with $T = 18.2 \pm 1.2$ dpm/ml (b) D_2O with $T = 18.2 \pm 1.2$ dpm/ml

Separation factor $s = 0.71$

Sampling volume $V_s = 1.60 \pm 0.01$ ml

Sampling Date	i/mA	$\Delta t/\text{min}$	ϵ_r	V_s/ml	Tritium	dpm/ml
					Electrolyte	Gas
9-8	-5 -7.5 -100	1703 8280 8732	.49	9.08 ± 0.02^a	19.2 ± 1.2	13.8 ± 1.1
9-9	-300	1463	.90		19.4 ± 1.2	13.5 ± 1.1
9-10	-500	1488	.96	15.14 ± 0.02^b	22.3 ± 1.2	14.8 ± 1.2
9-11	-600	1768	.92		21.1 ± 1.2	14.6 ± 1.2
9-12	-800	1414	.93	18.17 ± 0.02^b	21.2 ± 1.2	14.5 ± 1.2
9-13	-900	1076	.96		21.4 ± 1.2	16.3 ± 1.2
9-14	-1000	1626	.90	18.17 ± 0.02^b	24.6 ± 1.2	16.3 ± 1.2
9-15	-1000	1449	1.00		23.6 ± 1.2	16.2 ± 1.2
9-16	-1000	1157	.83		25.0 ± 1.2	17.4 ± 1.2

Table A-II: Inventory of Input Parameters for Figure 4b

Run: 4 Aug 1993 to 18 Aug 1993

Electrolyte - volume 24.80 ± 0.01 ml

- composition 0.3 M LiOD + 133 ppm B (as B_2O_3) in D_2O with $T = 19.3 \pm 1.2$ dpm/ml

- additions: 0.1 M LiOD + 50 ppm B in D_2O with $T = 19.0 \pm 1.2$ dpm/ml

Separation Factor $s = 0.71$

Sampling volume $V_s = 1.60 \pm 0.01$ ml

Sampling Date	i/mA	Δt /min	ϵ_r	V_s /ml	Tritium	dpm/ml
					Electrolyte	Gas
8-8	-50 -100	1421 4270	.68		19.4 \pm 1.2	15.0 \pm 1.2
8-9	-200	1738	.65	12.11 \pm 0.02	19.8 \pm 1.2	15.7 \pm 1.2
8-10	-300	1315	.91		20.0 \pm 1.2	13.8 \pm 1.2
8-11	-400	1442	1.00		19.7 \pm 1.2	13.6 \pm 1.2
8-12	-400	1593	1.00	12.11 \pm 0.02	22.2 \pm 1.2	15.5 \pm 1.2
8-14	-400	2460	.96	18.17 \pm 0.02	22.6 \pm 1.2	16.6 \pm 1.2
8-15	-600	1498	1.00		21.4 \pm 1.2	14.6 \pm 1.2
8-16	-800	1458	1.00	18.98 \pm 0.03	22.9 \pm 1.2	14.8 \pm 1.2
8-17	-1000	1668	1.00		20.3 \pm 1.2	14.8 \pm 1.2
8-18	-1000	1249	.98		24.6 \pm 1.2	15.8 \pm 1.2

TABLE III-A: Inventory of Input Parameters for Figure 5

Run: 27 May 1993 to 26 June 1993

Electrolyte - volume: 24.84 ± 0.01 ml

- composition: 0.01M Pd Cl₂ + 0.314 M LiCl in D₂O with T= 17.8 ± 1.2 dpm/ml

- additions: 0.1 M LiCl + 200 ppm MgCl₂ in D₂O with T= 17.0 ± 1.2 dpm/ml

Separation factor $s=0.71$

Sampling volume $V_s = 1.58 \pm 0.01$ ml

Sampling Data	i/mA	$\Delta t/\text{min}$	ϵ_r	V_s/ml	Tritium	dpm/ml
					Electrolyte	Gas
6-7	-1 -2 -3	8612 1645 5546			17.7 \pm 1.2	
6-14	-50 -100	2947 7281	.53		18.9 \pm 1.2	12.4 \pm 1.1
6-15	-200	1496	.72	8.93 \pm 0.03	18.7 \pm 1.2	12.6 \pm 1.1
6-16	-200	1217	1.00		19.7 \pm 1.2	13.5 \pm 1.1
6-17	-300	1430	.83	8.93 \pm 0.03	20.0 \pm 1.2	13.1 \pm 1.1
6-19	-400	2801	.99	11.90 \pm 0.03	20.5 \pm 1.2	12.7 \pm 1.1
6-21	-300	3282	.87		20.7 \pm 1.2	13.6 \pm 1.1
6-22	-300	1435	.83	11.90 \pm 0.03	25.3 \pm 1.2	17.6 \pm 1.1
6-23	-500	1411	.96		25.2 \pm 1.2	17.8 \pm 1.1
6-24	-600	1366	.98	17.87 \pm 0.03	25.7 \pm 1.2	13.9 \pm 1.1
6-25	-800	1211	.99		20.8 \pm 1.2	12.5 \pm 1.1
6-26	-1000	1363	1.00		23.3 \pm 1.2	13.3 \pm 1.1

Table IV-A: Inventory for Input Parameters for Figures 6a & 6b

Run: 15 Apr 1993 to 21 May 1993

Electrolyte - volume: 48.89 ± 0.01 ml

- composition: 0.333 M Li_2SO_4 + 100 ppm Be (as BeSO_4) in D_2O with $T=15.9 \pm 1.2$ dpm/ml

- additions: (a) 0.1 M Li_2SO_4 in D_2O with $T=15.9 \pm 1.2$ dpm/ml

(b) 0.1 M Li_2SO_4 + 100 ppm Be (as BeSO_4) in D_2O with $T=15.9 \pm 1.2$ dpm/ml

(c) D_2O with $T=16.0 \pm 1.2$ dpm/ml

Separation factor: $s=0.63$

Sampling volume $V_s = 2.06 \pm 0.01$ ml

TABLE IV-A: FIGURES 6A AND 6B

Sampling Date	i/mA	$\Delta t/\text{min}$	ϵ_r	V_s/ml	Tritium	dpm/ml
					Electrolyte	Gas
4-19	-50 -100	1212 4286	.62		16.1 \pm 1.2	11.5 \pm 1.1
4-21	-100	2950	.73		16.9 \pm 1.2	11.4 \pm 1.1
4-23	-100	3016	.83		18.7 \pm 1.2	11.0 \pm 1.1
4-30	-100	9845	.83		20.2 \pm 1.2	12.0 \pm 1.1
5-1	-200	1424	1.00	8.94 \pm 0.01 ^a	20.8 \pm 1.2	12.0 \pm 1.1
5-3	-200	2977	.93	20.85 \pm 0.02 ^a	19.4 \pm 1.2	13.5 \pm 1.1
5-4	-400	1470	1.00		19.4 \pm 1.2	12.5 \pm 1.1
5-5	-400	1325	.87		21.4 \pm 1.2	12.5 \pm 1.1
5-6	-400	1487	.96		20.4 \pm 1.2	12.6 \pm 1.1
5-7	-400	1524	.95		21.2 \pm 1.2	12.1 \pm 1.1
5-8	-400	1734	.98	19.88 \pm 0.02 ^a	24.2 \pm 1.2	13.9 \pm 1.1
5-9	-400	1090	.98		20.1 \pm 1.2	12.5 \pm 1.1
5-10	-400	1667	1.00		21.0 \pm 1.2	12.8 \pm 1.1
5-11	-500	1396	1.00	23.83 \pm 0.02 ^b	24.8 \pm 1.2	13.5 \pm 1.1
5-12	-500	1305	.96		20.9 \pm 1.2	12.8 \pm 1.1
5-13	-500	1551	.99		23.0 \pm 1.2	13.2 \pm 1.1
5-14	-600	1194	1.00	25.34 \pm 0.02 ^b	24.6 \pm 1.2	13.0 \pm 1.1

5-15	-700	1450	1.00		21.8±1.2	13.0±1.1
5-16	-700	1543	.94		22.4±1.2	12.4±1.1
5-17	-800	1622	1.00	26.81±0.02 °	24.1±1.2	12.9±1.1
5-18	-800	1355	1.00		23.0±1.2	13.8±1.1
5-19	-900	1442	.99		25.2±1.2	14.3±1.1
5-20	-900	1421	.96	10.45±0.01 °	29.6±1.2	16.1±1.1
5-21	-1000	1489	1.00		31.2±1.2	16.1±1.1

Table A-V: Inventory of Input Parameters for Figure 7

Run: 30 June 1993 to 19 July 1993

Electrolyte - volume: 24.71 ± 0.01 ml

- composition: 0.053 M PdCl_2 + 0.602 M LiCl in D_2O with $T = 17.9 \pm 1.2$ dpm/ml

- additions: D_2O with 17.9 ± 1.2 dpm/ml

Separation factor $s = 0.67$

Sampling volume $V_s = 1.58 \pm 0.01$ ml

Sampling Date	i/mA	$\Delta t/\text{min}$	ϵ_r	V_s/ml	Tritium	dpm/ml
					Electrolyte	Gas
7-6	-0.5	1392			18.1 \pm 1.2	
	-1	1432				
	-2	5862				
7-9	-200	4227	.36	11.90 \pm 0.03	19.5 \pm 1.2	19.2 \pm 1.2
7-11	-200	2848	.78		20.4 \pm 1.2	15.9 \pm 1.2
7-12	-300	1476	.92	11.90 \pm 0.03	20.8 \pm 1.2	14.4 \pm 1.2
7-13	-400	1406	.95		20.6 \pm 1.2	13.8 \pm 1.1
7-14	-500	1515	.94	14.88 \pm 0.03	21.2 \pm 1.2	14.8 \pm 1.2
7-15	-600	1361	.98		21.3 \pm 1.2	14.2 \pm 1.2
7-16	-700	1421	1.00		21.3 \pm 1.2	14.9 \pm 1.2
7-17	-800	1329	.99	23.81 \pm 0.04	25.3 \pm 1.2	16.1 \pm 1.2
7-18	-900	1561	.99		24.4 \pm 1.2	15.9 \pm 1.2
7-19	-1000	1471	1.00		24.3 \pm 1.2	14.4 \pm 1.2

CALORIMETRY OF OPEN ELECTROCHEMICAL CELLS.

S. Szpak and P.A. Mosier –Boss
Naval Control, Command and Ocean Surveillance Center
RTD&E Division, San Diego CA 92152-6171

ABSTRACT

A special case of calorimetry of open electrochemical cells, that employing adiabatic enclosures, is examined. Conditions for an experimental realization of such enclosures is discussed in detail. Practical arrangement and method for data collection are presented.

1.0 INTRODUCTION

Following the announcement by Fleischmann and Pons(1) that anomalous effects, among them excess heat generation, can be observed when deuterium is electrochemically compressed in the Pd-lattice, the discussion of the calorimetry of open electrochemical cells became of considerable interest. A calorimeter is an apparatus designed to measure quantities of heat associated with the occurrence of specific processes (eg, heat of reaction, heat of absorption, etc.) or the property of matter (eg, specific heat). The basis for such measurements is the conservation of energy and requires knowledge of the process(es) under consideration, the sequence of events, the construction of the apparatus and the experimental procedure employed. In other words, the development of the calorimetric equation for an operating electrochemical cell employs conservation of energy and adjusts the applicable walls and constraints in a manner consistent with cell design and relevant experimental procedure(s).

2.0 PROCESSES IN OPEN ELECTROCHEMICAL CELLS

In the simplest arrangement, an electrochemical cell is a three phase, multi-component assembly wherein the charge transfer reaction(s) and associated transport processes occur. Initially, this system is in thermal, mechanical and chemical equilibrium. Upon initiation of current flow, significant changes in temperature and concentration take place, viz., the development of gradients which, in turn, initiate transport processes in the electrolyte phase and across the electrolyte/gas interface. The increase in the temperature arises from the irreversible processes: the joule heating, the electrodic processes and the exothermic absorption of deuterium by the palladium electrode as well as due to the exchange with the environment. In the absence of the electrolyte stirring, temperature and concentration gradients promote the development of convective flow. If the convective flow is sufficiently intense, it results in a uniform composition and temperature distributions throughout the electrolyte phase.

With the initiation of current flow, not only the equilibrium is disturbed but both the composition and temperature change with time. In particular, the removal of water from the electrolyte is by electrolysis and vaporization. These processes reduce the electrolyte volume by $dV^{(1)}$ while the volume of the gas phase is increased by $dV^{(2)}$, their sum being calculated from the quantity of charge transferred, faradaic efficiency and the gas laws. A constant pressure can be maintained by adjusting (reversibly) the position of a piston or allowing the outflow of gas from the cell head space. (Note: thermal effects associated with the change in the electrolyte composition due to water removal, are neglected).

3.0 CONSERVATION OF ENERGY

Equilibrium state in any system is completely characterized by the internal energy, U , the volume, V , and the mole number, n_j , of chemical components, ie, $U = U(T, V, n_j)$, of which the first differential is

$$dU = \frac{\partial U}{\partial T} \Big|_{V,n_j} dT + \frac{\partial U}{\partial V} \Big|_{T,n_j} dV + \sum_j \frac{\partial U}{\partial n_j} \Big|_{T,V} dn_j \quad (1)$$

where: $\frac{\partial U}{\partial V} \Big|_{T,n_j} = -p$; $\frac{\partial U}{\partial n_j} \Big|_{T,V} = \mu_j$ are the intensive parameters. In the energy representation, the independent variables are the extensive properties with the intensive properties as derived quantities.. If a constant pressure processes are examined, the use of the enthalpy function is more convenient. In the enthalpy representation, the pressure is substituted for volume, ie, $H = H(T, p, n_j)$. Both quantities, U and H , are unambiguously defined in closed and open systems because the changes in state variables are independent of whether the change in composition, dn_j , is due to an exchange or chemical reaction. Consequently, in open systems, the only valid statements are:

$$U = \sum U^a ; H = \sum H^a ; H^a = U^a - \sum_j L_j^a l_j^a ; \alpha = 1, 2, \dots ; j = 1, 2, \dots$$

while terms “work” and “heat” are ambiguous. The ambiguity is removed. however, if we define work and heat by

Eqs. (2) and (3) respectively

$$dW = \sum_j L_j dl_j + dW_{diss} + dW_a \quad (2)$$

and

$$dQ = dU - dW - \sum_k \frac{\partial U}{\partial T} \Big|_{V,n_j} dT + Vdp + \sum_j \frac{\partial U}{\partial n_j} \Big|_{T,V} dn_j \quad (3)$$

and, if it is understood that dW measures the work that would have been done if the system under consideration were closed(2,3).

While the infinitesimal change in the internal energy is given by Eq. (1), the change in the enthalpy ($H = U + pV$), is given by Eq. (4)

$$dH = \frac{\partial U}{\partial T} \Big|_{V,n_j} dT + Vdp + \sum_j \frac{\partial U}{\partial n_j} \Big|_{T,V} dn_j \quad (4)$$

which, at $p = \text{const.}$, because of the equality $\frac{\partial U}{\partial n_j} \Big|_{T,V} = \frac{\partial H}{\partial n_j} \Big|_{p,T} = \mu_j$ becomes Eq. (5)

$$dH(T, n_j) = \frac{\partial H}{\partial T} \Big|_{n_j} dT + \sum_j \frac{\partial H}{\partial n_j} \Big|_T dn_j \quad (5)$$

4.0 FORMULATION OF CALORIMETRIC EQUATION

In deriving the calorimetric equation, we balance the change in the enthalpy of the electrolyte phase with the enthalpy gain or loss attributed to the participating processes. In particular, applying the enthalpy balance to an open electrochemical system (not including cell walls and electrodes), illustrated in Fig. 1, we obtain, with $dn_j < 0$

$$\frac{\partial H^{(1)}}{\partial T} \Big|_{n_j} dT - \sum_j \frac{\partial H^{(1)}}{\partial n_j} \Big|_T dn_j = dH^* - dw + \sum dH^{(1 \rightarrow v)} + \sum dH^{(1 \rightarrow e)} \quad (6)$$

where dH^* is the energy produced (excess enthalpy), dw is the work done on the surroundings, $\sum dH^{(1 \rightarrow v)}$ is the enthalpy transferred between the electrolyte and gaseous phases and $\sum dH^{(1 \rightarrow e)}$ is the enthalpy transferred to or from the environment. The direction of transfer determines the sign, viz., the quantity removed from the system is negative. As written, the left side of Eq. (6) denotes change in the enthalpy that is measured. The right hand side contains contributions attributed to known as well as unknown processes, including the term representing an excess of enthalpy. The corresponding change in the gas phase is

$$\frac{\partial H^{(v)}}{\partial T} \Big|_{n_j} dT + \frac{\partial H^{(v)}}{\partial n_j} \Big|_T dn_j = \sum dH_j^{(1 \rightarrow v)} + \sum dH_j^{(1 \rightarrow e)} \quad (6a)$$

In formulating the calorimetric equation, only the rate of the enthalpy change in the electrolyte phase is considered. By dividing each term of Eq. (6) by dt , and identifying participating processes, we obtain the governing differential equation, Eq. (7)

$$\frac{\partial H^{(1)}}{\partial T} \cdot \frac{dT}{dt} - \sum_j \frac{\partial H^{(1)}}{\partial n_j} \cdot \frac{dn_j}{dt} = J^* + I(E_c - E_{th}) + \sum_j J^{(1 \rightarrow 2)} + \sum_j J^{(1 \rightarrow e)} \quad (7)$$

The information sought to confirm the initiation of the F-P. effect, is the numerical value of the first term on the right hand side, J^* . (For completeness, the J^* term includes also thermal effects arising from the interaction between the adsorbed-absorbed deuterium and palladium lattice.)

5.0 REMARKS CONCERNING THE OPEN CELL CALORIMETRY

The solution of Eq. (7) requires specification of the initial conditions and evaluation of all other terms consistent with the mode of operation and cell design. The initial conditions are the equilibrium conditions, ie, the temperature of the whole system is that of the environment and the composition of gas phase is $D_2: O_2 = 2:1$ with the D_2O vapor in equilibrium with the electrolyte. The rate of heat transfer out of the cell depends on the cell geometry, construction of the enclosure and mode of transport. The simplest case is that of an adiabatic wall. If, however, the enclosure is a diathermal wall, then the heat transfer may occur either via radiation with some convective contributions or via convection with minor radiative contributions.

The criticism of the open cell calorimetry is centered around the assumption of a steady state heat transport to the environment and the selected calibration procedure. To assure correct interpretation of thermal behavior of the electrolyte phase it is necessary to know the rate controlling process, its temperature dependence and relaxation time. The concept of the relaxation time is well defined in thermodynamics, viz., the relaxation time expressed in terms of variable, $\xi(t)$, is the decrease of its value to the equilibrium (or the steady state) value, ξ_{eq} . The approach to the equilibrium follows an exponential law $\xi(t) = \xi_{eq} + Ce^{-t/\tau}$ where C is the integration constant and τ is the relaxation time. The temperature dependence of the terms in Eq. (6/7) is discussed below.

5.1 Heat Content of the Electrolyte Phase

As written, the first term on the left hand side represents the rate of change in the heat content of the electrolyte as a function of time, evaluated at temperature $T(t)$. Assuming a 100% faradaic efficiency, the consumption of solvent equivalent, $s = D_2O$, in a cell operating for time t seconds at the current density, I amperes, is: $It/2F$, so that the rate of change in the electrolyte heat content is

$$m_o c_s \left(1 - \frac{It}{2Fm_o} \right) \text{ where } m_o \text{ is the initial amount of solvent.}$$

5.2 Electrical Work, dw

An unique feature of an electrochemical cell is the occurrence of charge transfer reaction(s) whereby electrons generated at the negative are transferred in an external circuit and consumed at the positive electrode in another charge transfer reaction. In a steady state, the number of electrons leaving and entering the cell is the same which means that the electrochemical cell can be considered a closed system with regard to the electrical charge (potential difference build up occurs at the phase boundary only). Irrespective of the direction of current flow, the product, $I E_c$, must be a positive quantity. By convention, the positive current is flowing out of the cell, so that the electrical work term in Eq. (7) is positive. The enthalpy input to the cell, expressed as an electrical work and corrected for the recoverable enthalpy is $I(E_c - E_{th})dt$, where $E_{th} = -\Delta H/zF$ is the thermoneutral potential.

5.3 Rate of enthalpy transfer, $J^{(1 \rightarrow v)}$, $J^{(1 \rightarrow e)}$

In the system under consideration, the $J^{(1 \rightarrow v)}$ – term represents the sum of the enthalpy carried out by the rising gas bubbles, saturated with D_2O vapor at the cell temperature and that due to the phase

change: $D_2O(s) \rightarrow D_2O(v)$. The respective rates are: $\frac{I}{F} \left[\frac{1}{2} c_{D_2}^{(v)} + \frac{1}{4} c_{O_2}^{(v)} + \frac{3}{4} \frac{p}{p^* - p} c_{s,g} \right]$ and

$$\frac{3}{4} \frac{I}{F} \frac{p}{p^* - p} \cdot L^{(1 \rightarrow v)}.$$

Parenthetically, we note that excluding chemical reaction(s) in either system and the energy transfer from the environment, we have for the mass balance and mass flux, Eq. (8)

$$dn_k^{(1)} + dn_k^{(2)} = 0; J_m = dn^{(1)}/dt = - dn^{(2)}/dt \quad (8)$$

and for the enthalpy transfer, Eq. (9)

$$\left[dq^{(1)} + \sum_k \left(\frac{\partial H}{\partial n} dn \right)^{(1)} \right] + \left[dq^{(2)} + \sum_k \left(\frac{\partial H}{\partial n} dn \right)^{(2)} \right] = 0 \quad (9)$$

from which the heat flux, $J_q^{(1 \rightarrow 2)}$, is given by equation

$$J_q^{(1 \rightarrow 2)} = - \sum_k \frac{\partial H}{\partial n} \cdot J_m^{(1 \rightarrow 2)} \quad (10)$$

Equation (10) states that the equality: $dq^{(1)} = dq^{(2)}$ can occur only in the absence of mass transport. The $J_q^{(1 \rightarrow e)}$ – term is, as a rule, of the form of the generalized Ohm's law, ie. $J_q^{(1 \rightarrow e)} = k(T^{(1)} - T^{(e)})$, where k is usually taken to be a constant within the temperature range $(T^{(1)} - T^{(e)})$. Its numerical value depends upon the composition of the wall with the applicable computation methodology described in textbooks on heat transfer.

5.5 Temperature Dependent Parameters

Excluding the J^* – term, all terms on the right hand side of Eq. (7) are temperature dependent in a simple way except for the $I(E_c - E_{th})$ – term. The temperature dependence of the specific heat is usually taken as a linear function of temperature. The term, accounting for the enthalpy transport to the vapor phase, consists of two parts: $J_1(I, T)^{(1 \rightarrow v)}$ and $J_2(p^*, T)^{(1 \rightarrow v)}$ of which $J_1^{(1 \rightarrow e)}$ identifies the small amount of heavy water evaporating into the D_2 and O_2 gas bubbles. This term is a function of the cell current and temperature and is negligible, except at higher solution temperatures and current densities. The second contribution, $J_2^{(1 \rightarrow e)}$ denotes the loss of water due to evaporation. The rate of

evaporation is proportional to the solution temperature and as the solution temperature approaches the boiling point, the $J_2^{(1 \rightarrow e)}$ term dominates. The $p(T)$ dependence is calculated using the ClausiusClapeyron formula, $dp/dT = L/T[v^{(g)} - v^{(s)}]$. The contribution $J_2^{(1 \rightarrow e)}$ can be evaluated quite easily, but not the $J_1^{(1 \rightarrow e)}$ because of a number of factors must be considered, among them the size of gas bubbles, the degree of their saturation, etc.

Less clear is the temperature dependence of the term $I(E_c - E_{th})$. Employing the procedure adapted by Pons and Fleischmann(6), the correction factor is

$$\psi = \left\{ \frac{dE_c}{dT} + \frac{3}{4F} \cdot \frac{d}{dT} \left[\frac{P}{p^* - p} (c_s^{(v)} \Delta T + L^{(1 \rightarrow v)}) \right] \right\} \Delta T.$$

This procedure involves expanding the temperature dependent $(E_c - E_{th})$ term into the Taylor series, retaining the first term only on account of smallness of ΔT and expressing E_{th} by the change in the enthalpy function of the electrolyte due to the increase by ΔT . It is noted that, if a chemical (electrochemical) reaction occurs at a constant pressure and temperature, the heat of reaction is the change in enthalpy while the change in mole number is the change in the Gibbs function.

5.6 Complete Calorimetric Equation

The expression for a complete energy/mass balance is obtained upon integration of

$$\left[\sum m_i c_i \frac{dT}{dt} \right] + m_o c_s \left(1 - \frac{It}{2m_o F} \right) \frac{dT}{dt} - \frac{c_s IT}{2F} = J^* + I(E_c - E_{th} + psi) + \sum J^{(1 \rightarrow 2)} + \sum J^{(1 \rightarrow e)} \quad (11)$$

where the first term accounts for the contribution of all cell components except the electrolyte. This term must be carefully evaluated during the course of long term experiments and, in particular, during the calibration procedure because the relaxation time is strongly affected by the physico-chemical properties of walls and enclosures. Note: henceforth superscript (2) is employed to identify the bath as separate from the environment.)

6.0. CALORIMETER DESIGN AND MODELING

Consider a system consisting of an electrochemical cell containing a known amount of electrolyte and totally immersed in a water bath. Initially, this system is in equilibrium and, for the duration of an experiment, the bath is in contact with an infinite heat sink. (ie, $T^{(e)} = \text{const}$). Applying the conservation of energy, in the form of condensed Eq. (6/7), the rate of the temperature change with time in the cell, after its activation, is

$$C_1 \frac{dT_1}{dt} = Q_1 - J_q^{(1 \rightarrow 2)} - J_q^{(1 \rightarrow 3)} \quad (12)$$

and in the water bath

$$C_2 \frac{dT_2}{dt} = Q_2 + J_q^{(1 \rightarrow 2)} - J_q^{(2 \rightarrow e)} \quad (13)$$

where $C_1 = \sum m_{1,i} c_{1,i}$ is the heat capacity of the electrolyte and includes all cell components (cell constant), C_2 is the heat capacity of the bath fluid, $Q_1 = [J^* + I(E_c - E_{th})]$ denotes the rate of heat production in the electrolyte phase, Q_2 is the heat supplied to the bath in order to maintain $T^{(1)} = T^{(2)}$, and the J 's are the heat fluxes exchanged between system elements, viz., the electrolyte, bath and environment.

6.1 Construction of an Adiabatic Wall

Equation (12) is the energy balance expressed in terms of the rate of heat generation due to the irreversibilities of the charge transfer process(es), the rate of heat exchange between the cell and the water bath, and the rate of heat loss to the environment. Since the term, Q_1 is always positive, it follows that $T^{(1)} > T^{(2)}$ resulting in an outflow of heat generated within the cell. The construction of an adiabatic wall requires that $J_q^{(1 \rightarrow e)} = J_q^{(2 \rightarrow 1)} = 0$ at all times. This requirement is fulfilled as long as $\Delta T = T^{(1)} - T^{(2)} = 0$, ie, as long as $J_q^{(2 \rightarrow e)} = Q_2 - C_2(Q_1 - J_q^{(1 \rightarrow e)})/C_1$ which, for $Q_1 \gg J_q^{(1 \rightarrow e)}$, is further simplified to $J_q^{(2 \rightarrow e)} = Q_2 - C_2 Q_1 / C_2$ and provides a rough guide for design and operation of an adiabatic wall separating the cell from bath. In practice, $\Delta T \neq 0$; consequently, the maintenance of an adiabatic wall requires that $\int_t^{J^{(1 \rightarrow 2)}} dt = \int_t^{J^{(2 \rightarrow 1)}} dt$ ie, that ΔT oscillates about its zero value.

Employing, for thermal flux, an expression of the form $J = k\Delta T$ and introducing a new set of variables, viz., $\Delta T = T^{(1)} - T^{(2)}$ and $\theta = T^{(1)} - T^{(e)}$ with $T^{(e)} = \text{const}$, Eq. (12) becomes Eq. (14)

$$\frac{d\theta}{dt} = q_1 - k_{12}\Delta T - k_{1e}\theta \quad (14)$$

Using the same variables, by subtracting Eq. (13) from (12), we obtain an expression for the change in T , Eq. (15)

$$\frac{d\Delta T}{dt} = (q_1 - q_2) - (k_{12} + k_{12}^* + k_{2e})\Delta T + (k_{2e} - k_{1e})\theta \quad (15)$$

where $q_i = Q_i/C_i$; $k_i = k_i/C_i$ and $k^* = k_{12}/C_2 = k_{12}C_1/C_2$. Conditions forcing ΔT to oscillate about zero can be determined by solving the set of coupled differential equations, Eqs. (14) and (15).

To maintain an adiabatic wall, the positive ΔT due to $q_1 > 0$ must be countered by q_2 to reverse the direction of heat flow, Eq. (15). One way to construct and maintain an adiabatic wall is as follows: At $t < t_0$, the system is in equilibrium. At t_0 the flow of cell current is initiated causing the system's temperatures to rise (cf. Eq. (14)), as schematically shown in Fig. 2 by solid, $T^{(1)}$, and dashed, $T^{(2)}$, lines. At t_1 the difference ΔT reaches an a priori specified value, and the heat source in the bath, q_2 , is activated. If $q_2 > q_1$, then the temperature $T^{(2)}$ -rises faster than $T^{(1)}$, in time—at t_2 —reducing ΔT to zero. Within this time period there is net heat flow from the cell to the bath. To maintain an adiabatic wall it is necessary to transfer the same amount of heat from bath to cell ($H^{(1 \rightarrow 2)} = H^{(2 \rightarrow 1)}$) by activating the q_2 and operating it for a required time period. These periods are determined by numerically solving Eqs. (14) and (15).

Some useful information concerning the form of the $\Delta T(t)$ function can be derived if the cell temperature, θ , is considered a constant. Rewriting Eq. (15) in an equivalent form, Eq. (16)

$$\frac{d\Delta T}{a - b\Delta T} = dt \quad (16)$$

where $a = (q_1 - q_2) + (k_{2e} - k_{1e})$ and $b = (k_{12} + k_{12}^* + k_{2e})$, we obtain, upon integration Eqs. (17) and (18) for $q_2 = 0$ and for $q_2 > q_1 + (k_{2e} - k_{1e})\theta$, respectively.

$$\Delta T(t) = \frac{a}{b} + \left[\frac{a}{b} - \Delta T(0) \right] e^{-b(t-t(0))} \quad (17)$$

$$\Delta T(t) = -\frac{a}{b} + \left[\frac{a}{b} - \Delta T(0) \right] e^{-b(t-t(0))} \quad (18)$$

Evidently, the system relaxes with the characteristic time constant $= 1/(k_{12} + k_{12}^* + k_{2e})$; That is, the relaxation time is governed by the C_1/C_2 ratio, the cell temperature, materials of construction and the system's contact with the environment. For any selected $\Delta T^{(1)}$ there is a corresponding $\Delta T^{(2)}$ which assures that $(H^{(1 \rightarrow 2)} = H^{(2 \rightarrow 1)})$ is realized. For all practical purposes, this condition is satisfied by the requirement that $\Delta T(t)$ oscillates about zero.

6.2 Temperature Tracking

In any implementation of a calorimeter based on equations (14) and (15), a means of controlling the heat input to the bath surrounding the reaction cell must be provided so as to maintain the temperature difference, $\Delta T = 0$, or, at least, so that it averages to zero over an experimental run. Because of the large amount of temperature data required for an experiment, digital acquisition of the data is necessary; consequently, digital control of the experiment is a natural choice. In a digital system, the relevant temperature measurements are made in sequence in a repetitive cycle, with some dead time for writing data to a disk and the analog values are to the precision of the analog-to-digital converter being used. These two procedures should not be considered independently because often the truncation error exceeds the allowable temperature error and appropriate averaging is required. In order for averaging to improve a measurement, the analog signal must be dithered, either deliberately or by noise over a range corresponding to the least significant bit of the digitized signal. For example, with a twelve-bit analog-to-digital converter having an input of -20 to $+20$ mV, the least significant bit corresponds to a $10 \mu\text{V}$ input signal change or a change 0.25 C for a T-type thermocouple where the sensitivity is about $25 \text{ mC}/\mu\text{V}$. Typically, there might be present $10 \mu\text{V}$ rms noise referred to the input, so that averaging 100 samples would be expected to reduce the error to about 0.03 C without having to dither the input. Averaging 100 samples has other implications, however, since the averaging takes place over a range of temperature difference, ΔT , that depends on both, the cooling rate of the cell and the heating rate of the bath as given by Eqs. (14,15). On average, a temperature offset occurs that depends on whether T takes longer to recover from a positive value than from a negative value, which would increase the likelihood that the bath heater will be incorrectly turned on rather than incorrectly turned off. These effects exhibit temperature dependence that can be demonstrated in modeling the calorimeter by introducing truncation and noise into the test as to whether the heater should be on or off.

6.3 Calorimetry of Co-Deposition Process

The codeposition process is the process where the electroreduction of Pd^{2+} ions occurs simultaneously with the evolution of deuterium. The principal advantage of this technique is elimination of the prolonged charging time required for, and a better reproducibility of, the initiation of the Fleischmann-Pons effect. The codeposition process modifies somewhat the calorimetric equation, Eq. (7), making its interpretation less clear. The modification involves the $I(E_c - E_{th})$ term. The cell current is split into two currents, viz., I_1 , representing the rate of Pd^{2+} ion reduction and I_2 participating in the reduction of heavy water. The division of currents is potential and time dependent (6). However, as the concentration of Pd^{2+} becomes less, the I_2 current increases and, upon compilation of the codeposition, being equal to the cell current.

An example of thermal behavior during the codeposition process is illustrated in Fig. 3, where excess enthalpy is plotted against the energy supplied to the cell from an external source. During data collection the cell was isolated from the environment by adiabatic wall constructed in manner described above. Clearly, during the initial period, considerable portion of the total current was used up to reduce the Pd^{2+} ions, resulting in the negative excess enthalpy. However, with the passage of time, as I_1 became less, an excess enthalpy was measured. The rate of production was not uniform,

ie showing occasional small bursts, and, in general, became higher with an increase in cell temperature.

This example is included to demonstrate that useful information concerning thermal behavior of open cells can be obtained without elaborate instrumentation. Further discussion is outside of the scope of this communication and will be given elsewhere.

7.0 SUMMARY

A discussion of thermal behavior of open electrochemical cells employed to confirm and examine the Fleischmann–Pons effect for a special case of electrodes prepared by codeposition in is presented. The calorimetric equation, written in the enthalpy representation, contains statements of energy/mass conservation, accounts for participating processes and examines the relaxation times. Conditions for construction and data collection in the case of adiabatic enclosure are given. An example of the thermal behavior of the Pd/D system prepared by the codeposition technique showing substantial production of excess enthalpy is included.

Symbols

c - specific heat

C - cell constant, intergration constant

e - environment

F - Faraday constant

E - cell potential, V

H - enthalpy, Jmol⁻¹

I - cell current, A

j - running index

J - flux,

J* - rate of excess enthalpy production

k - coefficient

L - work coefficient, latent heat of vaporization

l - work coordinate

n - mole number

m - mass

p - pressure

Q - heat

q - heat source

s - superscript/subscript refers to solvent

T - temperature, K

U - internal energy

V - volume

W - work

α - phase (superscript)

$k = k_i/C_i$ - coefficient

$\theta = T^{(1)} - T^{(e)}$ temperature

μ - chemical potential

τ - relaxation time

ζ - variable

References

1. M. Fleischmann and S. Pons, *J. Electroanal. Chem.*, **261**, 301(1989)
2. H.B. Callen, **Thermodynamics**, John Wiley & Sons, Inc., New York – London - Sydney, 1966
3. R. Haase, **Thermodynamics of Irreversible Processes**, Addison-Wesley Publishing Co, Inc., Reading - Menlo Park-London, 1969
4. P. Van Rysselberghe, in **Modern Aspects of Electrochemistry**, Vol. 4, J.O'M. Bockris and B.E. Conway, eds., Plenum Press, New York, 1966
5. S.R. de Groot, **Thermodynamics of Irreversible Processes**, North-Holland Publishing Co, Amsterdam, 1952
6. S. Szpak, P.A. Mosier-Boss and J.J. Smith, *J. Electroanal. Chem.*, in the press

Figure captions

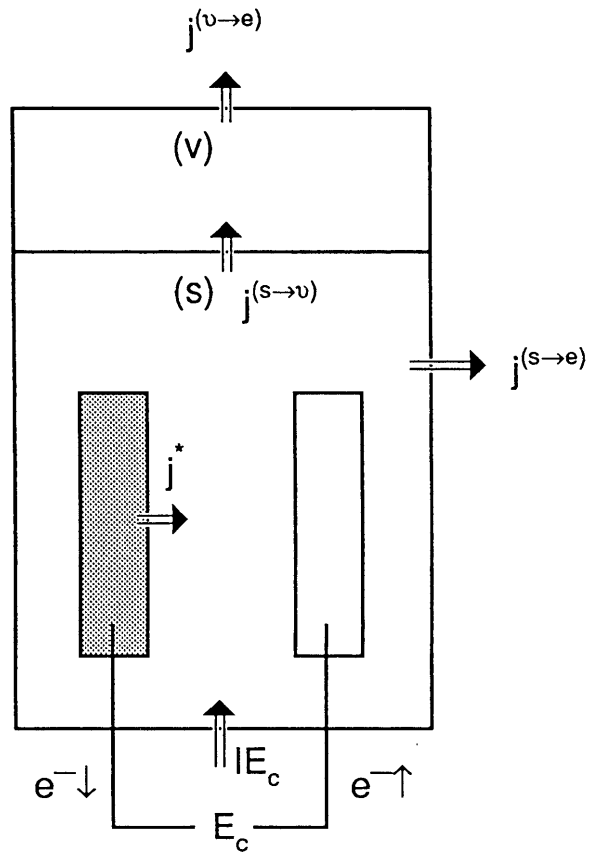
Fig. 1 -Thermodynamic boundary for open electrochemical cell system.

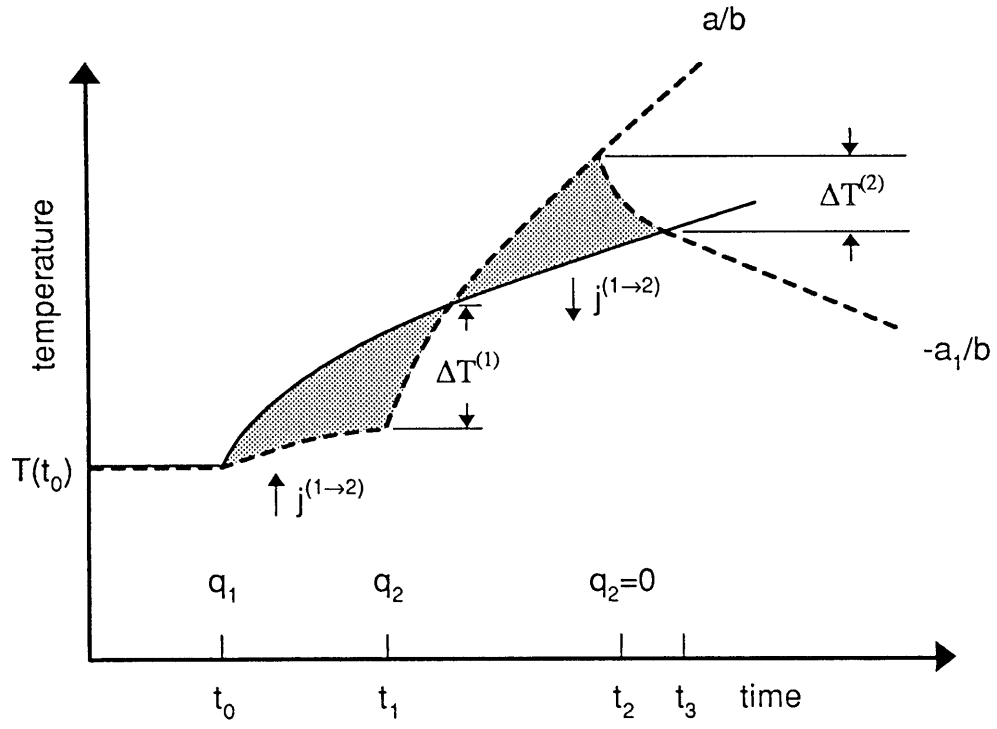
The J 's represent the rate of enthalpy transfer across boundary (system walls) indicated by the superscript

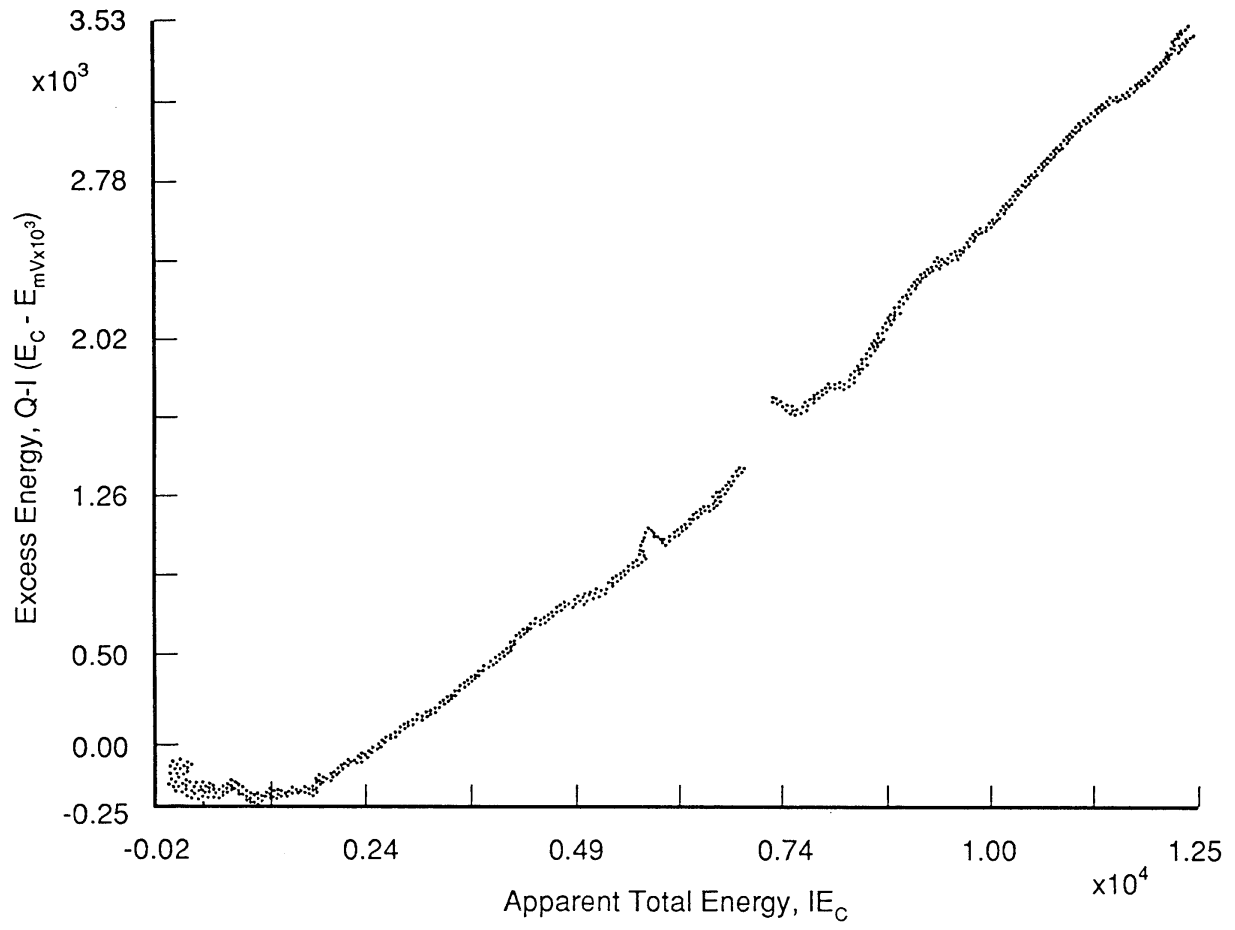
Fig. 2 -Temperature tracking to maintain an adiabatic wall ($1 \rightarrow 2$).

$\Delta T^{(1)}$ and $\Delta T^{(2)}$ are the temperature differences that trigger (on/off) the heat source in the bath

Fig. 3 - Excess enthalpy generated in the course of Pd/D codeposition from LiCl containing electrolyte.







ON THE BEHAVIOR OF THE CATHODICALLY POLARIZED Pd/D SYSTEM: SEARCH FOR EMANATING RADIATION

S. Szpak and P.A. Mosier-Boss

Naval Command, Control and Ocean Surveillance Center RDT & E Division

San Diego, CA 92152 - 5000

and

J.J. Smith

Department of Energy, Washington, DC 20585

ABSTRACT

Evidence for the emission of low intensity X-rays during cathodic polarization of the Pd/D system(s) is presented. The Pd/D system was prepared by charging with electrochemically generated deuterium both, palladium foil and palladium electrodeposited from D₂O electrolytes. Experimental and analytical procedures are described in detail.

1.0 INTRODUCTION

Production of excess energy in a cathodically polarized Pd/D system has been reported by Fleischmann and Pons(1). In particular, they stated that the energy delivered by cells in the course of their operation exceeds the energy input in amounts requiring the occurrence of nuclear events. The difficulty in accepting this view is the lack of correlation between the excess energy produced and the quantity of nuclear debris generated. Reported quantities of nuclear products, e.g., ${}^4\text{He}$, ${}^3\text{H}$, n^0 , γ -rays are so small that the energy generating process(es) could not be reconciled with known classical nuclear paths. However, irrespective of the origin of the source of excess heat production, the requisite energy deposited within the Pd- lattice should result in the emanation of X-rays arising from the disturbance of the electronic structure of the Pd/D system(2-5).

In this Letter, we present data collected in the investigation of the emanation of soft X- and γ -rays in the course of the Pd/D- codeposition and during the period of deuterium evolution on such electrodes reported by us previously(6). In support of our conclusions, we provide detailed information on cell design, data collection and examine the statistics of background radiation measured for a period of months. In the interpretation of the X-ray data we include also computer synthesis of events that tend to reproduce the experimentally observed spectra.

2.0 EXPERIMENTAL

The reported low level, burst-like events (eg., excess heat, tritium production) observed during cathodic polarization of the Pd/D system is expected to produce low level, intermittent emanation of γ - or X-rays. Thus, to minimize interference from background radiation, adequate shielding of the electrochemical cell and the detector is imperative. The detection of low level soft radiation requires a short distance between source and detector while to identify the nature of the energy generating processes, resolution in spectral lines is necessary.

2.1 BACKGROUND RADIATION – SHIELDING

Background radiation was monitored continuously by a NaI(Tl) detector placed in a lead-shielded cave and intermittently by Ge and Si(Li) detectors in a separate lead-shielded cave when the electrolytic cell was not in operation. Both caves, located approximately 2.0 meters from each other, were

shielded by ca 5 cm thick lead bricks. The Pb shielding reduced the background radiation, defined here as the spectrum recorded with the electrolytic cell in place but with no cell current, by a factor of twenty. Both detectors showed remarkably constant background over a period of several months. The γ - and X-ray detectors and the electrolytic cell remained in a fixed position during experimental runs. Examples of the background spectrum, recorded in the cave and covering regions 7 to 40 keV and 15 to 300 keV are illustrated in Figs. 1a and 1b, respectively. It is seen that the region 7 to 40 keV is featureless; in contrast, the region between 15 and 300 keV exhibits well defined peaks.

2.2 Radiation Detection; X-, γ -rays

The procedure and data reduction are as follows: Signals from the p-type high purity Ge detector (HPGe – EG & G Ortec) with crystal dimensions: 5.8 cm dia and 6.8 cm length, are amplified and analyzed by a Davidson portable multichannel analyzer using 4096 channels with a gain of either 30 or 300. Other features: the crystal has an absorbing layer of Al (1 mm) and inactive Ge (0.7 mm); the number of equivalent attenuation lengths equals to 13, 1.9 and 0.6 at 20,40 and 60 keV, respectively. The relative efficiency of the crystal is 37% at 1.33 MeV (defined as Ge efficiency/3 “x3” NaI(Tl) at 25 cm). The spectral data are recorded on mini-cassette tape and transferred to a personal computer work station for processing. Cell spectra which have equivalent calibration parameters are compared with the background spectrum on a bin-by-bin basis using the standard χ -square distributed test statistics. The signed square root of the test statistics for each bin is plotted in units of standard deviation as a function of bin energy. Procedures and data reduction for the continuous monitoring of background radiation by the NaI(Tl) detector (2”x8” crystal coupled to RCA 8575 PMT) are as follows: PMT signals are amplified and analyzed with a Nuclear Data Portable MCA using 512 channels. Spectral data (50 – 1500 keV) are recorded on minicassette tape for further processing. Each data accumulation periods count rate for 75 – 1500 keV range is calculated and plotted. The intensity of the X-rays flux was measured with a Si(Li) detector, (Kevex model PSI – amplifier model 4561), placed in close proximity to the operating electrochemical cell.

2.3 Cell Design

Three types of electrochemical cells were employed. The first type, shown in Fig. 2a, was designed to provide overall information on spectra up to ca 3000 keV and to monitor the temperature of cell elements in order to observe, in a crude fashion, time dependent heat generation in the course of Pd/D codeposition, respectively electrolysis of D₂O. For this purpose, the working Pd electrode and the spirally wound Pt counter electrode were centrally located and the thermocouples attached accordingly.

In the second design, Fig. 2b, the working and counter electrode assembly was modified to provide an open structure of the counter electrode. A flat foil, instead of a cylinder, was used as the working electrode. The uniformity of the charging current was realized by maintaining a uniform distance between electrodes. This design allowed us to record lower energy levels of the emitted X-rays by placing the whole electrode assembly within 0.5 to 0.7 cm of the detector beryllium window. However, the increase in the sensitivity was at the expense of temperature measurements; the latter was monitored in the electrolyte phase only.

Finally, to extend the detection capabilities to still lesser intensities of radiation flux and lower energy levels, the third design employing a cathode in the form of open wire mesh and placed in close proximity to a thin, ca 0.03 mm wall cell made of Mylar, Fig. 2c, was introduced. The cell design differs from that used by Bennington et al (2) or Ziegler et al(7) in two ways: it assures a more uniform distribution of the charging current density and, because of the open structure of the working

electrode and the close proximity to the detector, it substantially reduces the attenuation of X-rays while maintaining uniform current density.

The cells were connected to a power source and operated under either potentiostatic or galvanostatic control (EG & G model 362). Only a limited set of calorimetric data could be secured in the cells designed for the detection of electromagnetic radiation. Of these designs, Figs. 2a to 2c, the calorimetric data recorded for the cylindrical electrodes, Fig. 2a, are deemed to be more reliable than the designs employing mesh electrodes. The cell current, potential and temperature were recorded every 10 minutes.

3.0 RESULTS

In what follows, we consider observations made on Pd electrodes prepared by (i) electrodeposition from an aqueous solution of $\text{Pd}(\text{NH}_3)_4\text{Cl}_2$ at low current densities (eg, $200 \mu\text{A cm}^{-2}$) for a period of ca 20 hours followed by codeposition from D_2O -electrolyte for the spectral region 15 – 3000 keV; (ii) using commercially available Pd foil for spectral region 15 – 300 keV; and (iii) codeposition of Pd/D from $\text{PdCl}_2\text{-LiCl-D}_2\text{O}$ solution for the spectral region 7 – 40 keV.

3.1 Spectral Region: 15 – 3000 keV

The first set of experiments was designed to provide an overview of the electromagnetic spectrum associated with events occurring during the cathodic polarization of the Pd/D system. The effect of two charging techniques was examined, viz., charging by a codeposition process and by absorption of electrochemically generated deuterium. It is noted that these two techniques produce vastly different surface morphologies: in the first case, a dendritic surface is created(6) and in the second case, prolonged charging promotes the formation of surface fissures(8). In both cases, the spectral region 15 – 3000 keV, after subtraction of background, was featureless. Examining the data in terms of counts per second, we note an overall $1.8 \pm 0.1 \%$ increase in the count rate during the cell operation, Figs. 3a and 3b.

While an increase in the count rate (ca 4 %) occurred shortly after the initiation of the Pd/D codeposition process on a dendritic surface, Fig. 3a, several days of charging were required to observe the same effect on a smooth surface, Fig. 3b. Common features for the two surface morphologies are (i) low level radiation as evidenced by the increase in the count rate and the effect of surface active agents, eg, thiourea, on the initiation and/or re-activation of the X- ray producing process(es), Figs. 3b and 3a respectively. Of interest is the thermal behavior observed on dendritic surface. As shown in Fig. 3a, the ca 4% increase in the count rate terminated after the completion of the codeposition process (ca 50 hours). During the Pd/D codeposition, the count rate was not affected by the cell current profile and the emitted radiation is not accompanied by excess enthalpy production, as inferred from the lower temperature of the working electrode as compared with the electrolyte phase. After completion of the codeposition process, a decrease in the count rate is observed. The addition of thiourea resulted in an increase in count rate and the temperature of the bulk electrode exceeded the temperature of the electrolyte, clearly indicating the excess enthalpy production. Similarly, in Fig. 3b, an increase in count rate is observed with the addition of thiourea.

3.2 Spectral Region: 15 – 300 keV

Analyses of the 15 – 3000 keV spectral region indicate that the increase in count rate occurs at low energy. To gain further insight into this spectral region, we redesigned the cell to reduce the attenuation of the radiation flux, Fig. 2b, and to increase the reliability of conclusions by employing two independently operating detectors capable of viewing overlapping regions, viz., one for the X-ray and

one for the γ -ray regions. Four experiments, each of ca one month duration, showed the same characteristic features, namely a simultaneous increase of the count rate as observed by both detectors. In this set of experiments, a Pd foil was charged under controlled overpotential in the sulfate electrolyte with a varying amount of added BeSO_4 . Results, summarized in Fig. 4, are as follows: No radiation above background is noted during the initial period of charging (ca first eight days). The initiation of the radiation flux is triggered by the addition of BeSO_4 in the ppm concentration range. The flux intensity varies with time, being to some degree affected by the overpotential (also cell current). Upon subtraction of the background, no clearly discernible peaks were found within this spectral region.

3.3 Spectral Region: 7 – 40 keV

The electrolytic cell shown in Fig. 2c was employed to examine the low energy spectral region, eg., 7 – 40 keV. In all runs we observed an increase in the count rate especially in the low energy end. In some instances, as illustrated in Fig. 5, it appears that weak peaks are emerging, one at ca 11 keV, point A the other at ca 20 keV, point B. Of these peaks the position of point B is unchanged while that of peak A tends to shift to lower energies without clearly defined changes in experimental conditions.

4.0 DISCUSSION

Early investigations of the Fleischmann–Pons effect placed limited priority on monitoring X - rays emissions despite the recommendations of Miley et al.(10). The cells were designed for calorimetric work and not for monitoring soft X-rays. Nonetheless, there have been numerous attempts to verify the emanation of X-rays during the course of electrolysis by placing a film in the proximity of the cathode. However, as noted by Worledge(11), the expected 21 keV X-rays can only be seen in specially designed cells and only after long exposure times. Furthermore, blackening of photographic film is not always indicative of the emission of X-rays(12).

An electromagnetic flux emitted from cathodically polarized Pd/D electrode is a strong indication that a nuclear event(s) has occurred although, by itself, does not identify the event. More definitive information concerning the identification of events can be derived from the energy distribution of the emitted radiation. As a rule, without an a priori knowledge of the reaction path, most useful information is extracted from a wide energy spectrum. Here, we selected a spectral range of 15 – 3000 keV and employed a high resolution Ge detector for data collection and subsequent analysis.

4.1 METHODOLOGY OF MEASUREMENTS

Reliable analysis of low level radiation fluxes requires that the detectors and cell be shielded. However, even with shielding the background radiation arises from cosmic rays interacting with the heavy atoms of the shielding material, e.g., Pb, cf. Fig. 1b. To insure an acceptable interpretation of weak signals, a continuous and independent monitoring of background is needed, preferably by an instrument having higher sensitivity. For this purpose we selected the NaI(Tl) detector. In our experimental arrangement the background radiation, in identically shielded caves, was five times higher than when measured by the Ge detector. The argument usually offered for the rejection of the reported behavior of the polarized Pd/D system is that the low intensity of the radiant flux is, in reality, due to electrical noise. This argument is less compelling if a dual detection system is employed. Here, the dual system, consisting of Si(Li) and the Ge detectors, viewing simultaneously the electrochemical cell and operating independently from each other, exhibited the same behavior, ie, a simultaneous increase in the count rate as illustrated in Fig. 4.

4.2 ANALYSIS

Several factors support the argument that the observed increases in the count rates can be attributed to electromagnetic emanation from the cell. First, as shown in Fig. 4, there is definite correspondence

in count rates vs time between the X-ray and γ -ray detectors. Second, the additives, eg, thiourea and Be^{2+} ions, affect the intensity of the radiation flux, cf. Figs. 3 and 4. Third, the codeposition method of loading exhibited a shorter initiation time before the appearance of positive count rate deviations than the electrochemically charged electrodes; and finally, the increased count rates are observed sporadically, similar to other reported activities in these systems.

The low energy spectral distribution, cf. Fig. 5, reveals two features, viz., an increase in the count rate and the presence of rather weak peaks, one at ca 20 keV and another at ca 8 – 12 keV. This behavior is in general agreement with statements presented by others. For example, Bennington et al(2) stated: “any nuclear event depositing its energy within the Pd- lattice will, in theory, produce X-rays by refilling of the K_α -shell of the excited Pd atoms”. Buehler et al(3) noted that charged particles, generated in the course of a nuclear event, eg., p^+ , t^+ , α^{2+} -particles, would ionize the Pd atoms to produce the K_α or K_β X-rays. On the other hand, because of the high density of oscillating plasma, a broad energy spectrum is expected(4,5,14).

It can be shown, by computer simulation, that the spectrum illustrated in Fig. 5 can be interpreted as consisting of a weak peak(s) superimposed upon a featureless background, eg., the sharp peak of Pd- K_α superimposed upon the bremsstrahlung arising from the oscillating plasma of the cathodically polarized Pd/D system. To demonstrate we proceed as follows: First, as expected, the subtraction of two backgrounds recorded for the same arrangement within two time periods, is symmetrical around zero, Fig. 6a. Second, to simulate the bremsstrahlung, we recorded the thorium oxide spectrum, Fig. 6b. Third, the americium spectrum was selected to represent the contribution of sharp peak(s) as well as for calibration purposes, Fig. 6c. Finally, we added these spectra and subtracted the background, Fig. 6d. Evidently, the resulting spectrum exhibits the same or similar structure as that illustrated in Fig. 5. While this is not definitive evidence that Fig. 5 is a composite, it at least demonstrates that a spectrum consisting of a few energy peaks superimposed on a bremsstrahlung background is consistent with the observed spectrum shown in Fig. 5. Based upon the cell composition, the emerging point B, Fig. 5, is most likely the Pd- K_α peak. The identification of peak B is less certain. For example, employing the approximate formula relating the energy of the K series to the number of protons, Z, viz., $\text{Ry}(Z-1)^2$; $\text{Ry} = 13.5 \text{ eV}$ and found for the 11 – 12 keV energy the value of $Z = 28 - 30$. One of the elements having the required number of protons is nickel, used here as the substrate onto which the Pd/D system was deposited. However, energy of the Ni-K series is substantially less.

5.0 CONCLUSIONS

1. The cathodically polarized Pd/D system reliably emits broad energy X-rays distribution with an occasional emergence of recognizable peaks similar to those that can be created by computer synthesis. Because of the low intensity of the electromagnetic flux, its detection requires that cells be constructed accordingly.
2. As with other manifestation of an anomalous behavior, the emission of X-rays appears to be sporadic and of limited duration.
3. Codeposited Pd/D electrodes have much shorter initiation time; again in agreement with other manifestation of unusual activities. Surface morphology as well as impurities, eg Be, $\text{CS}(\text{NH}_2)_2$, are factors in the initiation of activities.

REFERENCES

1. M. Fleischmann and S. Pons, J. Electroanal. Chem., **261**, 301(1989)
2. S.M. Bennington, R.S. Sokhi, P.R. Stonadge, D.K. Ross, M.J. Benham, T.D. Beynon, P. Whithey, I.R. Harris and J.P.G. Farr, Electrochim. Acta, **34**,1323(1989)

3. D.B. Buehler, L.D. Hansen, S.E. Jones and L.B. Rees, **Is Reported "Excess Heat" Due to Nuclear Reactions?**, in **Frontiers of Cold Fusion**, p. 245, Universal Academy Press, Inc., Tokyo, 1993
4. Y. Kucherov, A. Karabut and I. Savvatimova, **Heat release and product yield of nuclear reactions in Pd-D systems**, in **Fourth ICCF**, Dec., 1993, Lahaina, Hawaii
5. J.-P. Vigier, **New Hydrogen Energies in Specially Structured Dense Media: Capillary Chemistry and Capillary Fusion**, in **Frontiers of Cold Fusion**, p. 409, Universal Academy Press, Inc., Tokyo, 1993
6. S. Szpak, P.A. Mosier-Boss and J.J. Smith, *J. Electroanal. Chem.*, **302**, 255(1991)
7. J.F. Ziegler, T.H. Zabel, J.J. Cuomo, V.A. Brusica, G.S. Cargill, E.J. O'Sullivan and A.D. Marwick, *Phys. Rev. Letters*, **62**, 2929(1989)
8. DR. Rolison, W.E. O'Grady, R.J. Doyle and P.P. Trzaskoma, **Anomalies in the Surface Analysis of Deuterated Palladium**, in **First ICCF**, p. 272, SaltLake City, UT
9. S. Szpak, P.A. Mosier-Boss and J.J. Smith, *J. phys. Chem.*, submitted
10. G.H. Miley, M.H. Ragheb and H. Hora, **On aspects of nuclear products**, in **First ICCF**, Salt Lake City
11. D.H. Worledge, **Technical status of cold fusion results**, in **First ICCF**, Salt Lake City
12. R.K. Rout, A. Shyan, M. Srinivasan and A.B. Garg, **Phenomenon of low energy emissions from hydrogen/deuterium loaded palladium**, in **Frontiers of Cold Fusion**, Universal Academy Press, Inc., Tokyo, 1993
13. R.K. Rout, A. Shyam, M. Srinivasan and A. Bansal, *Indian J. Technol.*, **29**, 571(1991)
14. R. Antanasijevic, I. Lakicevic, Z. Maric, D. Zevic, A. Zaric and J.-P. Vigier, *Phys. Lett. A* **180**, 25(1993)

FIGURE CAPTIONS

Fig. 1 – Background spectra in the Pb – cave.

a – featureless region 7 to 45 keV; Total count – $1.2 \cdot 10^4$; counting time – 361.2 hr

b – 0 to 300 keV region with spectral peaks unidentified; Total count – 1.06.106; counting time – 275.6 hr

Fig. 2 – Electrolytic cells

A – γ -ray detector; B – X-ray detector; C – reference electrode; Thermocouples: T_1 attached to the interior of the working electrode; T_2 immersed in the electrolyte; T_3 to measure cell wall temperature.

Fig. 2a – Centrally located electrodes assembly; Cell designed for examination of spectral region 15 – 3000 keV.

Fig. 2b – Movable electrode assembly: Closest approach of working electrode to detector window – 0.5 cm; Cell designed for spectral region 15 – 300 keV and provided with dual detection system.

Fig. 2c – Cell designed for detection of soft X-rays. The detector window separated from the working electrode by the thickness of Milar sheet.

Fig. 3 – Electromagnetic flux emitted during cathodic polarization of the Pd/D system; spectral region 15 – 3000 keV recorded by Ge detector. Cell design as Fig. 2a; electrode area – 2.51 cm^2 Ag deposited from cyanide solution at 2 mA cm^2 for 10 minutes; Pd layer deposited from a $\text{Pd}(\text{NH}_3)_2\text{Cl}_2 - \text{H}_2\text{O} - \text{LiCl}$ solution at $200 \mu\text{A cm}^2$ for 48 hours; cell current profile under galvanostatic control and electrolyte modifications indicated; background – solid circles; active cell – open circles

Fig. 3a – Electrolyte: $0.003\text{M PdCl}_2 - 0.3\text{M LiCl} - \text{D}_2\text{O}$ LiOD added after depletion of Pd^{2+} ions (indicated by an arrow); addition of $\text{CS}(\text{NH}_2)_2$ indicated by arrow.

Fig. 3b – Electrolyte: 0.1 M LiOD ; addition of $\text{CS}(\text{NH}_2)_2$ indicated

Fig. 4 – Electromagnetic flux emitted during cathodic polarization of the Pd/D system; spectral region 0 – 300 keV upper segment: spectral region 7 to 40 keV; lower segment: spectral region 40 – 300 keV.

Cell design – Fig. 2b; Electrode: Pd foil, area

Electrolyte: $0.3 \text{ M Li}_2\text{SO}_4 - \text{D}_2\text{O} - \text{Be}$ 100 ppm added as BeSO_4

Fig. 5 – Electromagnetic flux emitted during cathodic polarization of the Pd/D system; spectral region 7 – 40 keV Cell design – Fig. 2c

Fig. 6 – Computer simulation of the addition (superposition) of weak spectral lines to broad energy distribution (bremsstrahlung).

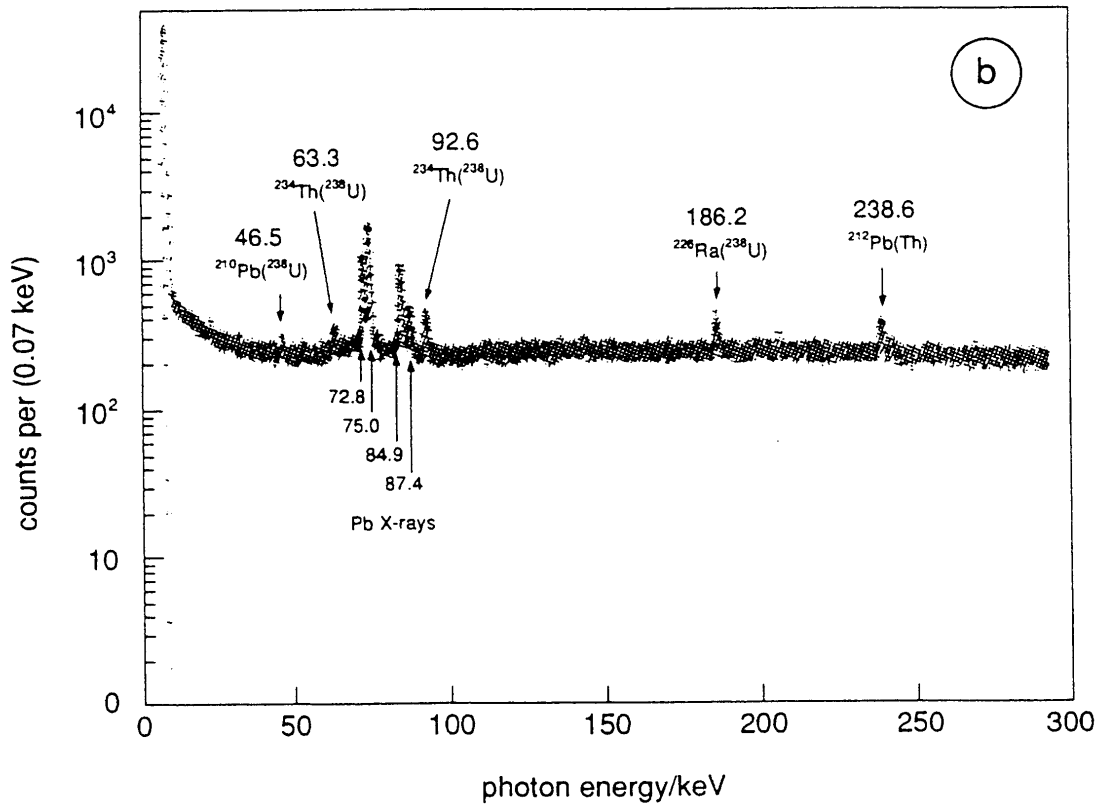
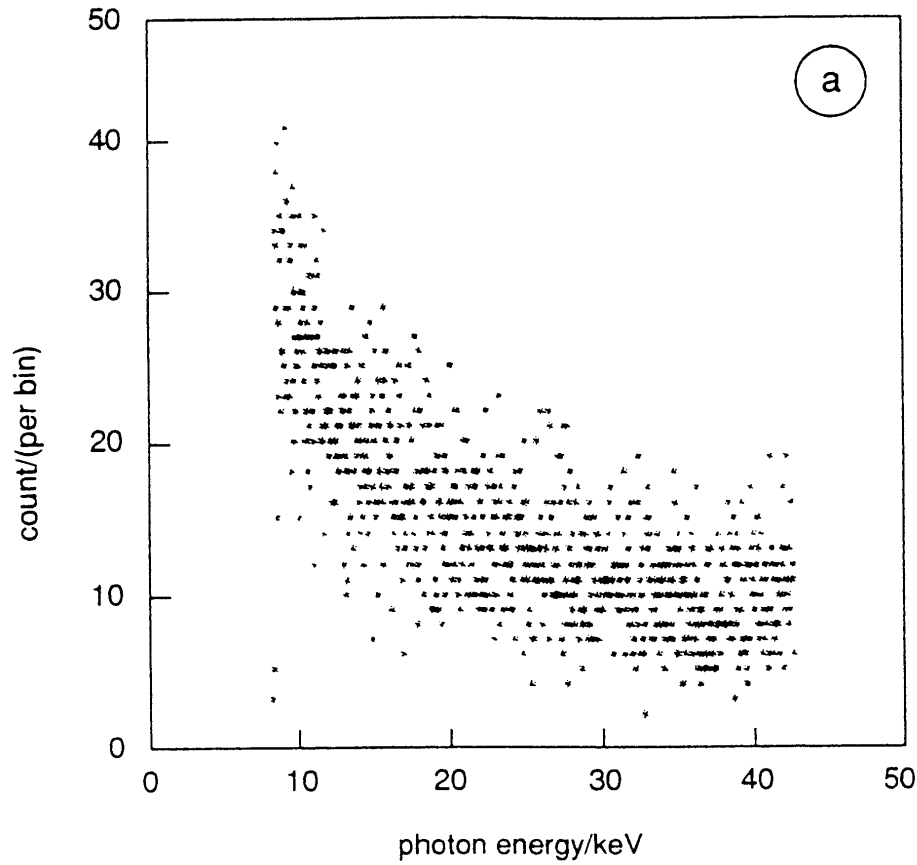
Fig. 6a – The difference of two background files illustrating a symmetric distribution about zero.

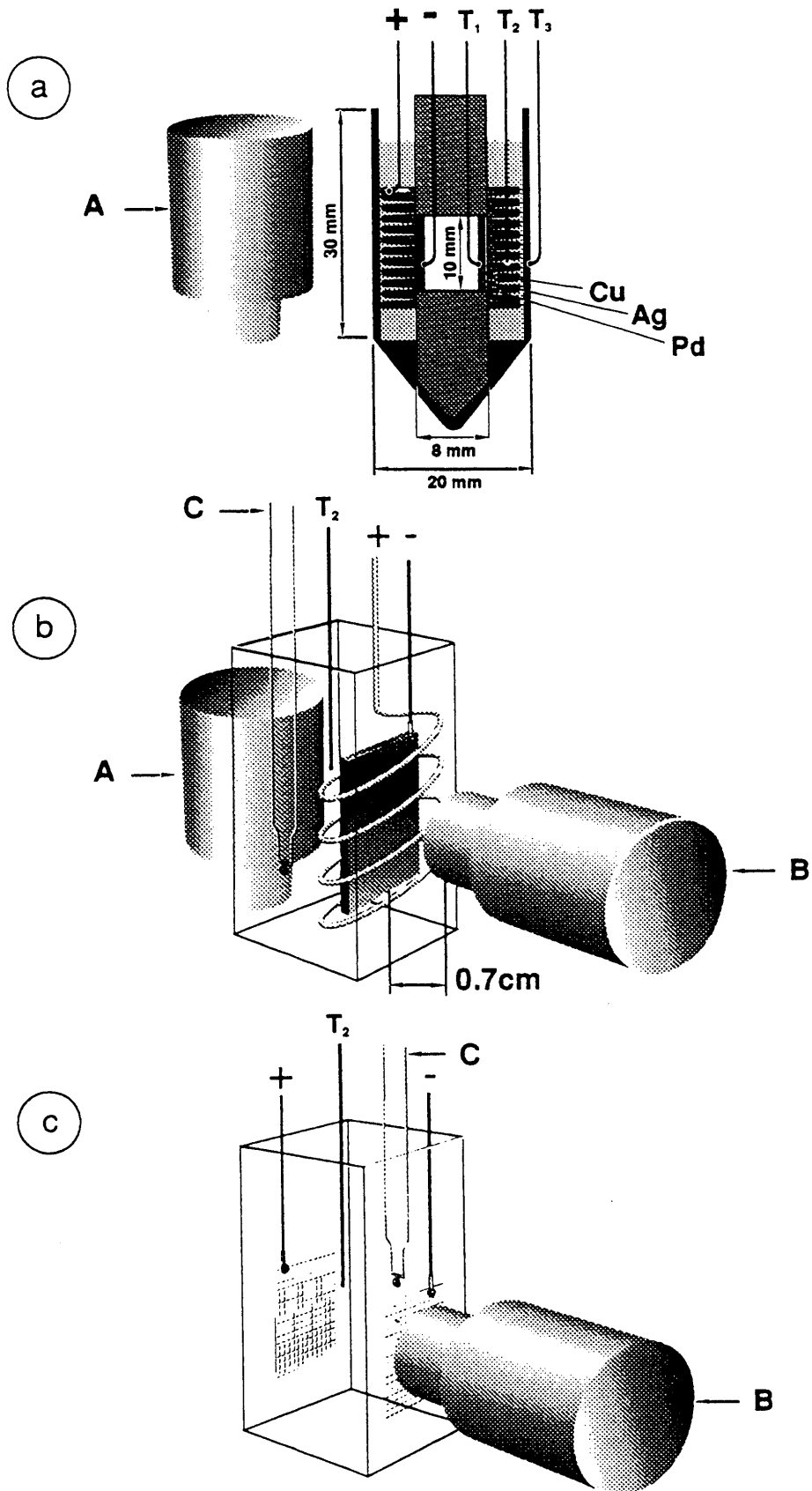
Fig. 6b – Energy distribution of X- emanating from thorium oxide

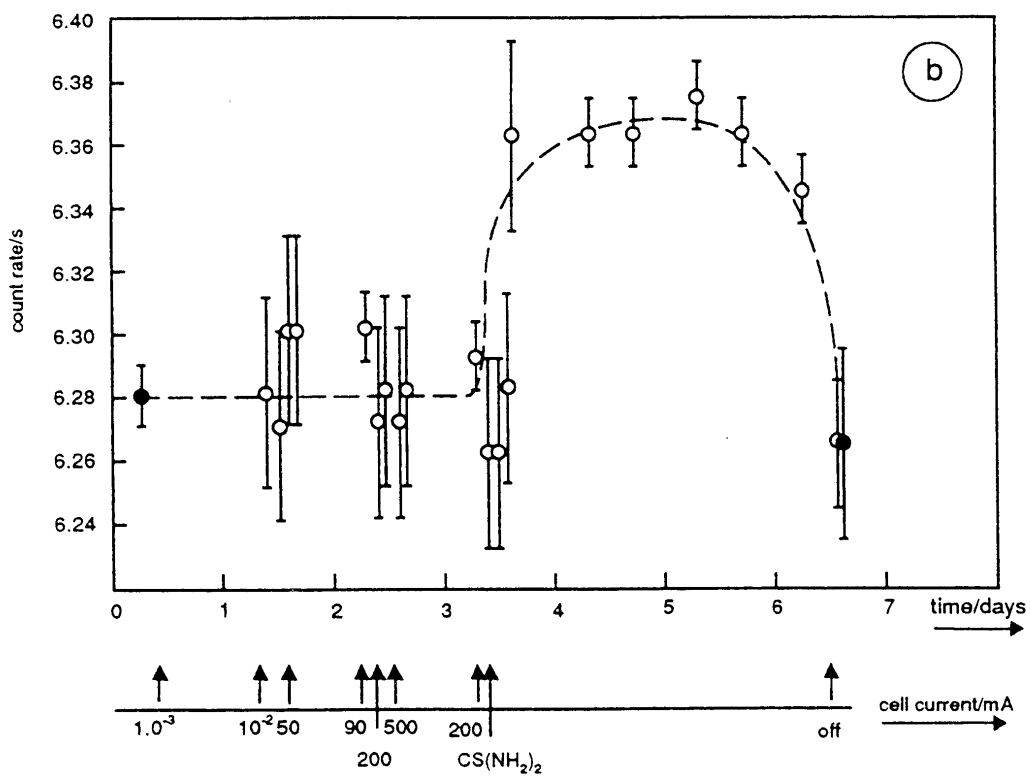
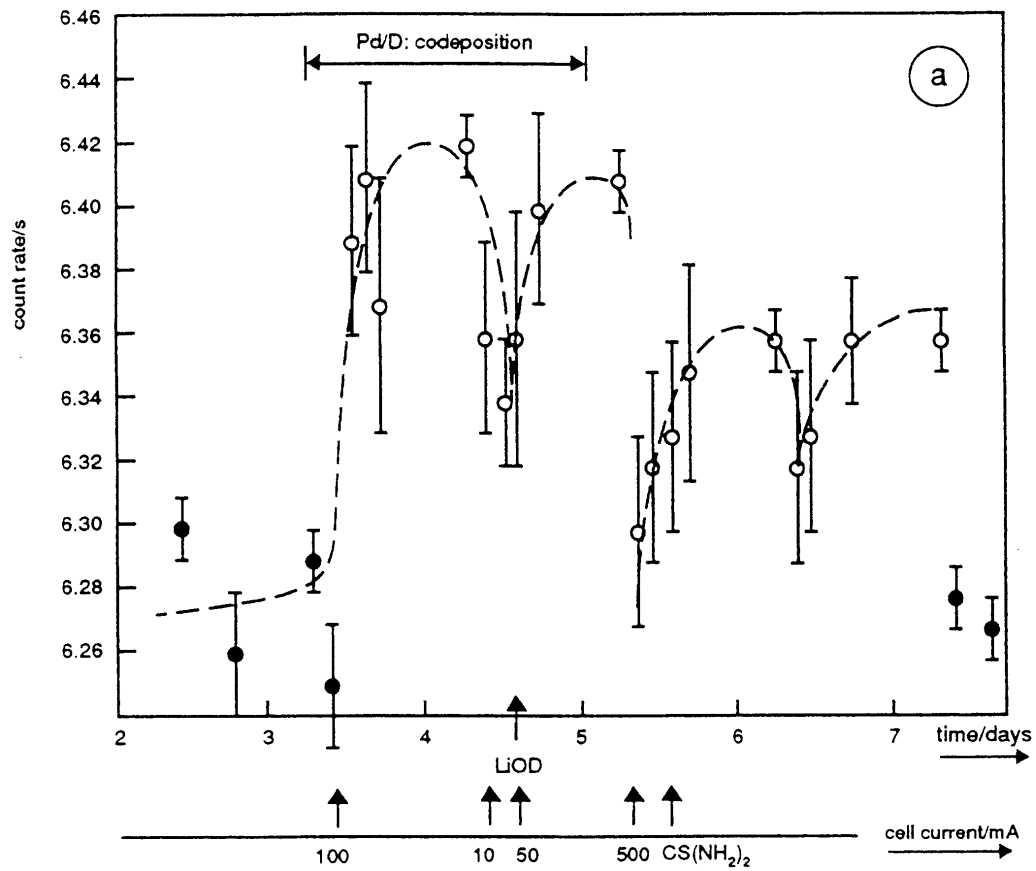
Fig. 6c – X-ray spectrum of Am.

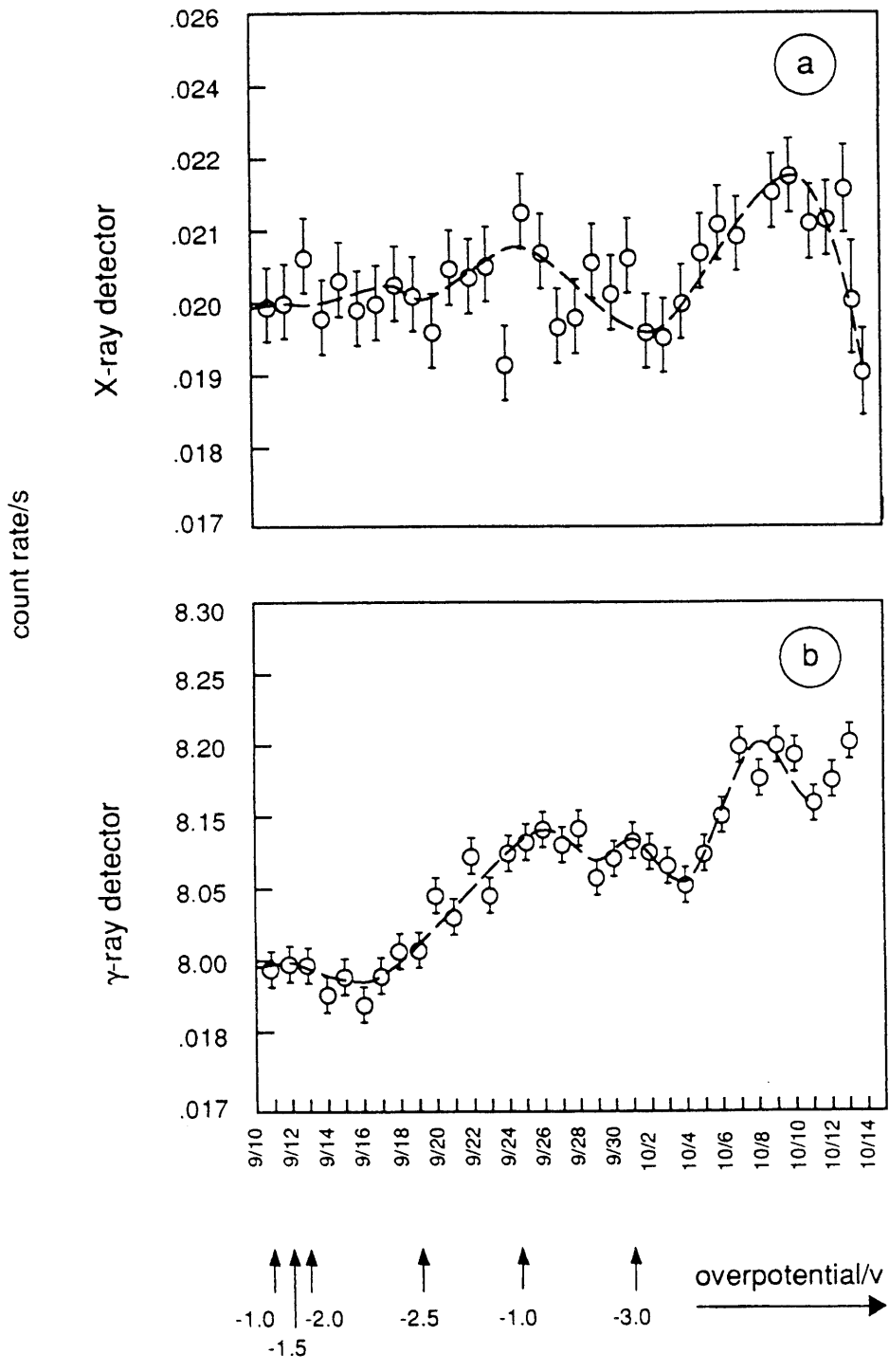
peakA – 13.76 keV $L_{\alpha 2}:L_{III}M_{IV}$; peak B – 17.71 keV $L_{\beta 1}:L_{II}M_{IV}$

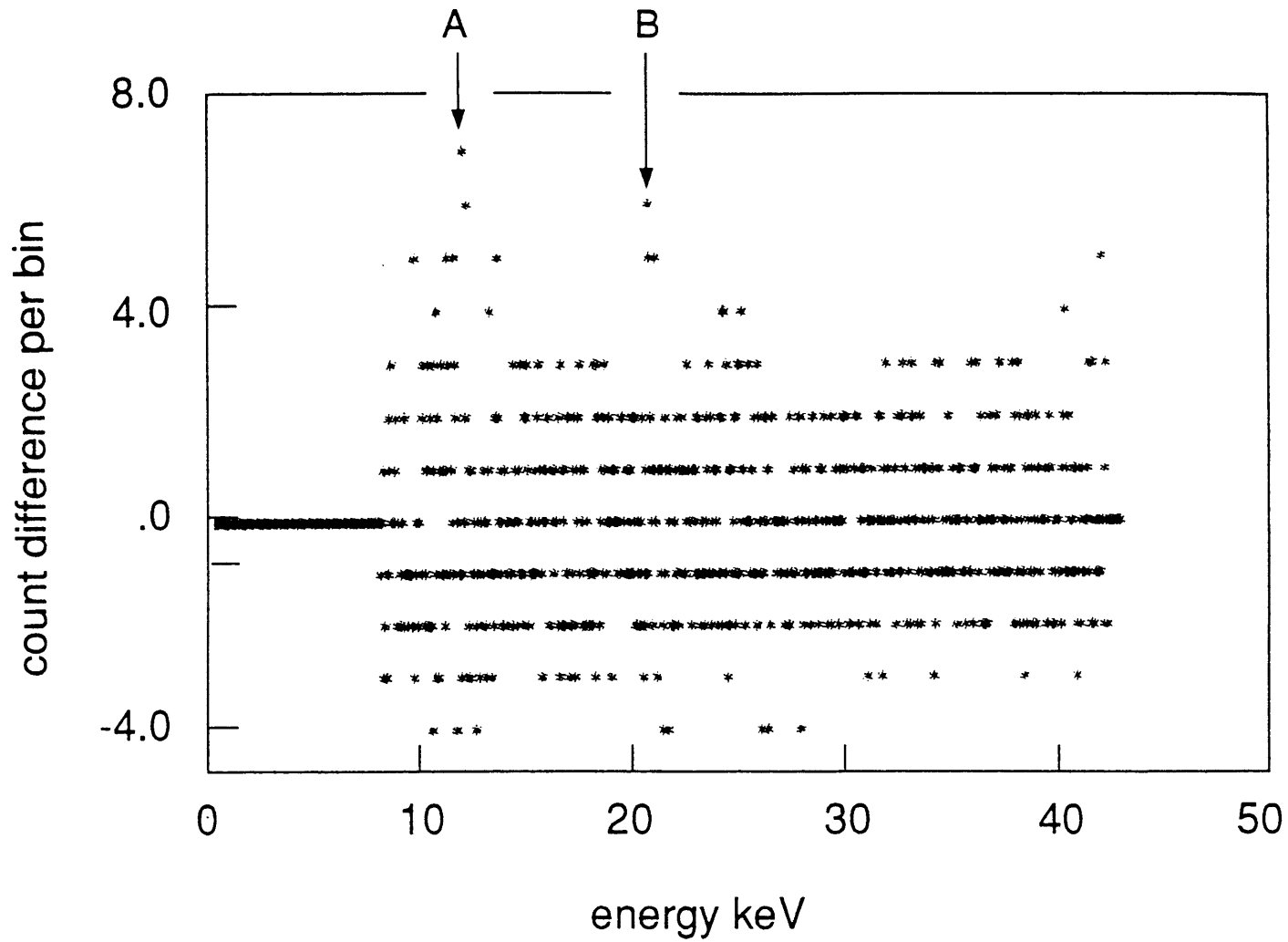
Fig. 6d – Computer simulated energy distribution for a sum of: 0.0015 Am spectrum (cf. Fig. 6c); 0.02 ThO spectrum (cf. 6b) and a difference of two separate backgrounds, all normalized to a 24 hour period. Note: (i) asymmetry about zero due to bremsstrahlung, (ii) the emergence of weak Am peaks A and B.

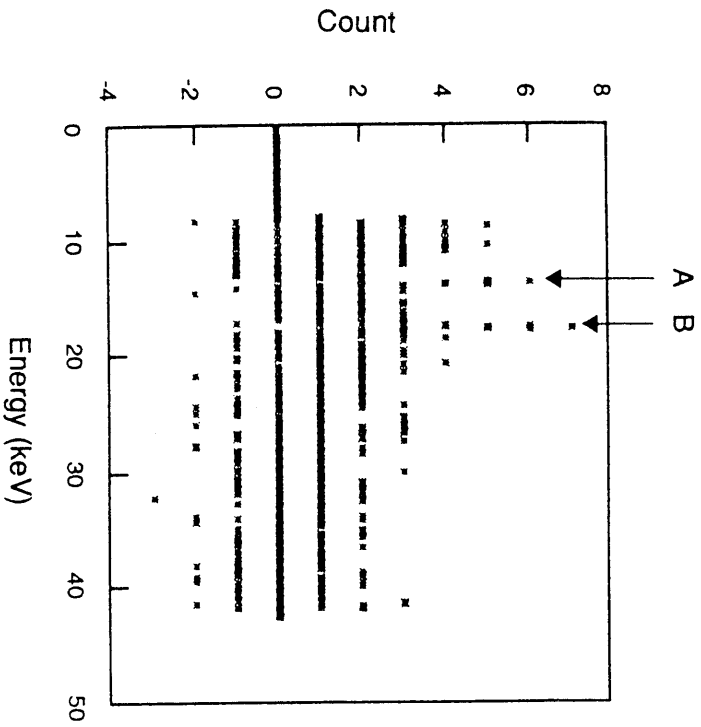
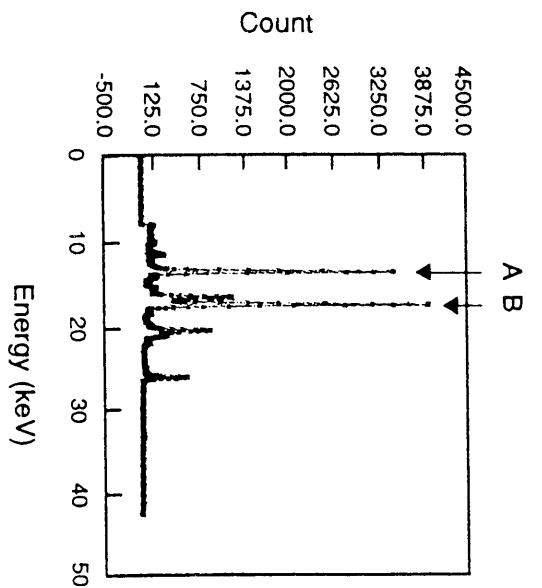
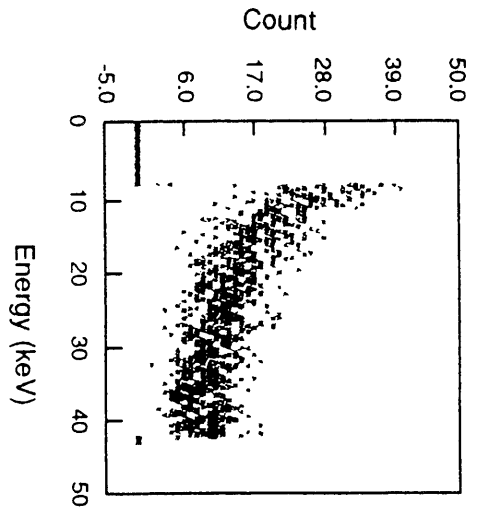
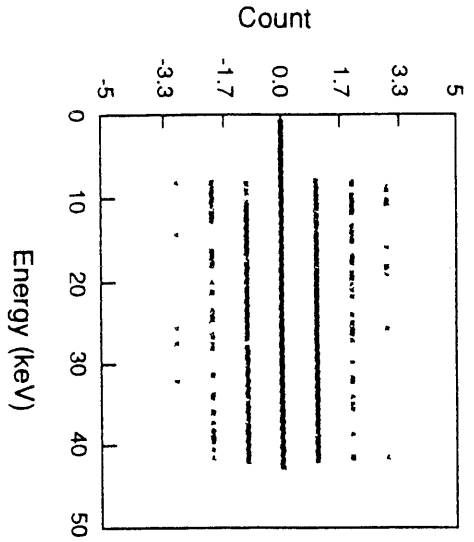












RELIABLE PROCEDURE FOR THE INITIATION
OF THE
FLEISCHMANN-PONS EFFECT

S. Szpak, * *P.A. Mosier-Boss* * and *J.J. Smith* **
* Naval Ocean Systems Center, San Diego, CA 92152-5000
** Department of Energy, Washington, DC 20585

ABSTRACT

Statistics on the initiation of the Fleischmann-Pons effect are rather poor. Reports presented at the First Annual Conference on Cold Fusion have indicated that, at best, only *ca* 1/10 of all attempts were successful in either producing excess enthalpy or yielding products associated with nuclear reactions. Here, we show that the Fleischmann-Pons effect can be reproducibly and rapidly initiated by employing electrodes prepared by electrodeposition from Pd²⁺ salts in the presence of evolving deuterium. The effectiveness of this procedure is examined in terms of tritium production.

1.0 INTRODUCTION

On 23 March 1989, the TV audience, worldwide, learned that substantial amounts of energy can be generated by nuclear events in an electrochemical cell(1). Of many attempts to reproduce reported results, few succeeded and often irreproducibly. Reasons for a low success rate are not known. A generally held opinion is as follows. the Fleischmann-Pons (F.-P.) effect is a threshold phenomenon of a non-steady state character. It is believed that a number of conditions must be met to “switch-on” an electrode with the degree of loading being of paramount importance. The electrode loading, in turn, is governed by processes occurring within the electrode/electrolyte interphase(2). It is generally believed that the F.-P. effect is caused by non-steady state processes which appear as steady-state because of an averaging of small perturbations. The nature of these perturbations is not known but, most likely, they can be expressed in terms of localized gradients of the chemical potential.

In this communication, we report on an experimental procedure to initiate the F.-P. effect, *viz.*, the *Pd/D* co-deposition(3). This approach takes advantage of the existence of localized, time dependent gradients generated by an ever expanding electrode surface, *i. e.*, one that is created under non-steady state conditions. More importantly, it eliminates long charging times. In what follows, we describe the procedure required, provide the evidence for the occurrence of nuclear events *via* tritium production, discuss the morphology of the electrodeposited palladium as well as examine some of the structural aspects of the *Pd* electrode prepared by co-deposition.

2.0 THE PD ELECTRODE

Palladium is very unique in its ability to absorb large quantities of hydrogen isotopes. Basic considerations of the electrochemical charging of the *Pd* rods have led to a model in which the inter-phase region plays a dominant role and the elementary processes govern the transport into the bulk. In particular, we adapted a model where the interphase is not an autonomous entity, *i. e.*, its structure as well as the operating driving forces are determined by participating processes occurring in the bulk phases in contact with each other. In addition to purely electrochemical considerations, the operating forces are subject to mechanical constraints arising from lattice expansion following the absorption of the interstitial, ^nH ; $n = 1,2,3$. This model assumes a position independent surface coverage of the reactive species—a rather unrealistic assumption, as demonstrated by the existence of a region in which there is preferred penetration of ^nH .

Regions of preferred penetration can be displayed using the Nomarski optics where very small dimensional changes can be observed and recorded on a video tape. An example of the changes of the electrode surface obtained by electronically subtracted images recorded on the tape, are shown in Fig. 1. Evidently, even within a single grain, there are preferred sites of absorption. Clearly, an assumption of uniform surface coverage of the *Pd* rod cannot be justified in modeling exercises. An even more serious deficiency is the employment of the simplest interphase when, in fact, a supercharged region exists as indicated by the X-ray diffraction spectra.



Figure 1. Evolution of surface morphology after 2 min. charging. Subtracted image is shown; individual grain is outlined.

2.2 IN SITU X-RAY DIFFRACTION SPECTROMETRY

The diffraction spectrum for the palladium foil immersed in an electrolyte at the rest potential is shown in Fig. 2. After two hours of charging at 1.5 V cathodic overpotential, while the electrode appearance has not changed, its structure has, namely, the formation of β -*PdD* is in evidence (peaks at 39.048° and 42.245° ; 2θ), Fig. 2b. With prolonged charging, the silvery color of metallic palladium has changed to black and, after 24 hours of charging, the recorded spectrum was that of the β -*PdD* phase only. With continued charging at somewhat higher overpotentials, a broadening of peaks is observed with no shift in their location, *i. e.*, indicating the presence of a supercharged layer.

It is of interest to note that, upon termination of the current flow, escape of large quantities of absorbed deuterium occurs.

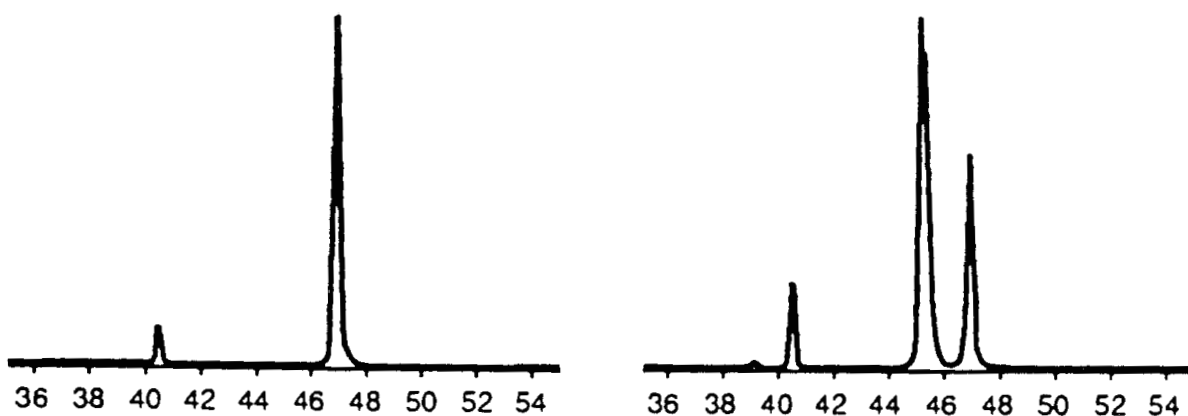


Figure 2. Progress in electrode loading by in situ X-ray diffraction. left – electrode at rest potential; right – after charging for 3 hrs at $\eta = 1.5$ V.

2.3 PREPARATION OF PD ELECTRODE BY PROCESS OF CO-DEPOSITION

Based on the above discussion, a rational approach to construct a *Pd* electrode suitable for rapid initiation of the F.- P. effect is by electrodeposition of palladium in the presence of evolving deuterium(3). In practice this can be done by deposition from a nearly saturated solution of *PdCl*₂, (approx. 0.05 M), in *D*₂*O* containing 0.3 N *LiCl*. The rate of deposition is potentiostatically controlled with the cell potential selected so as to promote vigorous deuterium evolution. Our present practice has been to begin the electrodeposition at a cathodic overpotential of 0.8 V and gradually increasing it to *ca* 3.0 V. The preferred substrate is a copper foil, although nickel has also been used. The evolving deuterium is co-deposited with *Pd* forming the β phase or, perhaps, containing even higher deuterium content. The *Pd* samples, electrodeposited in the presence of evolving deuterium were characterized by X-ray photoelectron microscopy. Resulting spectra were those of extremely pure palladium without traces of *Pt*, *Ag*, *Rh*, *Si*, *Cl*, *i. e.*, elements that could have been deposited in the course of electrolysis(4).

3.0 TRITIUM PRODUCTION

One way to demonstrate the initiation of the F.-P. effect is *via* the tritium enrichment in the electrolyte phase. In an open system and in the absence of nuclear events, the time rate of change of the tritium concentration arises from two sources, *viz.*, the isotopic enrichment and the addition of the tritium containing heavy water needed to maintain a constant electrolyte volume. Typical progress in the codeposition and the onset of tritium production, together with the applied overpotentials, is illustrated in Fig. 3. According to these results, the codeposition process is completed within the first six to eight hours. The onset of tritium production, measured as an increase in dpm in the electrolyte phase, occurs somewhat later, *e.g.*, within hours after completion of co-deposition. The difference between the calculated enrichment, lower curve, and measured tritium concentration in the electrolyte phase indicates tritium production during the process of electrolysis.

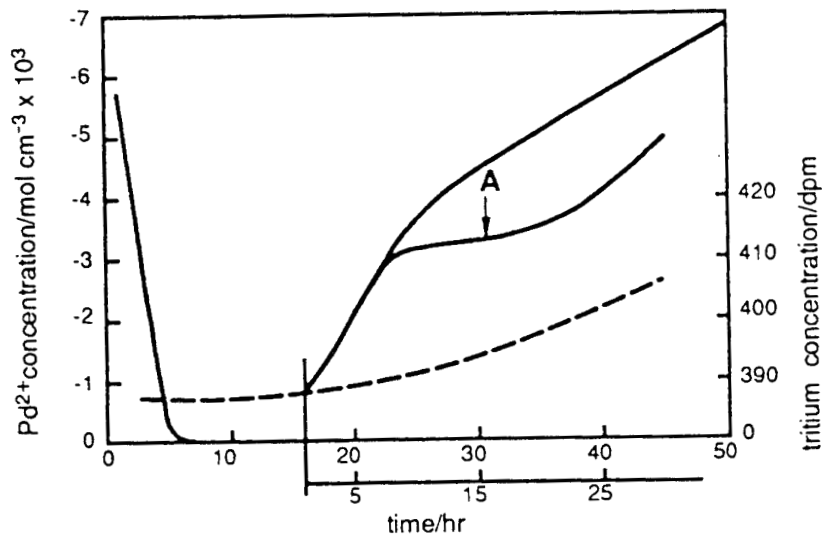


Figure 3. Early period in the co-deposition process. Left – Pd^{2+} concentration as a function of time; right – 3H as a function of time; point A indicates addition of $SC(NH_2)_2$; dashed line – calculated isotopic enrichment.

3.1 TRITIUM DISTRIBUTION: ELECTROLYTE/ELECTRODE/GAS PHASE

Nuclear events producing tritium can occur at one or more locations, *viz.*, at the electrode surface, within the interphase or within the bulk electrode. Our experimental evidence seems to rule out the existence of dendrite assisted processes. Consequently, we adopt the view that these events occur within the *Pd* lattice, inclusive of the metal side of the interphase region. The location of the nuclear events might have a bearing on the distribution of tritium.

Examples of tritium production in cells employing *Pd* electrodes prepared by co-deposition during the electrolysis of D_2O containing dissolved $LiCl$ and Li_2SO_4 (0.3 N) are shown in Fig. 4. The increase in tritium concentration in the electrolyte phase is far greater than that due to the isotopic effect. The same applies to the composition of the gas phase. Most of the tritium generated by the electrochemical compression of deuterium appears to enter the gaseous phase. A cursory examination reveals that the rate of generation is not constant. We cannot ascertain, at this time, whether the change in the rate of production is smooth, or occurs in bursts as in cells using a conventional electrode design.

4.0 ELECTRODE: ITS STRUCTURE AND BEHAVIOR

The reproducibility of the F.-P. effect in cells employing electrodes prepared by the co-deposition process may be attributed to their morphology and purity. The growth form of the electrodeposited *Pd* is affected by processes occurring within the ever-changing interphase, primarily by the surface processes and mass transport. It can be assumed that the electrocrystallization of palladium in the presence of evolving deuterium must accommodate as well as be affected by the presence of deuterium.

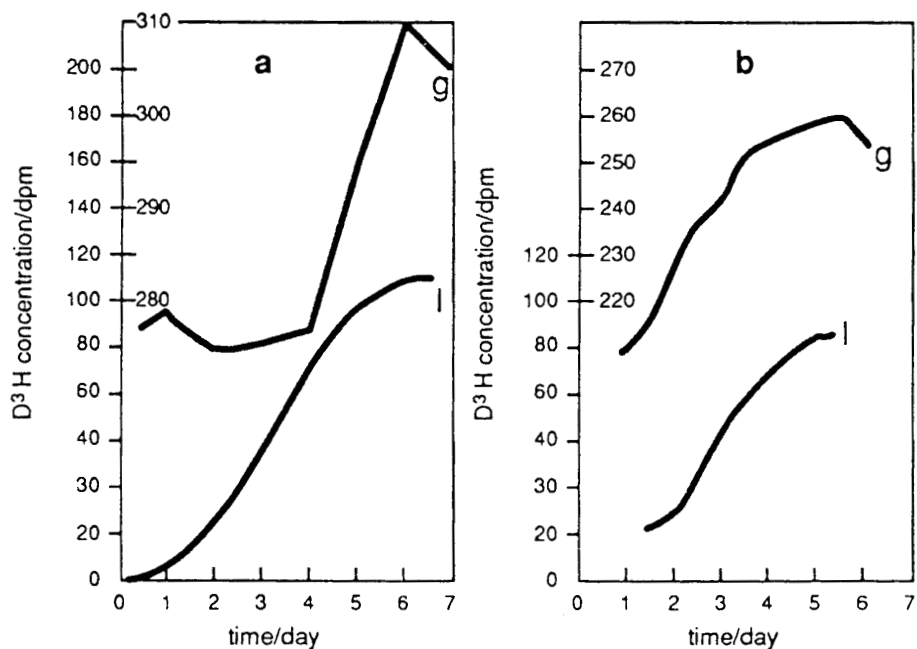


Figure 4. Distribution of 3H generated by electrochemical compression of 2H . Electrolyte: a – 0.3 N $LiCl$ in 2H_2O ; b – 0.3 N Li_2SO_4 in 2H_2O ; 1 – electrolyte phase, g – gas phase.

The SEM photograph is typical of a three-dimensional nucleation. The co-deposited palladium consists of submicron spherical particles, Fig. 5. Such a morphology provides a large surface to volume

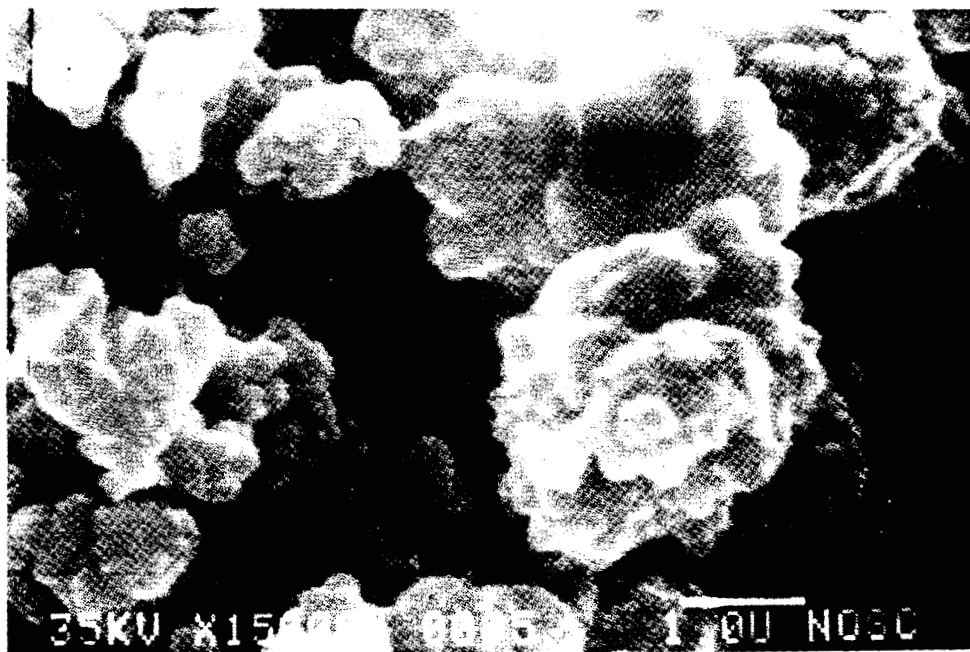


Figure 5. SEM photograph of co-deposited Pd.

ratio and, if a porous structure can be maintained, substantial amounts of deuterium can be absorbed. The remarkable feature of the deposit is its relatively high mechanical strength which can be attributed to the fact that the palladium is saturated with deuterium while being deposited so that further lattice expansion is not necessary. Dandapani and Fleischmann(5) concluded that the slow step is the discharge of D_3O^+ ions in acid solutions and D_2O molecules in alkaline electrolytes, *i. e.*, the charge transfer reaction is followed by a rapid absorption and $\alpha \rightarrow \beta$ phase transformation, followed by a rapid recombination, when the electrode charging has been completed. By charging we mean an accumulation of deuterium on the electrode surface, within the interphase, and within the bulk. Transport of deuterium in the bulk is by diffusion and governed by the time-dependent concentration at the plane separating the interphase from the bulk. Whether or not the electrode charging is controlled by the interphase or the bulk depends on the rate constants of the elementary processes involved in the charge transfer, and to a much lesser degree, by the thickness of the electrode(2).

4.0 CONCLUSIONS

(i) Predictions based on the modeling of the electrochemical charging of *Pd* rods are not reliable because of the lack of relevant input data and the existence of preferred absorption sites. Specification of surface coverage and electrode active areas is questionable.

(ii) At least three periods in the course of electrode charging can be identified. First, initially the β phase is dispersed throughout the *Pd* metallic phase. (The absence of the α phase indicates a rapid $\alpha \rightarrow \beta$ phase transition.) Second, total conversion to the β phase can be recognized by viewing the color of the electrode surface. (Transition from silvery to black). Third, a supercharged layer is formed. (When the $\beta - Pd-Pd$ phase is further charged at high overpotentials).

(iii) Electrodes prepared by the co-deposition process reliably initiate the F.-P. effect, at least in terms of tritium production.

5.1 REFERENCES

1. M. Fleischmann and S. Pons, TV interview, CBS - 23 March 1989 pm PST
2. S. Szpak, C.J. Gabriel, J.J. Smith and R.J. Nowak, *J. Electroanal. Chem.*, **309**, 273 (1991)
3. S. Szpak, P.A. Mosier-Boss and J. J. Smith, *J. Electroanal. Chem.*, **302**, 255 (1991)
4. D.R. Rolison, private communication, March 1991
5. B. Dandapani and M. Fleischmann, *J. Electroanal. Chem.*, **39**, 323 (1972)

6. COMMENTS ON METHODOLOGY OF EXCESS TRITIUM DETERMINATION

Stanislaw SZPAK and Pamela A. MOSIER-BOSS
NRaD, San Diego, CA 92152—5000 USA
Jerry J. SMITH
Dept. of Energy, Washington, DC 20585, USA

ABSTRACT

Three methods of tritium data analysis are considered—comparison between experimental and theoretical data, total mass balance and curve-fitting.

1.0 INTRODUCTION

The evidence for tritium production in electrochemical cells, with few exceptions (Will *et al*, 1992), is based on measurements of tritium increase in the electrolyte phase in excess of that predicted from the isotopic separation factor. Often, this enrichment was computed under conditions of constant electrolyte volume which, in turn, implies continuous additions and withdrawals, a somewhat unrealistic undertaking. In those instances where the total tritium content at the end of an experiment was ten times or more greater than what was present in the beginning, it cannot be disputed that generation of tritium occurred. However, for low levels of tritium production, care must be taken in the analysis, especially if open cells are used. In this communication, we comment on the methodologies of analysis used and point out their advantages and disadvantages.

2.0 USE OF SIMULATED DATA TO EVALUATE METHODS OF TRITIUM ANALYSIS

To evaluate the methods of analyzing tritium, we needed data that would show various degrees of tritium production and include measurements of both the electrolyte and gaseous phases over a fairly long period of time. In addition there could be no question of contamination of tritium from the cell, cell components or outside environment or of erroneous tritium measurements resulting from chemical reactions in the scintillator fluid. To meet all of these requirements, it was deemed necessary to use simulated data.

2.1 Development of Model

In an open cell, a volume of electrolyte, V , is electrolyzed. Throughout the experiment, electrolyte is being withdrawn for tritium analysis and is being replaced. Assuming sampling is instantaneous, for any given time the rate of change of tritium in the electrolyte, $\frac{dT_L}{dt}$; on the recombining electrode, $\frac{dT_R}{dt}$ and in the gas phase, $\frac{dT_G}{dt}$, are given by:

$$\frac{dT_L}{dt} = -\zeta(f_L m_L)\phi - \alpha(f_L m_L) + C \quad (1)$$

$$\frac{dT_R}{dt} = \zeta(f_L m_L)\phi - \alpha(f_R m_R) - \zeta_R(f_R m_R) \quad (2)$$

$$\frac{dT_G}{dt} = \zeta_R(f_R m_R) - \alpha(f_R m_R) \quad (3)$$

where ξ and ξ_R are the isotopic enrichment factor for tritium during electrolysis and on the recombining electrode, respectively; α and C are the radioactive decay rate and generation rate of tritium, respectively, both are in $atoms\ sec^{-1}$; f_L and f_R are the mass fraction of tritium in the electrolyte and on the recombiner, respectively; and $\phi = \frac{ieM_{D_2O}}{2F}$ where M_{D_2O} is the molecular weight of D_2O and ϵ is the Faradaic efficiency. In this model the amount of D/T absorbed/desorbed by the Pd-electrode and losses due to evaporation are not considered. Using these differential equations, simulated data for tritium in the gas and liquid phases were calculated under conditions of no production, low continuous production, continuous production near the end of an experiment, and pulse production. In constructing these data sets, the total volume was fixed at 50 ml; $\xi = 1.8$; $\xi_R = 1.0$, which corresponds to 100% efficiency of the recombiner; $\alpha = 250\ atoms\ sec^{-1}$; and Gaussian noise, with a 1% standard deviation, was superimposed on the calculated values. The simulated data for zero and pulse production are shown in Figure 1.

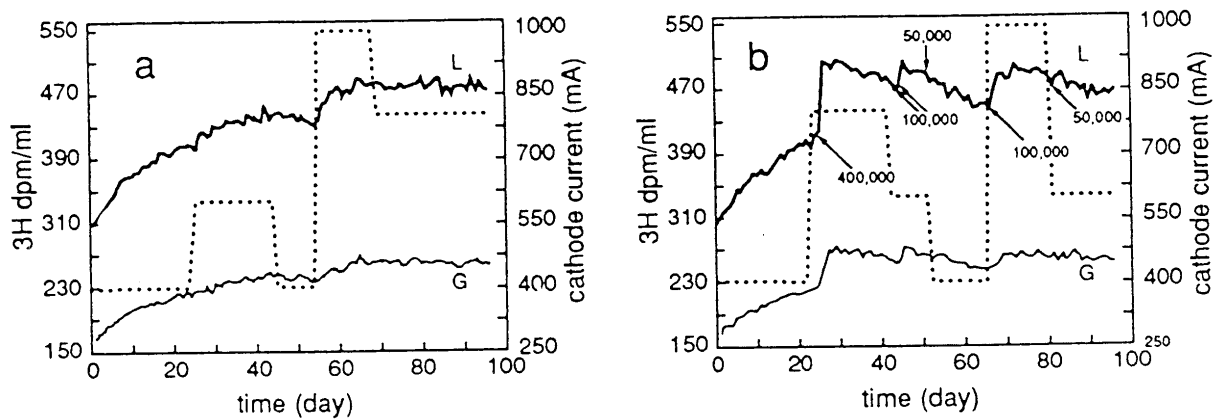


Figure 1. Simulated data for (a) zero tritium production and (b) pulse tritium production. Solid lines are the liquid, L, and gas, G, phase tritium measurements and dotted lines represent the cathodic current profile. Tritium production bursts, in $atoms\ sec^{-1}$, are indicated.

3.0 EXPERIMENTAL METHODS OF ANALYSIS

The methods of analysis fall into three general categories. In one method, samples of the gas and liquid are taken, the tritium content is measured and compared with the theoretical value. The second method is one of total mass balance. The third method utilizes curve-fitting.

3.1 Method 1: Comparison of Experimental and Theoretical Values

Usually theoretical values for the liquid and gas phases are calculated using the expression derived by Bockris et al. (Lin et al, 1990):

$$\frac{a(t)}{a(0)} = \xi - (\xi - 1) \exp\left(\frac{-ti}{2F\xi nV}\right) \quad (4)$$

where $a(0)$ and $a(t)$ are the activity of tritium initially and at time t , respectively, and n is the concentration of D_2O . Equation (4) assumes a constant current, i , and that the number of deuterium atoms far exceeds the number of tritium atoms. It also assumes a constant volume, V ; i.e., after electrolysis for a given time period, D_2O is added to restore the volume prior to sampling. The differential equations (1)–(3) were solved for this experimental procedure to yield data sets under the conditions of no tritium production, $i = 0.4A$, $\xi = 1.8$, $V = 50ml$, $a(0) = 300\ dpm\ ml^{-1}$ and no Gaussian noise on the data.

These data sets were compared to the $a(t)$ values calculated using Eqn. (4). Without correcting for sampling, the data agree well with one another for about one week. Afterwards, the values calculated using Eqn. (4) are much higher. When sampling is included, there is good agreement up to the one month period at which time the values calculated using Eqn. (4) were again larger.

3.2 Method 2: Total Mass Balance

In this approach, for a given time interval, the total amount of tritium in the beginning is compared to the total amount in the liquid and gas phases at the end. For the zero production case, the difference between the amount of tritium at the end and the beginning of a time interval (Δ), followed a Gaussian distribution with Δ 's evenly divided between positive and negative σ 's. In the cases of tritium production, *i.e.*, low continuous production, pulse production and production at the end, the overall distribution of Δ 's was not Gaussian and was skewed towards more positive σ 's. This skewing towards more positive σ 's clearly indicates that tritium was produced.

3.3 Method 3: Curve-fitting

If the initial mass of deuterium and tritium, $m(0)$, is electrolyzed at a constant cell current, i , for a specified period of time, τ , at which time a sample is withdrawn and analyzed for tritium and D_2O is added to restore the initial volume. The tritium mass fraction in the electrolyte, $f_L(t)$, is given by:

$$f_L(t) = [m(0) - \tau(i)t]^{\xi-1} \left[\frac{f_L(0)}{m(0)^{\xi-1}} + \int_{t=0}^{\tau} \frac{Cdt}{[m(0) - \tau(i)t]^{\xi}} \right] \quad (5)$$

where $\tau(i)$ is the rate of removal due to electrolysis. Equation (5) is a general solution of the differential equations (1)-(3) and neglects the radioactive decay and loss by evaporation. As written, Eqn. (5) has two adjustable parameters which will be strongly coupled to one another—the isotopic separation factor, ξ , and the tritium generation rate, C . The simulated data for all four cases were computer analyzed using Eqn. (5). In the zero tritium and low continuous production cases, there was excellent agreement between the data and the computer analyzed curves. However, the computer analyzed curves did not agree with the remaining two cases especially in the regions where the tritium production occurred.

4.0 CONCLUSIONS

All three methods discussed for analyzing tritium data require 100% efficiency of the recombining electrode. Efficiencies less than 100% result in a preferential loss of DT over D_2 in the gas phase. The technique advocated by Bockris and others, that of comparing the measured tritium values with those calculated using Eqn. (4), is valid for short term experiments. This approach requires that the isotopic separation factor, ξ be known. For the Pd/D system, ξ 's ranging from 2 to 10 have been reported. Furthermore, it is assumed that ξ remains constant throughout the course of the experiment. This assumption may not be valid since ξ depends upon the kinetics of the system as well as the current density. With the technique of total mass balance, ξ need not be known nor is it required to remain constant. Likewise with curve-fitting, one does not need to know the value of ξ , but ξ is assumed to be constant. Therefore, when the experimental and computer analyzed curves don't agree, it is not known if ξ was affected or if tritium production occurred. However, curve-fitting does indicate that something happened during the course of the experiment. The total mass balance and curve-fitting approaches require long term experiments in order to achieve a statistically significant analysis. Of the three techniques, curve-fitting is the least sensitive to detecting burst production of tritium.

5.0 References

1. Lin, G.H., Kainthla, R.C., Packham, N.J.C., Velev, O. and Bockris, J.O'M, 1990, *International J. Hydrogen Energy*, 15, 537.
2. Will, F.G., Cedzynska, K., Yang, M-C, Peterson, J.R., Bergeson, H.E., Barrowes, S.C., West, W.J. and Linton, D.C., 1991, Conference Proceedings of the Second Annual Conference on Cold Fusion, June 29- July 4, Como, Italy, pg.373.

The authors would like to acknowledge the contributions of Dr.'s Roger Boss and Cedric Gabriel and the support of Dr. Frank Gordon.